Entwicklung und Einführung eines neuartigen dosimetrischen Formalismus in der Brachytherapie

Dissertation

zur

Erlangung des akademischen Grades des Doktors der Ingenieurwissenschaften (Dr.-Ing.)

Dem Promotionszentrum für Ingenieurwissenschaften
am Forschungscampus Mittelhessen
vorgelegt von

Thomas Failing, M.Sc.

geb. in Wetzlar

Gießen, 2025

Betreuer:	Prof. Dr. Klemens Zink (Technische Hochschule Mittelhessen)
	Prof. Dr. Boris Keil (Technische Hochschule Mittelhessen)
Mentor:	Dr. Frank W. Hensley
Gutachter:	Prof. Dr. Martin Fiebich (Technische Hochschule Mittelhessen)
	Prof. Dr. Kai-Thomas Brinkmann (Justus-Liebig-Universität Gießen)

Angenommen vom Promotionszentrum für Ingenieurwissenschaften am Forschungscampus Mittelhessen

Datum der Disputation: 05. März 2026

Selbständigkeitserklärung

Ich erkläre: Ich habe die vorgelegte Dissertation selbstständig und ohne unerlaubte fremde Hilfe und nur mit den Hilfen angefertigt, die ich in der Dissertation angegeben habe. Alle Textstellen, die wörtlich oder sinngemäß aus veröffentlichten Schriften entnommen sind, und alle Angaben, die auf mündlichen Auskünften beruhen, sind als solche kenntlich gemacht. Ich stimme einer evtl. Überprüfung meiner Dissertation durch eine Antiplagiat-Software zu. Bei den von mir durchgeführten und in der Dissertation erwähnten Untersuchungen habe ich die Grundsätze guter wissenschaftlicher Praxis, wie sie in der entsprechenden Satzung der federführenden Hochschule niedergelegt sind und die mir ausgehändigt wurde, eingehalten.

Leer (Ostfriesland), 10. Juni 2025

Abstract

Brachytherapy is a special application of radiotherapy in which radioactive sources deposit their radiation over short distances to the irradiated target volume. The advantage of this procedure is reduced radiation exposure in the surrounding of the target volume. The special geometric constellation and the use of low energy radiation requires a special formalism for measurement and quantification of the applied dose which differs from the measurement conditions of external beam radiotherapy with linear accelerators.
Both experimental commissioning of a brachytherapy source and verification of a clinical dose rate distribution require precise determination of the dose rate at the investigated position. However, the direct detection of the radiation is accompanied by a disturbance of the actual therapy field, as a detector is introduced into the beam. Therefore the result of this measurement needs to be corrected for the disturbance of the radiation field. This procedure is part of the probe method in dosimetry. Due to the advanced development in computer technology, the associated correction factors can be calculated with sufficient accuracy using Monte Carlo methods. In addition to the absorbed dose, the Monte Carlo simulation also allows calculation of other dosimetric quantities such as the restricted cema also differential in energy, which can contribute to a deeper understanding of detector responses and their associated optimization for dosimetry.
The aim of this work is the development and application of a dosimetric formalism based on Monte Carlo and restricted cema in brachytherapy. For clinical applications, a systematic quantitative determination of correction factors for different detectors such as ionization chambers and solid state detectors in combination with selected brachytherapy sources as well as reference conditions is presented.

Kurzfassung

Bei der Brachytherapie handelt es sich um ein Spezialgebiet der Strahlentherapie, in welcher radioaktive Strahler ihre Dosis auf kurzen Distanzen direkt im bestrahlten Zielvolumen applizieren. Dieses Verfahren hat den großen Vorteil der verringerten Strahlenbelastung in der Peripherie des Zielvolumens. Aufgrund dieser speziellen geometrischen Konstellation und des Einsatzes geeigneter Strahlung bedarf die Bestimmung der absorbierten Dosis eines eigenen Formalismus, welcher sich von den sonstigen Messbedingungen der perkutanen Strahlentherapie mit Linearbeschleunigern abhebt.
Die experimentelle Kommissionierung eines Brachytherapiestrahlers oder die Verifikation einer klinischen Dosisleistungsverteilung erfordern die Messung der vom Strahler verursachten Dosisleistung in einem vorgegebenen Punkt. Zur Bestimmung der absorbierten Punktdosis mit einem realistischen Detektor müssen auf sein Signal einige Korrektionen angewandt werden. Zum einen für die unterschiedliche Energieabsorption vom Detektormaterial und Wasser sowie zum anderen zur Korrektion von Störungen des Strahlungsfeldes durch den Detektor. Dieses Verfahren wird in der Dosimetrie Sondenmethode bezeichnet. Aufgrund der fortgeschrittenen Entwicklung in der Computertechnik können die zugehörigen Korrektionsfaktoren mithilfe von Monte-Carlo Methoden mit hinreichender Genauigkeit berechnet werden. Die Monte-Carlo Simulation ermöglicht neben der absorbierten Dosis auch weitere dosimetrische Größen wie etwa die beschränkte Cema zu berechnen, welche unter anderem durch ihre energiedifferentielle Darstellung zum tieferen Verständnis des Ansprechvermögens von Detektoren und darauf aufbauender Optimierung beitragen können.
Ziel dieser Arbeit ist die Entwicklung und Anwendung eines Monte-Carlo basierten dosimetrischen Formalismus in der Brachytherapie auf Grundlage der beschränkten Cema. Für klinische Anwendungen wird hiermit eine systematische quantitative Bestimmung von Korrektionsfaktoren für verschiedene Detektortypen im Zusammenspiel mit ausgewählten Brachytherapiestrahlern sowie möglichen Referenzbedingungen vorgestellt.

Veröffentlichungen und Konferenzbeiträge

Artikel in peer-reviewed Journals

T. Failing, G. H. Hartmann, F. W. Hensley, B. Keil und K. Zink, "Enhancement of the EGSnrc code egs_chamber for fast fluence calculations of charged particles", Zeitschrift für Medizinische Physik **32**, 417–427 (2022).

G. Rossi, **T. Failing**, M. Gainey, M. Kollefrath, F. Hensley, K. Zink und D. Baltas, "Determination of the dose rate around a HDR ^{192}Ir brachytherapy source with the microDiamond and the microSilicon detector", Zeitschrift für Medizinische Physik **33**, 463–478 (2023).

T. Failing, F. W. Hensley, B. Keil und K. Zink, "Investigations on the beam quality correction factor for ionization chambers in high-energy brachytherapy dosimetry", Physics in Medicine & Biology **69**, 165002 (2024).

T. Failing, R. Behrens, F. W. Hensley, B. Keil, T. Schneider und K. Zink, "Angular dependence of detector responses in high-energy brachytherapy", Physics in Medicine & Biology **70**, 115020 (2025).

Vorträge

T. Failing, F. Hensley und K. Zink, "Anwendung der erweiterten Fluenz-basierten Grundgleichung auf die Dosimetrie niederenergetischer Strahlungsfelder", 51. Jahrestagung der DGMP (2020).

G. Rossi, **T. Failing**, M. Gainey, M. Kollefrath, F. Hensley, K. Zink und D. Baltas, "Investigation on using the microSilicon detector for measurements around high dose rate ^{192}Ir brachytherapy sources", Joint Conference of ÖGMP, DGMP and SGSMP (2021).

G. Rossi, **T. Failing**, M. Gainey, M. Kollefrath und D. Baltas, "Experimentelle Bestimmung der Radialen Dosisfunktion und Anisotropie Funktion einer Brachytherapie-^{192}Ir-HDR-Quelle mit der Semiflex 3D Ionisationskammer", 53. Jahrestagung der DGMP (2022).

T. Failing und K. Zink, "Potentiale des Cema Formalismus für die Dosimetrie hochenergetischer Strahlung", DGMP Arbeitskreis Monte Carlo (2023).

T. Failing, F. W. Hensley und K. Zink, “Strahlungsqualitätskorrektion k_{QR} für ausgewählte Ionisationskammern am TG-43 Referenzpunkt”, 54. Jahrestagung der DGMP (2023).

Poster

T. Failing, F. Hensley und K. Zink, “Quellenpositionierung eines Flexitron Ir-192 HDR Afterloaders mithilfe des Beamscan Wasserphantoms”, 53. Jahrestagung der DGMP (2022).

Inhaltsverzeichnis

Abkürzungsverzeichnis

AAPM	American Association of Physicists in Medicine
BIPM	Bureau International des Poids et Mesures, Frankreich
Co-60 (auch ^{60}Co)	Cobalt-60
CT	Computertomographie
DGMP	Deutsche Gesellschaft für Medizinische Physik e. V.
DIN	Deutsches Institut für Normung e. V.
EGSnrc	Electron Gamma Shower des National Research Council of Canada
ESTRO	European Society for Therapeutic Radiology and Oncology
GEC	Groupe Européen de Curiethérapie
HDR	High dose rate
HEBD	High Energy Brachytherapy Source Dosimetry
IAEA	International Atomic Energy Agency
ICRU	International Commission on Radiation Units and Measurements
Ir-192 (auch ^{192}Ir)	Iridium-192
LET	Linearer Energietransfer
MBDCA	Model-based dose calculation algorithm
MC	Monte-Carlo
mDD	microDiamond Detektor
NAR	DIN-Normenausschuss Radiologie
NIST	National Institute of Standards and Technology, USA
PTB	Physikalisch-Technische-Bundesanstalt, Deutschland
PTW	PTW Freiburg GmbH, Deutschland
Q	Strahlungsqualitätsindex
SEG	Sekundärelektronengleichgewicht
SI	Système international d'unités (internationales Einheitensystem für physikalische Größen)
TG	Task Group
VRT	Varianzreduktionstechnik
XCSE	Photon cross section enhancement
Z	Ordnungszahl

1 Einleitung

Etwa 10 % der Krebspatient*innen, die eine Strahlentherapie erhalten, werden mit Brachytherapie behandelt, entweder als Haupt- oder Zusatzbehandlung, um die Wirksamkeit der Hauptbehandlung zu erhöhen [1]. Der zunehmende Einsatz hochwertiger Behandlungen mit Brachytherapie erfordert eine genauere Dosimetrie auf der Grundlage von Primärstandards für die absorbierte Wasser-Energiedosis sowie ihrer räumlichen Verteilung, um die Genauigkeit bei der Behandlung zu erhöhen [2]. In der klinischen Praxis der Brachytherapie hat sich die Berechnung der absorbierten Wasser-Energiedosisleistung methodisch nach dem Formalismus des Task Group Report No. 43 (TG-43) der American Association of Physicists in Medicine (AAPM) [3, 4] etabliert, bei welchem die Kenn-Dosisleistung des verwendeten Brachytherapiestrahlers über die messbare Luftkermastärke bestimmt und anschließend in eine Wasser-Energiedosisleistung umgerechnet wird. Die zugehörige Referenzdosimetrie basiert üblicherweise auf der Ermittlung der Luftkermastärke mit auf Primärnormale rückführbar kalibrierte Schachtionisationskammern [5]. Die Bestimmung der Luftkerma in Luft entspricht jedoch nicht den Absorptions- und Streubedingungen bei der Bestrahlung. Zudem wird die Dosis in der Strahlentherapie über die absorbierte Wasser-Energiedosis definiert [6, 7]. Des Weiteren beinhaltet die Überführung von Luftkermastärke in absorbierte Wasser-Energiedosisleistung eine zusätzliche Unsicherheit. Aktuelle Dosimetrieprotokolle empfehlen deshalb als konsistente Bezugsgröße die absorbierte Wasser-Energiedosis [2, 7]. Es existieren bereits Primärstandards der absorbierten Wasser-Energiedosisleistung zur Referenzdosimetrie in der Brachytherapie, jedoch ist die Durchführung messtechnisch sehr aufwendig [8].
Das Ziel dieser Arbeit ist damit die Entwicklung und Anwendung eines Formalismus zur Bestimmung der absorbierten Dosisleistung in Wasser um Brachytherapiestrahler mit klinischem Equipment. Dabei ist entscheidend, welche Einflüsse das Ansprechvermögen von Detektoren in der Brachytherapie bestimmen, um daraufhin Korrektionsfaktoren zu ermitteln, welche hier auf Monte-Carlo (MC) Simulationen beruhen. Der Einsatz von universellen MC Applikationen zur Simulation des Strahlungstransports ermöglicht es zudem, neben der absorbierten Dosis weitere aufschlussreiche dosimetrische Größen wie etwa die beschränkte Cema auch energiedifferentiell zu untersuchen, um ein tieferes Verständnis über die Signalerzeugung in Detektoren zu erlangen [9].
In der Dosimetrie der perkutanen Strahlentherapie ist es gängige Praxis, Dosisverteilungen mit kleinen Detektoren zu messen. Dies ist für die Brachytherapie noch nicht der Fall, da aktuell vergleichbare Standards sowie etablierte Korrektionsfaktoren fehlen. Bisherige Messungen sind daher üblicherweise beschränkt auf einzelne Punkte im Strahlungsfeld eines einzelnen Strahlers [10–13]. Es existieren Daten zur Korrektion aufgrund veränderter Strahlungsqualität gegenüber der Kalibrierung (k_Q) [10, 13–18], jedoch fehlt

bisher ein systematischer Vergleich dieser Daten sowie eine detaillierte Untersuchung der zugrundeliegenden Einflüsse. Die bisher gewählten Ansätze zur Messung der absorbierten Wasser-Energiedosisleistung sind ausreichend für Verifikationen des TG-43 Formalismus, da sich die Dosisleistungsverteilung hier aus der Superposition einzelner Strahler in einer homogenen Wasserumgebung zusammensetzt. Mit der Einführung von ‚Model-based Dose Calculation Algorithms' (MBDCAs) ist es möglich, realistische klinische Streubedingungen zu berücksichtigen, welche zu einer genaueren Dosisberechnung führen [19]. Eine experimentelle Verifikation dieser Berechnungsalgorithmen, welche von der AAPM empfohlen wird [20], beschränkt sich bisher auf Machbarkeitsstudien [21, 22].

Die vorliegende Arbeit stellt die theoretischen Grundlagen zur Dosimetrie um hochenergetische Afterloadingquellen in der Brachytherapie zusammen, definiert die Zielsetzung, ordnet die zugehörigen Veröffentlichungen in den wissenschaftlichen Kontext ein und vergleicht abschließend auf übergeordneter Ebene die gewonnenen Ergebnisse, um daraus praktische Empfehlungen abzuleiten. Sie besteht als kumulative Dissertation aus vier aufeinander aufbauenden Publikationen. Die erste Publikation befasst sich dabei mit der Erweiterung eines bestehenden MC Codes zur Ausgabe der energiedifferentiellen Fluenz sowie beschränkten Cema, da dies bisher nur eingeschränkt möglich ist. Die zweite Publikation widmet sich der Verwendung von kalibrierten Halbleiterdetektoren zur Bestimmung der Dosisleistungsverteilung um Afterloadingstrahler, welche in Kooperation mit der Abteilung für Medizinische Physik aus der Medizinischen Fakultät der Universität Freiburg erfolgt ist. Die dritte Publikation befasst sich mit der Ermittlung und Untersuchung der Zusammensetzung von Strahlungsqualitäts-Korrektionsfaktoren für Ionisationskammern und zugehöriger Referenzbedingungen in der Brachytherapie. Die vierte Publikation untersucht die Winkelabhängigkeit des Ansprechvermögens der Detektoren für den Einsatz in klinisch relevanten Szenarien. Die Ergebnisse sollen die Grundlage für eine zukünftige DIN-Norm zur Bestimmung von Dosisleistungsverteilungen in der Brachytherapie bilden.

2 Grundlagen

2.1 Brachytherapie

Bei der Brachytherapie handelt es sich um ein Spezialgebiet der Strahlentherapie, in welcher umschlossene radioaktive Strahler ihre Dosisleistung auf kurzen Distanzen direkt oder in unmittelbarer Nähe des Zielvolumens applizieren. Die Dosisleistungsverteilung folgt dabei in erster Näherung dem Abstandsquadratgesetz. Dies besagt, dass sich durch die Divergenz der Strahlung die Dosisleistung umgekehrt proportional zum Quadrat des Abstands verhält. Die Brachytherapie hat damit den großen Vorteil der verringerten Strahlenbelastung in der Peripherie bei gleichzeitiger Dosiseskalation im Zielvolumen. Durch eine geeignete Applikation kann zudem sichergestellt werden, dass sich die Strahler an der vorgesehenen Position relativ zum Zielvolumen befinden, so dass Bewegungen kompensiert werden können.
Aktuell ist die häufigste Applikationsform der Brachytherapie das sogenannte Nachladeverfahren (englisch: afterloading). Die Strahlenquelle ist dafür an einem Draht fixiert und kann somit von einem Afterloading-Gerät ferngesteuert und strahlengeschützt bewegt werden. Über einen oder mehrere nichtaktive Platzhalter (Applikatoren), welche über Transferschläuche mit dem Afterloader verbunden sind, kann die Quelle an definierte Positionen im Applikator gebracht werden. Mithilfe von bildgebenden Verfahren wie Computertomographie (CT), Magnetresonanztomographie oder Sonographie wird dazu von der behandelten Person mit implantiertem Applikator ein dreidimensionaler Bilddatensatz erstellt, auf welchem die Bestrahlungsplanung erfolgt. Ziel der Bestrahlungsplanung ist die Berechnung und Optimierung der Dosisverteilung im Patienten. Beim Afterloading setzt sich die applizierte Dosis aus der Überlagerung einzelner Dosisleistungsverteilungen der Quelle zusammen. Diese enthält in der Regel einen Gammastrahler, so dass die Dosisleistung sowohl der räumlichen Verteilung als auch dem radioaktiven Zerfall unterliegt. Zusammenfassend wird die geplante Dosisverteilung beim Afterloading über Haltepunkte und Standzeiten der Strahlenquelle realisiert.
Zur sicheren und reproduzierbaren Anwendung der Brachytherapie ist somit die dosimetrische Charakterisierung der Strahler essentiell. Ziel dieser Arbeit ist die Entwicklung und Anwendung eines Formalismus, um die Dosisleistungsverteilung von Brachytherapiestrahlern mithilfe geeigneter Detektoren nach aktuellem Stand von Wissenschaft und Technik zu bestimmen. Diese Arbeit beschränkt sich dabei auf die Untersuchung von Iridium-192 (Ir-192) Afterloadingquellen. Die Methodik lässt sich jedoch auf andere Strahlertypen übertragen.

2.2 Fundamentale dosimetrische Größen

2.2.1 Wasser-Energiedosis

Die Menge an deponierter Energie wird durch die absorbierte Dosis D in der SI-Einheit Gray ($1\,\mathrm{Gy} = 1\,{}^{\mathrm{J}}/_{\mathrm{kg}}$) definiert und als Maß für die biologische Wirkung angenommen. Die als Punktgröße definierte absorbierte Dosis ergibt sich aus dem Differentialquotienten

$$D = \frac{\mathrm{d}\bar{\epsilon}}{\mathrm{d}m} = \frac{1}{\rho}\frac{\mathrm{d}\bar{\epsilon}}{\mathrm{d}V} \tag{2.1}$$

mit der Strahlungsenergie $\mathrm{d}\bar{\epsilon}$, welche in Materie der Masse $\mathrm{d}m$ oder Volumen $\mathrm{d}V$ mit zugehöriger Massendichte ρ über das Massen- oder Volumenelement gemittelt absorbiert wird. Die absorbierte Strahlungsenergie ϵ setzt sich aus allen Energiebeiträgen ϵ_i der beteiligten ionisierenden Strahlung in dem betrachteten Volumen (welches zu $\mathrm{d}m$ gehört) zusammen, so dass gilt $\epsilon = \sum_i \epsilon_i$. Jeder Energiebeitrag ϵ_i setzt sich jeweils aus einer einzelnen Wechselwirkung i zusammen. Der Nettobetrag für ϵ_i errechnet sich durch $\epsilon_i = \epsilon_{\mathrm{in}} - \epsilon_{\mathrm{out}} + U$, wobei ϵ_{in} der Energiebeitrag (ohne Ruheenergie) des ionisierenden Teilchens ist, welches in das Volumen eindringt, und ϵ_{out} die Gesamtenergie (ohne Ruheenergie) aller geladenen und ungeladenen ionisierenden Teilchen beziffert, welche das Volumen verlassen. U beschreibt die Änderung der Ruheenergie des Atomkerns und aller Elementarteilchen, die bei der Wechselwirkung beteiligt sind [23].
Da die zugeführte Energie wiederum vom Material abhängt, ist es essenziell, für die Dosis auch ein Bezugsmaterial anzugeben. Die absorbierte Dosis in menschlichem Gewebe lässt sich gut durch die Wasser-Energiedosis D_w annähern, so dass diese die zentrale dosimetrische Größe in der Strahlentherapie darstellt [24]. Darüber hinaus wird bei der Dosisberechnung in der Strahlentherapie üblicherweise angenommen, dass die Patient*innengeometrie aus Wasser unterschiedlicher Dichten besteht.

2.2.2 Fluenz

Die Fluenz Φ berechnet sich aus dem Differential $\Phi = {}^{\mathrm{d}N}/_{\mathrm{d}a}$ mit der Anzahl an Teilchen $\mathrm{d}N$, welche in ein infinitesimales Flächenelement $\mathrm{d}a$ eindringen und bezieht sich damit auf einen mathematischen Punkt in einem Medium. Für numerische Anwendungen wird häufig die mittlere Fluenz $\bar{\Phi}$ herangezogen, welche sich auf Grundlage eines Theorems von Kellerer [25] durch die Summe der Teilchenspurlängen $\mathrm{d}s$ im Volumenelement $\mathrm{d}V$ berechnet mit

$$\bar{\Phi} = \frac{\sum \mathrm{d}s}{\mathrm{d}V} \quad \left(\text{Einheit } \mathrm{cm}^{-2}\right). \tag{2.2}$$

Des Weiteren lässt sich die mittlere Zahl von Teilchen einer (kinetischen) Teilchenenergie E als Energiefluenz differentiell berechnen als

$$\bar{\Phi}_E = \frac{\mathrm{d}\bar{\Phi}}{\mathrm{d}E} \quad \left(\text{Einheit } \mathrm{cm}^{-2}\,\mathrm{MeV}^{-1}\right), \tag{2.3}$$

wobei $\mathrm{d}\Phi$ die Fluenz mit Energien zwischen E und $E + \mathrm{d}E$ darstellt [26].

2.2.3 Wirkungsquerschnitt

Ein Wirkungsquerschnitt σ ist für einfallende geladene oder ungeladene Teilchen auf das Zielobjekt bezüglich einer bestimmten Wechselwirkung definiert durch

$$\sigma = \frac{P}{\Phi} \quad \left(\text{Einheit cm}^2\right), \tag{2.4}$$

wobei P die Wahrscheinlichkeit für diese Interaktion bei der gegebenen Fluenz darstellt [26]. Für MC Simulationen des Strahlungstransports ist eine möglichst genaue Kenntnis der zugrundeliegenden Wirkungsquerschnitte essentiell; dieser Begriff ist in Abschnitt 2.3 definiert.

2.2.4 Bremsvermögen

Das lineare Bremsvermögen S in einem Medium der Massendichte ρ berechnet sich für geladene Teilchen durch

$$\frac{S}{\rho} = \frac{1}{\rho}\frac{\mathrm{d}E}{\mathrm{d}l} \quad \left(\text{Einheit MeV cm}^2\,\text{g}^{-1}\right) \tag{2.5}$$

mit dem mittleren Energieverlust $\mathrm{d}E$ den das geladene Teilchen auf der Strecke $\mathrm{d}l$ erfährt. Der Energieverlust setzt sich aus drei verschiedenen Wechselwirkungen zusammen:

$$\frac{S}{\rho} = \frac{1}{\rho}\left(\frac{\mathrm{d}E}{\mathrm{d}l}\right)_{\text{el}} + \frac{1}{\rho}\left(\frac{\mathrm{d}E}{\mathrm{d}l}\right)_{\text{rad}} + \frac{1}{\rho}\left(\frac{\mathrm{d}E}{\mathrm{d}l}\right)_{\text{nuc}}, \tag{2.6}$$

wobei sich die Indizes der Bremsvermögen auf (Stoß-)Wechselwirkungen mit Elektronen aus den Atomhüllen des Mediums („el“), Erzeugung von Bremsstrahlung im Feld des Atomkerns („rad“) und elastischen Coulomb-Wechselwirkungen mit dem Atomkern („nuc“) beziehen [27]. Für den betrachteten Energiebereich dieser Arbeit $\lessapprox 1\,\text{MeV}$ ist fast ausschließlich das elektronische Bremsvermögen, $\left({}^{\mathrm{d}E}/_{\mathrm{d}l}\right)_{\text{el}} = S_{\text{el}}$, zu berücksichtigen [28]; der dritte Term aus Gleichung 2.6 kann für Elektronen komplett vernachlässigt werden [27]. Auch wenn ${}^{S}/_{\rho}$ relativ zur Massendichte angegeben wird, kann für bestimmte Energien und nicht-gasförmige Medien ein zusätzlicher sogenannter Dichteeffekt beobachtet werden [29]; für den in dieser Arbeit betrachteten Energiebereich beträgt die Auswirkung einige Prozentpunkte, so dass dieser Effekt hier berücksichtigt werden muss [30].
Mit Report 37 der International Commission on Radiation Units and Measurements (ICRU) [31] wird das *beschränkte elektronische Bremsvermögen* $S_{\text{el}}(E, \Delta)$ definiert, welches den mittleren Energieverlust durch Elektronenstöße unterhalb einer bestimmten Grenzenergie Δ beschreibt. Die kinetische Energie der beteiligten Elektronen liegt somit unterhalb von Δ, so dass dieser Parameter die mögliche Reichweite der nachverfolgten Elektronen bestimmt. Ab einer bestimmten Grenzenergie $\Delta \geq {}^{E}/_{2}$ gilt für Elektronen $S_{\text{el}}(E, {}^{E}/_{2}) = S_{\text{el}}$, so dass es sich dann um das *unbeschränkte elektronische Bremsvermögen* handelt [31].

2.2.5 Linearer Energietransfer (LET)

Nach ICRU Report 85a [23] wird der lineare Energietransfer L_Δ durch den Differentialquotienten

$$L_\Delta = \frac{\mathrm{d}E_\Delta}{\mathrm{d}l} \quad \left(\text{Einheit MeV cm}^{-1}\right) \tag{2.7}$$

beschrieben mit dem mittleren Energieverlust $\mathrm{d}E_\Delta$ der geladenen Teilchen aufgrund von elektronischen Wechselwirkungen beim Durchqueren der Länge $\mathrm{d}l$, aber ohne die mittlere Summe der kinetischen Energien $E_{\mathrm{ke},\Delta}$ freigesetzter Elektronen mit Energien $\geq \Delta$. Der lineare Energietransfer hängt mit dem linearen elektronischen Bremsvermögen über $L_\Delta = S_{\mathrm{el}} - {}^{\mathrm{d}E_{\mathrm{ke},\Delta}}/_{\mathrm{d}l}$ zusammen, wobei der hintere Term der mittleren Summe der kinetischen Energien $> \Delta$ aller Elektronen entspricht, welche durch die geladenen Teilchen freigesetzt wurden. Der Unterschied zwischen dem beschränkten elektronischen Bremsvermögen $S_{\mathrm{el}}(E, \Delta)$ und L_Δ beruht auf der unterschiedlichen Berücksichtigung der Bindungsenergien freigesetzter Ladungsträger: L_Δ enthält die gesamte Bindungsenergie wohingegen $S_{\mathrm{el}}(E, \Delta)$ nur diejenige bis zur Schwellenergie Δ enthält.

2.2.6 Beschränkte Cema

Basierend auf der Definition aus ICRU Report 90 [27] berechnet sich die beschränkte *Converted Energy per MAss* (Cema) nach

$$C_\Delta = \int_\Delta^\infty \Phi_E \, {}^{L_\Delta}/_{\rho} \, \mathrm{d}E + TE_\Delta \tag{2.8}$$

mit den zuvor definierten Größen energiedifferentielle Fluenz Φ_E und linearer Energietransfer ${}^{L_\Delta}/_{\rho}$ für geladene Teilchen in einem Medium. Aufgrund des untersuchten Energiebereichs dieser Arbeit $E \lessapprox 1\,\mathrm{MeV}$ kann praktisch nur die Freisetzung von Elektronen als Sekundärteilchen angenommen werden. Analog zum LET ist die Angabe einer (unteren) Schwellenenergie Δ erforderlich, bis zu der die Elektronen verfolgt werden. Daraus ergibt sich der sogenannte ‚track end term' TE_Δ welcher alle Energiebeiträge $< \Delta$ umfasst. Die beschränkte Cema kann als Näherung für die von geladenen Teilchen absorbierte Dosis verwendet werden. Die Güte der Näherung hängt davon ab, inwieweit ein partielles Sekundärelektronengleichgewicht (SEG) besteht und überwundene Bindungsenergien sowie Strahlungsverluste vernachlässigbar sind. Ein partielles SEG bezieht sich auf die Ladungsträger mit kinetischen Energien unterhalb der Schwellenergie Δ und ist dann an einem Punkt erreicht, wenn die Fluenz der Sekundärelektronen mit kinetischen Energien $< \Delta$ innerhalb ihrer maximalen Reichweite konstant ist [9, 27, 32]. Hauptsächlich unterscheiden sich die absorbierte Dosis und die beschränkte Cema um die Bindungsenergien der freigesetzten Elektronen im beobachteten Volumen, so dass die beschränkte Cema immer kleiner als die absorbierte Dosis ist [33]. Die numerische Äquivalenz der beiden dosimetrischen Größen sowie deren Verhältnisse wurde bereits für punktförmige Volumina untersucht. Bei der Strahlungsqualität von Ir-192 und $\Delta = 10\,\mathrm{keV}$ gilt: ${}^{D_w}/_{C_{\Delta,w}} = 1,001$ und ${}^{D_{\mathrm{Luft}}}/_{C_{\Delta,\mathrm{Luft}}} = 1,0025$ [34]. Für Strahlungsqualitäten niedrigerer Energien als Ir-192 nehmen die Abweichungen zu [9, 34].

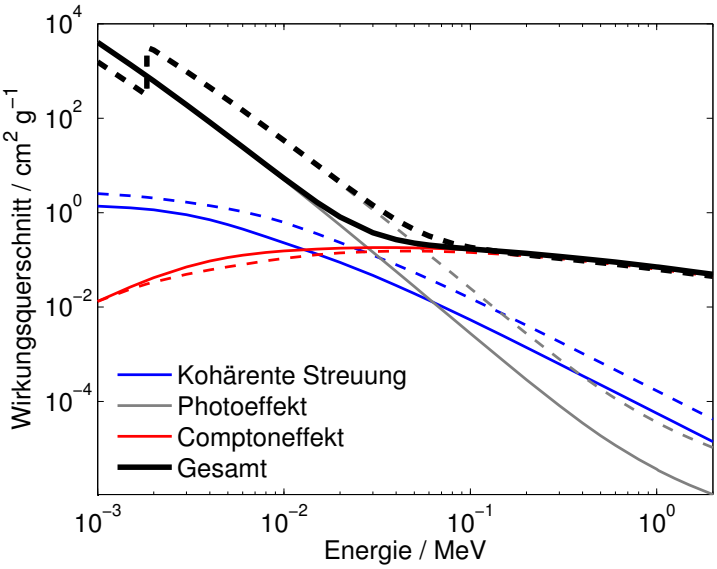

Abbildung 2.1: Numerische Darstellung der Wirkungsquerschnitte für den Photo- und Comptoneffekt sowie die kohärente Streuung in Wasser (durchgezogene Linien) und Silizium (gestrichelte Linien) bezogen auf deren Massendichte [35].

2.2.7 Photon-Elektron-Wirkungsquerschnitte

Im ICRU Report 90 [27] sind alle physikalischen Prozesse und Wechselwirkungen für die Berechnung des Strahlungstransports in MC Simulationen beschrieben. Für Photonen hat sich die XCOM Datenbank des National Institute of Standards and Technology (NIST) [35] als Referenz für Wirkungsquerschnitte etabliert; die Daten dieser beiden Werke dienen als Quelle für die hier durchgeführten Simulationen. Die Gesamtheit aller Wirkungsquerschnitte ungeladener Teilchen bezogen auf ihre Massendichte wird Massenabsorptionskoeffizient μ/ρ genannt. Aufgrund der typischen Energien in der Brachytherapie $\lessapprox 1\,\mathrm{MeV}$ sind der Photo- und Comptoneffekt sowie die kohärente Streuung für den Strahlungstransport relevant. Exemplarisch für alle verwendeten Materialien dieser Arbeit sind in Abb. 2.1 die zugehörigen Wechselwirkungsquerschnitte für Wasser und Silizium bezogen auf deren Massendichte dargestellt. Im Folgenden werden diese elementaren Prozesse kurz erklärt:
Der Photoeffekt (genauer photoelektrische Absorption) beinhaltet die Interaktion eines Photons und damit einhergehenden vollständigen Energieübertrags auf ein gebundenes Hüllenelektron, welches infolgedessen aus der Bindung mit dem Atomkern gelöst wird. Durch diesen Vorgang wird das Photon komplett absorbiert. Der Wirkungsquerschnitt des Photoeffekts hängt maßgeblich von der Ordnungszahl Z des absorbierenden Mediums sowie der Photonenenergie ab. Dies ist in Abb. 2.1 bezüglich der Energie und beim Vergleich der Materialien Silizium ($Z = 14$) und Wasser ($Z \approx 7$) zu erkennen.

Beim Comptoneffekt handelt es sich auch um eine Wechselwirkung eines Photons mit einem Elektron, jedoch findet hier kein vollständiger Übertrag von Energie und Impuls statt. Vielmehr wird das Photon gestreut, so dass dieses seine Energie teilweise an das Elektron überträgt und des Weiteren eine Richtungsänderung erfährt. Durch diese Wechselwirkung wird ein freies Elektron generiert. Für diesen Effekt gilt keine deutliche Abhängigkeit von der Photonenenergie oder Ordnungszahl, jedoch ist die Dichte des Mediums zu beachten.
Die kohärente Streuung beinhaltet auch die Interaktion von Photon und Hüllenelektronen, jedoch findet keine Ionisation statt. Vielmehr geschieht eine Anregung der Elektronen, in der Frequenz der einfallenden elektromagnetischen Strahlung zu schwingen. Der durch die Schwingung entstehende Dipol regt sich nun durch Emission eines Lichtquants gleicher Frequenz ab. Effektiv wird ein initiales Photon nur in seiner Richtung gestreut. Analog zum Photoeffekt begünstigen eine hohe Ordnungszahl und eine niedrige Photonenenergie diese Wechselwirkung (siehe Abb. 2.1).

2.2.8 Kerma

Die *Kinetic Energy Released per unit MAss* K ist die auf Sekundärteilchen der ersten Generation übertragene kinetische Energie E_{tr} im Verhältnis zur bestrahlten Masse eines Mediums. Daraus ergibt sich der Differentialquotient

$$K = \frac{\mathrm{d}E_{\mathrm{tr}}}{\mathrm{d}m} = \frac{1}{\rho}\frac{\mathrm{d}E_{\mathrm{tr}}}{\mathrm{d}V} \tag{2.9}$$

in der Einheit Gray. Obwohl hier im Unterschied zur absorbierten Dosis nur die initialen Energieüberträge auf geladene Sekundärteilchen betrachtet werden, wird diese Größe oft als Näherung für die absorbierte Dosis verwendet. Der numerische Wert der Kerma nähert sich dem der absorbierten Dosis in dem Maße, in dem ein Sekundärelektronengleichgewicht besteht, mögliche Strahlungsverluste vernachlässigbar und die Energien der ungeladenen Teilchen größer als die Bindungsenergien der freigesetzten geladenen Teilchen sind [27].

2.3 Monte-Carlo Simulationen

Mithilfe des Monte-Carlo (MC) Verfahrens ist es möglich, analytisch nicht oder nur aufwendig lösbare Probleme mit Hilfe der Wahrscheinlichkeitstheorie numerisch mit hinreichender Genauigkeit zu lösen. Bezogen auf den Strahlungstransport bedeutet dies, dass unter Annahme der Kenntnis der Streuquerschnitte für elementare Wechselwirkungen der Weg und die Energieübertragung jedes einzelnen ionisierenden Teilchens innerhalb des untersuchten Bereiches vollständig beschrieben wird. Aus der Überlagerung des Transports vieler einzelner ionisierender Teilchen mit statistisch verteilten Wechselwirkungsparametern lässt sich damit eine statistische Aussage über das Verhalten der Energiedeposition eines gesamten Strahlungsfeldes gewinnen. Aufgrund der Entwicklung der

Computertechnik ist es heute möglich, dieses Verfahren für eine hinreichende Genauigkeit im Bereich der Strahlentherapie zu nutzen, so dass dieses seitdem als der ‚Goldstandard' in der Dosimetrie gilt. Da es sich bei Computern a priori um deterministische Systeme handelt, verwendet man sogenannte Pseudo-Zufallszahlengeneratoren[1], um gegebene stochastische Problemstellungen numerisch zu lösen. Der Vorteil dieses Verfahrens ist die Reproduzierbarkeit, da aus den Anfangsbedingungen die Lösung determiniert ist. Die Unsicherheit der Simulation wird durch die Unsicherheit der physikalischen Wechselwirkungen bestimmt. Da die Simulation auf vereinfachenden Annahmen beruht, handelt es sich hier immer um eine Modellbildung, welche eine Verifikation benötigt. [36]
Für die MC Simulationen dieser Arbeit wurde EGSnrc (Electron Gamma Shower des National Research Council Canada) [37] verwendet. Ein wichtiger Parameter stellt hier die Transport-Schwellenergie `ECUT` dar, bis zu der geladene Teilchen nachverfolgt werden und entspricht Δ in der beschränkten Cema. Δ sollte dabei hinreichend klein gewählt werden, um die Simulationsergebnisse nicht zu verfälschen. Bei der Wahl eines geeigneten Werts von Δ ist jedoch zu berücksichtigen, dass abhängig vom MC Algorithmus, wie etwa bei EGSnrc, anstatt des LET in Gleichung 2.8 aus Abschnitt 2.2.5 das beschränkte elektronische Massen-Bremsvermögen aus Abschnitt 2.2.4 verwendet wird [38]. Dadurch könnten bei einem Wert von Δ in der Größenordnung der Ionisationsenergien des absorbierenden Mediums Abweichungen von mehreren Prozentpunkten entstehen [39, 40].

2.4 Detektoren

2.4.1 Ionisationskammern

Ionisationskammern sind die am häufigsten verwendeten Detektoren in der Strahlentherapie. In dieser Arbeit werden luftgefüllte Zylinderkammern untersucht, welche schematisch in Abb. 2.2 dargestellt sind. Eine elektrische Spannung von mehreren hundert Volt wird dafür zwischen der Zentralelektrode und der Innenseite der Kammerwand angelegt, so dass ionisierte Atome und Elektronen entlang des elektrischen Feldes innerhalb der Luftkavität zu den Elektroden wandern. Die Spannung ist dabei so groß zu wählen, dass Rekombinationsverluste möglichst unterdrückt werden, jedoch keine zusätzlichen Stoßionisationen der durch die absorbierte Strahlung freigesetzten Elektronen und Ionen auftreten. In diesem Arbeitsbereich der Ionisationskammer verhält sich die erzeugte Ladung proportional zur deponierten Energie der Strahlung und kann mithilfe eines Elektrometers ausgelesen werden. Um Leckströme zwischen der Zentralelektrode und Kammerwand zu vermeiden, sind bei den Ionisationskammern dieser Arbeit sogenannte Schutzringe (englisch: guard rings) zwischen den beiden Elektroden im Kammerstamm und angrenzend zum Luftvolumen verbaut. Die Schutzringe sind auf das gleiche Potential wie ihre zugehörigen Zentralelektroden gesetzt, aber nicht mit einem Elektrometer verbunden. Dadurch sind die sensitiven Volumina nicht identisch mit den Gesamtvolumina

[1] Es sind Zufallszahlengeneratoren, welche aber immer nur durch einen Pseudo-Zufall funktionieren. Damit lassen sich jedoch statistische Verteilungen bekanntermaßen gut simulieren.

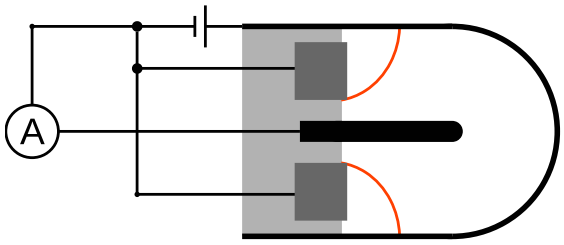

Abbildung 2.2: Schematische Darstellung einer luftgefüllten Ionisationskammer mit Kammerwand (äußere dicke Linie), Zentralelektrode (innere dicke Linie), Schutzring (dunkelgrau) und Kammerstamm (hellgrau) sowie Verschaltung mit einem Elektrometer zur Messung der erzeugten Ladung (eingekreistes ‚A'). Aufgrund des gleichen Potentials zwischen Zentralelektrode und Schutzring entsteht ein sogenanntes Totvolumen in der Luftkavität, in welchem freigesetzte Ladungsträger nicht zum Messsignal beitragen (abgegrenzt durch rote Linien).

der Luftkavitäten, da die Schutzringe Totvolumina erzeugen, welche nicht zum Messsignal beitragen [41, 42]. Zur einheitlichen Positionierung wird von der Herstellungsfirma ein Referenzpunkt auf der Zentralachse der Zylinderkammern festgelegt.
Für die Bestimmung der Luftkermaleistung von Brachytherapiequellen werden zudem großvolumige Schachtionisationskammern eingesetzt, die den Strahler bis auf den Einfuhrkanal vollständig umschließen. Auf diese Weise können das Messsignal maximiert und mögliche Positionierungsunsicherheiten des Afterloaders minimiert werden [5].

2.4.2 Festkörperdetektoren

Für diese Arbeit wurden Siliziumdioden sowie Diamantdetektoren bezüglich Ihrer Eignung zur Dosimetrie in der Brachytherapie untersucht. Die Funktionsweise dieser beiden Sandwich-artig aufgebauten Festkörperdetektoren ist dabei ähnlich: Durch ionisierende Strahlung werden Ladungsträgerpaare (Elektronen und Löcher) erzeugt, die aufgrund des intrinsischen elektrischen Feldes[2] zu den Elektroden wandern und damit zu einem messbaren Strom beitragen. Bei (Silizium-)Dioden wird dafür ein p- und n-dotierter Halbleiter in Verbindung gebracht. ‚p' meint dabei ein Material, das einen Überschuss an Löchern aufweist. Dies wird bei den Elementen Silizium und Diamant der Hauptgruppe IV über das Einbringen eines Elements der Hauptgruppe III (Bor oder Aluminium) realisiert. Das in der Gitterstruktur eingefasste Atom bringt somit ein Elektron weniger als seine Nachbarn ein, so dass ein Loch entsteht. Analog beinhaltet ein n-dotierter Halbleiter Einschlüsse von Elementen der Hauptgruppe V (Stickstoff oder Phosphor), so dass ein Überschuss an Elektronen erzeugt wird. Durch das Zusammenbringen der p- und n-dotierten Halbleiter entsteht eine sogenannte Verarmungszone, in der die Ladungsträger

[2] Beide Detektoren arbeiten spannungslos, es wird also keine externe Spannung angelegt.

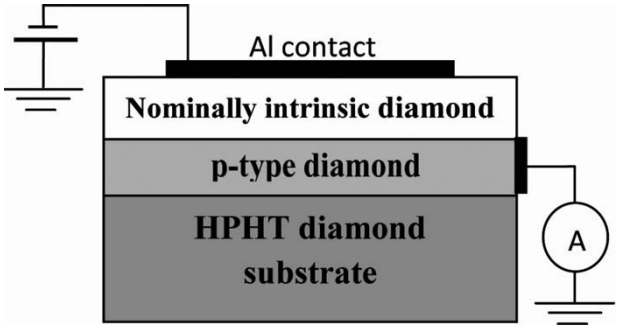

Abbildung 2.3: Schematischer Aufbau eines modernen Diamantdetektors in Sandwich Bauweise des Typs PTW microDiamond auf einem „high pressure high temperature“ (HPHT) Diamantsubstrat. Entnommen aus [43] mit Genehmigung von AIP Publishing.

durch das entstandene elektrische Feld eine Kraft zur gegenüberliegenden Schicht erfahren. In diesem Zustand fließt im gesamten Halbleiter fast kein Strom bis auf einen kleinen Leckstrom aufgrund thermischer Anregung. Der Unterschied von Diamant und Silizium besteht unter anderem in der Größe der Bandlücke von 5,6 eV gegenüber 1,1 eV, so dass Diamant als Nichtleiter und Silizium als (intrinsischer) Halbleiter eingestuft werden. Die Bandlücke ist der Energiebeitrag, welcher mindestens aufgebracht werden muss, um ein Elektron aus dem Valenz- ins Leitungsband zu befördern, so dass dieses zum Messsignal beitragen kann. Durch eine größere Bandlücke werden zwar weniger Elektron-Loch-Paare pro ionisierendem Teilchen erzeugt, dafür reduzieren sich aber auch die Leckströme, was sich positiv auf das Signal-Rausch-Verhältnis auswirkt. In Abb. 2.3 ist der schematische Aufbau eines modernen Diamantdetektors des Typs PTW microDiamond (mDD), bestehend aus einer p-dotieren Schicht und einem intrinsischen Diamant-Einkristall, gezeigt. Auf der Seite des Einkristalls ist ein Aluminium-Kontakt aufgedampft, so dass ein metallischer Schottky-Kontakt entsteht. Aufgrund der deutlich geringeren Dichte an Fehlstellen gegenüber der ersten Generation von Diamantdetektoren, welche aus natürlichen Diamanten bestehen, ist hier eine größere Reproduzierbarkeit der Detektoreigenschaften erreichbar, die für dosimetrische Anforderungen nötig sind [44].
Sowohl Siliziumdioden als auch Diamantdetektoren zeichnen sich durch ihre hohe räumliche Auflösung aus, da es möglich ist, verglichen mit Ionisationskammern aus sehr kleinen sensitiven Volumina genügend Messsignal zu gewinnen. Dies beruht auf der circa tausendfach größeren Dichte der Festkörper gegenüber Gasen wie etwa Luft. Aufgrund der höheren Ordnungszahl von Silizium ($Z = 14$) als Diamant ($Z = 6$) weist dieses eine größere Energieabhängigkeit für niedrige Photonenenergien aufgrund des Photoeffekts auf (siehe auch Abb. 2.1) [30]. Für die hier untersuchten Detektoren microDiamond und microSilicon der Firma PTW ist von dieser jeweils ein Referenzpunkt auf der Zentralachse definiert worden, welcher dem Mittelpunkt des sensitiven Volumens entspricht.

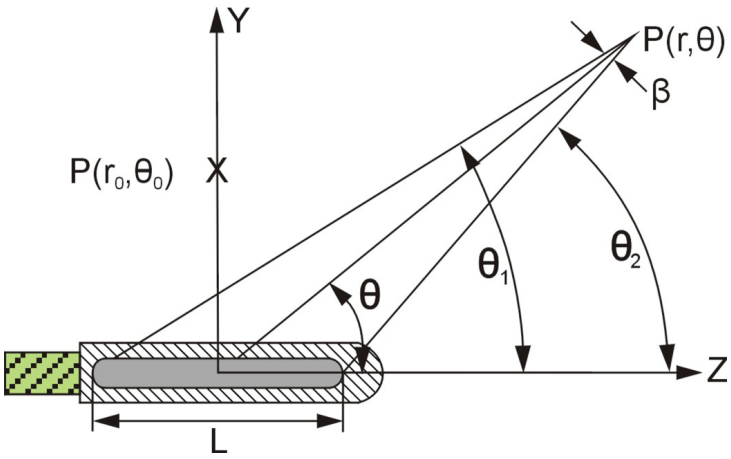

Abbildung 2.4: Das Koordinatensystem nach dem TG-43 Formalismus. Adaptiert aus [3] unter CC BY 3.0 Lizenz.

2.5 Dosimetrieprotokolle

2.5.1 AAPM Task Group Report No. 43

Die Dosisberechnung für die Brachytherapie mit umschlossenen radioaktiven Gammastrahlern wird seit 1995 durch den Bericht der Task Group 43 (TG-43) der American Association of Physicists in Medicine (AAPM) beschrieben und gilt seitdem als Richtwert für die Berechnung der absorbierten Wasser-Energiedosis [3]. Die von der TG-43 veröffentlichten Standard-Dosisleistungsverteilungen für Brachytherapiestrahler gelten somit als Referenz für weitere Messungen unter Referenzbedingungen. Der Bericht wurde bisher zweimal um zusätzliche Datensätze erweitert [4, 45]. Aufgrund dieser Datenlage und der systematischen Beschreibung von Strahlungsfeldern hat die Brachytherapie seitdem einen enormen Bedeutungszuwachs in der Strahlentherapie erhalten, da beispielsweise computergestützte Bestrahlungsplanungen hiermit international vereinheitlicht wurden [46].

Abb. 2.4 zeigt das zylindersymmetrische Koordinatensystem des TG-43 Formalismus. Ein Punkt P hat damit zwei Koordinaten: den Abstand zum Ursprung r, welcher durch den Mittelpunkt der Quelle definiert wird, und den Polarwinkel θ. Für diesen Ansatz wird der Strahler durch eine Linie der Länge L angenähert, welche der Länge des radioaktiven Materials entspricht. Üblicherweise betragen die Abmessungen der hier untersuchten aktiven Zylinder 3,5 mm Länge und weniger als 1 mm Durchmesser, so dass diese Näherung gerechtfertigt ist. Des Weiteren beschreibt β den Öffnungswinkel bei P im Dreieck mit den Endpunkten der Strecke $(L/2, 0)$ und $(-L/2, 0)$. Für Simulationen des Strahlungstransports wird natürlich die tatsächliche Geometrie der Quelle inklusive eines kurzen Drahtstücks modelliert, um beispielsweise Selbstabsorption zu berücksichtigen. Eine weitere Festlegung des TG-43 Formalismus besteht darin, dass sich der Strahler

in einer quasi-unendlichen Wasserumgebung befindet, so dass mindestens in einem hinreichenden Abstand um das Zentrum volle Streubedingungen herrschen. Dies bedeutet, dass sich das Strahlungsfeld gegenüber einer unendlichen Wasserumgebung praktisch nicht unterscheidet, da genügend Streumaterial (in diesem Fall Wasser) vorhanden ist. Der Referenzpunkt $P(r_0 = 1\,\mathrm{cm}, \theta_0 = 90\,^\circ)$ liegt in der Ebene senkrecht zur Mitte der Quellenachse. Die Dosisleistung $\dot{D}$ an einem Punkt um einen Brachytherapiestrahler in Wasser, wird berechnet mit

$$\dot{D}(r,\theta) = S_k \cdot \Lambda \cdot \frac{G_L(r,\theta)}{G_L(r_0,\theta_0)} \cdot g_L(r) \cdot F(r,\theta) \quad . \tag{2.10}$$

Die einzelnen Größen sind folgendermaßen definiert:

- Luftkermastärke S_k: Maß für die Quellenstärke über die Luftkermarate in einem definierten Abstand (üblicherweise 1 m) in der Ebene senkrecht zur Mitte der Quellenachse frei in Luft; Einheit $\mathrm{Gy\,m^2\,s^{-1}}$
- Dosisleistungskonstante Λ: Verhältnis der Dosisleistung am TG-43 Referenzpunkt zur Luftkermastärke; $\Lambda = {}^{\dot{D}(r_0,\theta_0)}/_{S_k}$, womit der Übergang von Luftkerma zu Wasser-Energiedosis erreicht wird; Einheit $\mathrm{m^{-2}}$
- Geometriefaktor G_L: beschreibt den Fluenzabfall aufgrund des Abstands von einer ausgedehnten näherungsweise linienförmigen, homogenen Verteilung von Radioaktivität; dieser Faktor bezieht sich unter Anwendung der Linienquellenapproximation nur auf L, so dass gilt $G_L(r,\theta) = {}^{\beta}/_{(Lr\sin\theta)}$; Einheit $\mathrm{m^{-2}}$
- Radiale Dosisfunktion $g_L(r)$: beziffert den Dosisleistungsabfall aufgrund von Absorption und Streuung in Wasser und Strahler entlang der transversalen Achse zur Quellenmitte (nach kürzen des auf $G_L(r_0,\theta_0)$ normierten Fluenzabfalls $G_L(r,\theta_0)$) über $g_L = {}^{\dot{D}(r,\theta_0)G_L(r_0,\theta_0)}/_{\dot{D}(r_0,\theta_0)G_L(r,\theta_0)}$ (dimensionslose Größe)
- Anisotropiefunktion $F(r,\theta)$: beschreibt die Anisotropie der Dosisleistungsverteilung um den Strahler aufgrund Selbstabsorption und Streuung in beliebigen Abständen zur Quelle (ebenfalls nach kürzen des auf $G_L(r_0,\theta_0)$ normierten Fluenzabfalls $G_L(r,\theta_0)$) über $F(r,\theta) = {}^{\dot{D}(r,\theta)G_L(r,\theta_0)}/_{\dot{D}(r,\theta_0)G_L(r,\theta)}$ (dimensionslose Größe).

Für die Größen Λ, $g_L(r)$ und $F(r,\theta)$ von klinisch verwendeten Strahlermodellen existieren Konsens-Datensätze, die gemeinsam von der AAPM und European Society for Therapeutic Radiology and Oncology (ESTRO) herausgegeben wurden [47]. Als Aufnahmekriterium müssen sich die Datensätze auf mindestens zwei unabhängige dosimetrische Studien beziehen, welche experimentell und mit MC durchgeführt wurden [20]. Die Messung der Luftkermastärke für jeden Strahler erfolgt mit kalibrierten Schachtionisationskammern in einem Primär- oder Sekundärlabor (z.B. bei der Physikalisch-Technischen-Bundesanstalt (PTB) oder bei der Herstellungsfirma) [48] und muss für die klinische Anwendung mithilfe eines geeigneten Verfahrens, wie etwa einer kalibrierten Schachtionisationskammer, verifiziert werden [49].

2.5.2 AAPM Task Group Report No. 186

Das Ziel dieses Reports besteht darin, die Anwendung von ‚Model-based Dose Calculation Algorithms' (MBDCAs) in der Brachytherapie zu vereinheitlichen [50]. Diese Algorithmen haben den Vorteil gegenüber dem Verfahren nach TG-43, dass die Dosisberechnung patient*innenspezifisch erfolgt. Für bestimmte klinische Szenarien sind lokale Dosisleistungsunterschiede $> 10\,\%$ zwischen diesen beiden Ansätzen, also der Dosisberechnung in Wasser gegenüber einer heterogenen Umgebung, möglich [51]. Die Bestimmung der Dosisleistung in klinischen Bestrahlungsplanungssystemen für diese gesonderten Streubedingungen erfolgt derzeit entweder mit Faltungsalgorithmen, welche Primär- und Streudosis getrennt berechnen und anschließend kombinieren [52, 53], aus einer rasterbasierten Lösung der linearen Boltzmann-Transportgleichung [54] oder über MC Simulationen [55]. Aus den Hounsfieldwerten eines CT-Datensatzes werden Dichtewerte zur Berechnung der Schwächung und Streuung bestimmt. Damit wird zudem die absorbierte Dosis im Gewebe berechnet. Diese muss dann gegebenenfalls in die Wasser-Energiedosis umgerechnet werden, was analog zum TG-43 Formalismus eine zusätzliche Unsicherheit beinhaltet. Zusammenfassend kann mit diesem Verfahren die Unsicherheit bei der Bestimmung der Schwächung und Streuung reduziert werden, da sie patient*innenspezifisch erfolgt.

2.5.3 DIN-Norm 6803-2

Die hier für die Brachytherapie anzuwendende Norm wird vom Arbeitsausschuss ‚NA 080-00-01 AA Dosimetrie' des DIN-Normenausschusses Radiologie (NAR) erarbeitet und vom Deutschen Institut für Normung e. V. (DIN) unter der Nummer 6803-2 ‚Dosimetrie für die Photonen-Brachytherapie – Teil 2: Strahler, Strahlerkalibrierung, Strahlerprüfung und Dosisberechnung' herausgebracht [7]. Das Dokument ist eine Verfahrensnorm für Dosisberechnungen in der Brachytherapie mit umschlossenen Gammastrahlern. Sie enthält dabei Anforderungen an die Dokumentation der Strahler-Referenzdaten und die Durchführung der Strahlerkalibrierung und -Prüfung sowie Regeln zur Dosisberechnung. In Übernahme des Verfahrens nach dem TG-43 Formalismus basiert die Kalibrierung auf der Luftkermastärke mithilfe von rückführbar kalibrierten Schachtionisationskammern oder Detektor-Phantom-Anordnungen. Dazu heißt es in einer Anmerkung: „Wünschenswert wäre es, wenn an die Stelle der Luftkermaleistung die Dosisleistung in Wasser treten würde, da bei der Strahlenbehandlung die verordnete Wasser-Energiedosis appliziert werden muss." [7]
Diese Norm ersetzt DIN-Norm 6809-2 ‚Klinische Dosimetrie: Brachytherapie mit umschlossenen gammastrahlenden radioaktiven Stoffen' aus dem Jahr 1993. In der älteren Version wird noch die Anwendung von Ionisationskammern zur Ermittlung der Wasser-Energiedosis um gammastrahlende Brachytherapiequellen beschrieben, welche die neue Version nicht mehr beinhaltet.

2.5.4 IAEA Technical Report Series No. 398 (Rev. 1)

Dieses von der International Atomic Energy Agency (IAEA) herausgegebene Dosimetrieprotokoll stellt einen Leitfaden zur Bestimmung der absorbierten Wasser-Energiedosis für Photonenspektren mit nominellen Strahlungsenergien von 100 keV bis 25 MeV sowie Elektronen, Protonen und schwerere Ionen in der perkutanen Strahlentherapie dar. Für die Dosimetrie werden hauptsächlich Ionisationskammern oder andere Detektoren verwendet, sofern für diese ein Kalibrierfaktor in Bezug auf die absorbierte Wasser-Energiedosis existiert. Bereits in der ersten Version dieses Reports aus dem Jahr 2000 [56] ist für die hier genannten Strahlungen ein Übergang von Kalibrierungen auf der Grundlage von Primärnormalen der Luftkerma zu Kalibrierungen auf der Grundlage der Wasser-Energiedosis vollzogen worden. Dies hat den Vorteil, dass die Wasser-Energiedosis auch als Grundlage für die Dosis in der Strahlentherapie dient. Darüber hinaus bieten Normen auf der Grundlage der Wasser-Energiedosis ein robusteres System von Primärnormalen als Normen auf der Grundlage der Luftkerma, ermöglichen die Verwendung eines einfachen, konsistenten Formalismus und bieten die Möglichkeit, die Unsicherheit bei der Dosimetrie von Strahlenbehandlungen zu verringern [2]. Letzteres konnte mit der Einführung MC basierter Korrektionsfaktoren aufgrund veränderter Strahlungsqualität (k_Q) [57] und der Berücksichtigung neuer Daten für Wechselwirkungsquerschnitte und Anregungsenergien („Key data“) [27] erreicht werden [2].
Als Grundlage für alle Messungen wird die Sondenmethode „zur Bestimmung der Energiedosis in einem Material an einem bestimmten Punkt, bei dem eine Dosimetersonde in das interessierende Material eingebracht oder an diesem befestigt und mit diesem zusammen bestrahlt wird“ [58] angewandt. Die Messung der absorbierten Wasser-Energiedosis $D_{\mathrm{w},Q}$ in einem Photonenstrahl der Strahlungsqualität Q bezogen auf Kalibrierbedingungen der Strahlungsqualität Q_0 erfolgt nach der ‚Grundgleichung der Dosimetrie‘ [59] über

$$D_{\mathrm{w},Q} = M_Q \cdot N_{D,\mathrm{w},Q_0} \cdot k_{Q,Q_0} \cdot \prod_i k_i \tag{2.11}$$

mit der Messanzeige M_Q des Detektors bei Bestrahlung mit der Strahlungsqualität Q, dem Kalibrierfaktor N_{D,w,Q_0} des Detektors in Bezug auf die absorbierte Wasser-Energiedosis, dem Korrektionsfaktor k_{Q,Q_0} aufgrund eines veränderten Ansprechvermögens zwischen Strahlungsqualität Q und Q_0 sowie eines zusammenfassenden Korrektionsfaktors $\prod_i k_i$, der alle weiteren Effekte korrigiert, die zu Abweichungen des Ansprechvermögens gegenüber Kalibrierbedingungen führt. Bei Kalibrierung mit Cobalt-60 (Co-60) und Einhaltung aller sonstigen Kalibrierbedingungen kann Q_0 in der Notation weggelassen werden [2]. Der Korrektionsfaktor aufgrund veränderter Strahlungsqualität k_{Q,Q_0} berechnet sich somit durch

$$k_{Q,Q_0} = \frac{f_Q}{f_{Q_0}} = \frac{(D_\mathrm{w}/\bar{D}_\mathrm{det})_Q}{(D_\mathrm{w}/\bar{D}_\mathrm{det})_{Q_0}} \quad , \tag{2.12}$$

also aus dem Verhältnis der Dosiskonversionsfaktoren f unter Q und Q_0, welche wiederum das Verhältnis der absorbierten Wasser-Energiedosis zur mittleren Dosis im Detektor

(‚det') darstellen [60]. Gleichung 2.12 ist nur dann anwendbar, wenn die mittlere Energie zur Erzeugung eines Ionenpaares in Luft (W_{air}) zwischen Q und Q_0 konstant ist, was für kinetische Energien von Elektronen ab 10 keV angenommen werden kann [27].

3 Zielsetzung der Arbeit

Wie in DIN-Norm 6803-2 und im aktualisierten Protokoll TRS-398 der IAEA angemerkt, erweist sich ein Paradigmenwechsel von der Luftkermaleistung hin zur absorbierten Wasser-Energiedosisleistung als Bezugsgröße in der Brachytherapie als wünschenswert. Das Ziel dieser Arbeit ist damit die Entwicklung eines Formalismus zur Bestimmung der absorbierten Dosisleistung von Brachytherapiestrahlern in Wasser und zur Anwendung mit klinischem Equipment. In Anlehnung an den Dosimetrieformalismus nach Protokoll TRS-398 und im Koordinatensystem des TG-43 Reports kann die absorbierte Dosisleistung um eine Brachytherapiequelle in Wasser mit einem in der Einheit Wasser-Energiedosis kalibrierten Detektor mittels Gleichung 2.11

$$\dot{D}_{\mathrm{w},Q}\left(r,\theta\right) = M_Q \cdot N_{D,\mathrm{w}} \cdot k_Q \cdot \prod k_i \tag{3.1}$$

experimentell bestimmt werden. Dedizierte Korrektionen aufgrund geänderter Strahlungsqualität k_Q beruhen dabei auf MC Simulationen. Gegenüber einem perkutanen Bestrahlungssetup ergeben sich aufgrund des steilen Dosisgradienten in der Brachytherapie und damit verbundener Volumenmittelung größere Unterschiede im Ansprechvermögen der Detektoren in Abhängigkeit von der Ausrichtung zur Quelle; diese können ebenfalls in Parametern von k_Q berücksichtigt werden. In Abb. 3.1 sind die drei untersuchten Ausrichtungen ‚parallel', ‚frontal' und ‚gekreuzt' zur Strahlungsquelle im Koordinatensystem des TG-43 Formalismus dargestellt. Es erscheint naheliegend, den TG-43 Referenzpunkt ($r_0 = 1\,\mathrm{cm}, \theta_0 = 90\,^\circ$) zu übernehmen, um konsistente Referenzwerte und damit Vergleichbarkeit herzustellen. Vor- und Nachteile der Ausrichtung des Detektors sowie einer bestimmten Positionierung werden in dieser Arbeit untersucht.
Es ist bekannt, dass geometrische Unsicherheiten in der Brachytherapie aufgrund des steilen Dosisgradienten einen sehr großen Einfluss auf das Messsignal haben. In den zu dieser Arbeit gehörenden Publikationen wird ein Verfahren vorgestellt, das Unsicherheiten in der Positionierung des Detektors mithilfe von Profilmessungen um die Strahlenquelle reduziert.
Neben der reinen Bestimmung der absorbierten Dosisleistung an einem Referenzpunkt sind weitere Messungen unter Nichtreferenzbedingungen, also zum Beispiel an anderen Positionen relativ zur Quelle, möglich. Diese können der Messung oder Verifikation von TG-43 Parametern sowie Dosisberechnungen mit MBDCAs dienen. Des Weiteren ist die Richtungsabhängigkeit der verwendeten Detektoren interessant, um die Robustheit der Messungen oder Eignung zur *in vivo* Dosimetrie zu untersuchen.

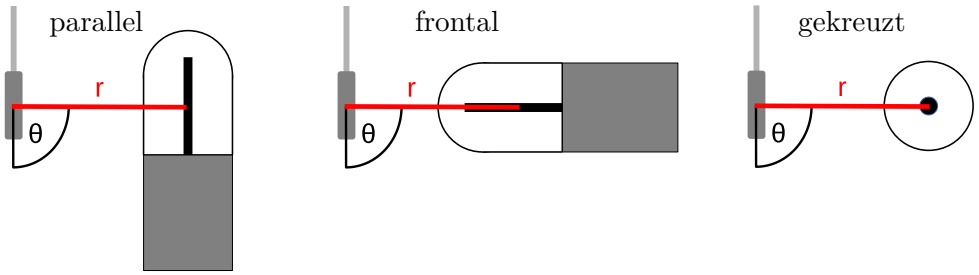

Abbildung 3.1: Ausrichtungen der Detektoren zur Quelle im Koordinatensystem des TG-43 Formalismus als Grundlage zur Untersuchung von Referenzbedingungen in der Brachytherapie. Die gekreuzte Ausrichtung in der rechten Darstellung zeigt den radialen Querschnitt der Kavität am Referenzpunkt des Detektors auf der Radialachse der Quelle. Übersetzt aus [61].

Hartmann et al. haben einen „Vorschlag für eine Erweiterung der Grundgleichung“ für die Sondenmethode formuliert, um den Korrektionsfaktor aufgrund veränderter Strahlungsqualität k_Q anschaulich in spezifische Sondeneigenschaften aufzuteilen [34]. Allgemein besteht dieser Korrektionsfaktor aus dem Quotienten der Dosiskonversionsfaktoren f unter Kalibrier- und Messbedingungen (siehe Unterabschnitt 2.5.4). Aufgrund der guten Übereinstimmung von absorbierter Dosis und beschränkter Cema für hinreichend große Strahlungsenergien und möglichst niedrige Ordnungszahlen der Detektormedien [34] kann für f die sogenannte Cema Approximation [9] angewendet werden, so dass k_Q infolge aus dem Verhältnis der Cemaquotienten für Wasser $C_{\Delta,w}$ und Detektor $\bar{C}_{\Delta,\mathrm{det}}$ besteht. Mit zwei Erweiterungen dieses Bruchs [62] können anschließend drei Faktoren extrahiert werden:

$$f \stackrel{!}{=} \frac{C_{\Delta,w}}{\bar{C}_{\Delta,\mathrm{det}}} = s_{w,\mathrm{med}} \cdot p_{\mathrm{int}} \cdot p_{\mathrm{ext}} \tag{3.2}$$

mit den Indizes für Wasser ‚w‘ und dem Detektormedium ‚med‘. Bei diesen Faktoren handelt es sich im Einzelnen um

- das Bremsvermögensverhältnis $s_{w,\mathrm{med}} = \frac{C_{\Delta,w}}{C_{\Delta,\mathrm{med}}} = \frac{\int_\Delta^\infty \Phi_E (L_\Delta/\rho)_w \mathrm{d}E + T E_{\Delta,w}}{\int_\Delta^\infty \Phi_E (L_\Delta/\rho)_{\mathrm{med}} \mathrm{d}E + T E_{\Delta,\mathrm{med}}}$ von Wasser und Detektormedium (‚Spencer-Attix stopping power ratio‘) [63] und
- den internen Störungsfaktor $p_{\mathrm{int}} = \frac{C_{\Delta,\mathrm{med}}}{\bar{C}_{\Delta,\mathrm{cav}}} = \frac{\int_\Delta^\infty \Phi_E (L_\Delta/\rho)_{\mathrm{med}} \mathrm{d}E + T E_{\Delta,\mathrm{med}}}{\int_\Delta^\infty \bar{\Phi}_{E,\mathrm{cav}} (L_\Delta/\rho)_{\mathrm{cav}} \mathrm{d}E + T \bar{E}_{\Delta,\mathrm{cav}}}$, das Verhältnis der beschränkten Cemas in einem punktförmigen ($C_{\Delta,\mathrm{med}}$) und einem bloßen, mit dem Detektormedium gefüllten, Detektorvolumen ($\bar{C}_{\Delta,\mathrm{cav}}$), das damit Volumenmittelungseffekte berücksichtigt und
- den externen Störungsfaktor $p_{\mathrm{ext}} = \frac{\bar{C}_{\Delta,\mathrm{cav}}}{\bar{C}_{\Delta,\mathrm{det}}} = \frac{\int_\Delta^\infty \bar{\Phi}_{E,\mathrm{cav}} (L_\Delta/\rho)_{\mathrm{cav}} \mathrm{d}E + T \bar{E}_{\Delta,\mathrm{cav}}}{\int_\Delta^\infty \bar{\Phi}_{E,\mathrm{det}} (L_\Delta/\rho)_{\mathrm{det}} \mathrm{d}E + T \bar{E}_{\Delta,\mathrm{det}}}$, das Verhältnis der mittleren beschränkten Cemas in den Volumina des bloßen und vollständig modellierten Detektors, das damit die durch Detektorbauteile verursachten Störeinflüsse Rechnung trägt.

Neben der Universalität dieses Ansatzes ermöglicht es die beschränkte Cema, die Signalbeiträge im Detektorvolumen energiedifferentiell darzustellen. Damit kann ein tieferes Verständnis der Auswirkung einzelner Charakteristika der verwendeten Detektor erlangt werden. Daraus ergeben sich dann Kriterien, die für eine möglichst korrektionsarme Dosimetrie förderlich sind.

4 Einordnung der Veröffentlichungen und deren Ergebnisse

4.1 Enhancement of the EGSnrc code `egs_chamber` for fast fluence calculations of charged particles

Diese Arbeit stellt die theoretische Grundlage dieses Promotionsprojekts dar. Das Ziel besteht darin, ausgehend von vorhandenen EGSnrc [37] MC Anwendungen die dosimetrischen Größen energiedifferentielle Fuenz, beschränkte Cema und absorbierte Dosis zu bestimmen. Die Applikationen `DOSRZnrc` sowie `FLURZnrc` [64] sind in der Lage, entweder die absorbierte Dosis oder die energiedifferentielle Fluenz zu berechnen, beide jedoch limitiert auf eine zylindersymmetrische Geometrie. Die Weiterentwicklung `cavity` beruht zur Definition der räumlichen Parameter auf dem egs++ geometry package [65], einem modifizierten C++ Code, in welchem eine Vielzahl an geometrischen Körpern, Transformationen und Kombinationen implementiert sind. `cavity` wird damit, inklusive der Ausgabe von absorbierter Dosis sowie energiedifferentieller Fluenz, zu einer sehr mächtigen Applikation. Für zeitkritische Anwendungen oder wenn eine sehr kleine statistische Unsicherheit benötigt wird, kann dieser Code jedoch nachteilig sein, da bestimmte Varianzreduktionstechniken (VRT) wie etwa ‚photon cross section enhancement'[1] (XCSE) [64, 66] nicht implementiert sind. In dieser Arbeit wurde der vorhandene EGSnrc Code `egs_chamber` [66], welcher eine Weiterentwicklung von `cavity` (inklusive XCSE) darstellt, um die Ausgabe der energiedifferentiellen Fluenz erweitert. Die Ergebnisse des erweiterten `egs_chamber` Codes wurden im Anschluss gegen `cavity`, `FLURZnrc` sowie `DOSXYZnrc` [67] verifiziert. Bei der letztgenannten Anwendung handelt es sich ebenfalls um eine Erweiterung des bestehenden Codes [68]. Die Testszenarien bestanden aus einer externen Bestrahlung eines Wasserphantoms mit Co-60 Strahlung [69] sowie ein hochenergetisches Bremsstrahlungsspektrum mit 6 MeV nomineller Strahlungsenergie [70] als auch eine punktförmige Ir-192 Brachytherapiequelle [71], welche sich im Wasser befand. Die dosimetrischen Größen wurden in einem kleinen Wasservolumen und in einer Ionisationskammer berechnet.

[1] Hiermit kann der Photonen-Wechselwirkungsquerschnitt in einem beliebigen Bereich der simulierten Geometrie um einen bestimmten Faktor erhöht werden, so dass sich die Wechselwirkungsdichte um diesen Faktor steigert. Um die Energieerhaltung zu gewährleisten, wird das statistische Gewicht der zusätzlich erzeugten Teilchen aus dem des primären Photons abgezweigt. Diese Technik ist hilfreich, wenn die Dosis in einem vergleichsweise kleinen Volumen der Bestrahlungsgeometrie simuliert werden soll [64].

Die Ergebnisse von `egs_chamber` mit dem Einsatz von XCSE waren für alle Szenarien innerhalb einer Standardabweichung identisch mit den Vergleichswerten. Wenn keine VRT verwendet wurden, waren die Ergebnisse von `egs_chamber` und `cavity` exakt gleich. Des Weiteren wurde die Simulationseffizienz

$$\varepsilon \propto \frac{1}{T\sigma^2} \tag{4.1}$$

untersucht, mit der Zeit T, welche benötigt wird, um eine gewisse statistische Unsicherheit σ zu erreichen [72]. Hierbei konnte die Energieabhängigkeit von der Primärstrahlung [73] sowie die Abhängigkeit von weiteren Parametern des XCSE, wie etwa der (künstlichen) Vergrößerung der Wirkungsquerschnitte und Anwendungsvolumen, bestätigt werden [66, 74]. Insbesondere für niedrige Energien sowie einen unkollimierten Strahl zeigte sich das Potential von XCSE [66]. Für eine Ir-192 Quelle waren bei 1 cm Abstand Effizienzsteigerungen um den Faktor 100 möglich. Der modifizierte `egs_chamber` Code wurde in allen folgenden Arbeiten verwendet.

Enhancement of the EGSnrc code egs_chamber for fast fluence calculations of charged particles

Thomas Failing [a,b,*], **Günther H. Hartmann** [c], **Frank W. Hensley** [d], **Boris Keil** [b,g], **Klemens Zink** [b,e,f]

[a] Department for Radiotherapy and Radiooncology, University Medical Center Göttingen, Göttingen 37075, Germany
[b] Institute of Medical Physics and Radiation Protection (IMPS), University of Applied Sciences, Gießen 35390, Germany
[c] German Cancer Research Center (DKFZ), Heidelberg 69120, Germany
[d] Department for Radiotherapy and Radiooncology, University Medical Center Heidelberg, Heidelberg 69120, Germany
[e] Department for Radiotherapy and Radiooncology, University Medical Center Giessen-Marburg, Marburg 35043, Germany
[f] Marburg Iontherapy Center (MIT), Marburg 35043, Germany
[g] Diagnostic and Interventional Radiology, Philipps-University Marburg, Marburg 35043, Germany

Received 6 January 2022; accepted 14 April 2022

Abstract

Purpose: Simulation of absorbed dose deposition in a detector is one of the key tasks of Monte Carlo (MC) dosimetry methodology. Recent publications (Hartmann and Zink, 2018; Hartmann and Zink, 2019; Hartmann et al., 2021) have shown that knowledge of the charged particle fluence differential in energy contributing to absorbed dose is useful to provide enhanced insight on how response depends on detector properties. While some EGSnrc MC codes provide output of charged particle spectra, they are often restricted in setup options or limited in calculation efficiency. For detector simulations, a promising approach is to upgrade the EGSnrc code `egs_chamber` *which so far does not offer charged particle calculations.*

Methods: Since the user code `cavity` *offers charged particle fluence calculation, the underlying algorithm was embedded in* `egs_chamber`*. The modified code was tested against two EGSnrc applications and* `DOSXYZnrc` *which was modified accordingly by one of the authors. Furthermore, the gain in efficiency achieved by photon cross section enhancement was determined quantitatively.*

Results: Electron and positron fluence spectra and restricted cema calculated by `egs_chamber` *agreed well with the compared applications thus demonstrating the feasibility of the new code. Additionally, variance reduction techniques are now applicable also for fluence calculations. Depending on the simulation setup, considerable gains in efficiency were obtained by photon cross section enhancement.*

Conclusion: The enhanced `egs_chamber` *code represents a valuable tool to investigate the response of detectors with respect to absorbed dose and fluence distribution and the perturbation caused by the detector in a reasonable computation time. By using intermediate phase space scoring,* `egs_chamber` *offers parallel calculation of charged particle fluence spectra for different detector configurations in one single run.*

Keywords: Monte Carlo simulations; EGSnrc; Variance reduction techniques; Charged particle fluence

* Corresponding author: Department for Radiotherapy and Radiooncology, University Medical Center Göttingen, Göttingen 37075, Germany.
E-mail: thomas.failing@med.uni-goettingen.de (T. Failing).

Z Med Phys **32** (2022) 417–427
https://doi.org/10.1016/j.zemedi.2022.04.003
www.elsevier.com/locate/zemedi

1 Introduction

Publication of the international IAEA Code of Practice TRS-398 [4] in 2000 turned out to be the basis for a considerable quality improvement in dosimetry for external radiotherapy [5]. Since that, a number of further developments have taken place in the field of dosimetry for external radiotherapy. An important advancement is due to Monte Carlo (MC) simulation of radiation transport which has become a widely used technique in the accurate calculation of dosimetric quantities for all beam types. Such quantities are stopping-power ratios, dose conversion factors, or perturbation correction factors required both for reference ionization chamber dosimetry and for dosimetry in non-reference conditions. A comprehensive review was recently published [6]. MC calculated data have indeed superseded many of the approximations used to determine the data in TRS-398 and are therefore explicitly considered in a forthcoming update of TRS-398. Additionally, MC calculated beam quality correction factors are already established in other dosimetry protocols such as the AAPM's addendum to the TG-51 report [7] and the German DIN report 6800–2:2020–08 [8].

A key role is now taken by the MC calculated dose conversion factor which is defined as the ratio between the absorbed dose to water at a point of interest and the absorbed dose in the sensitive volume of a detector used for dosimetry. With this method, the factorization of the dose conversion factor into the stopping power ratio and one or more perturbation correction factors and hence the associated limitation to Bragg-Gray conditions can be avoided [1,9]. A particularly appropriate tool to produce data for this approach is the MC code `egs_chamber` [10]. In order to reduce calculation time, a series of variance reduction techniques (VRTs) have been implemented in this user code. Additional to the VRTs photon splitting and Russian Roulette [11] which are already available in `cavity`, the photon cross section enhancement (XCSE) [12,10] is implemented. In XCSE, free electrons, positrons or scattered photons are induced along a photon's trajectory corresponding to increased reaction cross sections, while the original photon stays on its original track. To preserve the conservation of energy the generated particles have a reduced statistical weight. In addition, the methods of intermediate phase-space scoring (IPSS) and correlated sampling (CS) are included which allow the simulation of more than one geometry at the same time.

Another advantage of using MC simulations is to enable a closer look at the role of the charged particles, i.e. both primary and secondary electrons and positrons. There are a series of papers in which the fluence of charged particles differential in energy was recently considered in great detail [13,14,1,15]. It particularly turned out that understanding how the charged particle fluence differential in energy is influenced by radiation conditions and by detector properties can considerably contribute to better understand the response characteristics of this detector [2].

Recent papers particularly address the dosimetrical quantity restricted cema (acronym of: converted energy per mass) which can serve as bridge between absorbed dose and the charged particle fluence [16,3]. In these papers, a restricted cema based formalism for the determination of absorbed dose was suggested. For this purpose, but also for many other dosimetry related studies on the role of charged particles as listed above, there is an increasing use of detailed spectral fluence data. However, only a few MC codes provide these data. Examples are the codes `FLURZnrc` and `cavity`, both included in the EGSnrc system. Both codes have some limitations in application: the code `FLURZnrc` uses a cylindrical coordinate system which is not always appropriate to simulate a desired detector geometry while the code `cavity` is comparably inefficient for detector simulations. The code `egs_chamber`, on the other hand, better meets these requirements, however, it does not yet provide fast calculation of spectral charged particle fluence. The aim of this paper is to describe an enhancement of this code to become a general and at the same time fast MC calculation tool to provide data on absorbed dose and spectral fluence for various real detector and irradiation conditions. Results for calculated charged particle fluence, restricted cema as well as on the improved calculation efficiency are presented and compared with the results of existing MC codes for fluence calculations.

2 Theoretical background

2.1 Particle fluence

The quantity fluence, Φ, is given by $\Phi = \mathrm{d}N/\mathrm{d}a$, where $\mathrm{d}N$ is the number of particles incident on a sphere of cross-sectional area $\mathrm{d}a$. Thus, it refers to a mathematical point in a medium. However, it can be well approximated by the average fluence in a small volume which is assigned to that point. This approximation is most appropriate for MC simulations and therefore used in this work. The MC calculation of fluence within a volume is frequently based on a theorem of Kellerer [17], where the mean fluence is given by the sum of the track lengths of the particles, $\mathrm{d}s$, per unit volume $\mathrm{d}V$:

$$\bar{\Phi} = \frac{\sum \mathrm{d}s}{\mathrm{d}V} \tag{1}$$

with unit cm^{-2}. The quantity of interest in this work is the mean fluence differential in energy, $\bar{\Phi}_E$, with unit $\mathrm{cm}^{-2} \cdot \mathrm{MeV}^{-1}$. The method based on Eq. (1) is used, for example, in the code `FLURZnrc`. A compilation of further methods appropriate for the implementation in MC codes is found

in [15]. Since one of the methods was particularly useful for this work, it is also shortly described in the appendix.

2.2 Restricted cema

Based on the definition of ICRU Report 90 [18], the *restricted converted energy per mass* (cema) is calculated as:

$$C_\Delta = \int_\Delta^\infty \Phi_E \frac{L_\Delta}{\rho} \mathrm{d}E + TE_\Delta \tag{2}$$

where Φ_E is the distribution of the total electron and positron fluence with respect to energy E at a point in a medium, L_Δ/ρ is the corresponding mass linear energy transfer and TE_Δdenotes the track end term [19,18,20] representing the sum of the kinetic energy of all electrons and positrons in the scoring volume with energies below the selected energy threshold value Δ. Restricted stopping power $S_{\Delta,\mathrm{tot}}/\rho$ which is sometimes used in the definition of restricted cema is not exactly equal to linear energy transfer, however, at a value of $\Delta = 10$ keV, the difference is negligible [20].

2.3 Determination of efficiency

The metric to quantify the efficiency ε of a Monte Carlo simulation can be determined as

$$\varepsilon \propto \frac{1}{T\sigma^2} \tag{3}$$

using the total CPU hours T needed on a given computer to achieve a certain estimated statistical uncertainty σ. Since this is a general formalism, many quantities such as absorbed dose, fluence and restricted cema can be evaluated with that relationship. Any approach which decreases the time corresponding to a certain uncertainty or vice versa but does not injure the original result is called variance reduction technique.

3 Materials and Methods

3.1 Fluence calculations

In this work, four different MC codes of the EGSnrc system were applied for the calculation of the spectral fluence of charged particles and compared:

1. `FLURZnrc` [12] [1]
2. `cavity` [21]
3. a modified version of `DOSXYZnrc` [22,1]
4. `egs_chamber` [10] as modified in this work

The first two codes are generally available, whereas the two modified codes represent in-house developments that would be ready for further distribution on request. Since `cavity` is not restricted to RZ-geometries and provides virtually all investigated quantities out of the box we consider it as the archetype of this work. The code `DOSXYZnrc` was originally developed for dose calculations in a rectilinear voxel system [22]. `DOSXYZnrc` was modified by one of the authors in order to offer more versatile applications, for instance for dose calculations in other volumes such as cylinders, spheres and also for many common detector types, or to permit fluence calculations in such volumes. Additional information on the method for fluence scoring is provided in [1,15].

The modifications made to the user code `egs_chamber` in this work are briefly described next. Since `cavity` provides the full capability of fluence scoring and uncertainty estimation, the algorithm extracted from the corresponding section `ausgab` has been adopted. With this approach the built-in variance reduction techniques from `egs_chamber` such as photon cross section enhancement, Russian Roulette, intermediate phase space scoring and a region-based ECUT are conserved out of the box. However, the remaining VRT onegeom[2] and correlated sampling are not provided.

3.2 Calculation of restricted cema

Using the data of the spectral electron and positron fluence obtained as described in the section above, the computation of restricted cema is performed by

$$C_\Delta = \sum_{i=i_\Delta}^{i_{\max}} \bar{\Phi}_{E,i} \left(\frac{S_\Delta}{\rho}\right)_i \mathrm{d}W + TE_\Delta \tag{4}$$

where $\bar{\Phi}_{E,i}$ is the spectral fluence including liberated secondary charged particles, $(S_\Delta/\rho)_i$ is the restricted total mass stopping power at the energy of each bin center i beginning at the first bin above Δ (i.e. i_Δ), $\mathrm{d}W$ is the energy corresponding to the bin width, and $TE_\Delta$is the track end term representing the kinetic energy (E_{kin}) of all charged particles with energies below the threshold value for particle tracking. The restricted total stopping power and restricted linear energy transfer are equal in a good approximation since their difference for $\Delta = 10$ keV is negligible in our study [20,23]. Based on the assumption that all energy contributions E_{dep} below Δ are deposited locally, the track end term could be therefore directly calculated [3] as:

$$TE_\Delta = \sum E_{\mathrm{dep}}(E_{\mathrm{kin}} < \Delta). \tag{5}$$

[1] Since results on absorbed dose and restricted cema are usually not given with the standard version, this code was only slightly extended to provide such data as well. A publicly available alternative would be to use `cavity` with the charged particle scoring algorithm from `FLURZnrc` as stated in [21].

[2] This VRT allows several simulation geometries to be equal while using different scoring regions parallel. One useful application are Fano calculations.

This formula was implemented in the modified versions of DOSXYZnrc and egs_chamber. However, this formula is usually not implemented in standard codes. Under the condition that a MC code provides the data of spectral fluence the restricted cema without track end term can be computed. If the absorbed dose is accessible too, the track end term can then be obtained due to the close agreement between absorbed dose D and restricted cema [16,18] by:

$$TE_{\Delta} \approx D - \sum_{i=i_{\Delta}}^{i_{\max}} \bar{\Phi}_{E,i} \left(\frac{S_{\Delta}}{\rho} \right)_i \mathrm{d}W. \tag{6}$$

For all EGSnrc user codes, the calculation of the relative standard uncertainty of restricted cema was performed using the history-by-history statistical estimator method [24] as applied for the uncertainty determination of absorbed dose.

3.3 Test setups and comparison

Results obtained with the modified user code egs_chamber were compared with those from FLURZnrc (which was specifically designed for fluence computation), from a modified version of DOSXYZnrc, and from cavity. Results were obtained for fluence spectra of electrons and positrons, for restricted cema, and for data on efficiency. Fig. 1 shows the investigated test setups. Two external radiation setups were simulated for a collimated point source geometry at SSD = 95 cm. As external sources the 6 MV Mohan spectrum [25] and the Co-60 Mora spectrum [26] were used. The third setup consisted of a point source emitting the spectrum of an Ir-192 microSelectron v2 HDR source immersed at the center of the water phantom. Results were scored in a small water disc of 0.1 cm radius and height or in the sensitive volume of a fully modelled PTW 31014 ionization chamber. Table 1 shows the chosen EGSnrc Monte Carlo parameters and simulation setups.

However, normalization of charged particle fluence computation is not performed identically in the investigated MC codes. One reason are different definitions of the incident primary photon spectrum: For a collimated point source FLURZnrc and DOSXYZnrc use the primary photon fluence per beam area (unit cm^2) at the SSD. Because the beam area is cancelled out, the secondary charged particle fluence is then given in units of MeV^{-1}. In cavity and egs_chamber the incident photon spectrum is referred to steradian and independent on the SSD. For comparison, all external beam radiation spectra were therefore normalized per incident photon fluence per MeV^{-1} independent of the SSD but normalized to the field size at reference depth. The immersed point source is normalized per initial particle in every user code thus the secondary charged particle spectra have units $MeV^{-1}cm^{-2}$. Regarding comparable examples as shown in Fig. 1 and no use of VRTs, all investigated user codes yield similar calculation efficiencies. Therefore all efficiency enhancements can be compared to the original cavity code. The variance reduction technique from egs_chamber used in this work was photon cross section enhancement. To investigate the resulting efficiency gain, the detectors were embedded in water shells of varying sizes with radii r in which XCSE was applied, as shown in Fig. 1. For the ionization chamber the water shells had a fixed length extending outside the active volume. For water disc cases both radii and height were extended by the same amount. Each simulation had one fixed XCSE value that was assigned to all detector parts including an extended stem and the surrounding shell.

It is noteworthy that the investigation of VR-techniques can become quite tedious due to the interference of the

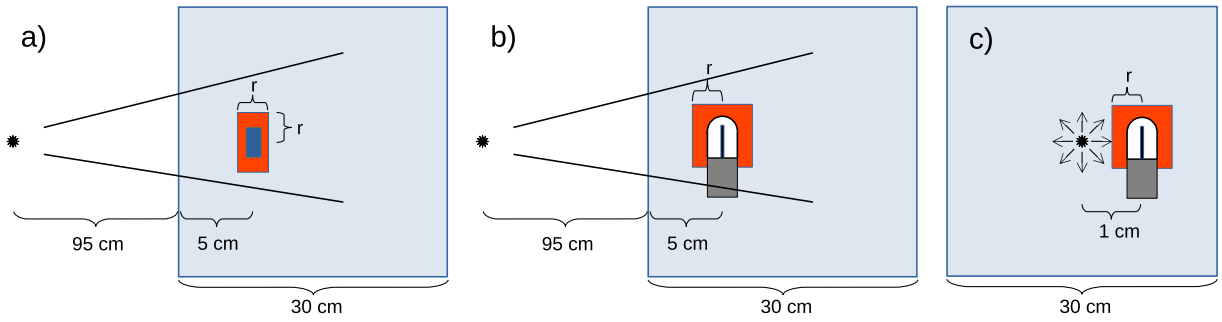

Figure 1. Schemes of the investigated beam setups. In all cases the XCSE water region in which XCSE is switched on in the egs_chamber simulations is marked by red cylinders with radius r. The water disc XCSE shell (shown in (a)) also varies the height in beam direction by the same. In case of an ionization chamber (shown in (b) and (c)) the height of the cylinder is fixed to 1.5 cm outstanding the active volume whereas the radius varies. Example (a): External point source collimated to a 4×4 cm^2 square field size at 100 cm distance to the detector. The detector (here: blue water disc) is placed at 5 cm depth in a $30 \times 30 \times 30$ cm^3 cubic water phantom. Example (b): Same as (a) but with different detector such as PTW 31014 ionization chamber. Example c): Immersed point source located at the center of a $30 \times 30 \times 30$ cm^3 water phantom. The detector's reference point (here: PTW 31014 ionization chamber with its sensitive volume in white) was at the same spot translated one centimeter away from the source. An analog immersed-source setup replacing the ionization chamber by a water voxel and XCSE region is not explicitly shown. Drawings are not to scale. (For interpretation of the references to colour in this figure legend, the reader is referred to the web version of this article.)

Table 1
Summary of the EGSnrc simulation parameters as used in this study. According to good practice the recommendations of AAPM report TG-268 [27] were followed.

Item name	Description	References
Code, version	EGSnrc (v2019a), `egs_chamber`, `cavity`, `FLURZnrc`, `DOSXYZnrc`, egs++ geometry package	[28,22,21]
Validation	—	[29]
Hardware & timing	12 cores, Intel® Xeon® CPU E5-2620 0 @ 2.00 GHz, 0.1 to 1000 total CPU hours	
Source description	Tabulated point sources, either collimated to a 4×4 cm^2 square field size at SSD or isotropic	[25,26]
Cross-sections	xcom photon cross sections. NIST ESTAR density effect corrections and mean excitation energies with ICRU 90 values where applicable. NIST Bremsstrahlung cross sections	[18,30]
Transport parameters	ECUT = AE = 521 keV PCUT = AP = 10 keV Photon cross section = xcom Bound Compton Scattering = On/ norej Rayleigh scattering = On Atomic Relaxations = On/ eadl Brems cross sections = NIST Boundary crossing algorithm = exact Electron step algorithm = EGSnrc/ PRESTA-II ESTEPE = 0.25 All other parameters set to default	[28]
VRT	Varying XCSE factors from 0 to 2048 to determine optimum efficiency conditions	[10,28]
Scored quantities	Absorbed dose, restricted cema, track end terms and charged particle fluence differential in energy to a water disc (radius and height 1 mm) or ionization chamber (PTW 31014). Detailed simulation setups are shown in Fig. 1.	
# histories/ statistical uncertainty	10^7 to 10^{11} histories depending on efficiency evaluations or benchmark simulations, uncertainty of 0.1 % for the latter ($k = 1$)	
Statistical methods	History-by-history estimator	[24]
Post-processing	Collimated point source: Normalization per incident fluence, Isotropic point source: normalization per primary photon; De-noising of the spectra (6 MV Bremsstrahlung: averaging over 5 bins; otherwise over 2 bins), no filtering	

different techniques [31] or the dependency on radiation setups because several VRT parameters have to be considered together in every beam setup [10]. For this reason we investigated the efficiency gain due to XCSE only. Additionally, it is found in [31] that XCSE offers the greatest efficiency enhancement when the VRTs are considered individually. The aim at this point is to compare the charged particle fluence scoring techniques and the corresponding efficiency gain resulting from XCSE in `egs_chamber` systematically in a given scenario.

4 Results

4.1 Charged particle fluence spectra and restricted cema computation

As initial verification - and based on the same initial random numbers - the enhanced `egs_chamber` as well as the original `egs_chamber` and `cavity` user codes yield exactly the same results regarding all investigated quantities if no additional VRTs from `egs_chamber` are used. This is even the case for charged particle fluence data although not provided by the original `egs_chamber` user code.

Fig. 2 shows the electron spectra differential in energy and the corresponding restricted cema in the volume of interest obtained using the user code `cavity` and the corresponding relative deviations from `egs_chamber`, `FLURZnrc` and `DOSXYZnrc`. For the sake of clarity the spectra of secondary positrons differential in energy are not shown since they are at most responsible for only about 1 % of the response in a 6 MV Bremsstrahlung photon beam. The analyzed volume refers to the sensitive, air-filled cavity of the fully modelled ionization chamber, type PTW 31014.

All datasets belonging to one simulation setup agree with each other within their statistical uncertainties. Numerical deviations between `cavity` and the other user codes exceed 5 % only at high energies. For the line spectra of Co-60 and Ir-192 the corresponding Compton edges at about

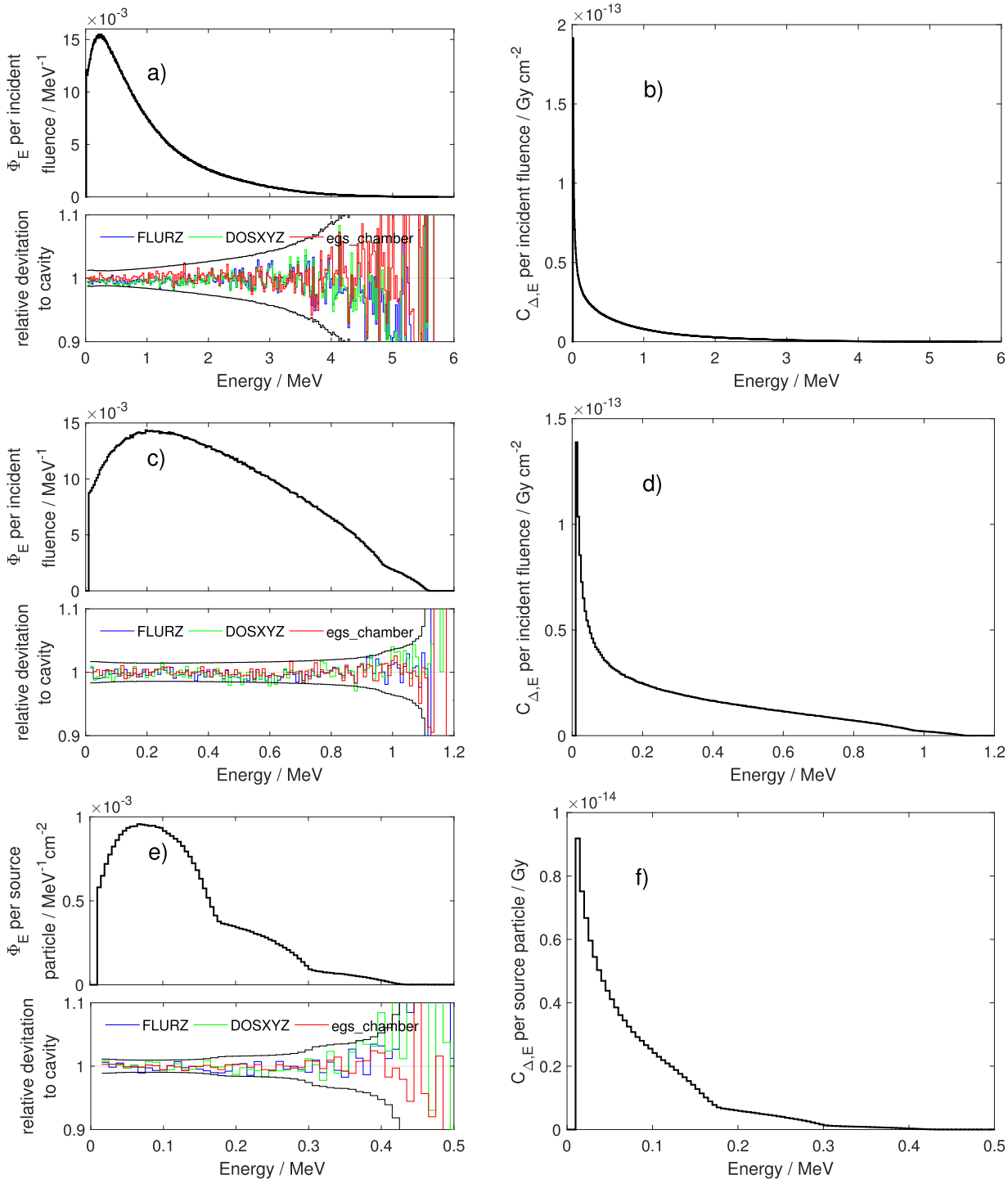

Figure 2. Electron fluence (left: (a), (c), (e)) and restricted cema (right: (b), (d), (f)) differential in energy calculated with `cavity` (bold black lines) with 5 keV bin width for an irradiation of a PTW 31014 ionization chamber with external-beam 6 MV Bremsstrahlung (top row), Co-60 (second row) or immersed-source Ir-192 photons (bottom row) as shown in Fig. 1(b) and (c). Due to the almost identical results, only the graphs of `cavity` are shown. The relative deviations of the results from other user codes in comparison to `cavity` are shown under the corresponding spectra with the mean standard deviations of the quotients in black.

Table 2
Absorbed dose D, restricted cema C_Δ (as calculated by Eq. (4) including TE_Δ as calculated by Eq. (5) and track end term TE_Δ per incident photon fluence (i.e. in Gy cm^{-2}) calculated for the irradiation of a water disc with Co-60 photons in the external beam setup from Fig. 1 a). The relative standard uncertainty of the final digit is shown in parentheses for each value.

	D	C_Δ	TE_Δ
`egs_chamber`	$3.78(1) \cdot 10^{-12}$	$3.78(1) \cdot 10^{-12}$	$0.280(1) \cdot 10^{-12}$
`cavity`	$3.78(1) \cdot 10^{-12}$	—	$0.280(3) \cdot 10^{-12}$
`DOSXYZnrc`	$3.77(2) \cdot 10^{-12}$	$3.77(2) \cdot 10^{-12}$	$0.279(2) \cdot 10^{-12}$
`FLURZnrc`	$3.79(3) \cdot 10^{-12}$	$3.79(3) \cdot 10^{-12}$	$0.275(4) \cdot 10^{-12}$

1.1 MeV and 0.95 MeV or 0.42 MeV, 0.3 MeV and 0.18 MeV, respectively, are clearly visible in all fluence scoring algorithms. Contrary to the electron or positron fluence differential in energy, the peak values of the restricted cema differential in energy appear at the first bin above Δ (i.e. 10 keV). This observation can be explained by the strong energy dependence of the restricted stopping powers used for the computation of restricted cema which decrease monotonically at low energies.

Table 2 shows the results concerning absorbed dose, restricted cema and track end term for external irradiation with Co-60 photons as in Fig. 1(a). The normalization was performed independent of the SSD for a beam area of 4×4 cm^2 at 100 cm distance to the source. Again the results agree within their statistical uncertainties.

For radiation qualities of 6 MV Bremsstrahlung and higher energies the contributions from positrons to restricted cema exceed 1 % and are therefore not negligible. Additionally, the relative contributions from TE_Δ are energy dependent and vary from 6% for 6 MV Bremsstrahlung up to 14 % for Ir-192.

4.2 Efficiency evaluation

Fig. 3 shows the relative efficiency gain of `egs_chamber` simulations with various XCSE factors and shell thicknesses in the calculation of absorbed dose or restricted cema without track end term. The track end term was omitted in the efficiency evaluation because the restricted cema was calculated in the user code based on the charged particle fluence scoring algorithm which ignores particle energies below Δ. For these calculations a PTW 31014 ionization chamber was placed in a water phantom and externally irradiated with Co-60 photons as shown in Fig. 1(b). In this example the efficiencies first increase with increasing enhancement of the cross sections. This behavior reaches a maximum after which the computation time to trace the growing number of secondary charged particles initiated by the higher cross sections begins to increasingly reduce the efficiency.

The photon cross section enhancement shell thickness also has an impact on the simulation efficiency. Similar to an increased XCSE value, a thicker shell around the detector leads to more photon interactions causing an increase in charged particles scored in the detection volume. And again more interactions require more computation resources. Both with enhancement of the value of the cross sections and enhancement of the volume in which XCSE is applied, the relative efficiency gain depends on the computed quantity. In the example shown in Fig. 3 the maximum achievable relative efficiency gains concerning restricted cema without TE_Δ and absorbed dose calculations

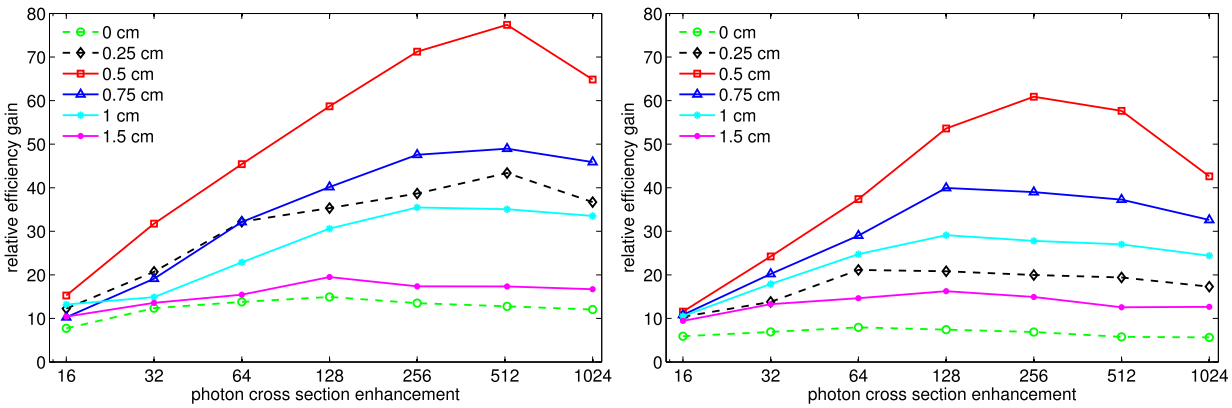

Figure 3. Relative efficiency gains in the calculations of absorbed dose (left) and restricted cema without TE_Δ (right) using photon cross section enhancement with various shell thicknesses r compared to no use of VRTs. The investigated setup consisted of the PTW 31014 ionization chamber externally irradiated with a Co-60 point source as shown in Fig. 1(b). A shell thickness of 0 cm corresponds to a cross section enhancement of the ionization chamber parts only.

Table 3
Relative efficiency gain in the calculation of absorbed dose and restricted cema without track end term with `egs_chamber` at the optimum values of photon cross section enhancement conditions compared to no use of VRTs. The parameter r depicts the surrounding XCSE shell where $r = 0$ means an enhancement of the cross sections of only the components of the ionization chamber. The calculations were performed in the external beam setup for 6 MV Bremsstrahlung and Co-60 photons as shown in Fig. 1(a) and (b), and in the immersed-source setup for Ir-192 photons as shown in Fig. 1(c).

		absorbed dose			restricted cema without TE_Δ		
		XCSE	r/cm	rel. eff. gain	XCSE	r/cm	rel. eff. gain
6 MV	water voxel	64	1	19.3	64	1	19.3
	PTW 31014	128	0.75	48.9	128	0.75	26.3
Co-60	water voxel	256	0.75	51.4	256	0.75	51.7
	PTW 31014	512	0.5	77.4	256	0.5	60.9
Ir-192	water voxel	512	0.25	89.2	512	0.25	92.6
	PTW 31014	1024	0	97.7	512	0	147.7

are different and the efficiency peaks are achieved at different values of XCSE.

Table 3 shows the relative efficiency gain for all investigated beam setups at the optimum XCSE value and shell thickness. Several observations can be made:

First, the relative efficiency gain depends on the radiation quality and increases with decreasing particle energies. Second, the optimum cross section enhancement value increases with decreasing particle energies whereas the optimum shell thickness shows an inverse behavior. Third, the efficiency improvement potential is larger in ionization chamber simulations in every investigated setup. Fourth, the optimum XCSE conditions for absorbed dose and restricted cema without TE_Δ calculations are equal for water voxels. The parameters differ only slightly for the ionization chamber simulations where the setups referring to restricted cema without TE_Δ tend to smaller enhancement values.

5 Discussion

As stated in the EGSnrc C++ class library [21] the track length based fluence scoring algorithm as used in `FLURZnrc` assumes the stopping powers to be constant along a charged particle step. This might affect spectra at regions where the progression of the stopping powers is steep. Our results show that this applies only to the first bin above Δ (i.e. 10 keV) in water disc simulations, which yields about 5 % more than the other algorithms in certain energy bins. One workaround is the reduction of the MC parameter ESTEPE so that the condensed history steps are small enough for an accurate scoring with constant stopping powers. This miscalculation on charged particle fluence scoring in `FLURZnrc` does not impair the resulting restricted cema since its impact is considerably smaller than the statistical uncertainty of restricted cema calculation. Thus the effect is negligible in our study and may be accounted for in the overall uncertainty budget.

The investigated VR-technique photon cross section enhancement is well established since several years in various EGSnrc user codes [11,28,12]. With the introduction of XCSE in `egs_chamber`, the application to charged particle fluence computations was explicitly mentioned in [10]. Furthermore the EGSnrc standard statistical uncertainty history-by-history estimator is also explicitly dedicated to arbitrary quantities such as fluence [24]. XCSE as used in `egs_chamber` offers a dramatic efficiency gain especially for small scoring regions compared to the irradiated volume [10]. Our results confirm this especially regarding an internal irradiation as shown in Fig. 1(c).

The relative efficiency gains between absorbed dose and restricted cema without TE_Δ differ for ionization chamber simulations. Fluence scoring in `cavity` is done using track-length estimation by precomputed stopping powers from the EGSnrc database. Restricted cema can then be obtained as described in Section 3.2. Absorbed dose scoring tallies up the energy deposited due to ionization (continuous energy losses) and discrete interactions. As the energy of the charged particles changes, the scoring can be more or less efficient and hence the dose scoring may lead to a different statistical uncertainty than restricted cema computation for the same number of traced particles. A similar mechanism could occur in the calculation of kerma using photon fluence and mass-energy absorption coefficients in comparison to using the kerma approximation of depositing the energy of secondary charged particles on the spot.

By using other variance reduction techniques such as intermediate phase space scoring in the enhanced `egs_chamber` code the computation of several detector compositions needed for perturbation correction factors may be obtained in one single simulation run. Fig. 4 depicts one practical example of the combined simulation of the components related to the dose conversion factor for an ionization chamber split into stopping power ratio (Fig. 4(a) to (b)) and several perturbation correction factors (Fig. 4(b) to

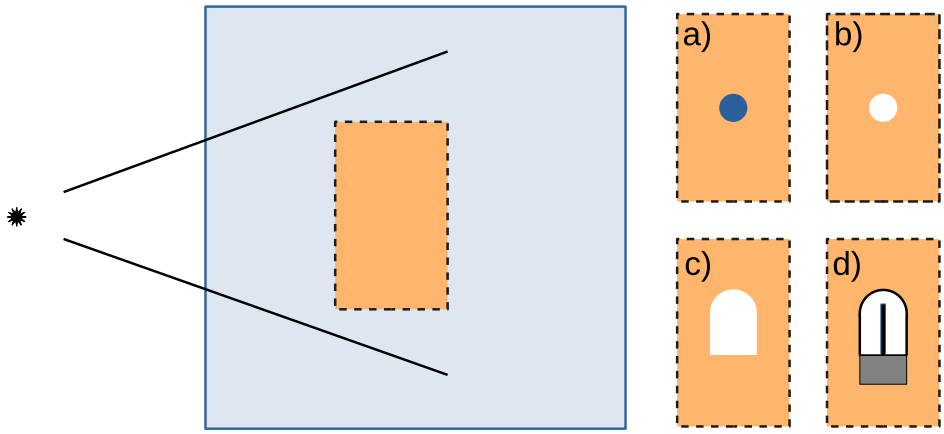

Figure 4. Practical example for the use of intermediate phase space scoring in an external beam setup. Particles, primary as well as secondary of nature, entering a specified region (orange dashed box) in the phantom are intermediately stopped and re-run several times from that point with different detectors inside. In this exemplary case the different detectors consist of (a) a water voxel, (b) an air voxel, (c) the bare air cavity volume and (d) the fully modelled thimble ionization chamber. With these different detector types it is possible to simulate perturbation factors as proposed in [15,2,16]. Drawings are not to scale. (For interpretation of the references to colour in this figure legend, the reader is referred to the web version of this article.)

(c) and (c) to (d)). Applying this example to the setups as shown in Fig. 1 with external or immersed source and adjusted XCSE conditions for each detector, a further relative efficiency enhancement of 1.52, 1.57 and 1.61 for external 6 MV Bremsstrahlung, external Co-60 and immersed source Ir-192 photon beams could be observed respectively.

If the phase space scoring volume is large enough and contains all detector components in every position, several detector positions inside a phantom can be simulated simultaneously. An additional enhancement would be the implementation of correlated sampling [28,21] for charged particle fluence scoring so that spectral resolved fluence or restricted cema quotients can be calculated.

6 Conclusions

This work shows a straightforward enhancement of `egs_chamber` to calculate charged particle fluence using methods already present in the EGSnrc framework and in particular in `cavity`. The EGSnrc applications are built modular so that there is not much interference with the inserted code. The comparison with several EGSnrc user codes show good agreement which proves that the implemented charged particle fluence scoring in `egs_chamber` does not impair the original code. Furthermore, in our calculations, the different radiation setups (external or immersed source) and the use of variance reduction techniques showed no influence on the charged particle fluence spectra.

Using VRT provided by EGSnrc such as XCSE an improved simulation efficiency could be observed. There are even more techniques to raise the efficiency implemented in `egs_chamber` such as a region-based ECUT, intermediate phase space scoring (IPSS), Correlated Sampling and onegeom. The latter allows several simulation geometries to be equal while using different scoring regions parallel. Region-based ECUT, XCSE and IPSS work out of the box whereas Correlated Sampling and onegeom require additional modifications.

With the given approach it is possible to achieve spectral information even for sophisticated demands within acceptable computing time. Additionally the restricted cema as a link between absorbed dose and charged particle fluence can also be calculated. Since the restricted cema methodology has the advantage of being applicable in setups which do not fulfill Bragg-Gray conditions [16] the enhanced `egs_chamber` code is well suited for further investigations on detector developments and non-reference conditions.

Conflict of Interest

This work is part of a dissertation project of Technische Hochschule Mittelhessen University of Applied Sciences at the Graduate Center of Engineering Sciences at the Research Campus of Central Hessen.

The authors declare that they have no known competing financial interests or personal relationships that could have appeared to influence the work reported in this paper.

Appendix A Calculation of spectral charged particle fluence

As stated in Eq. (1), the mean fluence of charged particles in a scoring volume can be derived from the sum of their path lengths per unit volume. In EGSnrc, an electron or posi-

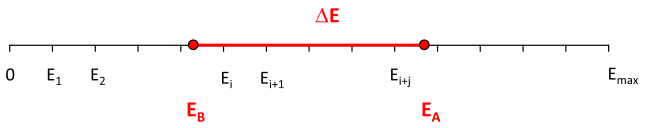

Figure 5. Diagram showing the energy deposition ΔE of an electron or positron in relation to a linear energy grid 0, E_1, E_2, ... E_{max}.

tron path length is obtained either in the single scattering mode, i.e. between two scattering events, or in the condensed history mode, i.e. between two hard (inelastic) interaction sites. In both cases, the relation between a given path length to the energy loss over this path and vice versa must be known. For this relation, the 'continuous slowing down approximation' is assumed where the energy loss results from sub-threshold processes only. Thus, the energy loss ΔE of an electron or positron is formally linked to its corresponding path length s through:

$$\Delta E = \int_0^s L_\Delta(s')\mathrm{d}s' \qquad (.1)$$

where L_Δ is the linear energy transfer, also called restricted stopping power. It follows that an electron or positron path can be characterized by three parameters of kinetic energy: The energy loss ΔE associated to the path length s, the energy E_A at the path start, and $E_B = E_A - \Delta E$ at its stop. The position of this parameter with respect to a linear energy grid 0, E_1, E_2, ... E_{max} is shown in Fig. 5.

The method of fluence calculation is now essentially based on two steps:

Step 1: Each energy deposition (equivalent with the energy loss ΔE) is split into a number of single subsections adjusted to the energy binning which will be used to present the electron or positron fluence differential in energy. Using the example of Fig. 5, the first subsection is E_i-E_B, the intermediate subsections are identical to the bin width $\mathrm{d}W$, and the last subsection is E_A-E_{i+j}. The quotient of each subsection by ΔE is termed α.

Step 2: By means of the quotient $\alpha_{i,j}$ where the index j refers to a specific energy loss ΔE during the MC simulation, the spectral fluence $\bar{\Phi}_{E,i}$ at bin i within the scoring volume V can now directly be derived.

The two methods used in this work are:

1. track length based: $\Phi_{E,i} = \sum_{j=1}^{M} \frac{1}{V} \cdot \frac{\alpha_{i,j}}{\mathrm{d}W} \cdot s_j$ where j refers to one particle track out of the total number of histories M, and s_j is the path length associated to the energy loss ΔE_j; this method is implemented in `FLURZnrc`.
2. energy deposition based: $\bar{\Phi}_{E,i} = \sum_{j=1}^{M} \frac{1}{V} \cdot \frac{\alpha_{i,j}}{\mathrm{d}W} \cdot \frac{\Delta E_j}{L_{\Delta,i}}$ where $L_{\Delta,i}$ is the linear energy transfer of the material in the scoring volume at bin i. In the modified version of `DOSXYZnrc`, $L_{\Delta,i}$ is taken at the energy of bin center, whereas in `cavity`, it is - according to the documentation - at the lower energy of each bin. Actually, however, it is also at bin center.

References

[1] Hartmann G. H., Zink K. Decomposition of the dose conversion factor based on fluence spectra of secondary charged particles: Application to lateral dose profiles in photon fields Med. Phys. 2018;45(9):4246–4256. https://doi.org/10.1002/mp.13081.
[2] Hartmann G. H., Zink K. A Monte Carlo study on the PTW 60019 microDiamond detector Med. Phys. 2019;46(11):5159–5172. https://doi.org/10.1002/mp.13721.
[3] Hartmann G. H., Andreo P., Kapsch R.-P., Zink K. Cema-based formalism for the determination of absorbed dose for high-energy photon beams Med. Phys. 2021;48(11):7461–7475. https://doi.org/10.1002/mp.15266.
[4] P. Andreo, D.T. Burns, K. Hohlfeld, M.S. Huq, T. Kanai, F. Laitano, V.G. Smith, S. Vynckier, Technical Report Series No. 398 Absorbed Dose Determination in External Beam Radiotherapy: An International Code of Practice for Dosimetry Based on Standards of Absorbed Dose to Water, International Atomic Energy Agency, Vienna.
[5] IAEA, Comprehensive Audits of Radiotherapy Practices: A Tool for Quality Improvement, International Atomic Energy Agency, Vienna, 2007.
[6] P. Andreo, Monte Carlo simulations in radiotherapy dosimetry, Radiat. Oncol., 13 (1). https://doi.org/10.1186/s13014-018-1065-3.
[7] McEwen M., DeWerd L., Ibbott G., Followill D., Rogers D. W. O., Seltzer S., Seuntjens J. Addendum to the AAPM's TG-51 protocol for clinical reference dosimetry of high-energy photon beams Med. Phys. 2014;41(4):041501. https://doi.org/10.1118/1.4866223.
[8] DIN-Normenausschuss Radiologie (NAR) DIN 6800-2:2020-08 Dosismessverfahren nach der Sondenmethode für Photonen- und Elektronenstrahlung - Teil 2: Dosimetrie hochenergetischer Photonen- und Elektronenstrahlung mit Ionisationskammern. Beuth Verlag GmbH: DIN-Standard; 2020. https://doi.org/10.31030/3152276.
[9] Andreo P., Burns D. T., Kapsch R. P., McEwen M., Vatnitsky S., Andersen C. E., Ballester F., Borbinha J., Delaunay F., Francescon P., Hanlon M. D., Mirzakhanian L., Muir B., Ojala J., Oliver C. P., Pimpinella M., Pinto M., de Prez L. A., Seuntjens J., Sommier L., Teles P., Tikkanen J., Vijande J., Zink K. Determination of consensus k_q values for megavoltage photon beams for the update of IAEA TRS-398 Phys. Med. Biol. 2020;65(9):095011. https://doi.org/10.1088/1361-6560/ab807b.
[10] Wulff J., Zink K., Kawrakow I. Efficiency improvements for ion chamber calculations in high energy photon beams Med. Phys. 2008;35(4):1328–1336. https://doi.org/10.1118/1.2874554.
[11] Kawrakow I., Fippel M. Investigation of variance reduction techniques for Monte Carlo photon dose calculation using XVMC Phys. Med. Biol. 2000;45(8):2163–2183. https://doi.org/10.1088/0031-9155/45/8/308.
[12] D.W.O. Rogers, I. Kawrakow, J.P. Seuntjens, B.R.B. Walters, E. Mainegra-Hing, NRC user codes for EGSnrc, Techreport PIRS-702, National Research Council Canada (2011 [version 2021]). https://nrc-cnrc.github.io/EGSnrc/doc/pirs702-egsnrc-codes.pdf.
[13] Benmakhlouf H., Andreo P. Spectral distribution of particle fluence in small field detectors and its implication on small field dosimetry Med. Phys. 2017;44(2):713–724. https://doi.org/10.1002/mp.12042.
[14] Andreo P., Benmakhlouf H. Role of the density, density effect and mean excitation energy in solid-state detectors for small photon fields

Phys. Med. Biol. 2017;62(4):1518–1532. https://doi.org/10.1088/1361-6560/aa562e.
[15] Hartmann G. H., Andreo P. Fluence calculation methods in Monte Carlo dosimetry simulations Zeitschrift für Medizinische Physik 2019;29(3):239–248. https://doi.org/10.1016/j.zemedi.2018.08.003.
[16] Hartmann G. H., Hensley F., Kapsch R.-P., Poppe B., Sauer O., Würfel J., Zink K. Ermittlung der Wasser-Energiedosis nach der Sondenmethode gemäß DIN 6800 Teil 1: Vorschlag für eine Erweiterung der Grundgleichung Zeitschrift für Medizinische Physik 2020;30(1):24–39. https://doi.org/10.1016/j.zemedi.2019. 05.001.
[17] Kellerer A. M. Considerations on the Random Traversal of Convex Bodies and Solutions for General Cylinders Radiat. Res. 1971;47 (2):359. https://doi.org/10.2307/3573243.
[18] ICRU, Report 90, J. Int. Commiss. Radiat. Units Meas. 14 (1). https://doi.org/10.1093/jicru/ndw043.
[19] Nahum A. E. Water/air mass stopping power ratios for megavoltage photon and electron beams Phys. Med. Biol. 1978;23(1):24–38. https://doi.org/10.1088/0031-9155/23/1/002.
[20] Kellerer A. M., Hahn K., Rossi H. H. Intermediate Dosimetric Quantities Radiat. Res. 1992;130(1):15. https://doi.org/10.2307/3578474.
[21] Kawrakow I. et al. EGSnrc C++ class library, Techreport PIRS-898. National Research Council of Canada; 2019. , https://nrc-cnrc.github.io/EGSnrc/doc/pirs898/index.html.
[22] Walters B., Kawrakow I., Rogers D. W. O. DOSXYZnrc Users Manual, Techreport PIRS-794. National Research Council of Canada; 2021, https://nrc-cnrc.github.io/EGSnrc/doc/pirs794-dosxyznrc.pdf.
[23] Andreo P., Burns D. T., Nahum A. E., Seuntjens J., Attix F. H. Fundamentals of Ionizing Radiation Dosimetry. John Wiley & Sons; 2017.
[24] Walters B. R. B., Kawrakow I., Rogers D. W. O. History by history statistical estimators in the BEAM code system Med. Phys. 2002;29 (12):2745–2752. https://doi.org/10.1118/1.1517611.
[25] Mohan R., Chui C., Lidofsky L. Energy and angular distributions of photons from medical linear accelerators Med. Phys. 1985;12 (5):592–597. https://doi.org/10.1118/1.595680.
[26] Mora G. M., Maio A., Rogers D. W. O. Monte Carlo simulation of a typical ^{60}Co therapy source Med. Phys. 1999;26(11):2494–2502. https://doi.org/10.1118/1.598770.
[27] Sechopoulos I., Rogers D. W. O., Bazalova-Carter M., Bolch W. E., Heath E. C., McNitt-Gray M. F., Sempau J., Williamson J. F. RECORDS: Improved Reporting of montE CarlO RaDiation transport Studies: Report of the AAPM Research Committee Task Group 268 Med. Phys. 2017;45(1):e1–e5. https://doi.org/10.1002/mp.12702.
[28] Kawrakow, I., Mainegra-Hing, E., Rogers, D.W.O., Tessier, F., Walters, B.R.B. The EGSnrc code system: Monte Carlo simulation of electron and photon transport; Report PIRS-701, Techreport PIRS-701, National Research Council Canada (2001–2015 [version 2021]). https://nrc-cnrc.github.io/EGSnrc/doc/pirs701-egsnrc.pdf.
[29] Kawrakow I. Accurate condensed history Monte Carlo simulation of electron transport. I. EGSnrc, the new EGS4 version Med. Phys. 2000;27(3):485–498. https://doi.org/10.1118/1.598917.
[30] Seltzer S. M. Stopping-Powers and Range Tables for Electrons, Protons, and Helium Ions NIST Standard Reference Database 1993;124. https://doi.org/10.18434/T4NC7P.
[31] Chandrasekaran S., Shanmugasundaram S. Optimization of variance reduction techniques used in EGSnrc Monte Carlo Codes J. Med. Phys. 2018;43(3):185. https://doi.org/10.4103/jmp.jmp_132_17.

4.2 Determination of the dose rate around a HDR ^{192}Ir brachytherapy source with the microDiamond and the microSilicon detector

Bei diesem Projekt handelt es sich um eine Kooperation mit der Abteilung für Medizinische Physik aus der Medizinischen Fakultät der Universität Freiburg, wodurch der Beitrag dieser Publikation für diese Dissertation anteilig gilt. In dieser Arbeit wurde die Dosisleistung um einen Ir-192 high dose rate (HDR) Brachytherapiestrahler mit zwei Festkörperdetektoren auf Grundlage des MC basierten Dosimetrieformalismus gemessen. Bei den Detektoren handelte es sich um die Modelle microDiamond und microSilicon der Firma PTW, welche sich aufgrund ihrer kleinen sensitiven Volumina und dadurch reduziertem Volumenmittelungs-Effekt für hochpräzise Messungen in der Brachytherapie potentiell eignen [47]. Auch die Energieabhängigkeit des Ansprechvermögens der Detektoren musste berücksichtigt werden, da das Strahlungsspektrum mit größer werdendem Abstand zur Quelle variiert [10]. Zur Bestimmung der Dosisleistung wurden die beiden Detektoren mithilfe eines Co-60 Strahls unter Kalibrierbedingungen nach DIN 6800-2 [58] im Labor der Herstellungsfirma kalibriert. Anschließend wurde die Messung der Dosisleistungsverteilung um die Ir-192 HDR Brachytherapiequelle in einem Wasserphantom durchgeführt. Die Detektoren wurden in radialen Abständen von 0,5 bis 10 cm zur Quelle bei einem Polarwinkel $\theta = 90\,^\circ$ nach dem TG-43 Koordinatensystem aus Abb. 2.4 platziert. Des Weiteren wurden Messungen bei festen Abständen von 1, 3 und 5 cm mit variierenden Polarwinkeln von 0 bis zu 168 ° durchgeführt. Die Ergebnisse wurden mit Dosisleistungen nach dem TG-43 Formalismus verglichen. Da das Wasserphantom (neben einer möglichen Störung der reinen Wasserumgebung durch hoch-Z Bauteile) eine endliche Größe aufweist, wurde ein MC simulierter Phantom-Korrektionsfaktor angewandt [75, 76]. Das veränderte Ansprechvermögen der Detektoren (‚det') aufgrund der Messung im Ir-192 Strahlungsfeld gegenüber Kalibrierbedingungen mit Co-60 Strahlung, hier $k_{\text{Ir-192,Co-60,det}}$, wurde ebenfalls berücksichtigt. Zur Untersuchung der Zusammensetzung dieses Korrektionsfaktors wurden kleine Wasservolumina, die sensitiven Volumina bestehend aus Wasser sowie die realen Detektoren simuliert. Das Verhältnis der Dosen in den unterschiedlichen Wasservolumina beschrieb dabei den Effekt der Volumenmittelung $f_{V,Q,\text{det}}$ in der jeweiligen Strahlungsqualität Q (und unterscheidet sich damit von p_{int}). Die Störung durch den voll modellierten Detektor gegenüber des sensitiven Wasservolumens wurde hier energieabhängiger Faktor $f_{E,Q,\text{det}}$ bezeichnet. $k_{\text{Ir-192,Co-60,det}}$ setzte sich somit, bezogen auf die jeweilige Strahlungsqualität, aus dem Produkt der beiden beschriebenen Faktoren zusammen, was im Ergebnis k_Q aus Gleichung 2.12 entspricht. Die Ergebnisse bezüglich $k_{\text{Ir-192,Co-60,det}}$ für den microDiamond Detektor lagen insbesondere für größere Abstände zur Quelle deutlich dichter an 1 als beim microSilicon Detektor. Dies lässt sich durch die ausgeprägte Energieabhängigkeit des Siliziumchips erklären, da dieses hoch-Z Material einen im Vergleich zu Diamant großen Wirkungsquerschnitt für photoelektrische Absorption aufweist [35] (siehe dazu Unterabschnitt 2.2.7). Lediglich für sehr kleine Abstände zur Quelle ≤ 1 cm führten die Volumenmittelungs-Effekte zu Abweichungen $> 1\,\%$. Diese waren aufgrund des kompakteren sensitiven Volumens

beim microSilicon Detektor weniger ausgeprägt. Innerhalb der erweiterten kombinierten Unsicherheit ($k = 2$) konnten die Dosisleistungen nach dem TG-43 Formalismus für $\theta \neq 0\,^\circ$ bestätigt werden. Dies galt für den microDiamond Detektor auch dann, wenn keine Korrektion bezüglich der veränderten Strahlungsqualität, also $k_{\text{Ir-192,Co-60,det}} \stackrel{!}{=} 1$, angewandt wurde. Die Detektoren microDiamond sowie microSilicon zeigten untereinander sowie verglichen mit den Dosisleistungsverteilungen nach TG-43 konsistente Ergebnisse. Damit erweisen sie sich als gut geeignet für die Messung der Dosisleistung um Ir-192 HDR Brachytherapiequellen. Diese Untersuchung war dabei nicht nur die erste, in welcher der microSilicon Detektor um einen Ir-192 Strahler eingesetzt wurde, sondern auch die erste, in der zwei direkt auslesbare, kalibrierte Festkörperdetektoren für diese Art von Messungen in einem Wasserphantom verwendet wurden. Dabei wurde zudem ein breites Spektrum an radialen Abständen und Polarwinkeln untersucht. Die hier gezeigten Ergebnisse bestätigen die praktisch vernachlässigbare Energieabhängigkeit und – für Abstände $> 3\,\text{cm}$ – den ebenfalls vernachlässigbaren Volumenmittelungseffekt des microDiamond Detektors sowie des Vorgängermodells [10, 77, 78].

Determination of the dose rate around a HDR ^{192}Ir brachytherapy source with the microDiamond and the microSilicon detector

Giulio Rossi [a,b,*], **Thomas Failing** [c,d], **Mark Gainey** [a,b], **Michael Kollefrath** [a,b], **Frank Hensley** [e], **Klemens Zink** [c,f,g], **Dimos Baltas** [a,b]

[a] Division of Medical Physics, Department of Radiation Oncology, Medical Center, Faculty of Medicine, University of Freiburg, Germany
[b] German Cancer Consortium (DKTK) Partner Site Freiburg, German Cancer Research Center (DKFZ), Heidelberg, Germany
[c] University of Applied Sciences Giessen, Institute of Medical Physics and Radiation Protection, Giessen, Germany
[d] University Medical Center Göttingen, Department of Radiation Oncology, Göttingen, Germany
[e] University Hospital of Heidelberg, Department of Radiation Oncology, Heidelberg, Germany
[f] University Medical Center Giessen-Marburg, Department of Radiotherapy and Radiation Oncology, Marburg, Germany
[g] Marburg Ionbeam Therapycenter (MIT), Marburg, Germany

Received 10 May 2022; accepted 25 July 2022

Abstract

Purpose: *To employ the microDiamond and the microSilicon detector (mDD and mSD, both PTW-Freiburg, Germany) to determine the dose rate around a HDR ^{192}Ir brachytherapy source (model mHDR-v2r, Elekta AB, Sweden).*
Methods: *The detectors were calibrated with a ^{60}Co beam at the PTW Calibration Laboratory. Measurements around the ^{192}Ir source were performed inside a PTW MP3 water phantom. The detectors were placed at selected points of measurement at radial distances r, ranging from 0.5 to 10 cm, keeping the polar angle $\theta = 90°$. Additional measurements were performed with the mSD at fixed distances r = 1, 3 and 5 cm, with θ varying from 0 to 150°, 0 to 166°, and 0 to 168°, respectively. The corresponding mDD readings were already available from a previous work (Rossi et al., 2020). The beam quality correction factor of both detectors, as well as a phantom effect correction factor to account for the difference between the experimental geometry and that assumed in the TG-43 formalism, were determined using the Monte Carlo (MC) toolkit EGSnrc. The beam quality correction factor was factorized into energy dependence and volume-averaging correction factors. Using the abovementioned MC-based factors, the dose rate to water at the different points of measurement in TG-43 conditions was obtained from the measured readings, and was compared to the dose rate calculated according to the TG-43 formalism.*
Results: *The beam quality correction factor was considerably closer to unity for the mDD than for the mSD. The energy dependence of the mDD showed a very weak radial dependence, similar to the previous findings showing a weak angular dependence as well (Rossi et al., 2020). Conversely, the energy dependence of the mSD decreased significantly with increasing distances, and also showed a considerably more pronounced angular dependence, especially for the smallest angles. The volume-averaging showed a similar radial dependence for both detectors: the correction had a maximal impact at 0.5 cm and then approached unity for larger distances, as expected. Concerning the angular dependence, the correction for the mSD was also similar to the one previously determined for the mDD (Rossi et al., 2020): a maximal impact was observed at $\theta = 0°$, with values tending to unity for larger angles. In general, the volume-averaging was less*

* Corresponding author: Giulio Rossi, Division of Medical Physics, Department of Radiation Oncology, Medical Center, Faculty of Medicine, University of Freiburg, German Cancer Consortium (DKTK) Partner Site Freiburg, German Cancer Research Center (DKFZ), Heidelberg, Germany.
E-mail: giulio.rossi@uniklinik-freiburg.de (G. Rossi).

Z Med Phys **33** (2023) 463–478
https://doi.org/10.1016/j.zemedi.2022.07.004
www.elsevier.com/locate/zemedi

pronounced for the mSD due to the smaller sensitive volume radius. After the application of the MC-based factors, differences between mDD dose rate measurements and TG-43 dose rate calculations ranged from −2.6% to +4.3%, with an absolute average difference of 1.0%. For the mSD, the differences ranged from −3.1% to +5.2%, with an absolute average difference of 1.0%. For both detectors, all differences but one were within the combined uncertainty (k = 2). The differences of the mSD from the mDD ranged from −3.9% to +2.6%, with the vast majority of them being within the combined uncertainty (k = 2). For θ ≠ 0°, the mDD was able to provide sufficiently accurate results even without the application of the MC-based beam quality correction factor, with differences to the TG-43 dose rate calculations from −1.9% to +3.4%, always within the combined uncertainty (k = 2).

Conclusion: *The mDD and the mSD showed consistent results and appear to be well suitable for measuring the dose rate around HDR ^{192}Ir brachytherapy sources. MC characterization of the detectors response is needed to determine the beam quality correction factor and to account for energy dependence and/or volume-averaging, especially for the mSD. Our findings support the employment of the mDD and mSD for source QA, TPS verification and TG-43 parameters determination.*

Keywords: microDiamond; microSilicon; ^{192}Ir; brachytherapy; dosimetry; Monte Carlo simulations

1 Introduction

The number of detectors suitable for accurate dose/dose rate determination around ^{192}Ir brachytherapy sources is restricted by the steep dose gradient in their vicinity and the considerable spectrum softening at larger distances [1,2]. According to the societal recommendations [1], a suitable detector should have a negligible, or at least well-characterized, volume-averaging effect and energy dependence, and it should also be able to determine the dose with type A uncertainties $\leq 3\%$ and type B $\leq 6\%$ (both with $k = 1$). Although strict fulfillment of these requirements is not easy in practice, it would be desirable to have such detectors which could be employed to perform source QA, TPS verification and TG-43 parameters determination. Historically, dosimetry with ^{192}Ir sources has been performed mainly with TLDs [3–7], radiochromic films [8,9], ionization chambers [10,11] and, less often, with semiconductor detectors such as silicon diodes [5,12,13]. Concerning semiconductor detectors, recent works have investigated the performance of the microDiamond detector (mDD, PTW-Freiburg, Germany): Kaveckyte et al. [2] have shown that the mDD is able to determine the dose around different ^{192}Ir sources, while the authors of the present work who belong to the University Medical Center Freiburg have shown that the mDD is suitable to determine the radial dose function $g_L(r)$ [14] and the anisotropy function $F(r,\theta)$ [15] of the ^{192}Ir source model mHDR-v2r (Elekta AB, Sweden) in a MP3 water phantom (PTW-Freiburg). Having obtained promising results for the determination of TG-43 parameters (relative dosimetry) with the mDD, in the present work it is investigated whether it is possible to employ the mDD and the new microSilicon detector (mSD, PTW-Freiburg) to determine also the dose rate (absolute dosimetry) around the ^{192}Ir source mHDR-v2r, using the same setup and methodology of the previous work on the $F(r,\theta)$ determination [15]. The mSD was chosen because, similar to the mDD, it provides direct readout and it has a small cylindrical sensitive volume of 0.75 mm radius and 18 μm thickness, which could allow for measurements with high spatial resolution and relatively little volume-averaging. Furthermore, the employment of the mSD is interesting because at the present time this detector has been mainly investigated in small field dosimetry [16–19] and, to the best of the authors' knowledge, no application in brachytherapy source dosimetry has yet been reported. Monte Carlo (MC) simulations were also performed to determine the beam quality correction factor, the volume-averaging and the energy dependence of the mDD and the mSD, completing the previous MC investigations on the mDD [14,15] and providing the first exhaustive MC-based characterization of the two detectors in the context of ^{192}Ir source dosimetry. This is the first work in which the mDD and the mSD were employed to determine the dose rate around a ^{192}Ir source in a water phantom. Despite the fact that, as already mentioned, dose determination around ^{192}Ir sources with the mDD has already been performed [2] (although in a PMMA phantom instead of a water phantom as in the present work), this work provides new insights about the suitability of the mDD to measure both very close (0.5 cm) as well as far away (10 cm) from the source, using an orientation (laterally with respect to the source), which had never been adopted before

by other groups, and which appears to considerably reduce the energy dependence of the detector. A detailed uncertainty budget is provided as well. Our findings suggest that meaningful ^{192}Ir source dosimetry with direct readout semiconductor detectors is realizable, provided that an accurate measurement procedure is adopted and that the detector response is well-characterized.

2 Materials and methods

2.1 Detectors calibration

A mDD (SN 122225) and a mSD (SN 151914) underwent calibration in terms of dose to water in ^{60}Co quality (PTW-Freiburg Calibration Laboratory) with direct traceability to a national primary standard. According to the calibration certificate, both detectors were positioned at 5 cm depth inside of a PTW 41023 water phantom (dimensions of approximately 30 cm × 30 cm × 30 cm), with the long-axis parallel to the beam. The SDD was 100 cm and the field size was 10 cm × 10 cm at the nominal reference points of the detectors. The detectors were calibrated on the same day. The temperature was 21 ± 3 °C, the air pressure was 1000 ± 50 hPa, and the relative humidity was 40 ± 20%. The calibration coefficients for the mDD and the mSD were $N_{D,w,mDD} = 1.282 \times 10^9$ Gy/C and $N_{D,w,mSD} = 5.284 \times 10^7$ Gy/C, respectively. The uncertainties on the calibration coefficients were reported to be 1.5% at $k = 2$ (see also Table 3).

2.2 Measurements

The mDD and the mSD were employed to perform measurements around the ^{192}Ir source mHDR-v2r at selected points of interest in the MP3 phantom. The experimental setup (Fig. 1), the detector´s placement and the measurement procedure were essentially the same as in the previous work on the $F(r,\theta)$ determination [15].

Because of the source cylindrical symmetry, it was assumed that the measurements would not depend on the azimuth angle φ. Therefore, in order to investigate the radial dependence of the dose rate, the mDD and the mSD were moved along the x-axis in both the positive and the negative directions, i.e. along two equivalent measurement sides at $\varphi = 0°$ and $\varphi = 180°$, and five repeated measurements were performed along each side at the same radial distances as for the $g_L(r)$ consensus data [20], i.e. 0.5, 0.75, 1, 1.5, 2, 3, 4, 5, 6, 8, and 10 cm, always keeping $\theta = 90°$. For the mDD, the measurement time was 0.5 s for $r \leq 3$ cm and 1 s elsewhere, while for the mSD it was 2 s for $r \leq 2$ cm and 5 s elsewhere. The measurements with the mDD were performed with air kerma strength $S_k = 37085$ U (1 U = 1 cGy cm^2 h^{-1}) and distance Δz between the source center and the needle tip of 4.85 mm (see Fig. 1), while those with the mSD were performed with $S_k = 41049$ U and $\Delta z = 5.45$ mm. From now on, this set of measurements will be referred to as "radial measurements". Similarly, in order to investigate the angular dependence of the dose rate, the mDD readings already acquired for the previous $F(r,\theta)$ measurements [15] were re-used to obtain the dose rate (see Eq. (6)). The same measurements were then performed with the mSD, i.e. moving the detector along the two sides to perform five repeated measurements at fixed radial distances $r = 1$, 3, and 5 cm, with θ varying with the same resolution as for the $F(r,\theta)$ consensus data [20] from 0 to 150° for 1 cm, 0 to 166° for 3 cm, and 0 to 168° for 5 cm. The measurement parameters were $S_k = 32588$ U and $\Delta z = 4.95$ mm for $r = 1$ cm, and $S_k = 41049$ U and $\Delta z = 5.45$ mm for $r = 3$ and 5 cm. These measurements will be referred to as "anisotropy measurements" in the following. For both the radial and the anisotropy datasets, the mean and the standard

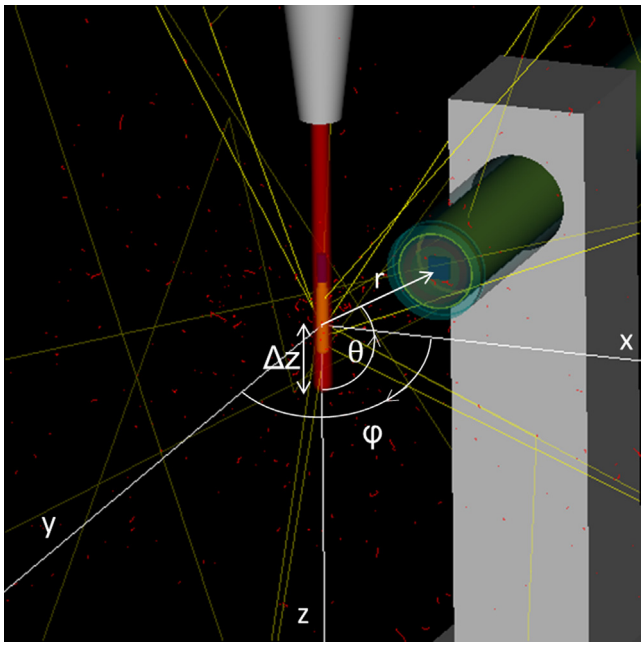

Figure 1. MC modelling of the measurements. The detector (green, in this case the mSD), kept in place with a PMMA holder (grey), is positioned laterally with respect to the long axis of the source and the drive cable (yellow and blue, respectively, with the source center at the origin of the coordinate system) at point of polar coordinates P(r = 1 cm, θ = 120°, φ = 0°). The tip of the mSD was made transparent to show the silicon chip (blue) hosting the cylindrical sensitive volume. The 4F needle (red) was also made transparent to allow the visualization of the source and of the air layer between the source and the needle itself. The air layer is characterized with the parameter Δz, i.e. distance between the source center and the needle tip [15]. A PMMA holder (grey) for the needle (red) and hence the source is also visible. The tracks of 20 photons (yellow) and 9000 electrons (red) are also shown.

deviation of the measured readings per unit time were first calculated for each side from the five repeated measurements. Then a mean over the two sides was calculated. The choice of the peculiar orientation of the detector, i.e. laterally with respect to the source instead of axially as recommended by PTW, was due to the following reasons: Firstly, with the available holders it would have been impossible to measure axially at angles $\theta \neq 90°$ and therefore, in order to keep a constant orientation of the detector with respect to the source for both the radial and the anisotropy measurements, the lateral orientation was preferred. Secondly, with this orientation it was possible to average the readings over two equivalent sides, thus considerably reducing the impact of the positional uncertainties [15]. Retrospectively, this orientation also appears to offer a further advantage, namely to reduce the energy dependence of the mDD, as it will be shown in what follows.

2.3 MC simulation parameters

MC simulations were performed using the user code egs_chamber [21] of the toolkit EGSnrc [22,23], in order to determine the dose conversion factor, the energy dependence, and the volume-averaging of both detectors under calibration and measurement conditions. The beam quality correction factor, as well as a phantom effect correction factor to account for the difference between our setup geometry and a TG-43 geometry that provides full scatter conditions at measurement points, were also determined. Additional simulations were carried out to assess the impact of the detector and source positional uncertainty on the measured dose rate. Four different simulation geometries were defined: (i) a water voxel placed at the calibration position in the calibration setup, (ii) the detector (mDD and mSD in turn) at the calibration position in the calibration setup, (iii) a water voxel at different points of interest in the measurement setup, and (iv) the detector at the same points of interest in the measurement setup. Following the existing recommendations on reporting MC studies [24], the main features of the simulations are summarized in Table 1 below. Further details about the simulation geometries, as well as the definition and modelling of the ^{60}Co and ^{192}Ir sources are provided in the previous work [15] and in the following Sections.

Table 1
Main features of the MC simulations.

Item name	Description	References
MC simulation toolkit	EGSnrc, release 2018, 2019a and 2020	[22,23]
User code	egs_chamber	[21]
^{60}Co source description	Collimated point source	[25]
^{192}Ir source description	Isotropic source with cylindrical shape	[15,26]
Cross-sections	XCOM photon cross-sections	[27]
Transport parameters	Boundary crossing algorithm: Exact.Global energy cutoff for photons (PCUT) and electrons (ECUT), as well as production threshold energy for photons (AP) and electrons (AE), were all set to 5 keV for the simulations of the water voxel as well as the detector in the calibration geometry, and to 10 keV for the simulations of the detector in the measurement geometry. For the simulations of the water voxels in the measurement geometry, the parameters were PCUT = AP = AE = 10 keV, and ECUT = 50 MeV (kerma approximation)	
Variance reduction techniques (VRT)	Cross-section enhancement (XCSE) with a factor of 1024 was applied to all the simulations. Russian Roulette (RR) with survival probability 1/1024 for electrons which cannot reach the cavity was applied to the simulations of the water voxel and the detector in the calibration geometry, as well as to the simulations of the detector in the measurement geometry. Correlated sampling (CS) was applied to all the simulations where the detector was present, and intermediate phase-space storage (IPSS) was also applied in some cases to the simulations of the water voxel and the detector in the measurement geometry	[21]
Scored quantities	Absorbed dose per emitted source photon to point-like water voxels, both in the calibration and in the measurement geometries. Absorbed dose per emitted source photon to the sensitive volumes of the mDD and mSD	
Number of histories (range)	2×10^9–1×10^{11}	
CPU time (range)	5.7 h (running in parallel on 63 CPUs) – 405.1 h (running in parallel on 200 CPUs)	
Statistical uncertainties	$\leq$0.4%	
Statistical methods	History-by-history estimator	
Postprocessing	None	

2.4 MC-based dose conversion factor

For a given radiation quality Q in water, the dose conversion factor of a detector is defined as follows:

$$f_{Q,det} = \frac{D_{w,Q}}{\bar{D}_{det,Q}} \quad (1)$$

where $D_{w,Q}$ is the dose to a watecr point-like volume and $\bar{D}_{det,Q}$ is the (average) dose to the detector's sensitive volume, both evaluated at a certain point of interest within the water phantom. As already shown in the previous works [14,15], in order to separate the effect of the energy dependence of the detector from that of the volume-averaging, $f_{Q,det}$ can be decoupled into an energy dependence correction factor $f_{E,Q,det}$ and a volume-averaging correction factor $f_{V,Q,det}$, defined as

$$f_{E,Q,det} = \frac{\bar{D}_{w-det,Q}}{\bar{D}_{det,Q}} \quad (2)$$

and,

$$f_{V,Q,det} = \frac{D_{w,Q}}{\bar{D}_{w-det,Q}} \quad (3)$$

where $\bar{D}_{w-det,Q}$ is the dose to the detector active volume comprised of water, instead of the real components. The ratio of the dose conversion factor under measurement conditions (in our case $Q = {}^{192}$Ir) to that under calibration conditions (in our case $Q_0 = {}^{60}$Co), gives the beam quality correction factor $k_{Q,Q_0,det}$.

2.4.1 Simulations of the calibration

To determine $f_{Co\text{-}60,det}$ of both detectors for the PTW calibration setup, a geometry consisting of a 30 cm × 30 cm × 30 cm water phantom embedded in a 500 cm radius air sphere with 40% humidity was modelled. Water was defined as pure degassed liquid water with a density of 0.998 g/cm^3 at 20 °C. Since a detailed model of the beam facility would be very cumbersome to perform in practice, a collimated point source was defined and a typical ^{60}Co therapy source spectrum was taken from Mora et al. [25]. At this point, two different simulations were performed: in one simulation, the detector was absent from the geometry and the dose was determined in a (0.1 mm)^3 water voxel. Following the calibration certificate, the voxel was placed at 5 cm depth in the phantom, resulting thus in a SDD of 100 cm, with a field size at the voxel position of 10 cm × 10 cm. In the other simulation, the water voxel was replaced by the detector (mDD and mSD in turn) with the nominal reference point positioned at a distance of 100 cm from the source. Within this geometry, two detector sub-geometries were defined: one where the detector was modelled following the PTW blueprints, and the other where all detector components were defined as water. Using the VRT CS (Table 1), it was possible to determine the dose to the active volumes of the real as well as of the water-made detector within one single run. In this way, $f_{Co\text{-}60,det}$ as well as the sub-factors $f_{E,Co\text{-}60,det}$ and $f_{V,Co\text{-}60,det}$ could be determined for both detectors according to Eqs. (1–3).

2.4.2 Simulations of the measurements

To determine $f_{Ir\text{-}192,det}$, the radial measurements with the mDD, as well as the radial and the anisotropy measurements with the mSD (Fig. 1), were simulated. The simulations of the anisotropy measurements with the mDD were already available from the previous work [15], where a detailed description of the modelling and the materials of the setup and of the source is also provided. Similar to the simulations to determine $f_{Co\text{-}60,det}$, the dose to a point-like water voxel [1,15] (in a geometry without detector) and to the detector (mDD and mSD in turn, real and water-made) were determined at different points of interest. Even if the measurements were performed along two sides, i.e. $\varphi = 0°$ and $\varphi = 180°$, it was expected that the differences in the MC results along these two sides would be negligible, and therefore only the measurements at $\varphi = 0°$ were simulated. For the radial measurements, simulations were performed placing the voxel and the detector at all selected points of measurements. For the anisotropy measurements, the water voxel and the mSD were simulated at selected angles $\theta = 0$, 10, 20, 30, 60, 120, 150, 160° (for 3 and 5 cm), 166° (only for r = 3 cm), and 168° (only for r = 5 cm), as previously done for the mDD [15]. The parameter Δz (see Fig. 1) was set according to the experimentally determined values. From the simulation results, the factor $f_{Ir\text{-}192,det}$, as well as the sub-factors $f_{E,Ir\text{-}192,det}$ and $f_{V,Ir\text{-}192,det}$ were determined for both detectors according to Eqs. (1–3). To determine the factors at points of measurements outside of the selected angles, a linear interpolation was performed. Assuming that the intrinsic energy dependence of the detectors would not considerably change when switching quality from ^{60}Co to ^{192}Ir, the beam quality correction factor $k_{Ir\text{-}192,Co\text{-}60,det}$ was determined as the ratio of $f_{Ir\text{-}192,det}$ to the constant $f_{Co\text{-}60,det}$:

$$k_{Ir-192,Co-60,det} = \frac{f_{Ir-192,det}}{f_{Co-60,det}} \quad (4)$$

2.5 MC-based phantom effect correction factor

A phantom effect correction factor $p_{phant,w}$ can be defined as follows [1]:

$$p_{phant,w} = \frac{D_{w,Q,TG-43}}{D_{w,Q,phant}} \quad (5)$$

where $D_{w,Q,TG-43}$ and $D_{w,Q,phant}$ are the dose to a point-like water volume for a radiation quality Q in a TG-43-like geometry and in the actual phantom geometry, respectively. In our case, $p_{MP3,w}$ was determined according to Eq. (5) for the radial measurements with the mDD and for the radial and the anisotropy measurements with the mSD, combining the results of the simulations in which the dose to the water voxels was determined in the MP3 geometry without detectors, together with the results of simulations in which the dose to the same water voxels was determined in a TG-43-like 40 cm radius water sphere. This latter dataset, as well as the $p_{MP3,w}$ values for the anisotropy measurements with the mDD, were already available from the previous work [15].

2.6 MC-based assessment of the positional uncertainties

A positional uncertainty of 0.1 mm was assigned to both the detector and the source [15]. Since it was expected that these uncertainties would have a maximal impact at the smallest distances and angles, two points of interest P_1 = (0.5 cm, 90°, 0°) and P_2 = (1 cm, 0°, 0°) were considered. The effect of the detector positional uncertainty and that of the source were separately assessed, using the same approach as in the previous work [15]: in order to determine the impact of the mDD positional uncertainty, simulations were performed in the MP3 geometry where the mDD was shifted from P_1 and P_2 by ± 0.1 mm along the x-, y-, and z-axis, always keeping the source at the origin of the coordinate system. Based on the guidelines of the Guide to the expression of Uncertainty in Measurements (GUM) [28], the standard uncertainty induced on the dose to the mDD at P_1 and P_2 was calculated for each single axis assuming a rectangular distribution, i.e. dividing the dose variation corresponding to the positive and negative shift by a reducing factor of $\sqrt{3}$. The calculation was essentially the same as shown for the $F(r,\theta)$ measurements, with the difference that in that case the dose to the mDD was normalized at 90°, and that a triangular distribution was assumed [15]. Finally, the overall uncertainty was determined summing in quadrature the contribution for the single axis. The same was done for the source positional uncertainty, this time letting the source move and keeping the mDD in place. Since it would have been impractical to repeat the same procedure for all the points of measurement, the dose variation induced by the detector and the source shifts at points closer to the source bisector plane, i.e. ($r > 0.5$ cm, $30° < \theta < 150°$), were calculated from those at P_1 using the inverse square law as a first approximation. The uncertainties were then again determined assuming a rectangular distribution and summing in quadrature the contributions along each axis. Similarly, the uncertainties at points further away from the source bisector plane, i.e. $\theta \leq 30°$ and $\theta \geq 150°$ were calculated from that at P_2 using the same method. Since preceding investigations showed similar results when the mSD was simulated instead of the mDD, it was assumed that the impact of the positional uncertainties would be the same and therefore the calculations were not repeated for the mSD. The uncertainties calculated from the simulation results are reported and discussed in Section 3.6.

2.7 Dose rate calculation

Once the mean detector reading per unit time $\dot{M}_{det}$ averaged over the five repeated measurements and the two sides and the MC-based factors were obtained, the mean dose rate at a point of measurement $P(r,\theta)$ for a TG-43-like geometry was calculated for both detectors as follows:

$$\dot{D}_{w,det}(r,\theta) = N_{D,w,det} k_{Ir-192,Co-60,det}(r,\theta) \dot{M}_{det}(r,\theta) p_{MP3,w}(r,\theta). \quad (6)$$

The measured dose rate for each dataset was compared to the dose rate calculated according to the TG-43 formalism [29,30] using the TG-43 consensus data of the source [20]. In order to enable the comparison between the two detectors, both the measured and the TG-43 based dose rate were normalized by the source air kerma strength, S_k, calculated from the source calibration certificate at the time at which the measurements were performed. To better evaluate the impact of $k_{Ir\text{-}192,Co\text{-}60,det}$, the measured dose rate was also calculated using the approximation $k_{Ir\text{-}192,Co\text{-}60,det} = 1$ everywhere.

3 Results

3.1 Dose conversion factor under calibration conditions

The dose conversion factor $f_{Co\text{-}60,det}$ of both detectors under calibration conditions, as well as the sub-factors $f_{E,Co\text{-}60,det}$ and $f_{V,Co\text{-}60,det}$, are shown in Table 2: it can be

Table 2
MC-based correction factors of the two detectors under calibration conditions. Values in parentheses correspond to $k = 1$ type A uncertainty applicable to the least significant digit of the results.

$f_{Co\text{-}60,det}$		$f_{E,Co\text{-}60,det}$		$f_{V,Co\text{-}60,det}$	
mDD	mSD	mDD	mSD	mDD	mSD
1.125 (5)	1.031 (5)	1.129 (4)	1.030 (5)	0.996 (4)	1.001 (5)

noticed that for the mSD the volume-averaging was negligible and the factors $f_{Co\text{-}60,mSD}$ and $f_{E,Co\text{-}60,mSD}$ were practically identical, indicating that in the calibration setup the mSD active volume is equivalent to a point-like volume. Conversely, for the mDD, which has a larger sensitive volume radius, the volume-averaging effect was greater albeit still relatively small.

3.2 Dose conversion factor under measurement conditions

3.2.1 Radial dependence of the dose conversion factor

Keeping a fixed angle $\theta = 90°$ and letting r vary, $f_{Ir\text{-}192,mDD}$ and $f_{Ir\text{-}192,mSD}$ behaved very differently (Fig. 2): for the mDD, a minimum at 0.5 cm was observed, followed by an increase up to 1.5 cm. After that, $f_{Ir\text{-}192,mDD}$ remained fairly constant up to 6 cm, where it started to slightly increase again. Conversely, $f_{Ir\text{-}192,mSD}$ showed a maximum at 0.5 cm followed by a steep falloff, with a −32.4% decrease from 0.5 to 10 cm. The behavior of $f_{Ir\text{-}192,det}$ can be better understood looking at the interplay of the factors $f_{E,Ir\text{-}192,det}$ (Fig. 2a) and $f_{V,Ir\text{-}192,det}$ (Fig. 2b): $f_{E,Ir\text{-}192,mDD}$ was more or less constant up to 6 cm, and then, similarly to $f_{Ir\text{-}192,mDD}$, showed a slight increase. Conversely, for $f_{E,Ir\text{-}192,mSD}$ the same sharp falloff as for $f_{Ir\text{-}192,mSD}$ was observed. This was due to the photon spectrum softening occurring at increasing distances, which caused the slight increase of $f_{E,Ir\text{-}192,mDD}$ (and thus of $f_{Ir\text{-}192,mDD}$) for $r > 6$ cm, and the decrease of $f_{E,Ir\text{-}192,mSD}$ and $f_{Ir\text{-}192,mSD}$, in accordance with the mass energy absorption coefficients ratios water to carbon and water to silicon. The factors $f_{V,Ir\text{-}192,mDD}$ and $f_{V,Ir\text{-}192,mSD}$ were considerably smaller than unity at the smallest distances, and then tended to approach unity. Therefore, the factor $f_{V,Ir\text{-}192,mDD}$ caused the increase of $f_{Ir\text{-}192,mDD}$ observed for $r \leq 1.5$ cm. The reason for this behavior can be easily understood by recalling the definition of Eq. (3): with the adopted orientation of the detectors a part of the water-made cylindrical sensitive volume was comparatively closer to the source than a point-like water voxel. Thus, at small distances the higher dose gradient generated within the cylinder led to a considerably larger dose with respect to the voxel, while at larger distances the difference became less pronounced, as expected. It is also worth noting that, for $r \leq 3$ cm, $f_{V,Ir\text{-}192,mDD}$ was always smaller than $f_{V,Ir\text{-}192,mSD}$, since the slightly larger sensitive volume radius of the mDD caused a more pronounced volume-averaging effect. It is interesting to compare the MC-based factors of the mDD presented here with those obtained in the previous work on the $g_L(r)$ determination [14]. In that work, the MC-based factors were determined using MCNP6.1 [31], with the mDD positioned axially with respect to the source (orientation recommended by PTW) instead of laterally, as done in the present work. In contrast to the present results, in the axial orientation the factors $f_{Ir\text{-}192,mDD}$ and $f_{E,Ir\text{-}192,mDD}$ showed a stronger radial dependence with a substantial increase with distance, especially for $r > 5$ cm. At 10 cm, in the axial orientation $f_{E,Ir\text{-}192,mDD}$ reached a maximum of 1.160, whereas in the lateral orientation it was much smaller, being equal to 1.125. The factor $f_{V,Ir\text{-}192,mDD}$ in the axial orientation was also very different from its counterpart: it showed a maximum of 1.023 at 0.5 cm and then decreased with distance. For $r > 2$ cm, it became equal to unity within

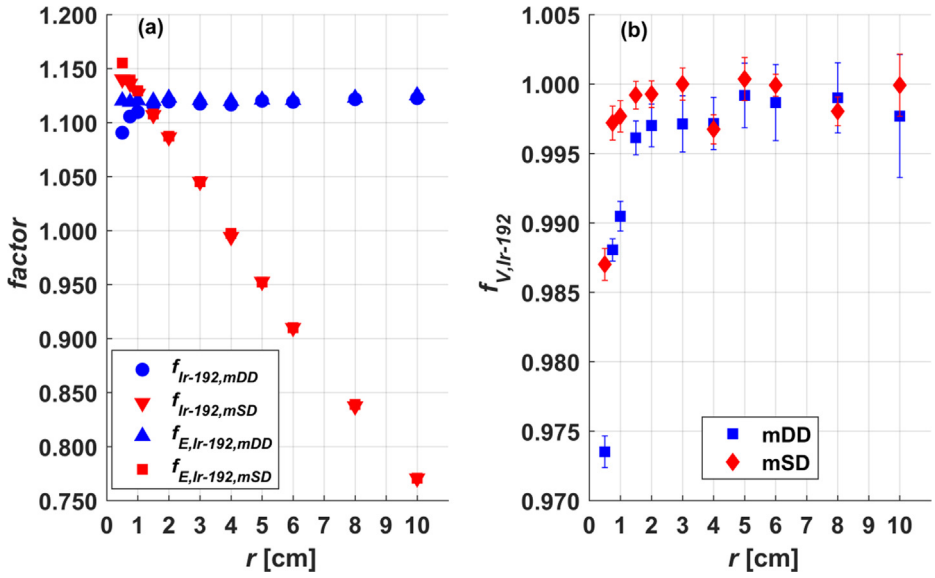

Figure 2. Radial dependence of the factors $f_{\text{Ir-192,det}}$, $f_{E,Ir\text{-}192,det}$ (a) and $f_{V,Ir\text{-}192,det}$ (b) for the mDD and the mSD. The MC type A uncertainty ($k = 1$) is also shown, although in (a) the uncertainty bars were smaller than the markers and therefore are not clearly visible.

the uncertainties. This difference between the two orientations was expected, because in the axial one the cylindrical surface of the (water-made) mDD sensitive volume was positioned frontally with respect to the source and therefore, since the cylinder diameter was considerably larger than the voxel size, the dose to the sensitive volume was in this case smaller than that to the voxel due to the contribution of comparatively more low-energy scattered photons.

3.2.2 Angular dependence of the dose conversion factor

Since the angular dependence of the MC-based factors of the mDD was already discussed in the previous work [15], the focus in what follows will be on the mSD. The mDD factors are nevertheless shown in Figs. 3–5 to allow for comparison. Keeping a fixed distance $r = 1$ cm and letting θ vary, $f_{Ir\text{-}192,mSD}$ (Fig. 3a) started with a global minimum at $\theta = 0°$, and then markedly increased up to $\theta = 20°$. After that, it tended to decrease down to a local minimum located at $\theta = 90°$, and finally increased again. This pattern of angular dependence was similar to that of $f_{Ir\text{-}192,mDD}$, although $f_{Ir\text{-}192,mSD}$ showed more pronounced fluctuations for $\theta > 10°$. In contrast to $f_{Ir\text{-}192,mSD}$, the factor $f_{E,Ir\text{-}192,mSD}$ did not show the sharp falloff observed for $\theta < 10°$, proving that this was not caused by the energy dependence of the detector. For $\theta > 10°$, $f_{E,Ir\text{-}192,mSD}$ behaved very similar to $f_{Ir\text{-}192,mSD}$. Generally, $f_{E,Ir\text{-}192,mSD}$ showed a stronger angular dependence than $f_{E,Ir\text{-}192,mDD}$ [15], which caused the more fluctuating behavior of $f_{Ir\text{-}192,mSD}$. One likely explanation for this is that silicon is far less water-equivalent than carbon. Therefore, the small spectral changes occurring at different angles might have induced more substantial variations in the dose ratio water to silicon than water to carbon. The factor $f_{V,Ir\text{-}192,mSD}$ was similar to its counterpart $f_{V,Ir\text{-}192,mDD}$ (Fig. 3b), showing a rapid falloff for $\theta \leq 10°$ (resembling the behavior at small distances with $\theta = 90°$, Fig. 2b), which caused the corresponding falloff observed for $f_{Ir\text{-}192,mSD}$. As explained in the previous work, this was due to the combined effect of the orientation of the detector, in a similar manner to what has already been observed concerning the radial dependence of $f_{V,Ir\text{-}192,mDD}$ and $f_{V,Ir\text{-}192,mSD}$, and of the air within the needle [15]. For $\theta \geq 10°$, $f_{V,Ir\text{-}192,mSD}$ became approximately angle-independent and was almost always slightly less than unity. Even in this case $f_{V,Ir\text{-}192,mSD}$ was larger than $f_{V,Ir\text{-}192,mDD}$ because of the smaller sensitive volume radius.

At $r = 3$ cm, $f_{Ir\text{-}192,mSD}$ started with a global minimum at 0° (as for $r = 1$ cm), tended to increase up to a maximum located at 90°, and then decreased again (Fig. 4a). Even in this case $f_{Ir\text{-}192,mSD}$ showed a stronger angular dependence than $f_{Ir\text{-}192,mDD}$, especially concerning the falloffs near the source axis ($\theta \leq 10°$ and $\theta \geq 160°$), which were considerably more pronounced. This was caused by the difference in the energy dependence: in fact, while $f_{E,Ir\text{-}192,mDD}$ was practically angle-independent [15], $f_{E,Ir\text{-}192,mSD}$ was very similar to $f_{Ir\text{-}192,mSD}$. The steeper falloffs of $f_{E,Ir\text{-}192,mSD}$ near the source axis with respect to $f_{E,Ir\text{-}192,mDD}$ can be explained by the fact that in this region the spectrum in the sensitive volumes of the detectors included comparatively more low-energy photons scattered mostly from water and, in minor part, from components of the source such as the capsule and the active core as well. In the case of the mDD, the contribution of these photons did not considerably alter the dose ratio water to carbon, while in the case of the mSD it

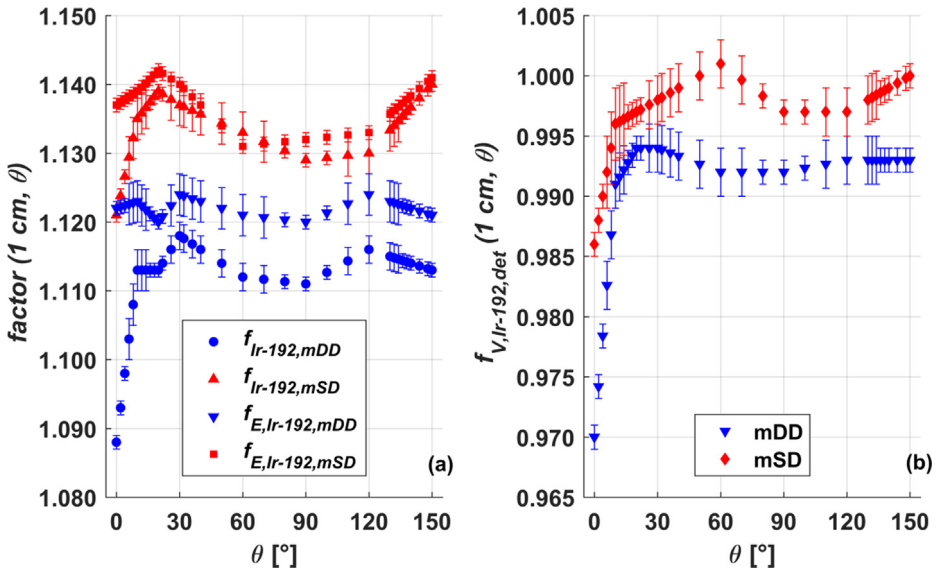

Figure 3. Angular dependence of the factors $f_{Ir\text{-}192,det}$, $f_{E,Ir\text{-}192,det}$ (a) and $f_{V,Ir\text{-}192,det}$ (b) for the mDD and the mSD at $r = 1$ cm. The MC type A uncertainty ($k = 1$) is also shown.

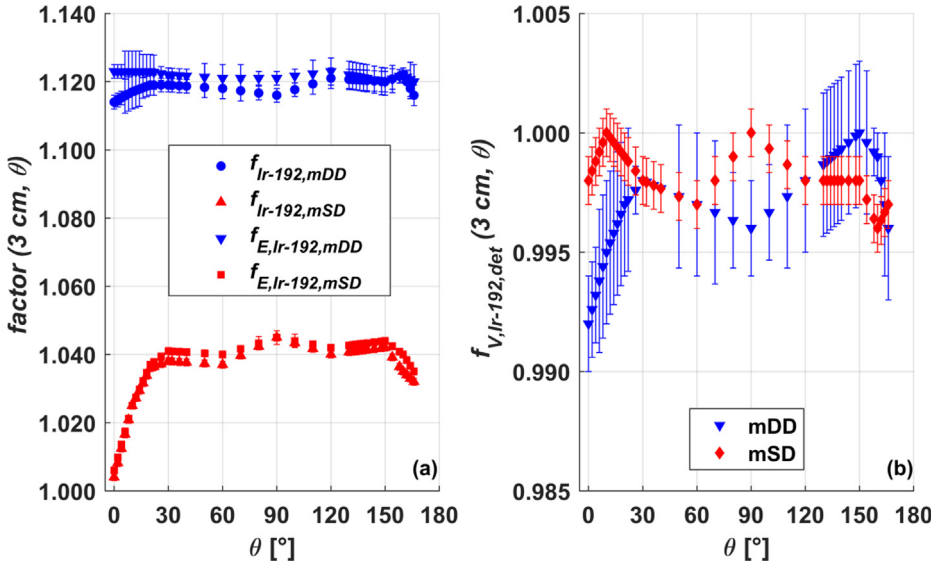

Figure 4. Angular dependence of the factors $f_{Ir\text{-}192,det}$, $f_{E,Ir\text{-}192,det}$ (a) and $f_{V,Ir\text{-}192,det}$ (b) for the mDD and the mSD at $r = 3$ cm. The MC type A uncertainty ($k = 1$) is also shown.

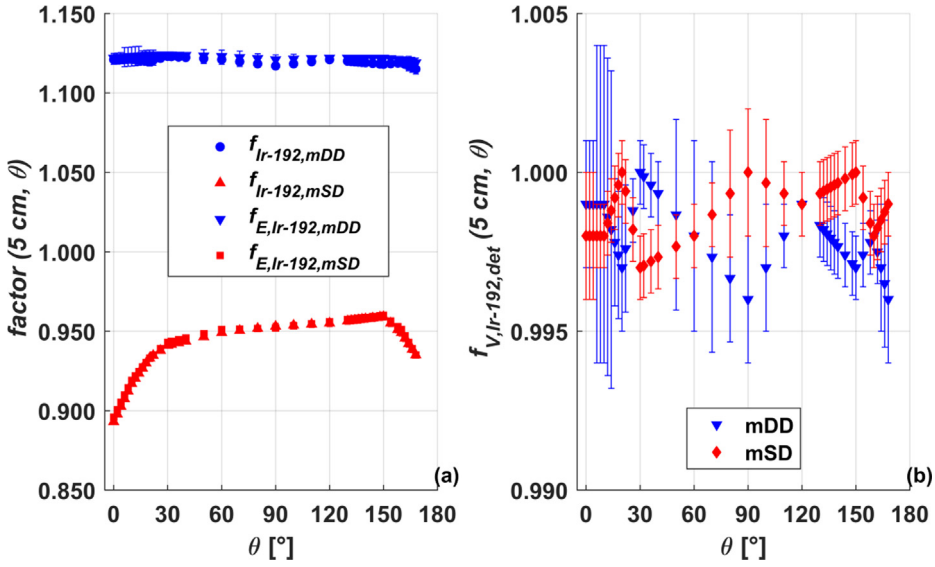

Figure 5. Angular dependence of the factors $f_{Ir\text{-}192,det}$, $f_{E,Ir\text{-}192,det}$ (a) and $f_{V,Ir\text{-}192,det}$ (b) for the mDD and the mSD at $r = 5$ cm. The MC type A uncertainty ($k = 1$) is also shown.

led to a substantial decrease of the dose ratio water to silicon. The factor $f_{V,Ir\text{-}192,mSD}$ (Fig. 4b) behaved similarly as for $r = 1$ cm, but showed a comparatively less marked falloff at small angles, because the volume-averaging had obviously a smaller impact at larger distances. Again $f_{V,Ir\text{-}192,mSD}$ at small angles was slightly larger than $f_{V,Ir\text{-}192,mDD}$.

At $r = 5$ cm, $f_{Ir\text{-}192,mSD}$ and $f_{E,Ir\text{-}192,mSD}$ showed sharp falloffs near the source axis like at 3 cm (Fig. 5a), in marked contrast to the very weak angular dependence showed by their counterparts $f_{Ir\text{-}192,mDD}$ and $f_{E,Ir\text{-}192,mDD}$ [15], again because of the contribution of low-energy photons. It is interesting to notice that $f_{Ir\text{-}192,mSD}$ and $f_{E,Ir\text{-}192,mSD}$ were always less than unity, meaning that at this distance the spectrum softening was considerable enough to reverse the dose ratio water to silicon, i.e. the dose to the real mSD became greater than that to the water-made mSD. Concerning the volume-averaging, $f_{V,Ir.192,mSD}$ was similar to $f_{V,Ir.192,mDD}$ [15], showing no falloff at small angles and being in general slightly less than unity, as it would be expected at larger

distances (Fig. 5b). A more oscillating behavior in comparison to 1 and 3 cm was observed, probably due to statistical fluctuations.

3.3 Beam quality correction factor

As expected, the beam quality correction factors $k_{Ir\text{-}192,Co\text{-}60,mDD}$ and $k_{Ir\text{-}192,Co\text{-}60,mSD}$ (Appendix A, Tables A1 and A2) showed the same behavior as $f_{Ir\text{-}192,mDD}$ and $f_{Ir\text{-}192,mSD}$, respectively. It was observed that the differences to unity were considerably larger for $k_{Ir\text{-}192,Co\text{-}60,mSD}$ than $k_{Ir\text{-}192,Co\text{-}60,mDD}$, confirming that, as expected, the mSD was more sensitive to the spectral changes occurring when changing quality from ^{60}Co to ^{192}Ir than the mDD. Moreover, in comparison to the MC-based beam quality correction factor determined by Kaveckyte et al. [2], it appears again that the lateral orientation reduced the energy dependence of the detector, as suggested in Section 3.2.1. In fact, the factor from Kaveckyte et al. [2], determined with the mDD positioned frontally with respect to the source at different distances from the source axis, increased from 1.003 at 1.5 cm up to 1.013 at 5.5 cm. Conversely, our factor showed a slighter increase in the same range, i.e. from 0.992 at 1.5 cm up to 0.995 at 6 cm.

3.4 Phantom effect correction factor

The phantom effect correction factor $p_{MP3,w}$ is shown in Appendix B, Tables B1 and B2. When keeping $\theta = 90°$ and letting r vary, $p_{MP3,w}$ was practically equal to unity within the statistical uncertainties ($k = 1$) for $r \leq 3$ cm and then gradually increased up to a maximum at 10 cm. Such an increase was due to the missing backscattered radiation at the points of interest closer to the phantom walls, which caused the dose in the MP3 geometry to be smaller than that in the TG-43 geometry providing full scatter conditions. This effect was instead practically negligible for the $p_{MP3,w}$ determined for the previous $g_L(r)$ measurements [14], because in that case the voxels were placed along the longer side of the MP3 phantom (y-axis) and therefore the lack of backscattering was considerably less pronounced. No substantial differences were found between the results with $\Delta z = 5.45$ mm (measurements with the mSD) and those with $\Delta z = 4.85$ mm (measurements with the mDD). The angular dependence of $p_{MP3,w}$ was similar to that observed in the previous work with the mDD [15], although $p_{MP3,w}$ at small angles was in this case considerably smaller due to the larger Δz values.

3.5 Dose rate determination

3.5.1 Radial measurements

Fig. 6 shows the ratio of the measured dose rate to the TG-43 dose rate calculations for the two detectors in the radial measurements arrangement, calculated using both the MC-based $k_{Ir\text{-}192,Co\text{-}60,det}$ values as well as the approximation $k_{Ir\text{-}192,Co\text{-}60,det} = 1$. The combined uncertainty on the dose rate ratio with coverage factor $k = 2$ is also shown (the detailed uncertainty analysis is presented in Section 3.6). Using the MC-based $k_{Ir\text{-}192,Co\text{-}60,det}$ values, for the mDD the percentage differences to the TG-43 dose rate ranged from −2.6% (3 cm) to -0.9% (10 cm), with an absolute mean difference of 1.7%. Although the mDD slightly underestimated the dose rate at all points with respect to the TG-43 formalism, the differences were always within the combined uncertainty. For the mSD, the differences ranged from −1.2% (0.75 and 1 cm) to −0.1% (3 cm), with an absolute mean difference of 0.6%. Even in this case the differences were always negative, but smaller than for the mDD and always well within the combined uncertainty. A good agreement was observed between the two detectors, with the differences of the mSD to the mDD ranging from −0.1% (10 cm) to +2.6% (3 cm). When using $k_{Ir\text{-}192,Co\text{-}60,det} = 1$, for the mDD the differences ranged from −1.9% (3 cm) to +1.5% (0.5 cm) with an absolute mean difference of 1.1%. All differences were within the combined uncertainty. For the mSD, the differences ranged from −10.5% (0.75 cm) to +32.4% (10 cm), with an absolute mean difference of 11.4%. In this case the differences were larger than the com-

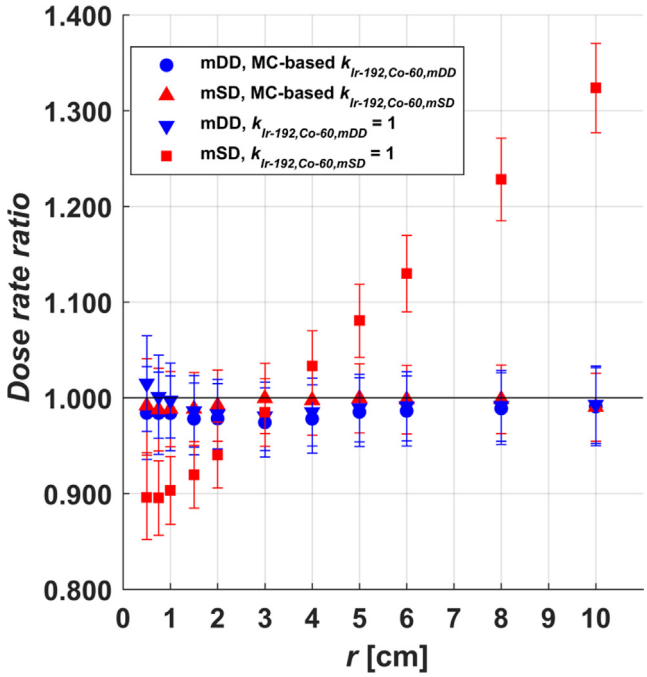

Figure 6. Measured to TG-43 dose rate ratio as a function of r for the mDD and the mSD, obtained using both the MC-based $k_{Ir\text{-}192,Co\text{-}60,det}$ and $k_{Ir\text{-}192,Co\text{-}60,det} = 1$. The combined uncertainty ($k = 2$) on the dose rate ratio is also shown.

bined uncertainty for 9 out of 11 points of measurements. It is worth pointing out how the use of the MC-based $k_{Ir\text{-}192,Co\text{-}60,mSD}$ values greatly reduced the very big differences observed for the mSD with $k_{Ir\text{-}192,Co\text{-}60,mSD} = 1$. Conversely, for the mDD the results with the MC-based $k_{Ir\text{-}192,Co\text{-}60,mDD}$ did not differ substantially from those with $k_{Ir\text{-}192,Co\text{-}60,mDD} = 1$.

3.5.2 Anisotropy measurements

Concerning the anisotropy measurements, at $r = 1$ cm (Fig. 7) and using the MC-based $k_{Ir\text{-}192,Co\text{-}60,det}$, for the mDD the differences ranged from −1.6% (22°) to +3.7% (0°), with an absolute mean difference of 0.9%. All differences were within the combined uncertainty ($k = 2$). For the mSD, the differences ranged from −3.0% (150°) to +5.2% (0°), with an absolute mean difference of 1.1%. In this case all differences except that at 0° were within the combined uncertainty ($k = 2$). The differences of the mSD to the mDD were from −2.9% (150°) to +1.8% (4 and 20°), all within the combined uncertainty ($k = 2$). When $k_{Ir\text{-}192,Co\text{-}60,det} = 1$ was used, for the mDD the differences ranged from -0.9% (30 and 60°) to +7.2% (0°), with an absolute mean difference of 1.1%. The differences were within the combined uncertainty ($k = 2$) for all the measurements except for that at 0°. Excluding this latter measurement, the agreement to the TG-43 dose rate was very good (within 2.6%). For the mSD, the differences ranged from −12.3% (150°) to −3.3% (0°), with an absolute mean difference of 9.5%. All differences except that at 0° were larger than the combined uncertainty ($k = 2$). Even in this case the use of the MC-based $k_{Ir\text{-}192,Co\text{-}60,mSD}$ substantially reduced the considerable differences observed for the mSD with $k_{Ir\text{-}192,Co\text{-}60,mSD} = 1$. For the mDD, the MC-based $k_{Ir\text{-}192,Co\text{-}60,mDD}$ reduced the differences observed at angles $\theta \leq 10°$ with $k_{Ir\text{-}192,Co\text{-}60,mDD} = 1$, while at other angles no substantial differences were observed.

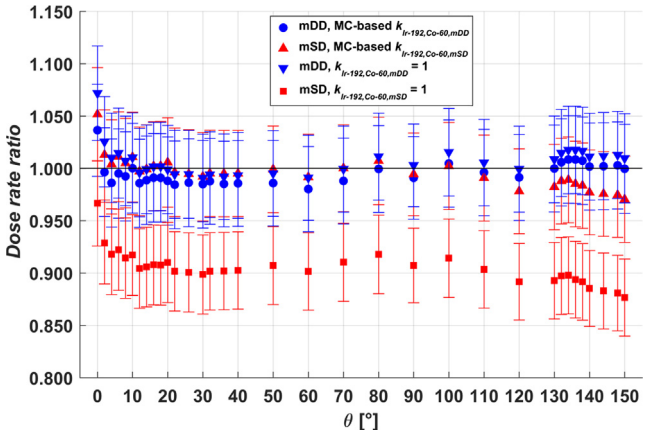

Figure 7. Measured to TG-43 dose rate ratio at 1 cm as a function of θ for both detectors, with the MC-based $k_{Ir\text{-}192,Co\text{-}60,det}$ and $k_{Ir\text{-}192,Co\text{-}60,det} = 1$. The combined uncertainty ($k = 2$) on the dose rate ratio is also shown.

At $r = 3$ cm and using the MC-based $k_{Ir\text{-}192,Co\text{-}60,det}$, for the mDD the differences ranged from +0.05% (110°) to +4.3% (0°), with an absolute mean difference of 0.9%. Although the mDD showed a tendency to slightly overestimate the dose rate at all points, all differences except that at 0° were within the combined uncertainty ($k = 2$). For the mSD, the differences ranged from −2.1% (26°) to +2.2% (0°), with an absolute mean difference of 1.0%. In this case all differences were within the combined uncertainty ($k = 2$). The differences of the mSD to the mDD were from −3.0% (14 and 16°) to +0.01% (110°), all within the combined uncertainty ($k = 2$). When $k_{Ir\text{-}192,Co\text{-}60,det} = 1$ was used, for the mDD the differences ranged from +0.5% (110°) to +5.2% (0°), with an absolute mean difference of 1.5%, while for the mSD from −2.8% (26°) to +4.8% (0°), with an absolute mean difference of 1.3%. For both detectors, all differences except those at 0° were within the combined uncertainty ($k = 2$). The use of the MC-based $k_{Ir\text{-}192,Co\text{-}60,mDD}$ and $k_{Ir\text{-}192,Co\text{-}60,mSD}$ substantially improved the overall agreement to the TG-43 dose calculations for both detectors. At $r = 5$ cm and using the MC-based $k_{Ir\text{-}192,Co\text{-}60,det}$, for the mDD the differences ranged from +1.1% (138°) to +3.2% (0°), with an absolute mean difference of 2.0%. For the mSD, the differences ranged from −1.4% (18 and 164°) to +1.0% (0°), with an absolute mean difference of 0.8%. For both detectors all differences were within the combined uncertainty ($k = 2$), although the mDD slightly overestimated the dose rate at all points of measurement, similarly to $r = 3$ cm. The differences of the mSD to the mDD were from −3.9% (16 and 18°) to −1.6% (110°). Although these differences were systematically less than unity due to the slight dose rate overestimation observed with the mDD, the majority of them (29 out of 41) were within the combined uncertainty ($k = 2$). When $k_{Ir\text{-}192,Co\text{-}60,det} = 1$ was used, for the mDD the differences ranged from +1.6% (2 and 138°) to +3.7% (0°), with an absolute mean difference of 2.4%. All differences were within the combined uncertainty ($k = 2$). For the mSD the differences ranged from +6.1% (138°) to +16.5% (0°), with an absolute mean difference of 8.5%. In contrast to the mDD, all differences were larger than the combined uncertainty ($k = 2$). Similar to the case $r = 3$ cm, the use of MC-based $k_{Ir\text{-}192,Co\text{-}60,mDD}$ and $k_{Ir\text{-}192,Co\text{-}60,mSD}$ substantially improved the overall agreement to the TG-43 dose rate calculations for both detectors, especially for the mSD.

3.6 Uncertainty analysis

Table 3 shows the relative percentage uncertainties ($k = 1$) on the mean measured dose rate per unit S_k of both detectors induced by different components (type A and B).

Table 3
Uncertainty analysis for the dose rate measurements with the mDD and the mSD.

Component	Type	Relative uncertainty ($k = 1$)
$\dot{M}_{mDD}$	A	0.1–1.1%
$\dot{M}_{mSD}$	A	0.03–0.4%
Detectors positional uncertainty	B	0.1–2.2%
Source positional uncertainty	B	0.1–2.2%
$k_{Ir\text{-}192,Co\text{-}60,mDD}$	A	0.5%–0.7%
$k_{Ir\text{-}192,Co\text{-}60,mSD}$	A	0.5%–0.6%
$p_{MP3,w}$	A	0.1%–0.2%
$N_{D,w,det}$	A	0.7%
S_k	B	1.07%
$\frac{\dot{D}_{w,mDD}}{S_k}$	A and B	1.0–2.4%
$\frac{\dot{D}_{w,mSD}}{S_k}$	A and B	1.0–2.4%

The overall combined uncertainty ($k = 1$), obtained by summing in quadrature the single contributions, is also shown. Since the uncertainties depended on the point of interest, the minimal and the maximal uncertainties are reported. Concerning the detector positional uncertainty, it was observed that a ± 0.1 mm shift along the x-axis from point P_1 = (0.5 cm, 90°) resulted in an approximately ∓ 4% variation in the MC dose to mDD, while a shift along the y-axis induced a variation of about ∓ 0.3%. Conversely, a shift along the z-axis induced a negative variation along both sides, i.e. the dose to the mDD became about 0.2% smaller for both the negative and the positive shift, because in both directions the source to detector distance slightly increased. Since this variation was considerably smaller than that along the x-axis, it was neglected in order to simplify the calculations. Considering point P_2 = (1 cm, 0°), a ± 0.1 mm shift along the x-axis resulted in a negligible dose variation (within 0.1%, positive for both directions), while a shift along the y-axis induced a variation of about ∓ 0.2%. A shift along the z-axis induced approximately ∓ 2% dose variation. Very similar results were observed for the source positional uncertainty. In comparison to relative measurements, with the MC dose normalized at P_0 = (1 cm, 90°), the dose variations induced by the shifts were approximately twice as large. This was because in the case of relative measurements the shifts affect both the point of interest and the normalization point, and thus the corresponding dose variations would be considerably reduced. The resulting detector- and source-related uncertainties on the measured dose rate, calculated as already explained in Section 2.6, were almost identical for the two detectors and were maximal at P_1, i.e. the shortest investigated distance, and decreased for larger distances. For $r \geq 1$ cm, the uncertainties were slightly larger at angles $\theta \leq 30°$ and $\theta \geq 150°$. These findings were very consistent with what would be expected with the adopted orientation of the detectors. The uncertainty on S_k was taken from de Werd et al. [32]. In our previous work it was shown from micro-CT images of four mDDs that submillimeter differences (< 0.2 mm) in the internal structure of the detector with respect to the nominal dimensions are possible, especially concerning the distance of the active volume to the detector tip. The impact of such constructional uncertainties on the measured $F(r,\theta)$ was assessed to be of about 2% [15]. However, successive MC-based investigations where the mDD active volume was shifted by 0.1 mm along the detector long-axis, showed no substantial differences in the dose to the mDD (within 0.1%). In view of the constructional similarities between the mDD and mSD, it was reasonable to assume that very similar results would be observed with the latter. Therefore, the influence of the constructional uncertainties of the two detectors on both the MC and the experimental results was neglected. A possible systematic uncertainty induced by the linear interpolation on the MC-based factors for the anisotropy datasets was also neglected. The uncertainty of TG-43 dose rate per unit S_k was determined summing in quadrature the uncertainties on the consensus dose rate constant Λ, taken from the estimate of Granero et al. [33], and those on the consensus $g_L(r)$ and $F(r,\theta)$, both taken based on the estimate of de Werd et al. [32]. The resulting uncertainty was determined to be within 1.2% ($k = 1$). Finally, the combined uncertainty ($k = 1$) on the measured to TG-43 dose rate ratio was calculated summing in quadrature the respective uncertainties.

4 Discussion

A detailed MC-based as well as experimental characterization of the mDD and of the mSD in the context of dose rate determination around a HDR ^{192}Ir brachytherapy source in a water phantom was performed. To the best of the authors' knowledge, this is not only the first study in which the mSD was employed with a ^{192}Ir source, but also the first in which two direct readout semiconductor detectors were employed for this kind of measurements in a water phantom, exploring a wide range of radial distances and polar angles. The MC simulations showed that for the mDD the energy dependence correction factor $f_{E,Ir\text{-}192,mDD}$ had a fairly weak radial dependence, completing the previous findings showing that the $f_{E,Ir\text{-}192,mDD}$ angular dependence is also practically negligible [15]. Conversely, for the mSD the factor $f_{E,Ir\text{-}192,mSD}$ showed a sharp falloff at larger distances as well as near the source axis, i.e. $\theta \leq 10°$ and $\theta \geq 150°$. This was expected, since carbon is far more water-equivalent than silicon. Incidentally, our findings suggest that the lateral orientation may reduce the energy dependence of the mDD in

comparison to the "recommended" axial orientation. However, caution must be used, because the energy dependence of the mDD in the axial orientation was calculated using MCNP6.1 [14,31], and therefore possible differences to EGSnrc might have contributed to the observed differences. The volume-averaging correction factors $f_{V,Ir\text{-}192,mDD}$ and $f_{V,Ir\text{-}192,mSD}$ for the radial measurements had both the higher impact for small distances $r \leq 1.5$ cm. The angular dependence of $f_{V,Ir\text{-}192,mSD}$ resembled that of $f_{V,Ir\text{-}192,mDD}$ [15], with a higher impact for small angles $\theta \leq 10°$. In general, the volume-averaging was more pronounced for the mDD, because of its larger sensitive volume radius. The beam quality correction factors $k_{Ir\text{-}192,Co\text{-}60,mDD}$ and $k_{Ir\text{-}192,Co\text{-}60,mSD}$ showed differences to unity which were larger than the MC type A uncertainty ($k = 1$) at almost all points of measurements. Such differences were much more pronounced for the mSD than the mDD, because the stronger energy dependence of mSD induced more variation in the response between calibration and measurement conditions. The phantom effect correction factor $p_{w,MP3}$ showed that, despite the presence of several accessories and the limited size, the MP3 phantom was able to fairly mimic TG-43 conditions for distances ≤ 6 cm and angles $30° \leq \theta \leq 150°$. This means that in the above-mentioned ranges of distances and angles our MC-based beam quality correction factors could be utilized for any other experimental setup capable to reproduce TG-43 conditions, provided that the detectors are positioned laterally as in this work. Conversely, for distances > 6 cm and angles $< 30°$ and $> 150°$, as well as for setups not able to mimic TG-43 conditions, the applicability of our phantom effect correction factors and of the beam quality correction factors should be verified and, where necessary, the MC calculations should be re-performed, especially in case of setups very different than the present one, such as for example multi-source arrangements employing other kinds of needles. Once the MC-based factors were applied to the measured readings, a good agreement to the TG-43 dose rate was observed with both detectors. Out of 126 overall measurement points, the differences to TG-43 were larger than the combined uncertainty ($k = 2$) at only one point for both the mDD (3 cm, 0°) and the mSD (1 cm, 0°). The detectors agreed to within the combined uncertainty ($k = 2$) at almost all points of measurements, showing a good consistency. When the approximation $k_{Ir\text{-}192,Co\text{-}60,mDD} = 1$ was used, for $\theta \neq 0°$ the mDD was able to provide sufficiently accurate results at all radial distances, with differences to TG-43 from −1.9% to +3.4%, always within the combined uncertainty ($k = 2$). In comparison to the corrected measurements, the agreement to TG-43 became worse only at angles $\theta \leq 10°$, because of the neglected contribution of the volume-averaging. Otherwise, in some cases the agreement was even slightly better, like for example in the radial measurements. This implies that, once a calibration coefficient is available, the MC-based determination of $k_{Ir\text{-}192,Co\text{-}60,mDD}$ is not strictly necessary to obtain accurate results, provided the mDD is employed to measure at angles $\theta \neq 0°$. Conversely for the mSD, the approximation $k_{Ir\text{-}192,Co\text{-}60,mSD} = 1$ led to considerable differences to TG-43 almost everywhere and therefore the use of the MC based $k_{Ir\text{-}192,Co\text{-}60,mSD}$ was strictly necessary in order to correct the detector reading. As already mentioned, this noticeable difference between the two detectors was due to the fact that the mDD is less sensitive than the mSD to the change in radiation quality from ^{60}Co to ^{192}Ir, and hence its beam quality correction factor was comparatively closer to unity. The substantial improvement in the accuracy of the results after the application of the MC-based $k_{Ir\text{-}192,Co\text{-}60,det}$ (especially for the mSD) also suggests that throughout the whole investigated measurement range the intrinsic energy dependence of both detectors does not considerably change from that under calibration with ^{60}Co. This would be a remarkable finding, considering that "extreme" distances $r > 5$ cm were explored. A detailed MC-based uncertainty analysis showed that, as expected, the positional uncertainties of the detectors and of the source played an important role, inducing an uncertainty on the dose rate which was approximately twice as much as in the case of relative (normalized) measurements. Therefore, our results also suggest that our setup and procedure are not only robust enough to allow for accurate relative measurements, but also for accurate dose rate determination with detectors which, due to the very small sensitive volume thicknesses, are extremely sensitive to positional uncertainties. It is interesting to note that the largest discrepancies to TG-43 were all observed at $\theta = 0°$, where both detectors tended to overestimate the dose rate. This trend was observed also in the previous work [15] and might have been caused by the interplay of the following factors:

1) Effect of the irradiation of the cable and/or other internal components of the detectors: at $\theta = 0°$ a comparatively larger part of the detectors is exposed to radiation. This might lead to a radiation-induced charge imbalance in the components of the detectors, which could cause an over-response, as shown by Looe et al. [34] for the mDD in small field dosimetry.

2) Systematic error in the Δz determination (e.g. parallax, being the determination based on visual inspection [15]), which may have resulted in a overestimation of $k_{Ir\text{-}192,Co\text{-}60,det}$ and/or $p_{MP3,w}$ at small angles, where Δz mostly affects measurements and MC simulations results.

3) Underestimation of the positional uncertainties: along the x- and the y-axis the dose rate to water has a local min-

imum at $\theta = 0°$ due to the self-absorption from the source capsule. Even though the MC results showed that a ± 0.1 mm shift of the detector and/or of the source along the x- and y-axis would induce practically negligible dose variations, possible larger shifts might have occurred. In this case the detector sensitive volume would be no more sufficiently aligned with the source capsule, thus allowing for more energetic photons to reach the sensitive volume necessarily resulting in a more or less pronounced dose rate overestimation.

Nevertheless, the differences to TG-43 of +3.7% with the mDD and of +5.2% with the mSD observed at (1 cm, 0°) may not be only related to the above-mentioned causes, but also to an inaccuracy in the TG-43 data themselves: in fact, in the previous work it was shown that the consensus anisotropy function ${}_{CON}F(r,\theta)$ of the source at (1 cm, 0°) is probably underestimated by a factor of 3% [15]. This fact, together with the consistency of the mDD and mSD results, might call for a reconsideration of ${}_{CON}F(r,\theta)$ as already pointed out in the previous work [15]. Incidentally, the effects described in points (2) and (3) could also explain some other observed slight systematic under/overestimations. For example, the fact that for points at $\theta = 90°$ a shift along the z-axis would result for both directions in a negative dose variation (Section 3.6), might account for the very small systematic underestimations observed with both detectors for the radial measurements. In any case, even at $\theta = 0°$ the differences to TG-43 were almost always within the combined uncertainty ($k = 2$), suggesting that both detectors are able to detect major inaccuracies in the absorbed dose to water at every point of interest. Our results further confirm the findings of the previous works about the mDD [14,15], as well as those from Kaveckyte et al. [2], and support that the mDD and the mSD satisfy the existing criteria for meaningful experimental dosimetry with high-energy brachytherapy sources [1]. The major strengths of these detectors lie in their direct readout, their excellent spatial resolution, the negligible intrinsic energy dependence in the investigated range, the almost negligible energy dependence of the mDD, and the weak volume-averaging of the mSD. This work could contribute to raise the awareness that accurate dose measurements around ^{192}Ir sources with direct readout detectors are possible, despite the well-known difficulties, and could prompt the development of protocols to employ such detectors in clinical practice.

5 Conclusion

The mDD and the mSD showed consistent results and appear to be well suitable to perform in-phantom dose rate measurements around HDR ^{192}Ir brachytherapy sources, spanning a wide range of distances and angles with excellent spatial resolutions. MC characterization of the detectors' response is needed to determine the beam quality correction factor and to account for energy dependence and/or volume-averaging at certain positions. The mDD is more favorable in terms of energy dependence, while the mSD is more favorable in terms of volume-averaging. Both detectors could be employed for brachytherapy source QA, TPS verification, and TG-43 parameters determination.

Declaration of Competing Interest

The authors declare that they have no known competing financial interests or personal relationships that could have appeared to influence the work reported in this paper.

Acknowledgments

The authors wish to thank PTW for calibrating the detectors and lending the mSD, as well as Jan Würfel and Konstantin Burzlaff for the explanations about the calibration procedure and the insightful discussions about the detectors. A warm thank-you also to Panagiotis Papagiannis for the precious suggestions to improve the manuscript.

Appendix A

Table A1
MC-based beam quality correction factors of the two detectors as a function of the radial distance r, at a fixed angle $\theta = 90°$. The parameter Δz was 4.85 mm for the mDD and 5.45 mm for the mSD. Values in parentheses correspond to $k = 1$ type A uncertainty applicable to the least significant digit of the results.

r [cm]	$k_{Ir\text{-}192,Co\text{-}60,det}$ (r, θ = 90°)	
	mDD	mSD
0.5	0.970 (5)	1.107 (6)
0.75	0.983 (5)	1.103 (6)
1	0.987 (5)	1.094 (6)
1.5	0.992 (5)	1.075 (6)
2	0.995 (5)	1.055 (6)
3	0.993 (5)	1.015 (5)
4	0.993 (5)	0.965 (5)
5	0.996 (5)	0.925 (5)
6	0.995 (5)	0.883 (5)
8	0.997 (5)	0.813 (4)
10	0.998 (6)	0.748 (4)

Table A2
MC-based beam quality correction factors of the two detectors as a function of the polar angle θ at fixed radial distances r = 1, 3 and 5 cm. For the mDD, the parameter Δz was 4 mm at all the distances, while for the mSD Δz was 5 mm at r = 1 cm and 5.45 mm at 3 and 5 cm. Values in parentheses correspond to k = 1 type A uncertainty applicable to the least significant digit of the results.

θ [°]	$k_{Ir\text{-}192,Co\text{-}60,det}$ (r, θ)					
	r = 1 cm		r = 3 cm		r = 5 cm	
	mDD	mSD	mDD	mSD	mDD	mSD
0	0.967 (5)	1.088 (6)	0.991 (5)	0.975 (5)	0.996 (5)	0.867 (5)
10	0.990 (5)	1.102 (6)	0.993 (6)	0.995 (5)	0.997 (5)	0.891 (5)
20	0.989 (5)	1.105 (6)	0.995 (6)	1.006 (5)	0.996 (5)	0.906 (5)
30	0.994 (5)	1.104 (6)	0.995 (5)	1.008 (5)	0.999 (5)	0.913 (5)
60	0.989 (5)	1.100 (6)	0.994 (5)	1.007 (5)	0.996 (6)	0.921 (5)
90	0.988 (5)	1.096 (6)	0.992 (5)	1.015 (5)	0.993 (5)	0.925 (5)
120	0.992 (5)	1.097 (6)	0.997 (5)	1.010 (5)	0.997 (5)	0.928 (5)
150	0.990 (5)	1.107 (6)	0.995 (6)	1.011 (5)	0.994 (5)	0.931 (5)
160			0.997 (5)	1.005 (5)	0.994 (5)	0.922 (5)
166			0.992 (6)	1.002 (5)		
168					0.991 (5)	0.908 (5)

Appendix B

Table B1
MC-based phantom effect correction factor as a function of the radial distance r, at a fixed angle $\theta = 90°$. The parameter Δz was 5.45 mm. Values in parentheses correspond to k = 1 type A uncertainty applicable to the least significant digit of the results.

r [cm]	$p_{MP3,w}$ $(r, \theta = 90°)$
0.5	1.001 (1)
0.75	1.000 (2)
1	1.001 (1)
1.5	1.000 (1)
2	1.000 (1)
3	1.000 (1)
4	1.002 (1)
5	1.002 (1)
6	1.004 (1)
8	1.009 (1)
10	1.013 (1)

Table B2
MC-based phantom effect correction factor as a function of the polar angle θ at fixed radial distances r = 1, 3 and 5 cm. The parameter Δz was 5 mm at r = 1 cm and 5.45 mm at 3 and 5 cm. Values in parentheses correspond to k = 1 type A uncertainty applicable to the least significant digit of the results.

θ [°]	$p_{MP3,w}$ (r, θ)		
	r = 1 cm	r = 3 cm	r = 5 cm
0	0.977 (1)	0.979 (1)	0.987 (2)
10	0.987 (1)	0.993 (1)	0.997 (2)
20	0.996 (1)	0.998 (1)	0.999 (2)
30	0.998 (1)	1.001 (1)	1.002 (2)
60	0.998 (1)	1.003 (1)	1.003 (1)
90	0.999 (1)	1.000 (1)	1.002 (1)
120	0.999 (1)	1.001 (1)	1.001 (1)
150	0.996 (1)	1.002 (1)	0.998 (2)
160		1.002 (1)	0.998 (1)
166		1.000 (1)	
168			0.996 (1)

References

[1] Perez-Calatayud J, Ballester F, Das RK, DeWerd LA, Ibbott GS, Meigooni AS, et al. Dose calculation for photon-emitting brachytherapy sources with average energy higher than 50 keV: report of the AAPM and ESTRO. Med Phys 2012;39:2904–2929.

[2] Kaveckyte V, Malusek A, Benmakhlouf H, Carlsson GA, Carlsson-Tedgren Å. Suitability of microDiamond detectors for the determination of absorbed dose to water around high-dose-rate ^{192}Ir brachytherapy sources. Med Phys 2018;45:429–437.

[3] Muller-Runkel R, Cho SH. Anisotropy measurements of a high dose rate Ir-192 source in air and in polystyrene. Med Phys 1994;21:1131–1134.

[4] Kirov AS, Williamson JF, Meigooni AS, Zhu Y. TLD, diode and Monte Carlo dosimetry on an ^{192}Ir source for high dose-rate brachytherapy. Phys Med Biol 1995;40:2015–2036.

[5] Meigooni AS, Kleiman MT, Johnson JL, Mazloomdoost D, Ibbott GS. Dosimetric characteristics of a new high intensity ^{192}Ir source for remote afterloading. Med Phys 1997;24:2008–2013.

[6] Karaiskos P, Angelopoulos A, Sakelliou L, Sandilos P, Antypas C, Vlachos L, et al. Monte Carlo and TLD dosimetry of an ^{192}Ir high dose-rate brachytherapy source. Med Phys 1998;25:1975–1984.

[7] Anctil J, Clark BG, Arsenault CJ. Experimental determination of dosimetry functions of Ir-192 sources. Med Phys 1998;25:2279–2287.

[8] Sharma SD, Bianchi C, Conte L, Novario R, Bhatt BC. Radiochromic film measurement of anisotropy function for high-dose-rate Ir-192 brachytherapy source. Phys Med Biol 2004;45:4065–4072.

[9] Ayoobian N, Asl AS, Poorbaygi H, Javanshir MR. Gafchromic film dosimetry of a new HDR ^{192}Ir brachytherapy source. J Appl Clin Med Phys 2016;17:194–205.

[10] Baltas D, Kramer R, Löffler E. Measurements of the anisotropy of the new Ir-192 source for the microSelectron-HDR. Activity Special Report 1993;3:2–8.

[11] Mishra V, Waterman FM, Suntharalingam N. Anisotropy of an ^{192}iridium high dose rate source measured with a miniature ionization chamber. Med Phys 1997;24:751–755.

[12] Zilio VO, Joneja OP, Popowski Y, Rosenfeld A, Chawla R. Absolute depth-dose-rate measurements for an ^{192}Ir HDR brachytherapy source in water using MOSFET detectors. Med Phys 2006;33:1532–1539.

[13] Piermattei A, Azario L, Monaco G, Soriani A, Arcovito G. p-type silicon detector for brachytherapy dosimetry. Med Phys 1995;22:835–839.

[14] Rossi G, Gainey M, Thomann B, Kollefrath M, Würfel J, Allgaier B, et al. Monte Carlo and experimental ^{192}Ir brachytherapy dosimetry with microDiamond detectors. Z Med Phys 2019;29:272–281.

[15] Rossi G, Gainey M, Kollefrath M, Hofmann E, Baltas D. Suitability of the microDiamond detector for experimental determination of the anisotropy function of High Dose Rate ^{192}Ir brachytherapy sources. Med Phys 2020;47:5838–5850.

[16] Schönfeld A, Poppinga D, Kranzer R, et al. Technical Note: Characterization of the new microSilicon diode detector. Med Phys 2019;46(9):4257–4262.

[17] Weber C, Kranzer R, Weidner J, et al. Small field output correction factors of the microSilicon detector and a deeper understanding of their origin by quantifying perturbation factors. Med Phys 2019;46(9):4257–4262.

[18] Blum I, Tekin T, Delfs B, et al. The dose reponse of the PTW microDiamond and microSilicon in transverse magnetic field under small field conditions. Phys Med Biol 2021;66:155003.

[19] Georgiou G, Kumar S, Würfel JU, et al. The PTW microSilicon diode: Performance in small 6 and 15 MV photon fields and utility of density compensation. Med Phys 2021;48(7):8062–8064.

[20] TG-43 database for ^{192}Ir HDR sources from GEC-ESTRO BRAPHYQS Working Group. https://www.estro.org/About/ESTRO-Organisation-Structure/Committees/GEC-ESTRO-Committee/GEC-ESTRO-BRAPHYQS/Ir-192-HDR. Accessed November 2021.

[21] Wulff J, Zink K, Kawrakow I. Efficiency improvements for ion chamber calculations in high energy photon beams. Med Phys 2008;35:1328–1336.

[22] Kawrakow I. Accurate condensed history Monte Carlo simulation of electron transport. I. EGSnrc, the new EGS4 version. Med Phys 2000;27:485–498.

[23] Kawrakow I, Rogers DWO. The EGSnrc Code System: Monte Carlo Simulation of Electron and Photon Transport. NRCC Report No. PIRS-701. National Research Council of Canada; 2006.

[24] Sechopoulos I, Rogers DWO, Bazalova-Carter M, Bolch WE, Heath EC, McNitt-Gray MF. RECORDS: improved Reporting of montE carlO RaDiation Studies: Report of the AAPM Research Committee Task Group 268. Med Phys 2018;45:e1–e5.

[25] Mora GM, Maio A, Rogers DWO. Monte Carlo simulation of a typical ^{60}Co therapy source. Med Phys 1999;26:2494–2502.

[26] Baglin CM. Nuclear Data Sheets for A = 192. Nuclear Data Sheets 2012;113:1871–2111.

[27] XCOM: Photon Cross Sections Database. NIST. https://www.nist.gov/pml/xcom-photon-cross-sections-database. Accessed April 2022.

[28] Jcgm. Evaluation of measurement data—Guide to the expression of Uncertainty in Measurement (GUM). Report 100. SEVRES-BIPM Joint Committee for Guides in Metrology WG1, 2008.

[29] Nath R, Anderson LL, Luxton G, Weaver KA, Williamson JF, Meigooni AS. Dosimetry of interstitial brachytherapy sources: Recommendations of the AAPM Radiation Therapy Committee Task Group No. 43. Med Phys 1995;22:209–234.

[30] Rivard MJ, Coursey BM, DeWerd LA, Hanson WF, Saiful Huq M, Ibbott GS, et al. Update of AAPM Task Group No. 43 Report: a revised AAPM protocol for brachytherapy dose calculations. Med Phys 2004;31:633–674.

[31] Goorley T, James M, Booth T, Brown F, Bull J, Cox LJ, et al. Initial MCNP6 release overview. Nucl Technol 2012;180(3):298–315.

[32] DeWerd LA, Ibbott GS, Meigooni AS, Mitch MG, Rivard MJ, Stump KE, et al. A dosimetric uncertainty analysis for photon-emitting brachytherapy sources: Report of AAPM Task Group No. 138 and GEC-ESTRO. Med Phys 2011;38:782–801.

[33] Granero D, Vijande J, Ballester F, Rivard MJ, et al. Dosimetry revisited for the HDR 192Ir brachytherapy source model mHDR-v2. Med Phys 2011;38:487–494.

[34] Looe HK, Poppinga D, Kranzer R, Büsing I, Tekin T, Ulrichs AB, et al. The role of radiation-induced charge imbalance on the dose-response of a commercial synthetic diamond detector in small field dosimetry. Med Phys 2019;46:2752–2759.

4.3 Investigations on the beam quality correction factor for ionization chambers in high-energy brachytherapy dosimetry

Ziel dieser Arbeit ist die Vorstellung des neuartigen Dosimetrieformalismus auf Basis der beschränkten Cema für die Anwendung in der Brachytherapie. Als methodische Grundlage dienten aktuelle Dosimetrieprotokolle wie etwa Protokoll TRS-398 der IAEA [2] oder DIN-Norm 6800-2 [58]. Dabei wurden mögliche Referenzbedingungen für die Brachytherapie nach Vorbild des TG-43 Formalismus [3, 4] analysiert.
Für diese Arbeit wurden insgesamt fünf Ionisationskammern von PTW und Standard Imaging für Messungen um einen Ir-192 HDR Brachytherapiestrahler in einem Wasserphantom untersucht. Die Positionierung der Detektoren erfolgte über Profilmessungen um die Quelle entlang der Bewegungsrichtungen der motorisierten Achsen des Phantoms [12]. Die Korrektion aufgrund veränderter Strahlungsqualität von Kalibrier- und Messbedingungen k_Q wurde für jeden Detektor mithilfe des erweiterten `egs_chamber` Codes simuliert. Die Unterschiede von k_Q bezüglich der absorbierten Dosis und beschränkter Cema waren hier deutlich kleiner als die statistische Unsicherheit der MC Simulationen, so dass hiermit die Annahme der Cema Approximation bestätigt werden konnte. Aufgrund der Untersuchung der beschränkten Cema war es möglich, die Signalbeiträge in den Detektoren spektral aufgelöst darzustellen. k_Q setzt sich nach Gleichung 2.12 aus dem Quotienten der Dosiskonversionsfaktoren f unter Kalibrier- und Messbedingungen zusammen [60]. f lässt sich mit Gleichung 3.2 in drei Faktoren aufteilen, um verschiedene physikalische Effekte zu verdeutlichen. Diese drei Faktoren beinhalten das ‚Spencer-Attix stopping power ratio' [63] sowie die detektorspezifischen Störungsfaktoren der Volumenmittelung p_{int} und Störungen aufgrund von Detektorbauteilen, p_{ext} [9]; siehe auch Abschnitt 3. Für k_Q wurde sowohl das gesamte Luftvolumen als auch nur das sensitive Volumen (ohne Totvolumen) der Ionisationskammern berücksichtigt. Die Unterscheidung des sensitiven Volumens hat durch die Dosimetrie in Magnetfeldern [79, 80] sowie kleinen Feldern [81] deutlich an Bedeutung gewonnen. Die Totvolumina wurden bisher noch nicht systematisch untersucht, so dass die Datenlage dünn ist. Im Zuge dieser Arbeit wurde das Totvolumen der Ionisationskammer PTW 31023 mithilfe der Finite-Elemente-Methode erstmalig bestimmt. Zur Prüfung der Ergebnisse wurden auch die anderen Totvolumina berechnet und anhand von Literaturwerten validiert.
Die korrigierten Messwerte der kalibrierten Ionisationskammern wurden mit den Kalibrierzertifikaten der Ir-192 HDR Brachytherapiestrahler verglichen, um die ermittelten Korrektionsfaktoren zu verifizieren. Die nach Gleichung 3.1 gemessenen Dosisleistungen stimmten mit den Angaben der Herstellungsfirma, welche sich nach Gleichung 2.10 berechnen, innerhalb der erweiterten Unsicherheit ($k = 2$) für alle Ionisationskammern bis auf einen Fall überein, bei dem das gesamte Luftvolumen (inklusive Totvolumen) berücksichtigt wurde. Das Ansprechvermögen der Detektoren wies zudem eine deutliche Richtungsabhängigkeit auf. Ein aussagekräftiger Vergleich mit Literaturwerten war nicht möglich, da zum Zeitpunkt der Publikation keine vergleichbaren Daten bezüglich der Ausrichtung der Detektoren existierten.

Mithilfe der Simulationen und Berechnungen der beschränkten Cema konnten p_{int} sowie p_{ext}, die zur Korrektion aufgrund veränderter Strahlungsqualität beitragen, auch spektral aufgelöst untersucht werden. Bei einem nominalen Abstand von 1 cm war der Volumenmittelungseffekt (p_{int}) hauptverantwortlich für die Störung der Messung, wenn die Symmetrieachsen der Detektoren zur Quelle hin zeigten. Die Störung aufgrund von Detektorbauteilen (p_{ext}) war am größten für Ionisationskammern mit Aluminium Schutzring. In diesem Fall ließ sich auch eine deutliche Energieabhängigkeit zu niedrigen Energien erkennen. Dies lässt sich unter anderem anhand der photoelektrischen Absorption für hoch-Z Materialien erklären; siehe Abb. 2.1 [35]. Des Weiteren wurde k_Q, p_{int} und p_{ext} für einen nominalen Abstand von 3 cm untersucht, da der steile Dosisgradient für größere Abstände weniger ausgeprägt ist. Damit ließen sich geometrische Unsicherheiten reduzieren. Fast alle Werte von k_Q näherten sich mit größerem Abstand dem Wert 1 an, jedoch führte diese Vergrößerung auch zu deutlich kleineren Messsignalen, so dass jede Konstellation von Quelle und Detektor individuell beurteilt werden sollte.
Für eine möglichst exakte Dosimetrie von Brachytherapiequellen mit Ionisationskammern empfiehlt es sich, Korrektionsfaktoren auf der Grundlage des sensitiven Volumens der Kammern zu verwenden und die Richtungsabhängigkeit des Ansprechvermögens zu berücksichtigen.

IOP Publishing Phys. Med. Biol. 69 (2024) 165002 https://doi.org/10.1088/1361-6560/ad638b

Physics in Medicine & Biology

IPEM Institute of Physics and Engineering in Medicine

OPEN ACCESS

RECEIVED
30 November 2023

REVISED
16 June 2024

ACCEPTED FOR PUBLICATION
15 July 2024

PUBLISHED
30 July 2024

PAPER

Investigations on the beam quality correction factor for ionization chambers in high-energy brachytherapy dosimetry

T Failing[1,*], F W Hensley[2], B Keil[1,3,4] and K Zink[1,4,5,6]

[1] Institute of Medical Physics and Radiation Protection (IMPS), University of Applied Sciences, Gießen, Germany
[2] Department for Radiotherapy and Radiooncology, University Medical Center Heidelberg, Heidelberg, Germany
[3] Department for Diagnostic and Interventional Radiology, Philipps-University Marburg, Marburg, Germany
[4] LOEWE Research Cluster for Advanced Medical Physics in Imaging and Therapy (ADMIT), TH Mittelhessen University of Applied Sciences, Giessen, Germany
[5] Department for Radiotherapy and Radiooncology, University Medical Center Giessen-Marburg, Marburg, Germany
[6] Marburg Iontherapy Center (MIT), Marburg, Germany
[*] Author to whom any correspondence should be addressed.

E-mail: thomas.failing@lse.thm.de

Keywords: Monte Carlo simulations, EGSnrc, high-energy brachytherapy dosimetry, restricted cema, ionization chamber, dead volume

Abstract

Objective. To enhance the investigations on MC calculated beam quality correction factors of thimble ionization chambers from high-energy brachytherapy sources and to develop reliable reference conditions in source and detector setups in water. *Approach*. The response of five different ionization chambers from PTW-Freiburg and Standard Imaging was investigated for irradiation by a high dose rate Ir-192 Flexisource in water. For a setup in a Beamscan water phantom, Monte Carlo simulations were performed to calculate correction factors for the chamber readings. After exact positioning of source and detector the absorbed dose rate at the TG-43 reference point at one centimeter nominal distance from the source was measured using these factors and compared to the specification of the calibration certificate. The Monte Carlo calculations were performed using the restricted cema formalism to gain further insight into the chamber response. Calculations were performed for the sensitive volume of the chambers, determined by the methods currently used in investigations of dosimetry in magnetic fields. *Main results*. Measured dose rates and values from the calibration certificate agreed within the combined uncertainty ($k = 2$) for all chambers except for one case in which the full air cavity was simulated. The chambers showed a distinct directional dependence. With the restricted cema formalism calculations it was possible to examine volume averaging and energy dependence of the perturbation factors contributing to the beam quality correction factor also differential in energy. *Significance*. This work determined beam quality correction factors to measure the absorbed dose rate from a brachytherapy source in terms of absorbed dose to water for a variety of ionization chambers. For the accurate dosimetry of brachytherapy sources with ionization chambers it is advisable to use correction factors based on the sensitive volume of the chambers and to take account for the directional dependence of chamber response.

1. Introduction

Dose calculation for brachytherapy sources using Ir-192, I-125 and PD-103 is usually performed using the recommendations by the report of Task Group No. 43 (TG-43) of the AAPM, first published in 1995 (Nath *et al* 1995) and its first update in 2004 (Rivard *et al* 2004). To include the effects of heterogeneities, model-based dose calculation algorithms (MBDCAs) have been developed (Carlsson Tedgren and Ahnesjö 2008, Zourari *et al* 2010) and are increasingly implemented in treatment planning systems. The MBDCAs rely entirely on theoretical model calculations, and the only presently available methods of verification are Monte Carlo (MC) calculations (Beaulieu *et al* 2012, 2023). Already for the TG-43 data additional

experimental verification is recommended by AAPM (Li *et al* 2006), and is now much more needed for the MBDCAs. The feasibility of dose measurement close to a brachytherapy source has been demonstrated as early as 1960 (Kondo and Randolph 1960), however, current dosimetry protocols (Almond *et al* 1999, IAEA 2024) are written for external beam therapy and provide practically no data for the determination of absorbed dose rate to water from the reading of an experimental detector in a brachytherapy setup. For this purpose this work investigated the dose conversion coefficients and correction factors calculated with Monte Carlo simulations for calibrated ionization chambers intended for use in measurements of absorbed dose to water from an Ir-192 source in an extended water surrounding. Measurements at short distances are challenging due to the steep dose gradients and radiation divergence. Additional to the requirement of precise positioning, the detector response can show a different behavior under these conditions than during calibration.

As verification of the MC calculations in this work, measured dose rates using the MC determined corrections were compared to values calculated by the TG-43 formalism at the reference point of the formalism, defined in water at 1 cm distance from the source center on its radial midplane for both low and high-energy sources (Pérez-Calatayud *et al* 2012). Recent developments of current dosimetry protocols based on Monte Carlo calculated beam quality correction factors (McEwen *et al* 2014, Andreo *et al* 2020) have led to decreased uncertainties of chamber response corrections. In these calculations the approximation of absorbed dose by restricted cema (Hartmann *et al* 2021) can provide further insight into signal generation in detectors. Additionally, the role of the sensitive volume of the chambers was investigated. This was first proposed generally in 2009 (Ross 2009) and has now gained further importance in the development of dosimetry in magnetic fields (Spindeldreier *et al* 2017, Pojtinger *et al* 2019, Delfs *et al* 2021).

2. Theoretical background

2.1. Dosimetry formalism

Following TRS-398 (IAEA 2024), the absorbed dose to water D_w in a photon beam of quality Q differing from that used in its calibration Q_0 is experimentally determined by

$$D_{w,Q} = M_Q \cdot N_{D,w,Q_0} \cdot k_{Q,Q_0} \tag{1}$$

where the beam quality correction factor k_{Q,Q_0} corrects the calibration coefficient N_{D,w,Q_0} for the difference between the reference beam quality Q_0 and the actual quality Q and the dosimeter reading M_Q has been corrected to the reference values of influence quantities other than the beam quality. This work investigated beam quality correction factors of calibrated thimble ionization chambers for Ir-192 HDR brachytherapy sources. The ionization chambers were calibrated in terms of absorbed dose to water from Co-60 (i.e. Q_0) so that the beam quality correction factor is denoted k_Q (IAEA 2024).

In the TG-43 formalism, the origin of the coordinate system lies in the center of the active source components, a polar angle θ is defined between the long axis of the source and the vector pointing from the source center to the chamber reference point and r denotes the distance between these two points. The absorbed dose rate to water at the TG-43 reference point, i.e. $(r_0 = 1\ \text{cm}, \theta_0 = 90°)$, is then determined according to TRS-398 by

$$\dot{D}_{w,Q}(r_0, \theta_0) = M_Q \cdot N_{D,w} \cdot k_Q \cdot \prod k_i \tag{2}$$

where M_Q is the detector reading, $N_{D,w}$ is the calibration coefficient for Co-60 calibration conditions and $\prod k_i$ corrects for influence quantities, i.e. any departure of the reference condition during measurement except beam quality. Following TG-43, the dose rate of a given source is calculated at the TG-43 reference point by

$$\dot{D}_{w,Q}(r_0, \theta_0) = S_k \cdot \Lambda \tag{3}$$

with the product of air kerma strength S_k traceable to a primary laboratory (Sander 2014) and the dose rate constant Λ (Nath *et al* 1995) which is confirmed to be valid for reference dosimetry within the measurement uncertainties (IAEA 2023). According to TRS-398, the beam quality correction factor is calculated by the ratio of the dose conversion factors f (Andreo *et al* 2020)

$$k_Q = \frac{f_Q}{f_{Q_0}} = \frac{f_{\text{Ir-192}}}{f_{\text{Co-60}}} = \frac{\left(D_w/\bar{D}_{\text{det}}\right)_{\text{Ir-192}}}{\left(D_w/\bar{D}_{\text{det}}\right)_{\text{Co-60}}} \tag{4}$$

where $\bar{D}_{\text{det}}$ is the mean absorbed dose to the detector. With the development of MC techniques, it was proposed to determine f_Q/f_{Q_0} directly using MC calculations (Sempau *et al* 2004), as they specifically

simulate the detector-specific process of energy absorption. This approach is meanwhile common practice in dosimetry protocols.

2.2. Restricted cema approximation to calculate the dose conversion factor

In the restricted cema formalism (Hartmann *et al* 2021), absorbed dose is approximated by the *restricted converted energy per mass* (cema) as defined in ICRU Report 90 (ICRU 2016) which describes the energy loss of secondary charged particles[7]. Restricted cema is calculated as

$$C_\Delta = \int_\Delta^\infty \Phi_E \, {L_\Delta}/{\rho} \, \mathrm{d}E + TE_\Delta \quad (=: \Phi \times S_{\mathrm{med}}) \tag{5}$$

where Φ_E is the distribution of the total electron fluence with respect to the energy E at a point in a medium, ${L_\Delta}/{\rho}$ is the corresponding restricted mass linear energy transfer and TE_Δ denotes the track end term representing the sum of the kinetic energy of all charged particles in the scoring volume with energies below a certain threshold energy Δ. On the right side of equation (5) an abbreviation is introduced for readability (Hartmann and Zink 2018). The approximation of absorbed dose is valid for high energy photons where, within the scoring volume, secondary charged particle equilibrium up to Δ exists and contributions to absorbed dose which are not due to the energy loss of charged particles are negligible. In particular, these contributions are binding energies of the released particles, absorbed dose due to locally absorbed photons with energies lower than the photon cutoff energy used for photon tracking in the MC simulation and energy losses due to elastic and inelastic nuclear photon interactions (Thomas 2012, Hartmann *et al* 2021).

The Monte Carlo simulation software (i.e. EGSnrc) used to compute the restricted cema values uses restricted mass stopping power ${S_{\Delta,\mathrm{tot}}}/{\rho}$ instead of restricted mass linear energy transfer (Kawrakow *et al* 2001-2015 version 2021). The differences are negligible with $\Delta = 10$ keV since they are caused by binding energies which are much smaller than unrestricted stopping powers for low-Z materials (Kellerer *et al* 1992).

The absorbed dose consists of the restricted cema and a remaining energy fraction. The ratio of both parts depends on the photon energy and the absorbing medium. The remaining energy fraction is usually very small (i.e. $< 0.1\%$) for low-Z materials and photon energies above 10 keV (Hartmann *et al* 2020). Due to the close agreement of absorbed dose and restricted cema for the photon energies and absorbing media in this study the restricted cema approximation (Hartmann *et al* 2021) is used to calculate the dose conversion factor

$$f \overset{!}{=} \frac{C_{\Delta,\mathrm{w}}}{\bar{C}_{\Delta,\mathrm{det}}} \tag{6}$$

with the restricted cema at the point of interest in water, $C_{\Delta,\mathrm{w}}$, and the corresponding mean restricted cema of the sensitive volume in the detector $\bar{C}_{\Delta,\mathrm{det}}$, when the chamber's reference point is placed at the same position. This formulation yields two advantages: Firstly, the restricted cema formalism is independent of a secondary charged particle equilibrium for $E > \Delta$ and secondly, it allows the investigation of energy resolved contributions of the involved charged particles. A further factorization on the far right side of the following equation with the restricted cema of a voxel filled with the detection medium $\Phi_\mathrm{P} \times S_{\mathrm{med}}$ and the mean value of the detector's bare cavity $\bar{\Phi}_{\mathrm{cav}} \times S_{\mathrm{med}}$ leads to

$$\frac{C_{\Delta,\mathrm{w}}}{\bar{C}_{\Delta,\mathrm{det}}} = \frac{\Phi_\mathrm{P} \times S_\mathrm{w}}{\bar{\Phi}_{\mathrm{det}} \times S_{\mathrm{med}}} = \underbrace{\frac{\Phi_\mathrm{P} \times S_\mathrm{w}}{\Phi_\mathrm{P} \times S_{\mathrm{med}}}}_{=:\, s_{\mathrm{w,med}}} \cdot \underbrace{\frac{\Phi_\mathrm{P} \times S_{\mathrm{med}}}{\bar{\Phi}_{\mathrm{cav}} \times S_{\mathrm{med}}}}_{=:\, p_{\mathrm{int}}} \cdot \underbrace{\frac{\bar{\Phi}_{\mathrm{cav}} \times S_{\mathrm{med}}}{\bar{\Phi}_{\mathrm{det}} \times S_{\mathrm{med}}}}_{=:\, p_{\mathrm{ext}}} , \tag{7}$$

where the indices *P* stand for a point-like voxel, *cav* for a bare cavity filled with detection medium and *det* for the fully modelled ionization chamber. In equation (7) one can identify the first factor $s_{\mathrm{w,med}}$ as the stopping-power ratio based on Spencer–Attix theory and the second factor p_{int} as a measure of the detector volume averaging. The third factor p_{ext} summarizes all perturbations of energy deposition due to components of the real detector such as chamber stem, guard ring, chamber wall and central electrode. This factorization is not necessary for MC calculations of the beam quality correction using full geometry simulations of the detector (Sempau *et al* 2004), however it provides insight into the impact of the components influencing the secondary electron fluence. The decomposition shows that the perturbation factors are caused by the perturbation of the secondary particle fluence by the different parts of the detector.

[7] By definition restricted cema refers to the fluence of electrons and positrons, however in the energy range considered in this work practically no positrons are present.

Table 1. Ionization chambers examined in this study including geometrical dimensions, construction materials surrounding the sensitive volume and technical drawings. The reference point specifies the distance to the tip on the central axis. Identical colors indicate identical materials. The dead volumes are outlined in red (discussed later in section 3.2) have practically the same shape in all chambers and differ in size mainly depending on the radius of guard ring and cavity. The element C denotes graphite (density ≈ 1.7 g cm^3) whereas C552 denotes an air-equivalent plastic (density 1.76 g cm). C* in the PTW 31010 chamber wall denotes a low density graphite of 0.82 g cm.

Model	PTW 31010	PTW 31021	PTW 31022	Exradin A26	PTW 31023
Cavity length (mm)	6.5	4.8	2.9	2.85	5
Cavity radius (mm)	2.75	2.4	1.45	1.65	1
Reference point (mm)	4.5	3.45	2.4	1.98	3.4
Nominal volume (cm^3)	0.125	0.070	0.016	0.015	0.015
Sensitive volume (cm^3)	0.111	0.053	0.011	0.016	0.013
Polarizing voltage (V)	400	400	300	300	300
Central electrode	Al	Al	Al	C552	Al
Wall	PMMA, C*	PMMA, C	PMMA, C	C552	PMMA, C
Guard ring	C	Al	Al	C552	Al
	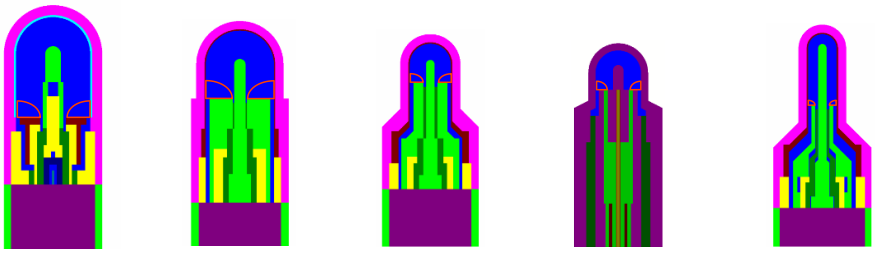				

3. Materials and methods

3.1. Ionization chambers used in this study

Five ionization chambers from two manufacturers, PTW (Freiburg, Germany) and Standard Imaging (Branding Exradin; Middleton, Wisconsin, USA), were investigated for brachytherapy dosimetry purposes. Table 1 specifies some of their technical characteristics such as geometrical dimensions and construction materials. All chambers had a cylindrically symmetric design. The selection included a wide variety of designs so that the effect of different chamber design could be investigated and possibly predictions for similar ionization chambers can be made. In particular, the nominal sensitive volumes range from 0.015 cm^3 to 0.125 cm^3 and include different shapes. Additionally, some detector pairs differ mainly in one criterion such as size of the sensitive volume (e.g. PTW 31021 vs PTW 31022) or construction materials (e.g. PTW 31022 vs Exradin A26). Direct comparison of these detector pairs provides the possibility to quantify the effects of specific detector components.

3.2. Sensitive volumes of the chambers

Dead volumes are observed in the air cavity of ionization chambers in the vicinity of the guard electrode (Butler *et al* 2015, Delfs *et al* 2021) influencing the chamber response (Miller *et al* 2016). To estimate the dead volume, the electric field in the air cavity can be derived by finite element method (FEM) calculations (Ross 2009, Pojtinger *et al* 2019, Delfs *et al* 2021). The goal is to define a region of air cavity in which the electric field lines lead from the inner chamber wall to the guard ring instead of the central collecting electrode so that radiation induced charge carriers in this region do not contribute to the signal current. A potential between the guard and the collecting electrode can occur during the measurement which further perturbs the electric field (Miller *et al* 2016). The software Quickfield (Tera Analysis Ltd, Svendborg, Denmark) was used for all FEM calculations in this study. The results were found to be in good agreement with the literature regarding the chambers PTW 31010 ((Cervantes *et al* 2020), software COMSOL Multiphysics from COMSOL AB, Stockholm, Sweden) and PTW 31021 as well as PTW 31022 ((Delfs *et al* 2021), software Quickfield and additional verification by proton point-beam scans). Details of the sensitive volume of the Exradin A26 chamber were already given in the manufacturer's blueprint (software Electrostatics Toolkit from Field Precision LLC, Albuquerque, USA). All previously mentioned ionization chambers have been investigated in one study using COMSOL (Margaroni *et al* 2022) which, however, yields

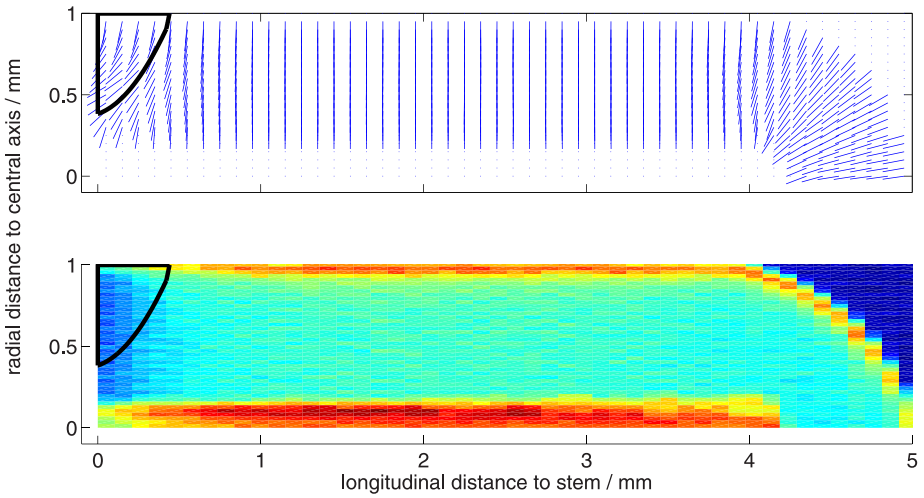

Figure 1. Top: Electric field lines as produced by the chamber voltage in the PTW chamber 31023 derived from finite element method (FEM) calculation by Quickfield. Bottom: Raw data of a point-beam scan with synchrotron radiation (Butler *et al* 2015). The dead volume from the FEM calculations combines all field lines that lead from the inner chamber wall to the guard ring and is shown as the black bordered area in both diagrams.

slightly larger dead volumes than the other studies. All dead volumes of thimble ionization chambers have practically the same shape and differ in size mainly depending on the chamber guard ring radii.

No comparable FEM derived data are available so far for PTW chamber 31023. But its comparable predecessor, PTW chamber 31014, was investigated in a point-beam scanning technique with synchrotron radiation (Butler *et al* 2015). The electric field in the ionization chamber PTW 31023 defining the sensitive volume as well as the raw data of the point-beam scan are shown in figure 1. The longitudinal propagation of both dead volumes matched well.

3.3. Monte Carlo calculations

An in-house enhanced MC application of `egs_chamber` from the EGSnrc framework (available from the corresponding author on request) was used to calculate the desired quantities including absorbed dose, restricted cema and charged particle fluence differential in energy in one simulation (Failing *et al* 2022). k_Q was calculated according to equations (4) and (6) and p_{int} as well as p_{ext} following equation (7). Table 2 specifies the used MC parameters. The Co-60 spectrum was taken from a fully modelled Co-60 treatment unit head simulation including air scatter (Mora *et al* 1999). For the requirement of this study it is not necessary to use the full phase space of a specific Co-60 unit (Wulff *et al* 2008, 2010). For calibration conditions at 1 m distance in air, the detectors were placed at 5 cm depth in a $30 \times 30 \times 30$ cm^3 cubic water phantom. The Flexisource was modelled as homogeneous line source in full geometric detail according to the construction described by the AAPM/ESTRO High Energy Brachytherapy Dosimetry Working Group (Pérez-Calatayud *et al* 2012) and the Ir-192 spectrum given in the Nudat 2 database (Baglin 2012). For the immersed source setups, the Flexisource was either surrounded by a $80 \times 80 \times 80$ cm^3 water cube ensuring full scatter contributions (Pérez-Calatayud *et al* 2004) or a fully modelled Beamscan water phantom (PTW-Freiburg, Freiburg, Germany). Preliminary MC calculations showed no perturbations due to the Beamscan phantom compared to TG-43 conditions at the TG-43 reference point which is also confirmed for a comparable water phantom (Rossi *et al* 2020). Small water volumes to calculate D_w and Φ_P consisted either for external beams of a disc with 1 cm radius and 0.025 cm thickness (Wulff *et al* 2008) or for immersed source setups of a cube with an edge length of 0.1 mm (Taylor and Rogers 2008). Where applicable, complete chambers were simulated with the dose being scored either in the detector cavity including the dead volume (full volume) or not (sensitive volume).

3.4. Chamber positioning

Figure 2 shows the detector in a coordinate system as defined in TG-43. The setups in water for calculations and measurements in this work were called *TG-43 conditions* as they consisted of brachytherapy sources defined by TG-43, composed of the active core, cladding and a short attached cable surrounded by a sufficiently large water envelope to ensure full scatter conditions.

Figure 3 shows the directions of MC calculated profiles of a detector passing by the radiation source, in a water surrounding used to locate the peak response. In the following the point of peak response on the

Table 2. Summary of the EGSnrc simulation parameters as used in this study. According to good practice the recommendations of AAPM report TG-268 (Sechopoulos *et al* 2017) were followed.

Item	Description	References
Code, version	EGSnrc (v2021), modified `egs_chamber` code to generate outputs of absorbed dose, restricted cema, track end terms and charged particle fluence differential in energy; `egs++` geometry package	(Kawrakow *et al* 2001-2015 version 2021, 2019, Walters *et al* 2021, Failing *et al* 2022)
Validation	Region-by-region Fano cavity tests appendix A	(Kawrakow 2000a)
Source description	Calibration conditions: tabulated Co-60 spectrum, collimated point source to 10×10 cm^2 at 100 cm distance, 5 cm depth in water. Immersed source setup: Tabulated isotropic Ir-192 spectrum in the active core of the fully modelled Flexisource	(Mora *et al* 1999, Baglin 2012, Pérez-Calatayud *et al* 2012)
Cross-sections	xcom photon cross sections. NIST ESTAR density effect corrections and mean excitation energies with ICRU 90 values where applicable. NIST bremsstrahlung cross sections	(Seltzer 1993, ICRU 2016)
Transport parameters	ECUT = AE = 521 keV PCUT = AP = 1 keV Photon cross section = xcom Bound Compton Scattering = On/norej Rayleigh scattering = On Atomic Relaxations = On/eadl Brems cross sections = NIST Boundary crossing algorithm = exact Electron step algorithm = EGSnrc/PRESTA-II ESTEPE = 0.25 All other parameters set to default	(Kawrakow *et al* 2001-2015 version 2021)
VRT	Photon cross section enhancement (XCSE), intermediate phase-space storage (IPSS)	(Kawrakow *et al* 2001-2015 version 2021, Wulff *et al* 2008)
Scored quantities	Absorbed dose, restricted cema, track end terms and charged particle fluence differential in energy with 5 keV bin width in small water volumes (see references) or fully modelled ionization chambers	(Taylor and Rogers 2008, Wulff *et al* 2008)
statistical uncertainty	$\leqslant 0.1\%$ ($k = 1$) regarding the scored absorbed dose in each simulation	
Statistical methods	History-by-history estimator	(Walters *et al* 2002)
Post-processing	Denoising of fluence quotient plots differential in energy by averaging over 5 bins for Co-60 spectra and over 3 bins for Ir-192 spectra; no filtering	

central axis of the detector is called the effective point of measurement (EPOM). This EPOM was needed in this work only for chamber positioning in water phantom measurements to locate the correct source position by detecting the chamber's peak signal in transversal source scans (Rossi *et al* 2020). In all calculations and measurements the chambers were positioned at the reference points stated by the manufacturers and given in table 1. Positioning at the EPOM as often performed in relative measurement of dose distributions in external beam therapy is impractical in the steep dose gradients close to the source where volume averaging in the detector cavity causes the EPOM to shift to different positions in the chamber at different distances from the source. This is seen in the differences of beam quality correction factors for low energy x-rays (Watson *et al* 2017) and is shown in more detail in appendix B.

3.5. Water phantom measurements

To verify the MC derived results of k_Q, measurements of the absorbed dose rate using equation (2) were performed with all ionization chambers in a Beamscan water phantom and compared to $S_k \cdot \Lambda$. The phantom

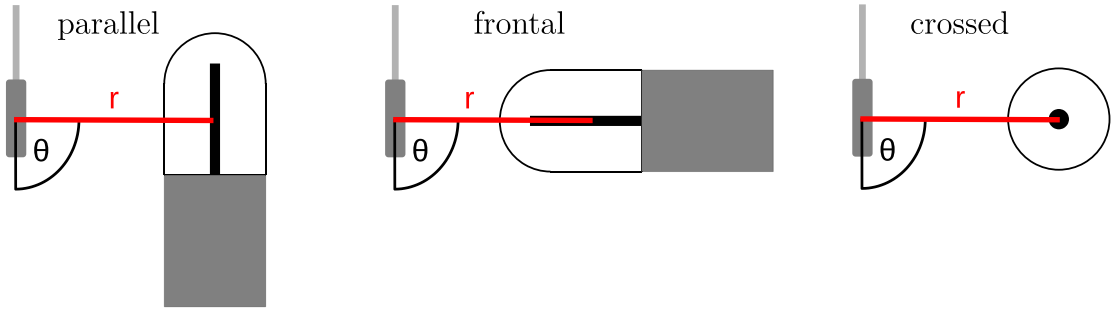

Figure 2. Coordinate system and chamber positioning for brachytherapy dosimetry as used in this study. The origin is located at the source center and the vector pointing at the reference point of the chamber is defined by the polar angle $\theta = 90°$ as well as the distance r between these two points. Three different chamber orientations with respect to the source are shown here and labeled parallel, frontal and crossed. The crossed setup on the right shows the radial cross section of the cavity volume at the reference point of the ionization chamber positioned on the radial axis of the source.

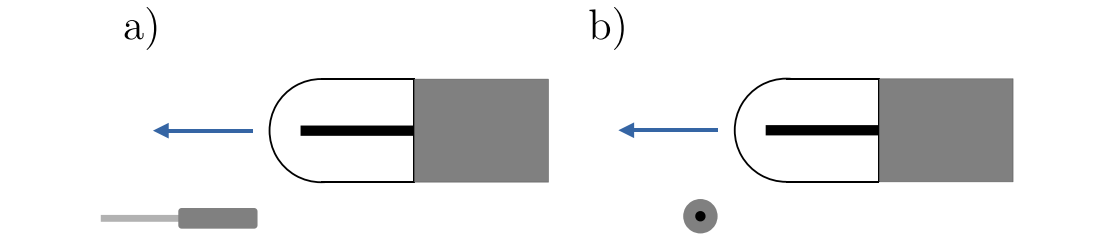

Figure 3. Setup to determine the effective point of measurement (EPOM) of the ionization chambers. In a MC simulated profile along the arrows at 1 cm distance, the EPOM is assumed to coincide with the position on the central electrode (central bold black lines). (a) profile parallel to the longitudinal, (b) profile across the radial source axis. The calculations were performed with source modelling according to the TG-43 assumptions, i.e. the brachytherapy source consists of the active core, cladding and a short cable within full scatter conditions in water (not shown).

translates the detector in the three spatial directions with a precision of 0.1 mm along two vertically arranged motor-driven moving arms. The source was positioned using a Flexitron afterloader with an Ir-192 HDR Flexisource guided by 4F plastic needles (all Nucletron/Elekta, Veenendaal, The Netherlands). The needle containing the source was fixed and secured in the phantom by an in-house manufactured carbon guiding tube. The source has some mechanical play in the 4F needle but this had no measurable effect on the absorbed dose because the origin was adjusted to the position of the source center by profile measurements as described in section 3.4 ahead of every dose measurement. The source was located in the center of a large water phantom and small spatial tolerances of the 4F needle and carbon guiding tube to the source were negligible as observed in dedicated MC simulations. The positioning of chamber and source were performed simultaneously assuming that simulation and measurement of the profiles lead to the same result. After positioning, the repeatability of the source position was checked before and after an additional source run of the afterloader. After a new source run the deviations perpendicular to the source axis lied within the control accuracy of the phantom of 0.1 mm. The average deviation of the source outdrive (along the source axis) was 0.3 mm with a maximum deviation of 0.6 mm. During a single source run the spatial deviations were negligible. To account for small variations of the source position, a check run of the chamber was performed immediately before an actual measurement.

Five repeated measurements were performed in each of the three chamber orientations shown in figure 2 to determine the mean chamber reading $\bar{M}_Q$. Since the carriage cannot be rotated around the source by the motorized drive, only one alignment was possible in the frontal orientation, two alignments in the crossed orientation, and theoretically any number of alignments in the parallel orientation to average a detector reading in dosimetric equivalent setups. Four equally distributed alignments in the parallel orientation were chosen. Standard deviations of the averaged aligned measurements were calculated to determine the relative uncertainty of $\bar{M}_Q$ in each orientation.

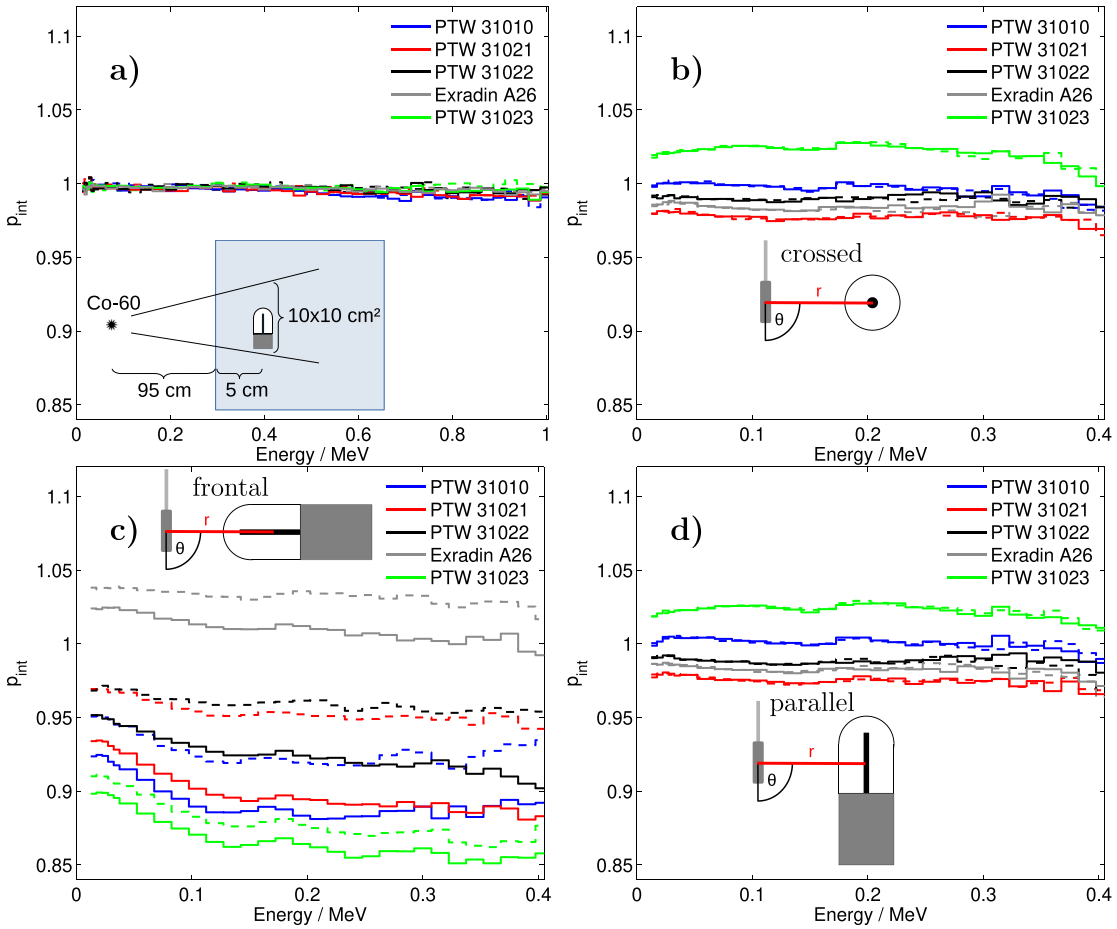

Figure 4. MC calculated internal perturbation factor $p_{\mathrm{int}} = {}^{\Phi_{\mathrm{P}} \times S_{\mathrm{air}}}/_{\bar{\Phi}_{\mathrm{cav}} \times S_{\mathrm{air}}}$, differential in energy, for various ionization chambers at (a) calibration conditions according to dosimetry protocol DIN 6800-2 (DIN 6800-2:2020-08 2020) and at the TG-43 reference point of an Ir-192 HDR Flexisource with different chamber orientations as shown in figure 2. In particular, the chambers are oriented (b) crossed, (c) frontal and (d) parallel to the source long axis. The solid lines correspond to the sensitive air volume of the chambers whereas the dashed lines correspond to the full cavity volume.

4. Results

4.1. Perturbation factors

Figure 4 shows the MC based internal perturbation factor $p_{\mathrm{int}} = {}^{\Phi_{\mathrm{P}} \times S_{\mathrm{air}}}/_{\bar{\Phi}_{\mathrm{cav}} \times S_{\mathrm{air}}}$, differential in energy, for the investigated ionization chambers calculated for the sensitive cavity volume in solid lines and for the full cavity volume in dashed lines. Four different scenarios (a) under calibration conditions according to dosimetry protocol DIN 6800-2 (DIN 6800-2:2020-08 2020) and at the TG-43 reference point of an Ir-192 HDR Flexisource in the Beamscan water phantom in three chamber orientations (b) crossed, (c) frontal and (d) parallel to the source long axis were investigated. In all cases the chambers were positioned at their manufacturer-stated reference points. Due to the small dose gradient of $-0.6\ {}^{\%}/_{\mathrm{mm}}$ of the Co-60 beam under calibration conditions, $p_{\mathrm{int}} \approx 1$ for all detectors. In the immersed source setups, the internal perturbation factor was affected by both cavity size and shape as well as by the orientation. The largest deviations of p_{int} from unity were found in frontal orientation (figure 4(c)). In (b) crossed or (d) parallel orientation the internal perturbation factors p_{int} were equal or smaller than 1, except for the PTW 31023 detector where $p_{\mathrm{int}} > 1.03$. The parallel and crossed setups showed nearly no dependency either on energy or cavity modelling. In frontal orientation, p_{int} deviated more from unity for all detectors. Here, for all detectors, the full air cavity led to a larger value of p_{int}. Additionally, there was an energy dependency in the first energy bins up to about 150 keV where p_{int} values decreased for all detectors. In frontal orientation, p_{int} was generally larger for calculations with full than for sensitive chamber modelling. The maximum difference between two curves occurred for the PTW 31021. In frontal orientation, $p_{\mathrm{int}} > 1$ for the Exradin A26.

Figure 5 shows the MC calculated external perturbation factor $p_{\mathrm{ext}} = {}^{\bar{\Phi}_{\mathrm{cav}} \times S_{\mathrm{air}}}/_{\bar{\Phi}_{\mathrm{det}} \times S_{\mathrm{air}}}$ differential in energy. Beam setups and presentation are identical to those in figure 4. In all cases $p_{\mathrm{ext}} < 1$ which means that the doses in the fully modelled chambers were always larger than those in the corresponding bare air cavities.

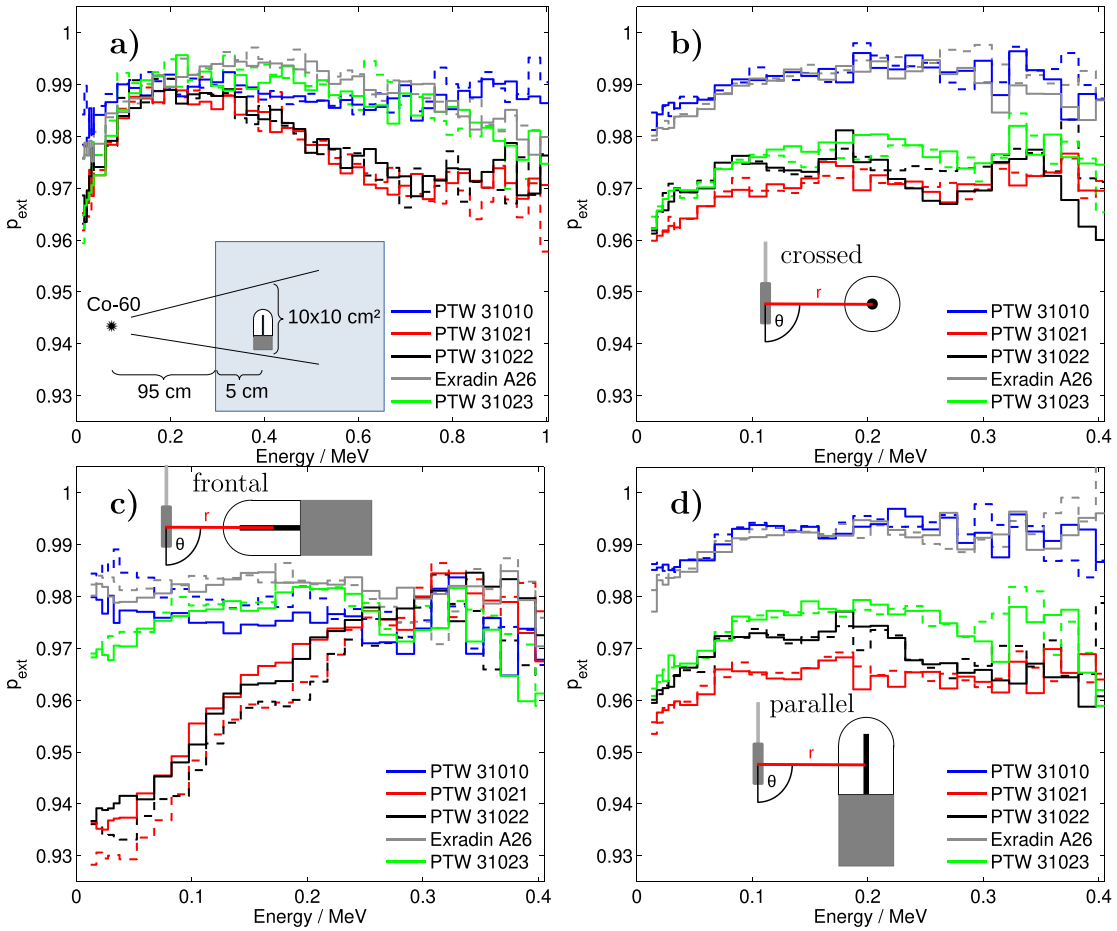

Figure 5. MC calculated external perturbation factor $p_{ext} = \bar{\Phi}_{cav} \times S_{air} / \bar{\Phi}_{det} \times S_{air}$, differential in energy, for various ionization chambers at (a) calibration conditions according to dosimetry protocol DIN 6800-2 (DIN 6800-2:2020-08 2020) and at the TG-43 reference point of an Ir-192 HDR Flexisource with different chamber orientations as shown in figure 2. In particular, the chambers are oriented (b) crossed, (c) frontal and (d) parallel to the source long axis. The solid lines correspond to the sensitive air volume of the chambers whereas the dashed lines correspond to the full air cavity volume.

Under (a) calibration conditions, no significant differences between the external perturbation factors for sensitive or full air cavity volumes were observed. Energy dependence of p_{ext} differed for the different chambers and is discussed in section 5. In (b) crossed and (d) parallel chamber orientation, p_{ext} showed a very similar behavior. External perturbation factors were nearly equal for calculations of the sensitive or full air volume. In both orientations the chambers could be divided into two groups, namely PTW 31010 and Exradin A26 showed similar curves, as did PTW 31021, 31022 and 31023. The first group of detectors showed perturbation factors up to 2%, approximating 1% above 150 keV. The second group ran parallel to the first at an offset of $\approx 2\% - 3\%$.

In frontal orientation (figure 5(c)), the detectors fell into three groups. The first, consisting of PTW 31010 and Exradin A26, yielded more or less constant perturbations of approximately 2%. In the second group, below 300 keV, the perturbation factors for the PTW chambers 31021 and 31022 increased nearly linearly with energy by up to 7%. Additionally the perturbation factor for the full air volume was about 1% larger than for the sensitive volume. The PTW chamber 31023 showed a unique behavior with p_{ext} increasing by $\approx 1\%$ below 200 keV with no difference between p_{ext} for the simulation of the full air cavity or the sensitive volume.

To summarize the impact of the perturbation factors differential in energy, table 3 shows the integral values of p_{int} and p_{ext} according to figures 4 and 5 using equations (5) and (7). The integral values with Ir-192 irradiation were mainly determined by the contributions from the first energy bins of the perturbation factors differential in energy. This could be seen clearly in frontal orientation for PTW chambers 31021 and 31022 in figure 5(c). The cavity of PTW chamber 31023 yielded the largest deviations of p_{int} from unity independent of considering the dead volume or orientation at the TG-43 reference point. In frontal

Table 3. MC calculated perturbation factors p_{int} and p_{ext} for a Flexitron Ir-192 source using equation (7). As shown in figures 4 and 5, simulations under calibration conditions as well as at the TG-43 reference point with three different chamber orientations crossed, parallel and frontal to the source long axis were investigated. The first value of a chamber refers to the full air cavity volume whereas the second value in italics considers only the sensitive volume. The relative standard deviation (Type A) of all results ranged between 0.1% and 0.15%.

	PTW 31010		PTW 31021		PTW 31022		Exradin A26		PTW 31023	
					p_{int}					
calibration	0.997	*0.995*	0.997	*0.995*	0.997	*0.996*	0.997	*0.996*	0.996	*0.997*
crossed	1.007	*1.004*	0.982	*0.984*	0.994	*0.995*	0.989	*0.990*	1.028	*1.027*
parallel	1.007	*1.004*	0.982	*0.984*	0.994	*0.995*	0.989	*0.989*	1.028	*1.028*
frontal	0.942	*0.910*	0.966	*0.920*	0.969	*0.943*	1.041	*1.023*	0.899	*0.887*
					p_{ext}					
calibration	0.987	*0.986*	0.978	*0.978*	0.979	*0.979*	0.987	*0.987*	0.985	*0.983*
crossed	0.989	*0.988*	0.962	*0.967*	0.968	*0.970*	0.987	*0.986*	0.970	*0.971*
parallel	0.989	*0.989*	0.962	*0.967*	0.967	*0.971*	0.989	*0.987*	0.970	*0.971*
frontal	0.982	*0.977*	0.941	*0.948*	0.942	*0.948*	0.982	*0.981*	0.975	*0.973*

Table 4. Percentage type B uncertainties in the MC calculations, $\left|u(k_Q)/k_Q\right|$, based on the variation of single uncertainties of cross sections and mean excitation energy values. All uncertainties are given for the PTW chamber 31021 except for the value for C552 which belongs to the Exradin A26 because this material is only assembled here.

		uncertainty (%)	source	$\left\|u(k_Q)/k_Q\right\|$ (%)
Cross section	Photo effect	2	(Wulff *et al* 2010)	0.01
	Compton effect	1		0.12
Mean excitation energy	H_2O	2.6	(ICRU 2016)	0.16
	C	2.2		0.17
	air	1.4		0.33
	Al	0.8		0.01
	PMMA	5	(Muir and Rogers 2010)	0.05
	C552	5		0.33

orientation, these were also the largest perturbations in this study exceeding 10%. PTW chambers 31021 and 31022 yielded the largest external perturbations of nearly 6%. The maximum differences of perturbations between full and sensitive volume occurred for the PTW chamber 31021.

4.2. Beam quality correction factor

To allow intercomparison of the results for the MC calculated beam quality correction factor k_Q, first the type B uncertainties are quantified. EGSnrc has been shown to be accurate to within 0.1% with respect to its own cross-sections (Kawrakow 2000b). Table 4 shows the percentage type B uncertainties occurring in the MC calculations with EGSnrc for k_Q at the TG-43 reference point when cross sections and mean excitation energies are varied. The methodology is based upon previous works with EGSnrc (Muir and Rogers 2010, Wulff *et al* 2010). All uncertainties in table 4 are given for the PTW 31021 chamber except for C552 which was only used in the Exradin A26. In preliminary MC simulations, it was found that the influences of chamber orientation, size and whether the dead volume was taken into account were negligible for the calculation of type B uncertainties. Therefore only this selection is shown here.

Table 5 shows the beam quality correction factors k_Q for dose measurements of an Ir-192 Flexisource at the TG-43 reference point in water. Results are shown for full and sensitive air volumes. The difference between the beam quality correction factors calculated for absorbed dose or restricted cema ratios was always below 0.02%. As the perturbation factors showed, the values of k_Q for the crossed and parallel orientation did not differ beyond the statistical uncertainty. The maximum differences of k_Q between full and sensitive volume occurred for the PTW chamber 31021 with 0.9% in crossed and parallel and 4% in frontal orientation. The PTW chamber 31023 yielded the largest deviations of k_Q from unity independent of cavity type or orientation and furthermore the largest directional dependence.

Table 5. Beam quality correction factors for radiation from an Ir-192 Flexisource using equations (4) and (6) at the TG-43 reference point. Three different chamber orientations crossed, parallel and frontal to the source long axis as shown in figure 2 are tabulated. The first value of a fully modelled chamber refers to the full air cavity volume whereas the second value in italics considers only the sensitive volume. The relative standard deviation (Type A) of all results ranges between 0.2% and 0.3%. With the results given in table 4 the combined percentage standard uncertainty ranges between 0.5% and 0.6%. Individual values are given in table 7.

	k_Q									
	PTW 31010		PTW 31021		PTW 31022		Exradin A26		PTW 31023	
crossed	1.011	*1.008*	0.965	*0.974*	0.983	*0.987*	0.989	*0.989*	1.014	*1.016*
parallel	1.009	*1.009*	0.965	*0.974*	0.982	*0.988*	0.989	*0.990*	1.015	*1.015*
frontal	0.937	*0.903*	0.930	*0.894*	0.935	*0.915*	1.036	*1.018*	0.891	*0.878*

Table 6. Percentage uncertainty $|u_{\text{det.geom.}}|$ on the calculation of k_Q due to geometric variations of the PTW chamber 31021 in the three orientations to the Ir-192 HDR Flexisource. The combined uncertainties due to detector variations are given for all chambers in table 7.

Geometry	outer wall	inner wall	central elec.	guard ring	wall air gap	dead vol.
Variation	0.1 mm	0.1 mm	0.05 mm	0.1 mm	0.1 mm	10%
$\lvert u_{\text{det.geom.}}\rvert_{\text{crossed}}$ (%)	0.05	0.04	0.04	0.16	0.04	0.32
$\lvert u_{\text{det.geom.}}\rvert_{\text{parallel}}$ (%)	0.06	0.04	0.00	0.13	0.07	0.29
$\lvert u_{\text{det.geom.}}\rvert_{\text{frontal}}$ (%)	0.04	0.29	0.12	0.84	0.11	0.57

4.3. Experimental verification

Table 6 shows the MC determined percentage uncertainties $|u_{\text{det.geom.}}|$ in the calculation of k_Q due to geometric variations (caused by manufacturing tolerances) of the PTW chamber 31021 for the three orientations towards the Ir-192 HDR Flexisource. Uncertainties were calculated by treating the variations as changes of the cavity volume. In all cases except for the outer wall the chamber parts protruded farther into the air cavity. The variations on the outer and inner chamber wall as well as the central electrode were adopted from Wulff *et al* (2010). The variation regarding the length of the guard ring was also chosen 0.1 mm to be consistent with the previous variations. These variations are larger than in a comparable work (Muir and Rogers 2010), so that they represent a conservative approach. To date, little information is available on detector geometric variations and their influence on k_Q. Air gaps of different size may occur between the inner graphite wall and outer PMMA wall of individual PTW chambers as observed in micro-CT images (Cervantes *et al* 2020). In this study, the enlarged wall air gap corresponds to a further hollowing out of the PMMA wall and is chosen 0.1 mm which again represents a conservative approach. An uncertainty in dead volumes of 10% was assumed because, for small deviations in electrode potentials, a percentage difference leads to equivalent perturbations of the collecting volumes (Miller *et al* 2016). Additionally, the uncertainty in the dead volumes also took the variation from other works into account as mentioned in section 3.2. To simulate the variations, the dead volumes were extended longitudinally into the chamber cavity. The combined uncertainties due to geometric variations of all chambers are shown in table 7. For all chambers, variations in frontal orientation led to the largest uncertainties for the calculation of k_Q because variations in inner wall, guard ring and dead volume had a direct impact on the center of the cavity in the direction of the steep dose gradient.

Table 7 shows the percentage standard uncertainties in the mean measured absorbed dose rate per unit $S_k \cdot \Lambda$ for all investigated chambers caused by different components of type A and type B uncertainties. The positional uncertainties for all detectors as well as the source were investigated by simulations at varying positions, yielding that a variation of the source-detector-distance of $\pm$ 0.1 mm altered all detector signals by approximately $\mp$ 2% at the TG-43 reference point. Only deviations in the order of statistical uncertainty of 0.1% were observable when shifting the components in other directions. Based on the guidelines of the Guide to the expression of Uncertainty in Measurements (BIPM *et al* 2008), the standard uncertainty induced on the absorbed dose rate to the chambers along each single axis was calculated assuming a rectangular probability distribution, i.e. dividing the dose variation corresponding to the positive and negative shift by a reducing factor of $\sqrt{3}$. As uncertainty in S_k, a value of 1.01% ($k = 2$) from a recent comparison by BIPM and PTB (Kessler *et al* 2024) was adopted here which is smaller than the value of 1.5% given in AAPM Task Group Report No. 138 (DeWerd *et al* 2011). For Λ, the value and uncertainty of 1.0% ($k = 1$) were adopted from the AAPM/ESTRO High Energy Brachytherapy Dosimetry Working Group (Pérez-Calatayud *et al* 2012). A total type B uncertainty of $S_k \cdot \Lambda = 1.12\%$ resulted from summing both contributions in quadrature.

Absorbed dose rates measured with all investigated chambers applying equation (2) were compared to $S_k \cdot \Lambda$ using the consensus dose rate constant for the Flexitron source $\Lambda = 1.112$ (Nath *et al* 1995, Rivard *et al*

Table 7. Percentage standard uncertainties of all components leading to the combined percentage standard uncertainty of the measured absorbed dose rate per air kerma strength S_k (Kessler *et al* 2024) and consensus dose rate constant Λ (Pérez-Calatayud *et al* 2012) by summing in quadrature the single components. Uncertainties in $N_{D,\mathrm{w,Co\text{-}60}}$ were adopted from the calibration certificates of the manufacturers.

Uncertainty	Type	PTW 31010	PTW 31021	PTW 31022	Exradin A26	PTW 31023
k_Q	total	0.47	0.48	0.55	0.59	0.53
Det. geom.$_{\mathrm{crossed}}$	B	0.30	0.37	0.37	0.39	0.22
Det. geom.$_{\mathrm{parallel}}$	B	0.29	0.34	0.39	0.36	0.22
Det. geom.$_{\mathrm{frontal}}$	B	0.89	1.07	1.24	1.22	0.65
Detector pos.	B	1.16	1.16	1.16	1.16	1.16
Source pos.	B	1.16	1.16	1.16	1.16	1.16
$\bar{M}_{Q_{\mathrm{crossed}}}$	A	0.01	0.07	0.11	0.06	0.11
$\bar{M}_{Q_{\mathrm{parallel}}}$	A	0.01	0.04	0.03	0.04	0.03
$\bar{M}_{Q_{\mathrm{frontal}}}$	A	0.13	0.37	0.35	0.19	0.36
$N_{D,\mathrm{w,Co\text{-}60}}$	A	1.10	0.55	0.55	1.05	0.55
k_{TP}	B	0.18	0.18	0.18	0.18	0.18
$S_k \cdot \Lambda$	B	1.12	1.12	1.12	1.12	1.12
$\dot{D}_{\mathrm{w},Q}(r_0,\theta_0)_{\mathrm{crossed}}/S_k\Lambda$	total	2.34	2.15	2.17	2.36	2.15
$\dot{D}_{\mathrm{w},Q}(r_0,\theta_0)_{\mathrm{parallel}}/S_k\Lambda$	total	2.34	2.15	2.16	2.36	2.14
$\dot{D}_{\mathrm{w},Q}(r_0,\theta_0)_{\mathrm{frontal}}/S_k\Lambda$	total	2.49	2.40	2.49	2.64	2.26

Table 8. Ratios of absorbed dose rate to the investigated ionization chambers using equation (2) and source air kerma strength which was further processed based on the TG-43 formalism using equation (3). The first value of a chamber refers to the full air cavity volume whereas the second value in italics only considers the sensitive volume.

	$\dot{D}_{\mathrm{w},Q}(r_0,\theta_0)/S_k\Lambda$									
	PTW 31010		PTW 31021		PTW 31022		Exradin A26		PTW 31023	
crossed	1.016	*1.015*	0.998	*1.005*	1.000	*1.005*	0.990	*0.991*	0.999	*0.999*
parallel	1.012	*1.011*	0.995	*1.003*	0.999	*1.003*	0.988	*0.990*	0.999	*0.998*
frontal	0.927	*0.972*	0.970	*0.992*	0.995	*1.007*	1.006	*1.012*	1.006	*1.015*

2004, Pérez-Calatayud *et al* 2012). S_k was taken from the manufacturer's calibration certificate, which was measured with a calibrated measurement setup, calibrated with a calibration source of the same source model, measured at PTB in accordance with the ICRU Report 90 recommendations. The specific source air kerma strengths were also verified using a calibrated well chamber traceable to PTB following the recommendations of AAPM code of practice TG-56 (Nath *et al* 1997). Corrections for air pressure and temperature in the chamber, k_{TP}, were performed as recommended by current dosimetry protocols (Almond *et al* 1999, DIN 6800-2:2020-08 2020, IAEA 2024).

Table 8 shows the ratios of measured and calculated dose rate for different chamber orientations and sensitive cavity volumes. The ratios for almost all chambers deviated from unity, the targeted value, by less than one standard deviation except for the full air volume of PTW chamber 31021 and both values for PTW chamber 31010, always in frontal orientation. The ratio of the PTW 31010 without consideration of the dead volume differed from unity even beyond the expanded uncertainty. The remaining deviations were in good agreement with a previous investigation using calibrated diode detectors (Rossi *et al* 2023).

5. Discussion

5.1. Perturbation factors

By the factorization in equation (7) the perturbation factors are defined as ratios of the energy deposited in the detector medium from secondary electrons with fluence distributions altered by changes in geometry and material. Increased secondary electron fluence will cause increased energy deposition which leads to a decreased perturbation factor and vice versa which both will result in a numerical value deviating more from unity (the ideal). Table 3 shows the numerical values of p_{int} and p_{ext}. p_{int} did not deviate more than 3% from unity except for the frontal orientation which could cause deviations up to $\approx 11\%$. As already described by Kondo and Randolph (1960), the volume averaging of energy deposition in the detector cavity and therefore the internal perturbation factor is determined by the cavity's size, geometry and position in the steep dose gradient. The calculated values of p_{int} by Kondo and Randolph which can be found in their work in table I as $1/K_S$ agree well with those in table 3 for crossed and parallel orientation.

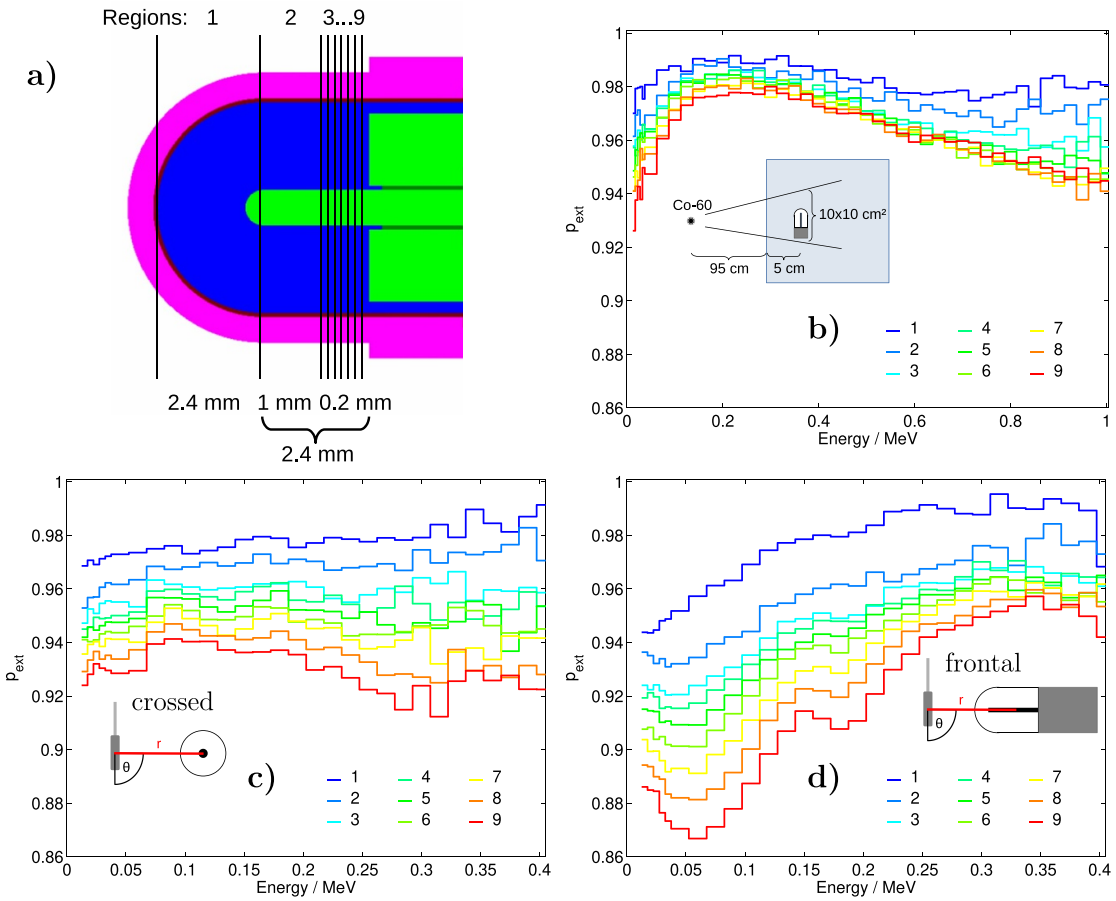

Figure 6. (a) Sketch of how the layers of the PTW chamber type 31021 were divided to achieve spatial information on the external perturbation factor p_{ext}. The entire air cavity (including the dead volume) of the chamber was taken into account here. Graphs (b)–(d) depict the corresponding results under calibration conditions as well as the crossed and frontal orientation under TG-43 conditions.

Material differences in the detector structures (wall, central electrode, guard ring etc) containing different cross sections lead to differences in secondary electron fluence and therefore p_{ext} values deviating from unity. The numerical values for the latter did not deviate more than 4% from unity except for the frontal orientation where they could amount up to $\approx 6\%$. The largest perturbations were found in the PTW chambers 31021, 31022 and 31023 whose guard rings are made of aluminum, having the highest atomic number and mass density in the vicinity of the cavities.

In summary it should be noted that all effects discussed here can affect the chamber perturbations in different ways depending on the beam setup. This means, for example, that a perturbation correction close to unity is not necessarily the result of a good chamber design (e.g. the use of water equivalent materials), but can also be caused by effects randomly canceling each other. For example, p_{ext} does not differentiate between individual chamber components but between the influence of all components simultaneously.

5.2. Spatially resolved external perturbation factor

The PTW chamber 31021 showed the largest external perturbations so that it was selected to investigate the spatial distribution of p_{ext}, differential in energy, in several slices of its air cavity. Figure 6(a) shows the nine different regions in which p_{ext} was resimulated as well under calibration conditions as in the crossed and frontal orientation. Results are shown in figures 6(b)–(d), respectively.

Under calibration conditions, the perturbations in the tip of the chamber in region 1 displayed only a small energy dependence. The difference between the slices around 200 keV was only 2% and increased up to 4% at lower and higher energies. At high energies, regions 5 to 9 exhibited similar perturbations, showing an increased deviation of p_{ext} from unity with energy, probably due to the increased energy of secondary electrons from Compton scattering. This was not seen in the tip slices, since the Compton electrons are most likely inclined by approx. $(65° - 15°)$ with respect to the incident photon beam (energy range from $(10 - 1000)$ keV) following the Klein–Nishina Theory (Klein and Nishina 1929) so that additional high energy electron contributions from the stem could not reach the chamber tip.

In the crossed orientation there was no pronounced energy dependence of the individual layers. Secondary electrons from photon interactions at the guard ring reached the entire cavity, however the interactions decreased with distance from the stem, so that p_{ext} increased, i.e. approaching unity.

In the frontal orientation there was an energy dependence of p_{ext} which increased towards the chamber stem. The differences between the different regions were up to 9% which might be caused by backscattered electrons at the guard ring. The dip at 180 keV in the curves closer to the stem (6 and above) could be related to a Compton edge that was seen in the restricted cema differential in energy. This is shown in a previous work for a comparable setup (Failing *et al* 2022).

5.3. Beam quality correction factor

Another possibility to prove the plausibility of the MC calculated quality correction factors—besides experimental verification—is the comparison with literature values. Chofor *et al* determined k_Q with a semi-empirical approach in which the mean photon energy at the point of measurement was used (2016). Based on the detector-specific response (mainly from other works), the radiation quality correction at arbitrary points with known mean photon energy could be determined. This is a fast and resource-saving method but it cannot describe e.g. the directional dependence of response as shown for the detector orientations presented in this work. In that work, beam quality correction factors were determined, among others, for the PTW chamber 31010 and a further unspecified PTW PinPoint chamber only in an external beam setup comparable to calibration conditions. Under these conditions the dependence of volume averaging on position and orientation in a water setup were not accounted for.

A work by Araki *et al* found $k_Q = 0.989$ for the PTW chamber 31010 under TG-43 conditions of a comparable Nucletron microSelectron-v2 Ir-192 HDR source (2013). Again the orientation of the chamber was not reported. From the observed poor repeatability the authors concluded that a large uncertainty of the measurement was caused by chamber positioning. Additionally, the lack of a source position control was regarded as a further source of uncertainty so that the authors did not verify k_Q. The size of the scored water voxel may lead to a significant perturbation of k_Q observable in a variation of $\approx 10\%$ for the same Farmer type chamber PTW 30013 in comparable immersed source setups (Araki *et al* 2015, Campos *et al* 2018) which were both validated against established TG-43 parameters (Taylor and Rogers 2008). To effectively replace the chamber with water neglects the volume averaging and therefore voxel sizes should be chosen small enough so that averaging effects can be excluded (Taylor and Rogers 2008).

In external beam reference dosimetry, the influence of the dead volume on k_Q is negligible since all publications for current dosimetry protocols, for instance TRS-398 (IAEA 2024), do not consider the dead volume. This is also confirmed by preliminary simulations of this work. At the TG-43 reference point the consideration of this influence has been shown to be indispensable and was most pronounced in frontal orientation since all chambers yielded a dependence of the dead volume beyond the uncertainty. For other orientations, the effect is smaller but there is still a dependence on the chamber geometry and the materials used which can be seen in table 3, respectively. To eliminate this possible source of error, it is recommended to consider the dead volume of ionization chambers in brachytherapy dosimetry.

In external beam setups the corresponding type B uncertainties on the EGSnrc based calculation of the beam quality correction factor k_Q range from 0.2% at 6 MV nominal photon energy up to 0.4% at 24 MV (Wulff *et al* 2010). If, in addition, the uncertainty for the average energy to create an ion pair in dry air, W_{air} (ICRU 2016), over the photon energies from Co-60 to 25 MV is also taken into account, the uncertainty increases up to 0.5% (Muir *et al* 2011). A variation of W_{air} can be excluded in the energy range of this study (ICRU 2016, IAEA 2024). In contrast, for photon energies below 200 keV, the uncertainties on calculating the absorbed dose to water increase with decreasing energy due to uncertainties associated with the photoelectric effect (Valdes-Cortez *et al* 2021). This could be one explanation for larger type B uncertainties in the calculation of k_Q compared to 6 MV external beams (Wulff *et al* 2010).

Detector geometry variations (e.g. constructional uncertainties) for the same model but different serial number were already investigated for ionization chambers as well as diamond detectors in measurements around Ir-192 HDR sources (Araki *et al* 2013, Kaveckyte *et al* 2017, Rossi *et al* 2020) and varied between 1% and 3% depending on the angle and distance to the source. The combined MC determined uncertainties in detector geometries and positioning were approximately equal to the uncertainties of the measurements. Comparable uncertainties were obtained when calculating detector variations with EGSnrc under the influence of magnetic fields and with a variation of the dead volume of only 1% (Cervantes *et al* 2020).

In the measurements at the TG-43 reference point the greatest sources of uncertainty were the positioning of detector and source. The positioning uncertainties can be reduced by measurements at larger distances (Schoenfeld *et al* 2018). Therefore beam quality correction factors as well as perturbation factors differential in energy were also investigated at 3 cm nominal distance in the immersed source setup. Results are shown in appendix C. With a larger distance the positioning uncertainties dropped below 0.5% following

the inverse square law so that the measured data were more reliable. p_{int} decreased significantly as shown in the left column of figure C1 especially for elongated chambers. At a distance of 3 cm the signal was reduced by approximately a factor of nine and the increased scattering contributions led to increased deviation of p_{ext} from unity especially for the chambers with aluminum guard ring as shown in the right column of figure C1. Thus the beam quality correction factor did not necessarily approach unity at larger distances as shown in table C1. Based on the reduced positioning uncertainties, the overall combined uncertainties approached values of megavoltage photon beams (Andreo *et al* 2020) so that it might be possible to obtain even smaller combined uncertainties of the absorbed dose rate to water with the investigated ionization chambers rather than by using the TG-43 formalism which does not use in-phantom measurements but calculates the absorbed dose rate to water via $S_k \cdot \Lambda$. Another elegant method to reduce the positioning uncertainty of the afterloader is to superimpose several source positions closely in one straight applicator so that the dose distribution becomes homogeneous in the longitudinal direction (Kaveckyte *et al* 2017). This is particularly helpful when source scans are not possible, for example in a solid phantom, but the angular dependence of the detector must be known for this.

6. Conclusion

Beam quality correction factors of five ionization chambers were calculated with MC simulations at the TG-43 reference point for three orientations of the detectors with respect to an Ir-192 HDR source. By factorization of the restricted cema in the air cavity and MC simulation with and without the different components of the ionization chambers (equation (7)), perturbations due to volume averaging (p_{int}) and material composition (p_{ext}) of the chambers could be analyzed. In the steep dose gradient at 1 cm nominal source-detector-distance, p_{int} of the elongated chambers represented the largest perturbations. Aluminum chamber components were most responsible for p_{ext}. k_Q factors could be verified by their use in water phantom measurements yielding the expected dose rate within the combined uncertainty ($k = 2$) except for one chamber in frontal orientation possessing the largest cavity radius when charge collection in the full air cavity was simulated, neglecting the dead volume. A dependence of the response on the chamber orientation in relation to the source was observed. In crossed and parallel orientation the calculated perturbation factors as well as k_Q values agreed within the determined uncertainties. Especially in frontal orientation different perturbation corrections were found when restricted cema was collected in the chamber cavity excluding the dead volume or when this omission was neglected.

For accurate measurements of absorbed dose rate to water, it is advisable to avoid the frontal detector orientation to the source which causes increased perturbations and uncertainties and to use correction factors based on the sensitive volume of the chambers, i.e. excluding the dead volume. In measurements in the clinical environment, positioning source and detector remains the largest challenge and is responsible for the largest uncertainties. Additionally, a larger source-detector-distance than the reference distance of 1 cm reduced positioning uncertainties and also internal perturbations (p_{int} shifted closer to 1). However, with increasing distances the detector reading decreases exponentially and the external perturbations increased (p_{ext} shifted to a larger difference to 1) due to increased scatter contributions (as shown in figure C1), so that a detector-specific optimum is yet to be found.

A compromise could be measuring dose rates at 2 cm distance as proposed in dosimetry protocols for low or medium energy x-rays (Klevenhagen *et al* 1929, Ma *et al* 2001, IAEA 2024) using correction and perturbation factors calculated for the respective depth, and then re-normalizing dose distributions to the TG-43 reference point to obtain comparability with published source data.

Data availability statement

All data that support the findings of this study are included within the article (and any supplementary information files).

Acknowledgments

The authors would like to thank Daniela Eulenstein, Konstantin Burzlaff and Jan Würfel from PTW-Freiburg for passing on technical drawings and for lending the PTW chamber 31023.

The authors would also like to thank Shannon Holmes and Brian Hooten from Standard Imaging for passing on the technical drawing and for lending the chamber Exradin A26.

Last but not least the authors express their gratitude to Bernd Thüne from the University Medical Center Göttingen for the construction of the source holder and guiding tube in the measurement setup.

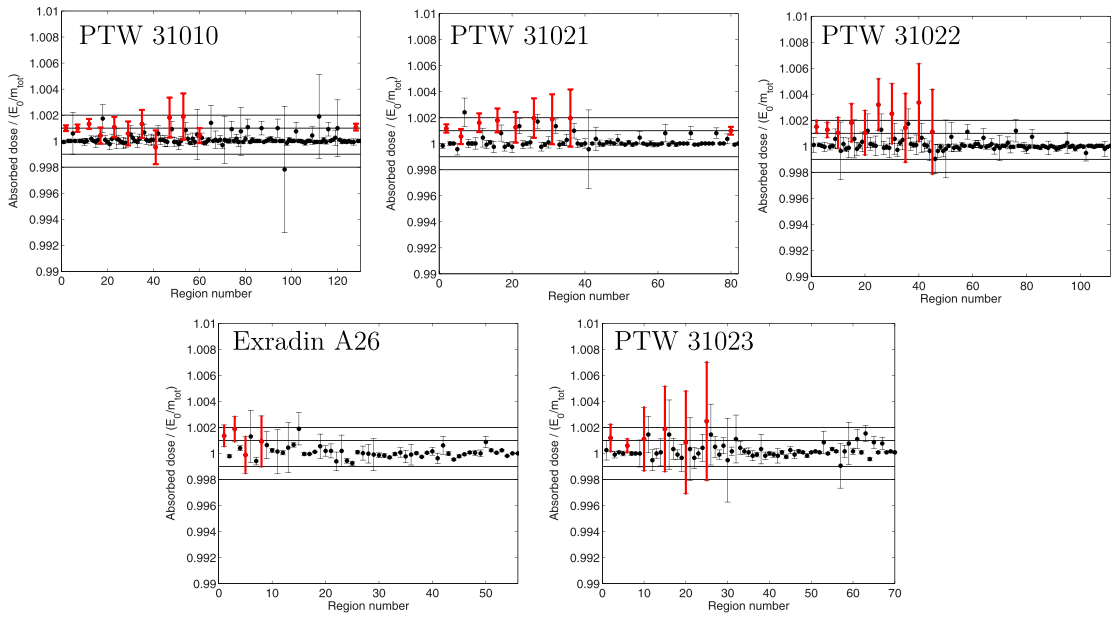

Figure A1. Results of the Fano tests as ratios of the absorbed dose and the expected values which are calculated by the ratio of the kinetic energy of the primary particles $E_0 = 100\,\text{keV}$ and the total mass of the Fano simulation m_{tot}. The sensitive air volumes are marked red.

Declaration

This work is part of a dissertation project of Technische Hochschule Mittelhessen University of Applied Sciences at the Graduate Center of Engineering Sciences at the Research Campus of Central Hessen.

Appendix A. Fano calculations

The results of the Fano tests performed for all investigated ionization chambers are presented in figure A1 as ratio of the absorbed dose per region and the theoretical value of the kinetic energy of the primary electrons E_0 divided by the total mass of the Fano simulation m_{tot}. An `egs_fano_source` with monoenergetic 100 keV electrons was used since this is also approximately the mean kinetic energy of the electrons liberated in the chamber cavities at the immersed Ir-192 HDR Flexisource setups (Failing *et al* 2022). The detector materials were substituted by water with the corresponding original material's density and density correction. For the Fano calculation, the detector is immersed in a large water cylinder i.e. whose dimensions are at least three electron ranges larger than the outer detector shell.

Appendix B. Effective point of measurement

The effective points of measurement (EPOMs) of the investigated chambers in the brachytherapy setup were determined by MC simulations of profiles of chamber response at distances of 1 cm from the source in water. At the maximum of the profiles as shown in figure B1, the EPOM was assumed to lie exactly opposed to the source. This maximum was determined in 4th order polynomial fits of the simulated response profiles (goodness of fit $R^2 > 0.975$ for all chambers). Table B1 shows that for all chambers the EPOM lies at different distances from the chamber tip (and the reference point) in the different simulated orientations. These shifts are caused by different volume averaging of the dose in the cavity at different positions in the steep dose gradient and will cause a variation of EPOM with distance from the source, making the use of the EPOM impractical for chamber positioning in setups close to the source. This effect is also present in the external beam situation, however much smaller in the lower dose gradients at 1 m distance. In all simulations and measurements in this work the chambers were therefore positioned at the manufacturer-stated reference point to avoid ambiguity. The EPOM was needed in the experimental dose measurements in this work to identify the exact source position by profile measurement as described in section 3.5. Here again the EPOM will be closest to the source in the profile maximum. To determine the source position in a coordinate system determined by the chamber position one must then correct the measured position by subtracting the distance between EPOM and indicated chamber position.

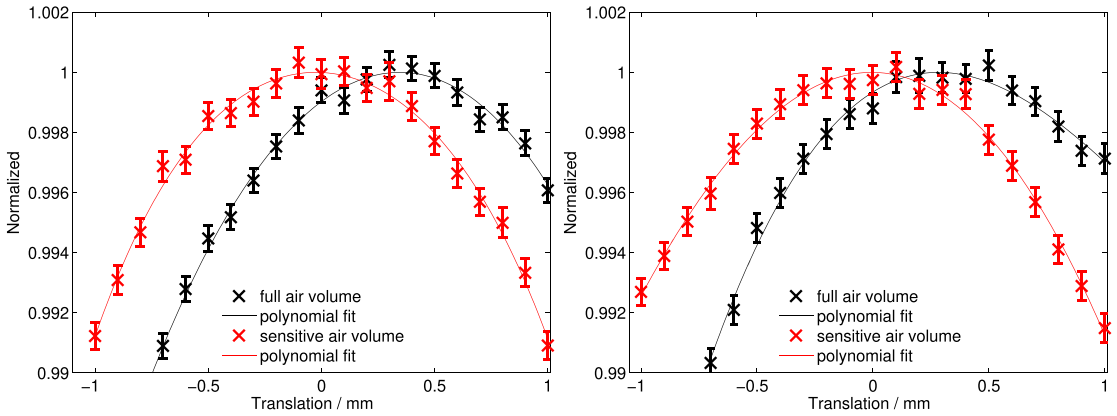

Figure B1. MC based determination of the effective point of measurement on the central axis of an ionization chamber. The diagrams show the normalized response of a fully modelled PTW 31010 chamber translated in water along profiles parallel to the source axis (i.e. in parallel orientation, left) and across the source axis (i.e. in crossed orientation, right). The indicated translation corresponds to the distance between the calculation position along the profile and the reference point of the chamber. The MC calculated normalized raw values are also shown with their standard deviation.

Table B1. MC calculated distance in millimeters from the tip of the ionization chamber to the effective point of measurement on the central axis. For comparison the distance from the tip of the manufacturer-stated reference point is given in the top row. Results are given for a HDR Ir-192 Flexisource in a Beamscan water phantom. The first value of a chamber refers to the full air cavity volume whereas the second value in italics only considers the sensitive volume.

	PTW 31010		PTW 31021		PTW 31022		Exradin A26		PTW 31023	
reference	4.5		3.45		2.4		1.98		3.4	
crossed	4.86	*4.47*	3.32	*3.02*	2.15	*1.98*	2.23	*2.09*	3.29	*3.17*
parallel	4.83	*4.46*	3.31	*3.01*	2.08	*1.96*	2.22	*2.08*	3.30	*3.19*

Appendix C. Results at 3 cm nominal distance

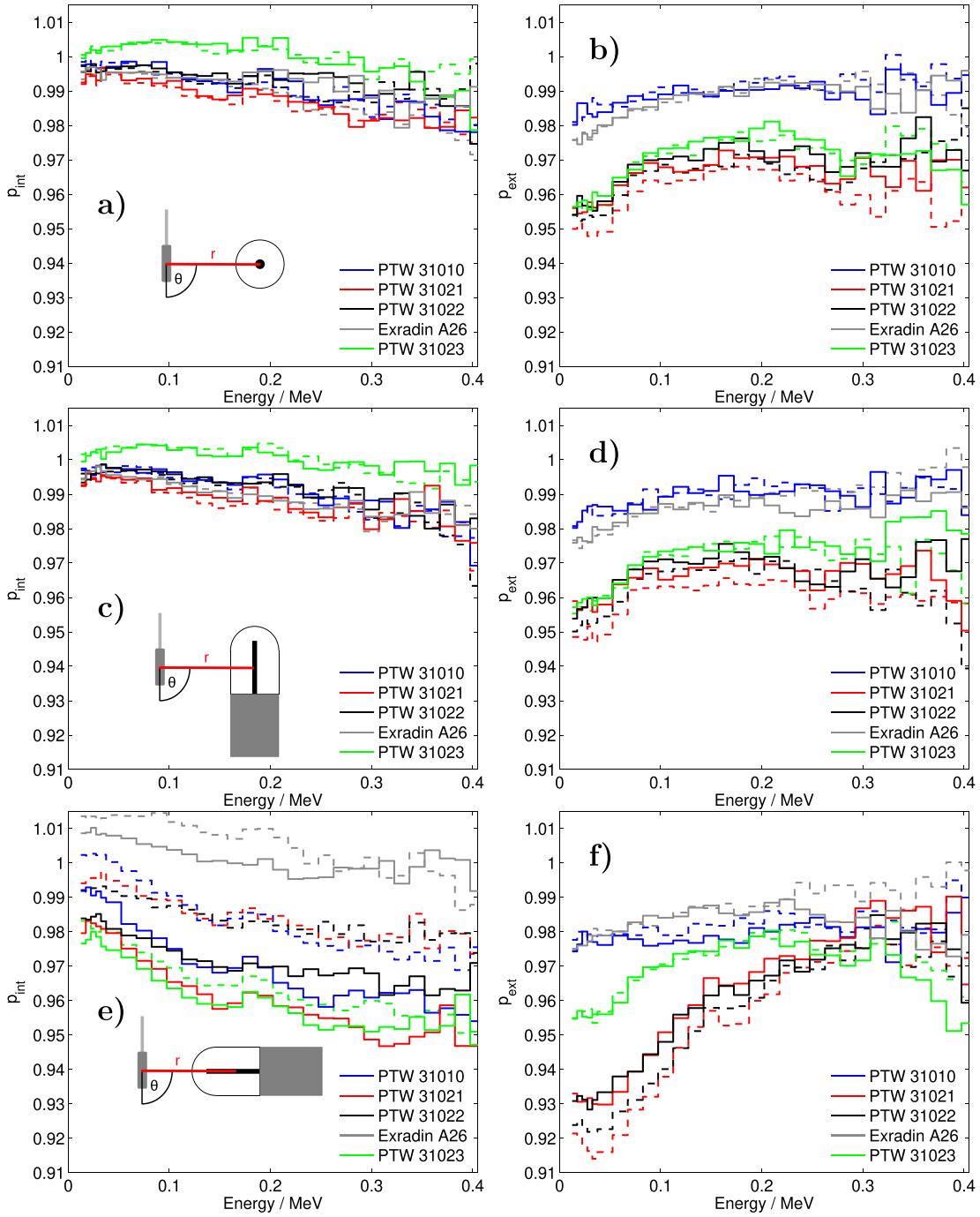

Figure C1. Internal (left column) and external (right column) perturbation factor differential in energy for various ionization chambers in crossed (first row), parallel (second row) and frontal orientation (third row) at 3 cm distance to an immersed Ir-192 HDR Flexisource. The solid lines correspond to the sensitive air volume of the chambers whereas the dashed lines correspond to the full cavity volume. All plots are scaled equally.

Table C1. Beam quality correction factors at 3 cm nominal distance to an immersed Ir-192 HDR Flexisource. Three different chamber orientations such as crossed, parallel and frontal to the source long axis were investigated. The first value of a fully modelled chamber refers to the full air cavity volume whereas the second value in italics only considers the sensitive volume. The relative standard deviation of all results ranges between 0.2% and 0.3%. The combined standard uncertainty, which takes into account other MC related uncertainties, ranges between 0.5% and 0.6%.

	$k_{Q,\,3\,cm}$									
	PTW 31010		PTW 31021		PTW 31022		Exradin A26		PTW 31023	
crossed	1.001	*1.003*	0.975	*0.984*	0.980	*0.986*	0.995	*0.996*	0.988	*0.991*
parallel	1.001	*1.003*	0.975	*0.984*	0.980	*0.985*	0.995	*0.996*	0.988	*0.989*
frontal	0.993	*0.980*	0.948	*0.945*	0.950	*0.948*	1.011	*1.004*	0.960	*0.955*

ORCID iDs

T Failing https://orcid.org/0000-0002-4554-7769
B Keil https://orcid.org/0000-0003-0805-8330
K Zink https://orcid.org/0000-0001-5785-4101

References

Almond P R, Biggs P J, Coursey B M, Hanson W F, Huq M S, Nath R and Rogers D W O 1999 AAPM's TG-51 protocol for clinical reference dosimetry of high-energy photon and electron beams *Med. Phys.* **26** 1847–70

Andreo P *et al* 2020 Determination of consensus k_Q values for megavoltage photon beams for the update of IAEA TRS-398 *Phys. Med. Biol.* **65** 095011

Araki F, Kouno T, Ohno T, Kakei K, Yoshiyama F and Kawamura S 2013 Measurement of absorbed dose-to-water for an HDR ^{192}Ir source with ionization chambers in a sandwich setup *Med. Phys.* **40** 092101

Araki F, Ohno T, Kakei K and Kawamura S 2015 Absorbed dose-to-water measurement of an HDR ^{192}Ir source with Farmer ionization chambers in a sandwich setup *Biomed. Phys. Eng. Express* **1** 037002

Baglin C M 2012 Nuclear Data Sheets for A = 192 *Nucl. Data Sheets* **113** 1871–2111

Beaulieu L *et al* 2023 AAPM WGDCAB report 372: a joint AAPM, ESTRO, ABG and ABS report on commissioning of model based dose calculation algorithms in brachytherapy *Med. Phys.* **50** e946–e960

Beaulieu L, Tedgren A C, Carrier J-F, Davis S D, Mourtada F, Rivard M J, Thomson R M, Verhaegen F, Wareing T A and Williamson J F 2012 Report of the task group 186 on model-based dose calculation methods in brachytherapy beyond the TG-43 formalism: current status and recommendations for clinical implementation *Med. Phys.* **39** 6208–36

BIPM, IEC, IFCC, ILAC, ISO, IUPAC, IUPAP and OIML 2008 Evaluation of measurement data — guide to the expression of uncertainty in measurement *Technical Report*

Butler D J, Stevenson A W, Wright T E, Harty P D, Lehmann J, Livingstone J and Crosbie J C 2015 High spatial resolution dosimetric response maps for radiotherapy ionization chambers measured using kilovoltage synchrotron radiation *Phys. Med. Biol.* **60** 8625–41

Campos L T, Magalhaes L A G and de Almeida C E V 2018 Determination of a beam quality conversion factor from ^{60}Co to ^{192}Ir *J. Radiat. Res. Appl. Sci.* **11** 249–54

Carlsson Tedgren A and Ahnesjö A 2008 Optimization of the computational efficiency of a 3D, collapsed cone dose calculation algorithm for brachytherapy *Med. Phys.* **35** 1611–8

Cervantes Y, Billas I, Shipley D, Duane S and Bouchard H 2020 Small-cavity chamber dose response in megavoltage photon beams coupled to magnetic fields *Phys. Med. Biol.* **65** 245008

Chofor N, Harder D, Selbach H-J and Poppe B 2016 The mean photon energy $\bar{E}F$ at the point of measurement determines the detector-specific radiation quality correction factor $k_{Q,M}$ in ^{192}Ir brachytherapy dosimetry *Z. Med. Phys.* **26** 238–50

Delfs B *et al* 2021 The role of the construction and sensitive volume of compact ionization chambers on the magnetic field-dependent dose response *Med. Phys.* **48** 4572–85

DeWerd L A, Ibbott G S, Meigooni A S, Mitch M G, Rivard M J, Stump K E, Thomadsen B R and Venselaar J L M 2011 A dosimetric uncertainty analysis for photon-emitting brachytherapy sources: report of AAPM Task Group No. 138 and GEC-ESTRO *Med. Phys.* **38** 782–801

DIN 6800-2:2020-08 2020 Dosismessverfahren nach der sondenmethode fur photonen- und elektronenstrahlung - teil 2: dosimetrie hochenergetischer photonen- und elektronenstrahlung mit ionisationskammern DIN-standard Beuth Verlag GmbH

Failing T, Hartmann G H, Hensley F W, Keil B and Zink K 2022 Enhancement of the EGSnrc code egs_chamber for fast fluence calculations of charged particles *Z. Med. Phys.* **32** 417–27

Hartmann G H, Andreo P, Kapsch R-P and Zink K 2021 Cema-based formalism for the determination of absorbed dose for high-energy photon beams *Med. Phys.* **48** 7461–75

Hartmann G H, Hensley F, Kapsch R-P, Poppe B, Sauer O, Würfel J and Zink K 2020 Ermittlung der Wasser-Energiedosis nach der Sondenmethode Gemäß DIN 6800 Teil 1: Vorschlag für eine Erweiterung der Grundgleichung *Z. Med. Phys.* **30** 24–39

Hartmann G H and Zink K 2018 Decomposition of the dose conversion factor based on fluence spectra of secondary charged particles: application to lateral dose profiles in photon fields *Med. Phys.* **45** 4246–56

IAEA 2023 Technical Report Series No. 492 dosimetry in brachytherapy - an international code of practice for secondary standards dosimetry laboratories and hospitals *Technical Report* International Atomic Energy Agency Vienna

IAEA 2024 Technical Report Series No. 398 Rev. 1 absorbed dose determination in external beam radiotherapy *Technical Report* International Atomic Energy Agency Vienna

ICRU 2016 Report 90 *J. Int. Comm. Radiat. Units Meas.* **14** 10.11, 31–41

Kaveckyte V, Malusek A, Benmakhlouf H, Carlsson G A and Tedgren A C 2017 Suitability of microDiamond detectors for the determination of absorbed dose to water around high-dose-rate ^{192}Ir brachytherapy sources *Med. Phys.* **45** 429–37

Kawrakow I 2000a Accurate condensed history Monte Carlo simulation of electron transport. I. EGSnrc, the new EGS4 version *Med. Phys.* **27** 485–98
Kawrakow I 2000b Accurate condensed history Monte Carlo simulation of electron transport. II. Application to ion chamber response simulations *Med. Phys.* **27** 499–513
Kawrakow I et al 2019 EGSnrc C++ class library Report PIRS-898 National Research Council of Canada (available at: https://nrc-cnrc.github.io/EGSnrc/doc/pirs898/index.html)
Kawrakow I, Mainegra-Hing E, Rogers D W O, Tessier F and Walters B R B 2001-2015 [version 2021] The EGSnrc code system: Monte Carlo simulation of electron and photon transport *Report* PIRS-701 National Research Council Canada
Kellerer A M, Hahn K and Rossi H H 1992 Intermediate dosimetric quantities *Radiat. Res.* **130** 15
Kessler C, Behrens R, Kasper A and Grote F 2024 Key comparison BIPM.RI(I)-K8 of high dose-rate ^{192}Ir brachytherapy standards for reference air kerma rate of the PTB and the BIPM *Metrologia* **61** 06002
Klein O and Nishina Y 1929 Über die Streuung von Strahlung durch freie Elektronen nach der neuen relativistischen Quantendynamik von Dirac *Z. Phys.* **52** 853–68
Klevenhagen S C, Aukett R J, Harrison R M, Morreti C, Nahum A E and Rosser K E 1996 The IPEMB code of practice for the determination of absorbed dose for x-rays below 300 kV generating potential (0.035 mm Al - 4 mm Cu HVL; 10 - 300 kV generating potential) *Phys. Med. Biol.* **41** 2605–25
Kondo S and Randolph M L 1960 Effect of finite size of ionization chambers on measurements of small photon sources *Radiat. Res.* **13** 37
Li Z, Das R K, DeWerd L A, Ibbott G S, Meigooni A S, Pérez-Calatayud J, Rivard M J, Sloboda R S and Williamson J F 2006 Dosimetric prerequisites for routine clinical use of photon emitting brachytherapy sources with average energy higher than 50 keva) *Med. Phys.* **34** 37–40
Ma C, Coffey C W, DeWerd L A, Liu C, Nath R, Seltzer S M and Seuntjens J P 2001 AAPM protocol for 40–300 kV x-ray beam dosimetry in radiotherapy and radiobiology *Med. Phys.* **28** 868–93
Margaroni V, Pappas E P, Episkopakis A, Pantelis E, Papagiannis P, Marinos N and Karaiskos P 2022 Dosimetry in 1.5T MR-Linacs: Monte Carlo determination of magnetic field correction factors and investigation of the air gap effect *Med. Phys.* **50** 1132–48
McEwen M, DeWerd L, Ibbott G, Followill D, Rogers D W O, Seltzer S and Seuntjens J 2014 Addendum to the AAPM's TG-51 protocol for clinical reference dosimetry of high-energy photon beams *Med. Phys.* **41** 041501
Miller J R, Hooten B D, Micka J A and DeWerd L A 2016 Polarity effects and apparent ion recombination in microionization chambers *Med. Phys.* **43** 2141–52
Mora G M, Maio A and Rogers D W O 1999 Monte Carlo simulation of a typical ^{60}Co therapy source *Med. Phys.* **26** 2494–502
Muir B R, McEwen M R and Rogers D W O 2011 Measured and Monte Carlo calculated kQ factors: accuracy and comparison *Med. Phys.* **38** 4600–9
Muir B R and Rogers D W O 2010 Monte Carlo calculations of, the beam quality conversion factor *Med. Phys.* **37** 5939–50
Nath R, Anderson L L, Luxton G, Weaver K A, Williamson J F and Meigooni A S 1995 Dosimetry of interstitial brachytherapy sources: recommendations of the AAPM radiation therapy committee task group no. 43 *Med. Phys.* **22** 209–34
Nath R, Anderson L L, Meli J A, Olch A J, Stitt J A and Williamson J F 1997 Code of practice for brachytherapy physics: report of the AAPM radiation therapy committee task group no. 56 *Med. Phys.* **24** 1557–98
Pérez-Calatayud J, Ballester F, Das R K, DeWerd L A, Ibbott G S, Meigooni A S, Ouhib Z, Rivard M J, Sloboda R S and Williamson J F 2012 Dose calculation for photon-emitting brachytherapy sources with average energy higher than 50 keV: Report of the AAPM and ESTRO *Med. Phys.* **39** 2904–29
Pérez-Calatayud J, Granero D and Ballester F 2004 Phantom size in brachytherapy source dosimetric studies *Med. Phys.* **31** 2075–81
Pojtinger S, Kapsch R-P, Dohm O S and Thorwarth D 2019 A finite element method for the determination of the relative response of ionization chambers in MR-linacs: simulation and experimental validation up to 1.5 T *Phys. Med. Biol.* **64** 135011
Rivard M J, Coursey B M, DeWerd L A, Hanson W F, Huq S M, Ibbott G S, Mitch M G, Nath R and Williamson J F 2004 Update of AAPM Task Group No. 43 Report: A revised AAPM protocol for brachytherapy dose calculations *Med. Phys.* **31** 633–74
Ross C K 2009 Comments on 'Ionization chamber volume determination and quality assurance using micro-CT imaging' *Phys. Med. Biol.* **54** 23–27
Rossi G, Failing T, Gainey M, Kollefrath M, Hensley F, Zink K and Baltas D 2023 Determination of the dose rate around a HDR ^{192}Ir brachytherapy source with the microDiamond and the microSilicon detector *Z. Med. Phys.* **33** 463–78
Rossi G, Gainey M, Kollefrath M, Hofmann E and Baltas D 2020 Suitability of the microDiamond detector for experimental determination of the anisotropy function of high dose rate ^{192}Ir brachytherapy sources *Med. Phys.* **47** 5838–51
Sander T 2014 Air kerma and absorbed dose standards for reference dosimetry in brachytherapy *Br. J. Radiol.* **87** 20140176
Schoenfeld A A, Büsing K, Delfs B, Chofor N, Jiang P, Harder D, Poppe B and Willborn K C 2018 Reference conditions for ion-chamber based HDR brachytherapy dosimetry and for the calibration of high-resolution solid detectors *Z. Med. Phys.* **28** 293–302
Sechopoulos I, Rogers D W O, Bazalova-Carter M, Bolch W E, Heath E C, McNitt-Gray M F, Sempau J and Williamson J F 2017 RECORDS: improved reporting of Monte Carlo radiation transport studies: report of the AAPM research committee task group 268 *Med. Phys.* **45** e1–e5
Seltzer S M 1993 Stopping-powers and range tables for electrons, protons, and helium ions, NIST standard reference database 124 *Technical Report* National Institute of Standards and Technology
Sempau J, Andreo P, Aldana J, Mazurier J and Salvat F 2004 Electron beam quality correction factors for plane-parallel ionization chambers: Monte Carlo calculations using the PENELOPE system *Phys. Med. Biol.* **49** 4427–44
Spindeldreier C K, Schrenk O, Bakenecker A, Kawrakow I, Burigo L, Karger C P, Greilich S and Pfaffenberger A 2017 Radiation dosimetry in magnetic fields with Farmer-type ionization chambers: determination of magnetic field correction factors for different magnetic field strengths and field orientations *Phys. Med. Biol.* **62** 6708–28
Taylor R E P and Rogers D W O 2008 An EGSnrc Monte Carlo-calculated database of TG-43 parameters *Med. Phys.* **35** 4228–41
Thomas D J 2012 ICRU report 85: fundamental quantities and units for ionizing radiation *Radiat. Prot. Dosim.* **150** 550–2
Valdes-Cortez C, Mansour I, Rivard M J, Ballester F, Mainegra-Hing E, Thomson R M and Vijande J 2021 A study of Type B uncertainties associated with the photoelectric effect in low-energy Monte Carlo simulations *Phys. Med. Biol.* **66** 105014
Walters B R B, Kawrakow I and Rogers D W O 2002 History by history statistical estimators in the BEAM code system *Med. Phys.* **29** 2745–52
Walters B, Kawrakow I and Rogers D W O 2021 DOSXYZnrc Users Manual *Report* PIRS-794 National Research Council of Canada
Watson P G F, Popovic M and Seuntjens J 2017 Determination of absorbed dose to water from a miniature kilovoltage x-ray source using a parallel-plate ionization chamber *Phys. Med. Biol.* **63** 015016

Wulff J, Heverhagen J T and Zink K 2008 Monte-Carlo-based perturbation and beam quality correction factors for thimble ionization chambers in high-energy photon beams *Phys. Med. Biol.* **53** 2823

Wulff J, Heverhagen J T, Zink K and Kawrakow I 2010 Investigation of systematic uncertainties in Monte Carlo-calculated beam quality correction factors *Phys. Med. Biol.* **55** 4481–93

Wulff J, Zink K and Kawrakow I 2008 Efficiency improvements for ion chamber calculations in high energy photon beams *Med. Phys.* **35** 1328–36

Zourari K, Pantelis E, Moutsatsos A, Petrokokkinos L, Karaiskos P, Sakelliou L, Georgiou E and Papagiannis P 2010 Dosimetric accuracy of a deterministic radiation transport based brachytherapy treatment planning system. Part I: single sources and bounded homogeneous geometries *Med. Phys.* **37** 649–61

4.4 Angular dependence of detector responses in high-energy brachytherapy

Die vorherige Publikation [61] hat bereits durch die Betrachtung von verschiedenen Ausrichtungen der Detektoren zur Quelle, wie in Abb. 3.1 dargestellt, einen Ausblick auf die systematische Untersuchung der Winkelabhängigkeit des Ansprechvermögens gegeben. Neben der Bestimmung der Dosisleistung einer Ir-192 HDR Brachytherapiequelle in einem definierten Bestrahlungssetup können sich weitere Anforderungen an die Dosimetrie in der Brachytherapie ergeben, in welchem die Richtungsabhängigkeit des Ansprechvermögens höchstens unter sehr großem Aufwand individuell berücksichtigt werden kann. Beispiele hierfür sind die Verifikation von ‚Model-based Dose Calculation Algorithms' [50] oder klinischen Dosisleistungsverteilungen mit vielen Quellenpositionen. Mit dieser Arbeit wurde die Winkelabhängigkeit in der Brachytherapie erstmals detailliert unter Berücksichtigung einzelner Störungsfaktoren untersucht. Zu diesem Zweck wurden insgesamt drei Kompakt-Ionisationskammern der Firmen PTW und Standard Imaging sowie ein PTW microDiamond Diamantdetektor verwendet. Die Winkelabhängigkeit wurde sowohl experimentell an der PTB als auch mithilfe der selbst entwickelten erweiterten Version der MC Applikation `egs_chamber` untersucht [82]. Für die Messung wurden die Detektoren an einem Roboterarm fixiert und im Strahlungsfeld einer Ir-192 HDR Brachytherapiequelle im Abstand von 10 cm um ihren Referenzpunkt rotiert. Dieser Messaufbau wurde ebenfalls mit der MC Software modelliert, simuliert und daraufhin experimentell verifiziert. Anschließend wurden weitere Simulationen in einer Wasserumgebung mit Abständen von 1, 3, 5 und 10 cm durchgeführt. Anhand dieser Bestrahlungssetups ließ sich der Unterschied zwischen einer Wasser- und Luftumgebung sowie die Winkelabhängigkeit des Ansprechvermögens mit dem Abstand in Wasser darstellen. Analog zur vorigen Arbeit wurden zusätzlich die Störungsfaktoren p_{int} und p_{ext}, welche die physikalischen Effekte der Volumenmittelung beziehungsweise der Störung durch Detektorbauteile beschreiben, mithilfe der beschränkten Cema, auch energiedifferentiell, untersucht.
Die MC Simulationen konnten anhand der Messungen in Luft experimentell verifiziert werden; die Abweichungen beliefen sich (außer bei großen Änderungen der Winkelabhängigkeit) innerhalb der kombinierten Standardunsicherheiten ($k = 1$). In Luft waren die Winkelabhängigkeiten ausgeprägter als bei vergleichbarem Abstand in Wasser. In Luft und Wasser zeigte sich, dass bei kleinen Auslenkungen der Detektoren gegenüber frontaler Ausrichtung zur Quelle von $< 20\,^\circ$ die Abweichungen $< 0,5\,\%$ betrugen. Im Extremfall konnten die Abweichungen beim microDiamond in Luft jedoch bis zu 7 % betragen. Die Winkelabhängigkeit des microDiamond ist in vergleichbaren Messungen mit niedrigeren Strahlungsenergien noch ausgeprägter [83, 84] und zeigte damit zusätzlich eine Energieabhängigkeit. Die Änderung der Winkelabhängigkeit nahm bei allen Detektoren mit der Drehung aus der frontalen Ausrichtung zu. Die Winkelabhängigkeiten des Ansprechvermögens in Wasser nahmen mit zunehmendem Abstand zur Quelle ab. Dies lässt sich unter anderem damit erklären, dass der Anteil an gestreuten Photonen mit größeren Distanzen zunimmt [52, 85]. Des Weiteren nimmt der Dosisgradient mit zunehmendem Abstand ab, so dass Volumenmittelungseffekte weniger ausgeprägt sind.

Die Winkelabhängigkeit hing auch davon ab, wie die Ionisationskammern bezüglich ihres Kammerreferenzpunkts positioniert wurden. Dies zeigte sich in den verschiedenen Ergebnissen von p_{int} für die Luftkavitäten der fast gleich dimensionierten Ionisationskammern PTW 31022 und Exradin A26. Störungen aufgrund von Detektorbauteilen (p_{ext}) zeigten ebenfalls eine Winkelabhängigkeit, da die Detektoren nicht kugelsymmetrisch aufgebaut sind. Insbesondere p_{ext} des microDiamond zeigte eine ausgeprägte Winkelabhängigkeit um 90 °. Dies lässt sich anhand der Abmessungen des Diamantsubstrats [86] erklären, da die Strahlung durch den Diamant für Winkel $> 90\,^{\circ}$ teilweise abgeschirmt wird und somit nicht mehr das sensitive Volumen erreichen kann [28, 87]. Da der microDiamond nicht zylindersymmetrisch aufgebaut ist, führten weitere Detektorbauteile bei sehr großen Winkeln $> 95\,^{\circ}$ zu einer Abhängigkeit von der Ausrichtung um die eigene Achse, welche in der Literatur bestätigt wird [83, 88, 89].

IOP Publishing Phys. Med. Biol. 70 (2025) 115020 https://doi.org/10.1088/1361-6560/adda8c

Physics in Medicine & Biology

IPEM Institute of Physics and Engineering in Medicine

OPEN ACCESS

RECEIVED
12 February 2025

REVISED
6 May 2025

ACCEPTED FOR PUBLICATION
19 May 2025

PUBLISHED
2 June 2025

PAPER

Angular dependence of detector responses in high-energy brachytherapy

T Failing[1,*], R Behrens[2], F W Hensley[3], B Keil[1,4,5], T Schneider[2] and K Zink[1,5,6,7]

[1] Institute of Medical Physics and Radiation Protection (IMPS), TH Mittelhessen University of Applied Sciences, Gießen, Germany
[2] Physikalisch-Technische Bundesantstalt (PTB), Bundesallee 100, 38116 Braunschweig, Germany
[3] Department for Radiotherapy and Radiooncology, University Medical Center Heidelberg, Heidelberg, Germany
[4] Department for Diagnostic and Interventional Radiology, Philipps-University Marburg, Marburg, Germany
[5] LOEWE Research Cluster for Advanced Medical Physics in Imaging and Therapy (ADMIT), TH Mittelhessen University of Applied Sciences, Gießen, Germany
[6] Department for Radiotherapy and Radiooncology, University Medical Center Gießen-Marburg, Marburg, Germany
[7] Marburg Iontherapy Center (MIT), Marburg, Germany
[*] Author to whom any correspondence should be addressed.

E-mail: thomas.failing@lse.thm.de

Keywords: Monte Carlo simulations, EGSnrc, high-energy brachytherapy dosimetry, restricted cema, ionization chamber, diamond detector

Abstract

Objective. To characterize three small volume ionization chambers and a diamond detector concerning their angular dependent response under Ir-192 irradiation. *Approach.* Monte Carlo (MC) simulations as well as experimental measurements of the angular dependent response were performed at 10 cm distance in air. Further simulations under TG-43 conditions were performed at distances of 1, 3, 5 and 10 cm in water. The detectors were placed in relation to their reference points specified by the manufacturer and rotated relative to the beam axis. Results for the different setups were compared to investigate the influence of water and air as well as a distance dependence of the angular response. Detector specific properties such as dead volumes of ionization chambers or asymmetries were taken into account. *Main results.* The MC simulations in air could be experimentally verified. The detectors showed an angular dependence $<0.5\%$ for rotations $\leqslant 20°$, $\leqslant 35°$, $\leqslant 40°$ and $\leqslant 50°$ at distances of 1, 3, 5 and 10 cm in water, respectively. In air at 10 cm distance, the angular dependence exceeded 0.5% for rotations of 20° for the microDiamond and for 50° for the Semiflex and PinPoint. Here, the angular dependence of the A26 was $<0.5\%$ at all angles. The slope of the angular dependence increased with rotation from frontal alignment for all detectors. Variations of the detector angular dependent response caused by volume averaging were largest close to the source, i.e. up to 8% at 1 cm distance. High-Z materials in the vicinity of the sensitive volumes were an additional source of angular response variations amounting up to 4% independent of the distance. *Significance.* To the best of the authors' knowledge, this work is the first investigation of perturbation factors, also differential in energy, leading to angular dependent detector response in high-energy brachytherapy dosimetry. The results could be useful to estimate the angular dependent response when measuring complex dose rate distributions, for example multiple source positions or in a heterogeneous environment.

1. Introduction

While it is common practice in external beam radiotherapy to measure dose distributions with small detectors in a clinical water phantom, this approach is not widely used in brachytherapy. Both standards for this practice and complete data sets of correction factors of suitable detectors are lacking so that measurements are usually restricted to single points in the radiation field of a single source. A number of papers have been recently published in which beam quality correction factors have been determined in Ir-192 brachytherapy (Araki *et al* 2013, Chofor *et al* 2016, Kaveckyte *et al* 2017, Campos *et al* 2018, Rossi *et al* 2023,

Failing *et al* 2024, Thrapsanioti *et al* 2024). Such an approach is sufficient for the verification of calculations with the TG-43 formalism (Nath *et al* 1995, Rivard *et al* 2004) since here clinical dose rate distributions are calculated as a superposition of dose rate distributions from single sources in homogeneous water. The introduction of model-based dose calculation algorithms in brachytherapy now allows the calculation of realistic clinical situations including patient-specific heterogeneities. This has improved accuracy in clinical dose rate calculation (Zourari *et al* 2012). AAPM recommends experimental dose rate verification of calculation algorithms in high-energy brachytherapy (Li *et al* 2007). However, verification of such a clinical dose rate calculation often requires that dose rate from multiple sources at different positions is measured in the same setup. In a previous investigation of the beam quality correction factor in high energy brachytherapy, a strong dependence of the response of the detectors on their orientation towards the source was found (Failing *et al* 2024). This indicates that angular response of a detector irradiated from one or multiple angles may need to be corrected. Angular response may look different in the steep gradient and varying scatter radiation in water than in the usually documented situation at a large distance. The results of the present work are intended to assess a source-detector alignment specific response correction factor for verification of a clinical dose distribution with multiple source positions.

To date, there are no concrete data in the literature addressing the angular response in brachytherapy in detail. Although it is assumed that this effect is small for the microDiamond detector investigated here (Kaveckyte *et al* 2017), there are only studies in other energy ranges and setups, which are discussed in section 4.1.

When using calibrated detectors, any change in the measurement that additionally influences the response should be corrected. In contrast to external beam therapy, the radiation field in brachytherapy has a much steeper dose rate gradient and the energy spectrum in media shows significant softening with distance due to multiple scattering. Response changes due to such set up differences from calibration including detector angle were observed in the comparison of Ir-192 dosimetry in water with diamond and silicon based solid state detectors in brachytherapy (Rossi *et al* 2023). The work presented here investigates the angular dependent response of three small volume thimble ionization chambers and a diamond detector in water and air with Monte Carlo (MC) simulations as well as experimentally in air. MC simulations of the restricted cema[8] are used to analyze both the response changes caused by volume averaging (described by the perturbation factor p_{int}) and by in-scatter from detector materials (described by the perturbation factor p_{ext}) and their influence on angular response separately and differential in energy and thus to identify criteria for selection of a favorable detector design for dosimetry for high-energy brachytherapy. Since volume averaging and spectrum softening may vary considerably in the brachytherapy field, it makes sense to investigate the corresponding perturbation factors p_{int} and p_{ext} separately to determine the suitable detector for a specific measurement task.

The consideration of the specific shape of the dead volume of an ionization chamber is a young field of research (first proposed in Ross (2009) but still not considered in current reference dosimetry protocols (McEwen *et al* 2014, Andreo *et al* 2020)). However, so far no consensus data exist on dead volumes of ionization chambers. Although the published data are similar (PTW chamber 31010: (Cervantes *et al* 2020, Failing *et al* 2024); PTW chambers 31021 & 31022: (Cervantes *et al* 2020, Delfs *et al* 2021, Failing *et al* 2024)), they can still differ by several percent (PTW chamber 30013: (Pojtinger *et al* 2019) vs (Margaroni *et al* 2022); PTW chambers 31010, 31021 & 31022: (Cervantes *et al* 2020, Delfs *et al* 2021) vs (Margaroni *et al* 2022)), so that the consideration of the total air volume of the ionization chambers was also included in the studies for comparison purposes. The results are planned to serve as basis for a dosimetry protocol of the German Institute for Standardization (DIN) addressing clinical brachytherapy dosimetry.

2. Materials and methods

2.1. Detectors used in this study

Four detectors from two manufacturers, PTW Freiburg (Freiburg, Germany) and Standard Imaging (Branding Exradin; Middleton, Wisconsin, USA), were examined regarding the angular dependence of their response to irradiation with a Nucletron mHDR-v2r Ir-192 source (Safigholi *et al* 2023). The term 'sensitive volume' refers to all detector regions, where the energy deposition of ionizing radiation contributes to the measurement signal of the detector. In ionization chambers, 'cavity' refers to the full air volume (including dead volumes), while in the term 'sensitive volume', the dead volumes are excluded. Table 1 specifies some of their detector characteristics, taken from the manufacturer data, such as the nominal response, geometrical dimensions and construction materials surrounding the sensitive volumes. In pairwise comparison, the three

[8] Converted energy to secondary electrons and positrons per mass (Seltzer *et al* 2014).

Table 1. Detectors examined in this study. The nominal responses and geometrical dimensions are adopted from the manufacturers. The reference points are specified by the distance from the detector tip on the central axis. C denotes graphite (density 1.7 g cm^{-3}), C552 denotes an air-equivalent plastic (density 1.76 $^{g}/_{cm^3}$) and C* denotes diamond (density 3.53 $^{g}/_{cm^3}$).

Model Short name	PTW 31021 Semiflex	PTW 31022 PinPoint	Exradin A26 A26	PTW 60019 mDD
Type	Ion chamber	Ion chamber	Ion chamber	Diamond
Response/$^{nC}/_{Gy}$	2	0.4	0.5	1
reference point/mm	3.45	2.4	1.98	1
Cavity dimensions				
radius/mm	2.4	1.45	1.65	1.1
length/mm	4.8	2.9	2.85	0.001
Sensitive volume/cm^3	0.053	0.011	0.016	$\approx 3.8 \cdot 10^{-6}$
Surr. materials	Al, PMMA, C	Al, PMMA, C	C552	C*, epoxy

ionization chambers differ mainly in one criterion such as dimensions of the cavity volume (Semiflex vs PinPoint) or construction materials surrounding the cavity (PinPoint vs A26). The comparison of these detector pairs allows allocation of the impact of specific detector properties. Figure 1 shows radiographs of the detectors which emphasize the high-Z and dense components possibly responsible for perturbations. Dead volumes are observed in the air cavity of ionization chambers in the vicinity of the guard electrode (Butler *et al* 2015, Delfs *et al* 2021) influencing the chamber response (Miller *et al* 2016). The dead volumes of the ionization chambers are not shown here but were determined in a previous work (Failing *et al* 2024). Their boundaries run from the inner guard ring radii to the inner chamber walls, forming approximately a quarter torus in the air cavity of the chambers.

The microDiamond detector (mDD) has already proven to be suitable for brachytherapy dosimetry in recent studies (Kaveckyte *et al* 2017, Rossi *et al* 2020). There are experimental data of the mDD yielding a small directional dependence for megavoltage external beams and in contrast a pronounced directional dependence for low and medium energy x-rays (which are discussed in section 4.1). However, a corresponding investigation in high-energy brachytherapy (also including full scatter conditions) has so far not been published to date. The sensitive volume of the mDD is a disk of 2.2 mm diameter and $\approx 1\ \mu$m thickness below a circular metallic Schottky contact lying centrally on top of the front surface of the diamond substrate measuring 3 mm edge length and 0.3 mm thickness (Marinelli *et al* 2016). Although the sensitive volume is very small compared to the ionization chambers, a directional dependence may still be possible due to the steep dose rate gradient and the constructive design. Note that the mDD has no cylindrical symmetry because of lateral metal contacts next to the diamond chip.

2.2. Experimental setup

The measurements were performed at Physikalisch-Technische-Bundesanstalt (PTB), Working Group 6.34 'Dosimetry for Brachytherapy and Beta Radiation Protection'. Figure 2 depicts a photograph of the measurement setup (left) as well as a visualization of the measurement by the EGSnrc application `egs_view` with two clipping planes so that only $^{3}/_{4}$ of the collimator is visible. The mHDR-v2r Ir-192 source (Curium Netherlands B.V., on behalf of Nucletron B.V., an Elekta subsidiary, Veenendaal, The Netherlands) (Safigholi *et al* 2023) was placed in a plastic catheter, which was fixed inside a polymethyl methacrylate (PMMA) cylinder inserted in a lead collimator housing. The radiation hit the detectors, which were fixed on a rotating robot arm (model FS020N, Kawasaki Heavy Industries Ltd Minato, Tokyo, Japan), at a nominal distance of 10 cm in air. The position reproducibility of the robot arm is specified as 0.1 mm. The detectors were mounted on a holder made of polyether ether ketone and PMMA so that the robot was not irradiated by the collimated Ir-192 beam. The tips of the detectors were pointed at the source as the starting position. The detectors were rotated around their manufacturer-stated reference points from $-100°$ to $100°$ in steps of $5°$, where $0°$ corresponds to a frontal alignment to the source. Due to the comparatively large source-detector distance (SDD) of 10 cm (which could not be further reduced because of the rotating arm), the measured signal currents amounted to a maximum of ≈ 1.3 pA for the Semiflex. The other detectors yielded smaller currents corresponding to the nominal response as stated in table 1. Each measuring point was therefore determined from the mean value of 5 measurements so that the rotation from $-100°$ to $100°$ took about eight hours. Due to these time differences a decay correction for the Ir-192 source was applied which amounted up to 0.3%. The ionization chambers were corrected for the air density at the corresponding time of measurement. Despite careful positioning of the detectors, there was an asymmetry in the results in the order of at most 3% for the detectors between positive and negative rotation. MC simulations revealed that this asymmetry was due to sub-millimeter misalignments of the pivot point and detector reference point.

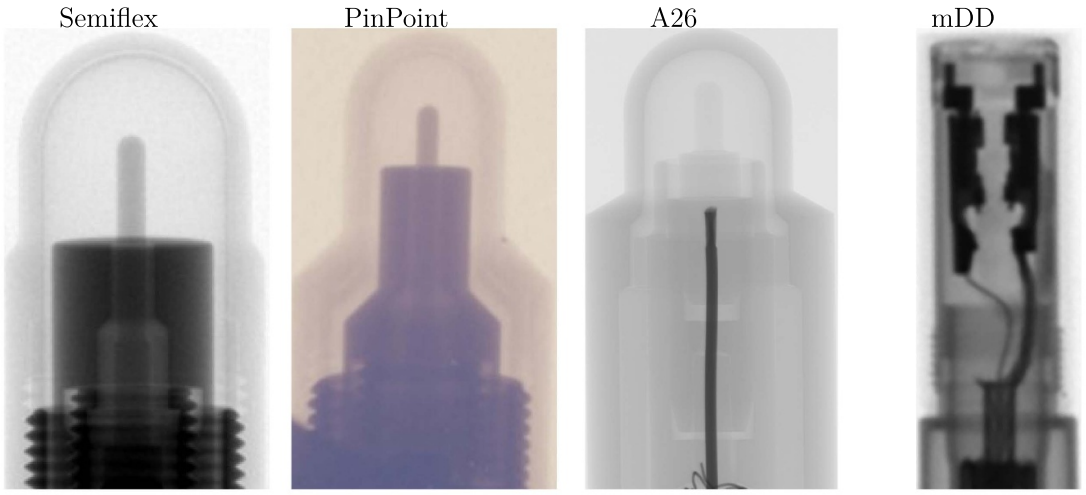

Figure 1. Radiographs of the detectors Semiflex (Cervantes *et al* 2020), PinPoint (Delfs *et al* 2021), A26 (Garcia Yip *et al* 2022) and mDD (Kampfer *et al* 2018). The guard rings of the ionization chambers can be seen as dense structures surrounding the central electrode. In the two PTW ionization chambers on the left-hand side, the guard ring is only faintly visible due to its high density. The dead volumes of the ionization chambers are not shown. Their boundaries run from the inner guard ring radii to the inner chamber walls, forming approximately a quarter torus in the air cavities. (far left) Reproduced from (Cervantes *et al* 2020) © IOP Publishing Ltd CC BY-NC-SA 3.0. (middle left) Reproduced from (Delfs *et al* 2021) CC BY 4.0. (middle right) Reproduced from (Garcia Yip *et al* 2022) © The Author(s). Published by IOP Publishing Ltd CC BY 4.0. (far right) Reprinted from (Kampfer *et al* 2018) *et al*, Copyright (2018), with permission from Elsevier.

More detailed information is given in the appendix. Also, the exact source position in the PMMA cylinder could, of course, not be verified by mechanical measurements. The response of each detector was corrected for its respective misalignment. The mDD was mounted in such way that the lateral metal contacts (shown on the radiograph in figure 1) were outside the rotational plane bisecting the source.

2.3. Monte Carlo calculations

Table 2 specifies the MC simulations that were performed with an in-house enhanced EGSnrc usercode `egs_chamber` (Failing *et al* 2022). The lower (total) charged particle cutoff energy (i.e. ECUT in EGSnrc) (Kawrakow *et al* 2001–2015) was set to the usual value for ionization chamber dosimetry of 521 keV (10 keV kinetic energy) which is justified by the comparatively high mean photon energies of ≈350 keV from the Ir-192 brachytherapy source (Brookhaven National Laboratory 2018). Comparative test simulations with an ECUT set to 512 keV (1 keV kinetic energy) yielded identical results. It was found that an additional photon cross section enhancement (XCSE) (Wulff *et al* 2008) shell surrounding the detectors did not further increase the simulation efficiency except for a point-like water voxel (which was used as the reference) with an edge length of 0.25 cm (Failing *et al* 2022). In general, an appropriate shell thickness that is smaller or equal to the maximum range of the electrons is recommended in order to avoid biasing the simulation results (Wulff *et al* 2008). For the maximum electron energies of ≈400 keV in this work, the CSDA range in water is ≈1 mm (Seltzer 1993) which is comparable to the detector walls. In addition, the omission of a XCSE shell for an immersed Ir-192 source was already validated in a previous study (Failing *et al* 2022). First, the experimental setup as described in section 2.2 was reconstructed including the fully modeled mHDR-v2r Ir-192 source. Additionally, the reference points of the detectors were also placed with small shifts (towards and laterally to the source) in the plane as shown in figure 2(right) to reconstruct the measured results. After determining the offset between reference point and rotation center in the in-air measurements, the ratios of the results with and without misalignment were used as a correction factor for the measured data in order to show the true angular dependence. More detailed information is given in the appendix.

Second, the angular response dependence was simulated under TG-43 conditions, i.e. the fully modeled mHDR-v2r Ir-192 source in a water environment, at the TG-43 reference point, i.e. 1 cm SDD in water, as well as at larger SDDs of 3, 5 and 10 cm. In the cylindrically symmetric setup, angular response was simulated from 0° (corresponding to a frontal alignment with the detector tip facing the source) to 100° in the plane bisecting the source center. As shown in figure 1 the design of the mDD is not cylindrically symmetric due to lateral metal contacts next to the diamond chip. Therefore, the simulations were performed with two orientations of the mDD. In the first orientation, the metal contacts were located in the rotational plane (as shown in the figure) so that they could cover the sensitive disc in very large rotations. In relation to the radiograph in figure 1, this corresponds to a source that is located in the paper plane above the

Table 2. Summary of the EGSnrc simulation parameters used in this study. According to good practice the recommendations of AAPM report TG-268 (Sechopoulos *et al* 2017) were followed.

Item	Description	Reference
Code, version	EGSnrc (v2021), enhanced `egs_chamber` code to generate outputs of absorbed dose, restricted cema and charged particle fluence differential in energy; `egs++` geometry package	Kawrakow *et al* (2001–2015, 2019) Walters *et al* (2021), Failing *et al* (2022)
Validation	Region-by-region Fano cavity tests; VRT biasing checks	Kawrakow (2000), Failing *et al* (2022, 2024)
Hardware & timing	Rocks Linux Computing Cluster with 1500 Intel® Xeon® CPUs; from ≈2 CPU hours / ion chamber position at 1 cm SDD to ≈115 CPU hours / mDD position at 10 cm SDD	
Source description	Tabulated isotropic Ir-192 spectrum in the active core of the fully modeled mHDR-v2r source	Baglin (2012), Pérez-Calatayud *et al* (2012), Safigholi *et al* (2023)
Cross sections	xcom photon cross sections. NIST ESTAR density effect corrections and mean excitation energies with ICRU 90 values where applicable. NIST bremsstrahlung cross sections	Seltzer (1987, 1993), Seltzer *et al* (2014)
Transport parameters	ECUT = AE = 521 keV PCUT = AP = 1 keV Photon cross section = xcom Bound Compton Scattering = On / norej Rayleigh scattering = On Atomic Relaxations = On / eadl Brems cross sections = NIST Boundary crossing algorithm = exact Electron step algorithm = EGSnrc / PRESTA-II ESTEPE = 0.25 All other parameters set to default	Kawrakow *et al* (2001–2015)
VRT	Photon cross section enhancement (XCSE): 512 or 1024, no extra XCSE shell except for small voxels with 0.25 cm; intermediate phase-space storage (IPSS)	Kawrakow *et al* (2001–2015), Wulff *et al* (2008), Failing *et al* (2022)
Scored quantities	Absorbed dose, restricted cema and charged particle fluence differential in energy with 5 keV bin width in small voxels, bare cavities and fully modeled detectors	Taylor and Rogers (2008), Wulff *et al* (2008)
statistical uncertainty	$<0.15\%(k=1)$ regarding the scored absorbed dose	
Statistical methods	History-by-history estimator	Walters *et al* (2002)
Post-processing	Smoothing of plots differential in energy by a moving average over 3 bins from (40–180) keV and over 6 bins for higher energies	

tip of the mDD, whereby the detector is rotated in the paper plane. The second orientation is selected so that the metal contacts are vertically above and below the plane of rotation. In relation to the radiograph in figure 1, the mDD would be rotated in or out of the paper plane. The same effect would also be achieved if the mDD is rotated 90° around its long axis and then rotated again in the paper plane. The main purpose of investigating the influence of the lateral contacts is to determine their importance as a source of uncertainty in certain scenarios. There are studies in which the mDD was irradiated from the side in a water phantom, which has the great advantage that it is possible to average measurements from two sides of the source. That leads to a further significant reduction in the overall uncertainties (Rossi *et al* 2020, 2023). However, this also increases the risk of the lateral contacts obscuring the primary radiation at certain positions, which justifies the investigation.

2.4. Perturbation factors based on restricted cema

According to ICRU Report 90 (Seltzer *et al* 2014), the restricted cema is calculated as

$$C_\Delta = \int_\Delta^\infty \Phi_E \, L_\Delta/\rho \, \mathrm{d}E + TE_\Delta \tag{1}$$

where Φ_E is the distribution of the total electron and positron fluence at energy E at a point in a medium, L_Δ/ρ is the corresponding restricted mass linear energy transfer and TE_Δ denotes the track end term representing the sum of the kinetic energy of all charged particles in the scoring volume with energies below a certain threshold energy Δ (10 keV in this work) (Failing *et al* 2024). The restricted cema formalism allows to deconstruct the absorbed dose and to describe perturbations due to detector components also differential in energy (Hartmann and Zink 2019, Hartmann *et al* 2020).

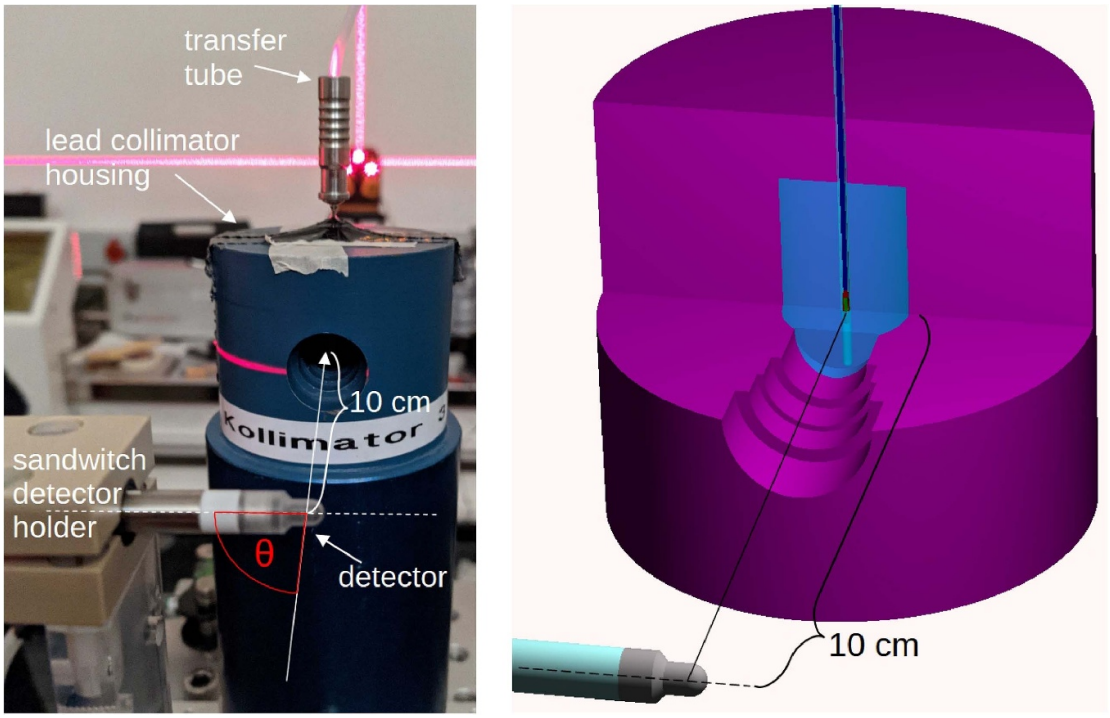

Figure 2. Left: Photograph of the measurement at PTB including the PinPoint ion chamber rotated by $\theta = -90°$ around its manufacturer-stated reference point (intersection point of dashed line and arrow) in the plane bisecting the source center. The angle is spanned between the detector long axis (dashed line) and the connecting line between the chamber reference point and the center of the source (arrow). Right: Visualization of the PTB measurement by the EGSnrc application `egs_view` with clipping planes so that only $^3/_4$ of the collimator is visible. Modeled here from the inside out of the collimator (visible in the left picture): the Ir 192 source (active volume in green) placed in a plastic catheter, fixed inside a PMMA cylinder (light blue) and then inserted in the lead collimator housing. The opening angle of the collimator is 20°. In the radiation field generated by this arrangement, the angular dependence of the detector responses is measured at a nominal distance of 10 cm in air.

The dose conversion factor $f = D_w/\bar{D}_{det}$, i.e. the ratio of absorbed point dose in undisturbed water, D_w, and mean absorbed dose in a detector at that point, $\bar{D}_{det}$, can be expressed by the *restricted cema approximation* (Hartmann *et al* 2021) which is the ratio of the corresponding restricted cemas $C_{\Delta,w}$ and $\bar{C}_{\Delta,det}$. With an additional factorization (Hartmann *et al* 2020) the dose conversion factor becomes

$$f \overset{!}{=} \frac{C_{\Delta,w}}{\bar{C}_{\Delta,det}} = s_{w,med} \cdot p_{int} \cdot p_{ext} \tag{2}$$

which is the product of the

- Spencer-Attix stopping power ratio $s_{w,med}$ of water ('w') and the detector medium 'med' (in this work air or diamond),
- internal perturbation factor $p_{ext} = \bar{C}_{\Delta,cav}/\bar{C}_{\Delta,cav}$, i.e. the ratio of the restricted cemas in a point-like ($C_{\Delta,med}$) and a bare detector cavity volume ($\bar{C}_{\Delta,cav}$) filled with the detector medium which therefore accounts for volume averaging effects and
- external perturbation factor $p_{ext} = \bar{C}_{\Delta,cav}/\bar{C}_{\Delta,det}$, i.e. the ratio of the mean restricted cemas in the cavities of the bare and the fully modeled detector which therefore accounts for perturbations due to the detector components.

3. Results

3.1. Measurement results

3.1.1. Uncertainty analysis

In order to estimate the significance of the verification measurements, the uncertainties in measurements and simulations were determined first. Exemplary for all detectors table 3 shows items of percentage uncertainties of type A or type B for the Semiflex which led to the total percentage uncertainty ($k = 1$) by summing in quadrature the single components. In the following, the items are discussed as shown in the order of table 3. As described in section 2.2 and the appendix small misalignments of the detectors in the

Table 3. Percentage uncertainties ($k = 1$) for the verification of the relative measurements in air as described in section 2.2 for the Semiflex ionization chamber. The total uncertainty is calculated by summing in quadrature the single components.

Item	Type	Uncertainty (%)
MC calculation	A	0.18
Det. geometry	B	0.14
Positioning	B	0.32
Decay correction	B	0
Air density corr.	B	0.1
Repeatability	B	0.41
Sum	total	0.58

sub-mm range were corrected by MC simulations (which yielded variations in the order of at most 3%) so that the measurements also contained statistical uncertainties of the corresponding MC simulations (here 0.18% for the Semiflex). Generally the uncertainty of a MC simulation consists of types A and B, but since type the B uncertainties in numerator and denominator are nearly equal they approximately cancel out in relative comparisons (Wulff *et al* 2010). The detector geometry uncertainty (caused by manufacturing tolerances or uncertainties of dead volumes) is the variation of detector response caused by small simulated geometric variations of single detector components near the sensitive volume as described in a previous work (Failing *et al* 2024). In that work, detector geometry variations caused the largest uncertainties when they altered the long dimensions of the ionization chambers' sensitive volumes such as variations of dead volume and guard ring. The new MC simulations confirmed the previous results although the measurement setup was in air and had a considerably larger SDD of 10 cm compared to 1 cm SDD in the previous work (Failing *et al* 2024). The variations of single detector components adopted from that work yielded a detector geometry uncertainty of 0.14% for the Semiflex. Although the misalignment of the detectors was subsequently corrected using MC simulations, it could not be ruled out that further positioning uncertainties remain. Therefore an additional positioning uncertainty of 0.3 mm was assumed leading to a combined uncertainty of 0.32%. The decay correction of the Ir-192 source was considered error-free. The uncertainty of the correction for varying air densities during the measurements amounted 0.1% and applied only for the ionization chambers. The influence of changing temperatures during the measurement was neglected because the temperatures were relatively constant (with ± 0.5 K) and therefore had no major influence. The largest uncertainty was identified in the repeatability of the measurement. Although the comparatively large SDD of 10 cm reduced the influence of geometric uncertainty, it also significantly decreased the measurement signal. The repeatability varied statistically matching the manufacturer-stated nominal response as stated in table 1 so that the smallest uncertainties were 0.41% for the Semiflex and grew up to 0.7% for the PinPoint. The total uncertainties ($k = 1$) were 0.58%, 0.81%, 0.72% and 0.64% for the Semiflex, PinPoint, A26 and mDD, respectively. An additional source of uncertainty may have been source movements during the measurement which took up to eight hours for each detector rotation. As shown in figure 2(right), the inner diameter of the plastic needle is 1.7 mm and the source diameter is 0.9 mm so that the maximum dose rate variation would be approximately 1.6% following the inverse square law. There was no mechanism to check this movement during the measurement but the following results do not indicate an abrupt change in the source position so that this uncertainty was neglected.

3.1.2. Experimental verification in air

Figure 3 shows the comparison of the angular dependence of the measured and simulated response for all detectors as well as their respective uncertainties ($k = 1$) under measuring conditions of 10 cm SDD in air specified in section 2.2 and figure 2. The measured data are shown after correction for misalignment of the detector reference points from the center of detector rotation as described in the appendix. The simulated data are calculated for correct positioning of the detector. The mDD showed the largest deviations from unity of up to -7% as compared to frontal alignment followed by the Semiflex and PinPoint with -4% whereas the A26 showed nearly no angular dependence. Almost all measurements confirmed the simulation results within their total uncertainty. Around $\pm 90°$ the mDD showed a very pronounced angular dependence so that individual outliers exceeding the uncertainty were observed. The mean absolute deviation between MC simulation and measurement of each detector was $\lessapprox 0.3\%$.

3.2. Simulation results

3.2.1. Angular dependence of the response in water

Figure 4 shows the angular dependence of the MC-calculated response of the detectors in water under TG-43 (i.e. full scatter) conditions at the TG-43 reference point, i.e. 1 cm SDD in water, and at larger distances of 3,

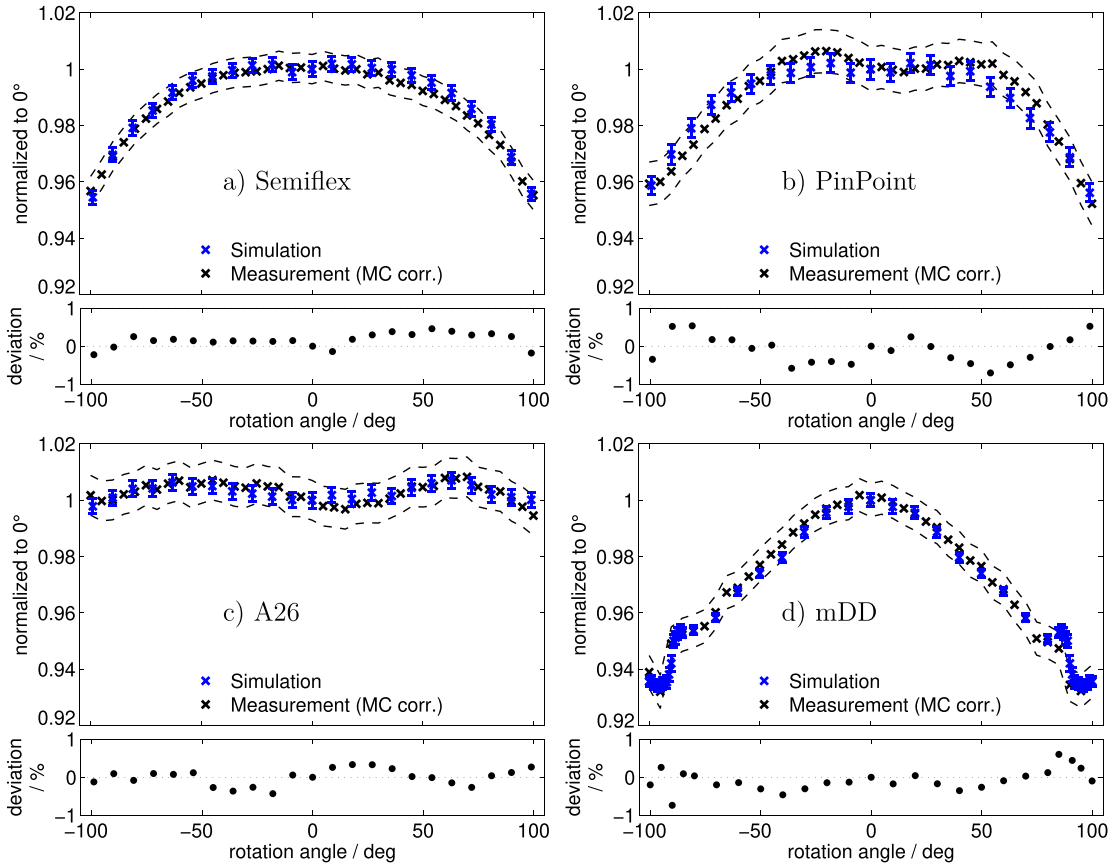

Figure 3. Comparison of the measured and simulated angular dependence of the response for the detectors (a) Semiflex, (b) PinPoint, (c) A26 and (d) mDD under measuring conditions of 10 cm SDD in air shown in figure 2. The measured data are shown after correction for misalignment of the detector reference points from the center of detector rotation as described in the appendix. The simulated data are calculated for correct positioning of the detector. The dashed lines show the total uncertainties of the measurements ($k = 1$).

5 and 10 cm. In the simulations of the ionization chambers, dose was scored either in the full air volume (circles) or in the sensitive volume (crosses) as already described in Failing *et al* (2024). The mDD was simulated in two orientations, i.e. with the metal contacts within the rotational plane (crosses) or outside (circles) by rotating the detector by 90° around its long axis (as described in section 2.3). The largest angular response dependencies, i.e. deviations from the frontal alignment at 0°, were observed at 1 cm SDD for all detectors and decreased with distance. For rotation angles $\lesssim$20° and all distances, all detectors showed less than 0.5% deviation from unity. Furthermore the impact of including the dead volumes to the scoring volumes of the ionization chambers decreased with distance. The increment of deviation of ion chamber response from frontal alignment increased with larger rotation angles. Although the Semiflex and PinPoint are of different size, their angular dependence curves became nearly equal for larger distance from the source. The angular dependence of the A26 decreased faster with larger distance than the Semiflex or PinPoint approaching nearly unity above 5 cm. For rotation angles up to 80° the mDD showed a similar angular dependence as the A26. From 85° to 95° the angular response of the mDD showed abrupt changes with a shift of up to -2%. Between 95° and 100° there was a difference of up to 1% for the two orientations of the mDD.

3.2.2. Perturbation factors p_{int} and p_{ext} in water

Figure 5 shows the simulated perturbation factors describing volume averaging, p_{int} (left column), and p_{ext} (right column) which describes the dose difference caused by construction materials of the detectors (as specified in section 2.4) at the TG-43 reference point as well as at 3 cm and 5 cm distance in water. In the simulations of the ionization chambers, dose was scored either in the full air volume (circles) or in the sensitive volume (crosses). For p_{ext} the mDD was simulated in the two orientations described (in section 2.3): with the metal contacts within the rotational plane (crosses) or outside (circles) by rotating the detector by 90° around its long axis.

Concerning volume averaging, the largest deviations of the perturbation factor p_{int} of up to 8% from frontal alignment at 0°, were observed at the TG-43 reference point and decreased considerably with

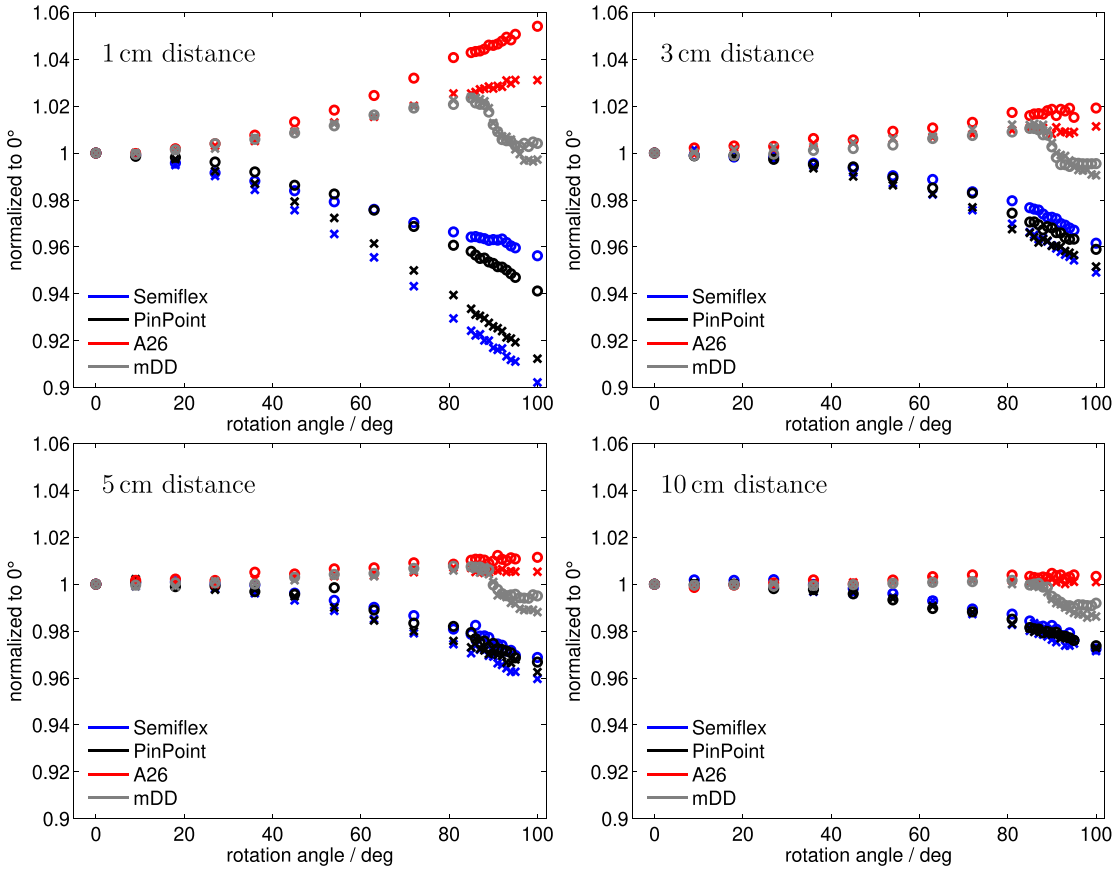

Figure 4. Simulated angular dependence of the detectors under TG-43 conditions at the TG-43 reference point, i.e. 1 cm SDD in water, and at larger distances of 3, 5 and 10 cm. Regarding the ionization chambers, dose was scored either in the full air volume (circles) or in the sensitive volume (crosses). The mDD was simulated in two orientations: with the metal contacts within the rotational plane (crosses) or outside (circles) by rotating the detector by 90° around its long axis. The statistical uncertainty was always below 0.15% and is, therefore, not shown for the sake of clearness.

distance. Furthermore the impact of considering the dead volumes decreased with distance. The slopes of the p_{int} curves of the ion chambers increased with increasing rotation from frontal alignment. Although the Semiflex and PinPoint are of different size, the angular dependence of their volume averaging factors became nearly equal with distance. The p_{int} curves for the Semiflex and PinPoint were always larger or equal to unity whereas those for the A26 and mDD were always smaller or equal to unity. Only at 1 cm SDD the angular dependence of p_{int} for the mDD had values deviating significantly from unity growing to a maximum of 1.5% around 90°. At 3 cm and 5 cm p_{int} for the mDD did not deviate from unity beyond the statistical uncertainty.

The factor p_{ext}, describing the dose difference in the detector's sensitive volume caused by its structure materials, showed the largest angular dependence for the Semiflex and PinPoint, where it increased up to 4% independent of distance from the source. The slope of angular dependence for these detectors increased with larger rotations. The A26 yielded nearly no angular dependence of p_{ext}. Excluding the dead volume from the cavity of the ionization chambers had a small effect of at most 1% for the Semiflex and PinPoint. Only the mDD showed angular dependence curves of p_{ext} smaller than unity with a minimum at 85°. At larger distances the minimum values approached unity. At rotation angles between 85° and 95° the mDD showed an abrupt change in angular dependence and shifted upwards by up to 2%. From 95° to 100° p_{ext} remained positive and diverged up to 1% based on the orientation of the mDD at all distances. Above a distance of 3 cm the external perturbation factors of the Semiflex and PinPoint exceeded the corresponding p_{int} values. The angular dependence of the A26 originated almost exclusively in changes of p_{int} while changes of p_{ext} were the nearly exclusive reason of angular dependence for the mDD.

4. Discussion

4.1. Comparison of the angular dependent responses

The following section compares the angular dependent response of the detectors in air, water and with the literature. Firstly, differences are to be expected between angular responses of the detectors in air and in water

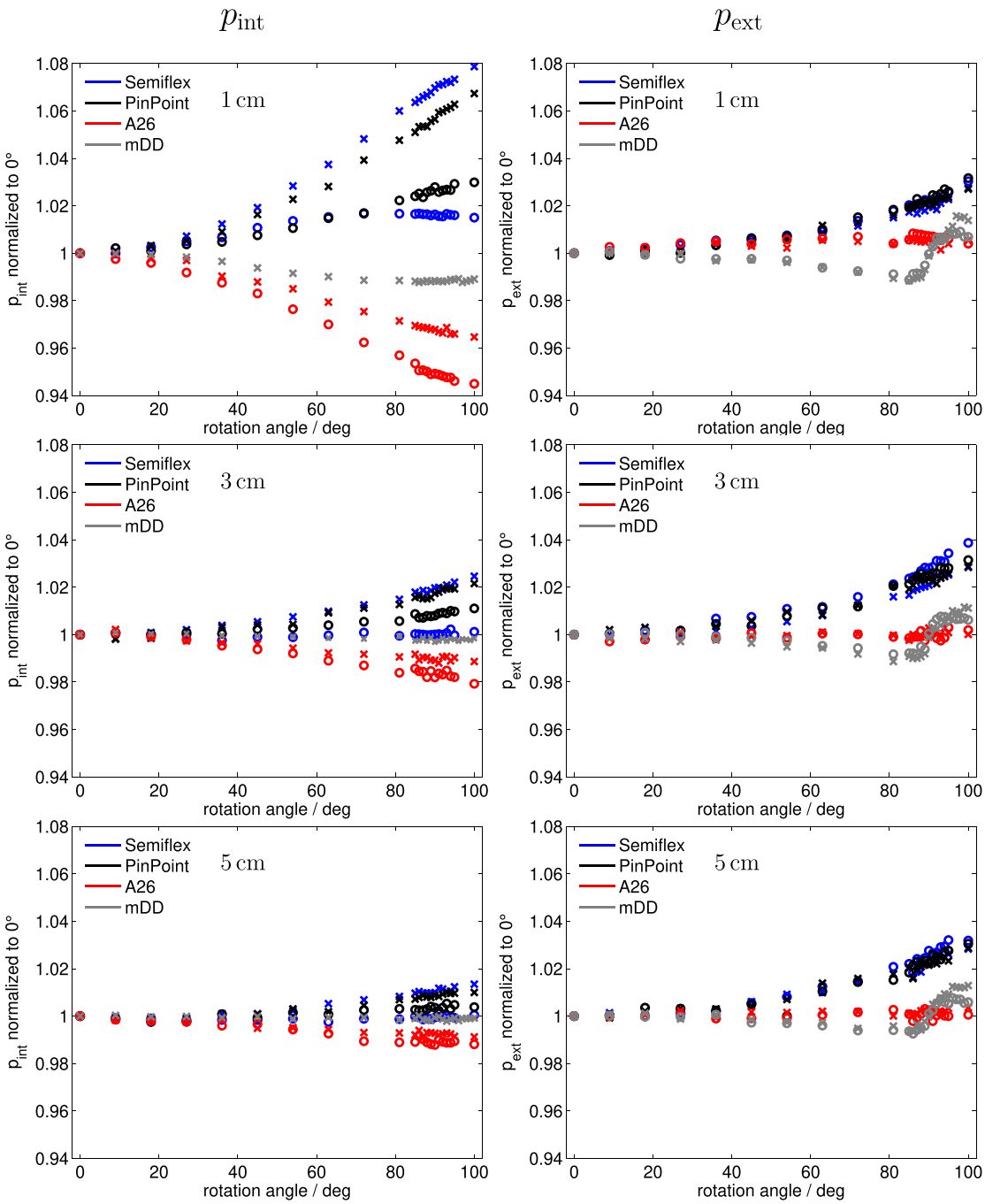

Figure 5. Simulated perturbation factors p_{int} (left column) and p_{ext} (right column) of the detectors as specified in section 2.4 at the TG-43 reference point as well as at 3 cm and 5 cm distance. Regarding the ionization chambers, dose was scored either in the full air volume (circles) or in the sensitive volume (crosses). For p_{ext} the mDD was simulated in two orientations: with the metal contacts within the rotational plane (crosses) or outside (circles) by rotating the detector by 90° around its long axis. The statistical uncertainty was always below 0.15% and is, therefore, not shown for the sake of clearness.

as shown in figures 3 and 4. As shown in Schoenfeld *et al* (2015), at 3.5 cm distance from a comparable Ir-192 high dose rate (HDR) brachytherapy source in water the absorbed dose rate to water from liberated electrons originates approximately in equal parts from primary and scattered photons whereas closer to the source, primary photons make larger contributions and farther away, scattered photons predominate. In the measurement setup at 10 cm SDD in air one can assume that the detector signal is produced almost entirely by electrons generated by primary photons moving away from the source. At 10 cm in water absorbed dose rate is mainly created by scatter radiation with a more isotropic angular distribution. More data on the composition of dose from primary and scattered radiation can be found in the CLRP TG-43 Parameter Database for Brachytherapy (Safigholi *et al* 2023). One can therefore expect less change in response when rotating the detector in water than in air. This difference was largest for the mDD, where the decrease of the cross section of the sensitive volume hit by primary radiation in air yielded a signal reduction to ≈0.93

Table 4. Overview of the angular dependent response of the mDD for different radiation qualities and setups compared to frontal alignment.

Source	Radiation quality	SDD/cm	Media	Response change (%)	
				at 45°	at 90°
Garcia Yip *et al* (2022)	50 kV	14.5	air	−15	−70
Kampfer *et al* (2018)	220 kV	35	air	−3	−20
this work	Ir-192	10	1 cm PMMA, air	−2	−6
this work	Ir-192	1	water	0.7	1
this work	Ir-192	3	water	0.3	0
this work	Ir-192	5	water	0	−0.2
this work	Ir-192	10	water	0	−0.7
Kawata *et al* (2023)	6 MV	100	air, 10 cm plastic	0	−0.1

between 0° and ±90° rotation. In water, at larger distances angular dependence almost disappeared. The effect could also be seen for the Semiflex and PinPoint where in water the reduction of response at large angles was ≈1% smaller than in air. In comparison, the angular dependence of the response of the A26 at 10 cm was small and almost independent of the surrounding medium because the chamber tip has a hemispherical shape and is uniformly made of C552.

Second, comparing detector response at different distances in water reveals a number of additional mechanisms causing angular dependence. As shown in figure 5, volume averaging in the sensitive cavity, described by p_{int}, changed stronger with distance than in-scatter contributions from detector components, described by p_{ext}. As already shown in a previous work (Failing *et al* 2024), the changes in volume averaging under rotation are caused by exposing different parts of the sensitive volume to different amounts of fluence in the steep and divergent beam gradient. This additionally depends on the position of the reference point around which the detector rotates. Both effects reduce with distance as the gradient decreases. Variation of response due to volume averaging was strongest for the cavities of Semiflex and PinPoint. The A26 cavity which has approximately the same geometric dimensions as the PinPoint cavity showed less variation of angular and distance response due to the position of its reference point which is located at the cavity center by the manufacturer. As seen for the Semiflex and PinPoint, variation of angular response must not always converge towards unity with distance due to persisting angular dependence of p_{ext} shown in the right column of figure 5. A detailed discussion for the Semiflex and mDD is given in section 4.2 with the additional information of the perturbation factors differential in energy.

Third, the findings of this work are compared with literature values. Table 4 shows the literature overview of the angular dependent response of the mDD for different radiation qualities and setups compared to frontal alignment. For energies up to Ir-192 there is a pronounced angular dependence in air which increases towards lower energies. For Ir-192 primary and increasing photon scatter radiation with distance the angular dependence decreased in the calculations of this work. At megavoltage photon beams mDD response may increase with rotation (Lárraga-Gutiérrez *et al* 2015). This behavior is also observed in a prototype of the mDD (Ciancaglioni *et al* 2012).

Concerning the other detectors, one previously cited work of Kawata *et al* (2023) states a negligible angular dependence for the PinPoint using 6 MV radiation and 100 cm SDD. The same is found by Garcia Yip *et al* (2022) for the A26 with 50 kV tube voltage and 14.5 cm SDD.

4.2. Perturbation factors differential in energy

In a previous study (Failing *et al* 2024) p_{int} and p_{ext} were already investigated differential in energy at 0° and 90° both at 1 cm and 3 cm SDD for the ionization chambers. That study yielded that the A26 showed nearly no energy dependence and that Semiflex and PinPoint created similar external perturbations. Therefore, regarding the ionization chambers, only p_{ext} of the Semiflex was investigated in this work. Figure 6 shows p_{ext} for the Semiflex, differential in energy, for rotation angles of 0°, 45°, 90° and 100° at 1 cm and 5 cm SDD. The curves belonging to rotation angles $\leqslant$90° showed an increase with energy (approaching unity) at both distances indicating a decrease of electrons scattered into the sensitive volume from structure materials. This is probably caused by the decrease of photoelectric absorption in aluminum with energy (Seltzer 1987) and energy losses of in-scattered electrons (Rogers 2020). Rotating the detector decreased the cross section of the guard ring (seen in the radiograph in figure 1) for primary radiation so that the number of photoelectrons scattered from aluminum into the cavity decreased and p_{ext} increased. At 5 cm, the amount of low energy scattered photons and consequently also low energy photoelectrons is larger, leading to lower values of p_{ext} at low energies. In total, p_{ext} varied in the range of 7% in the considered range of angle and energy. The angular dependence of differential p_{ext} was apparently largely averaged out when integrated over the complete Ir-192

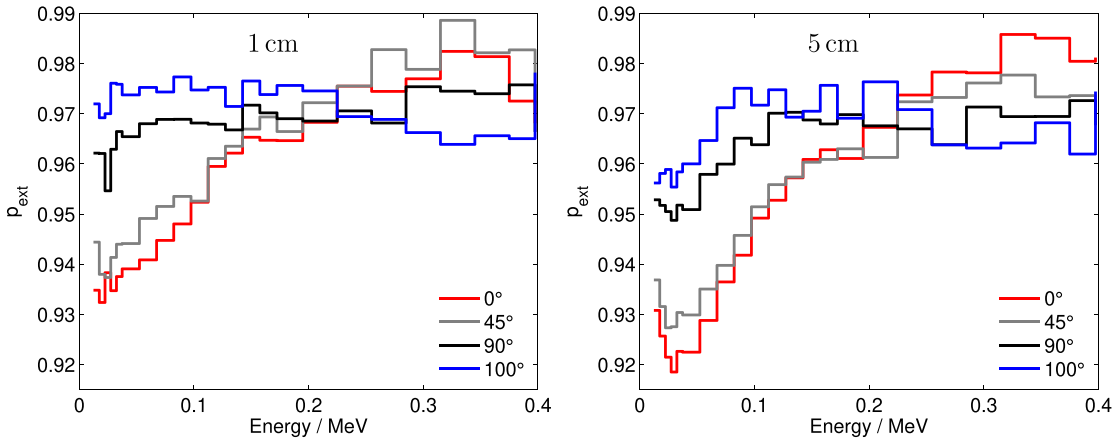

Figure 6. p_{ext} of the Semiflex differential in energy for rotation angles of 0°, 45°, 90° and 100° at 1 cm (left) and 5 cm (right) SDD.

spectrum yielding a smaller angular dependence $\lessapprox 4\%$ of the integrated factor shown in the right column of figure 5.

For the mDD, left column of figure 7 shows p_{int}, differential in energy, yielding nearly no energy dependence at any rotation angle apart from a certain shift of $\lessapprox 1.5\%$ with distance which is already visible in figure 5(left column, especially at 1 cm). This can be explained by volume averaging in the sensitive disc which further decreases as the dose rate gradient decreases with distance. The right column of figure 6 shows p_{ext} of the mDD, differential in energy, for rotation angles of 0°, 85°, 90° and 100° at 1 cm and 5 cm SDD. Two orientations are shown: with the metal contacts (dense parts seen aside the central diamond substrate in the radiograph in figure 1) in the rotational plane of the mDD (solid lines) and where the mDD is rotated 90° around the long axis so that the contacts are outside the plane (dashed lines). In total, p_{ext} varied $<2\%$ at each investigated angle in the considered energy range. Due to the extremely short electron ranges in diamond of e.g. <0.5 mm at 400 keV[9], practically no liberated electrons from outside the diamond substrate could reach the sensitive volume (Seltzer 1993) except for electrons from the epoxy resin detector housing where path lengths can be assumed similar to carbon. In a real detector, more energy dependent effects may be present, e.g. due to the density effect in the diamond crystal (Fernández-Varea *et al* 2021, Kaveckyte *et al* 2021) or due to in-scattered electrons from the Al Schottky and drain contacts and their connecting wires (Almaviva *et al* 2010), however, following the blueprint, these constructive details were not simulated in the MC calculations and could therefore not contribute to the results of this work. The angle and energy dependence seen in figure 7 must therefore have been caused by electrons produced in epoxy or diamond, whose primary photons may have been scattered anywhere in the detector. Since both media are approximately water equivalent, no pronounced energy dependence for p_{ext} is expected. Rotating the diamond chip in the beam between 0° and 85° caused an increase of in-scattered (Akbari 2023) and Compton (Klein and Nishina 1929) electrons and thus a decrease of the baselines of the energy curves. These increases are larger in mono-directional radiation than in more isotropic scatter, leading to larger shifts of the baseline at 1 cm and dilution at larger distance when the amount of scatter radiation increases. Above 85° rotation, the diamond substrate attenuated the primary beam and decreased the secondary electrons so that the curves increased, yielding values larger than unity from 90°. Only for very large rotations at 100° (discussed in section 4.3), the orientation of the mDD had an non-negligible impact shifting p_{ext} evenly in terms of energy.

4.3. Impact of the orientation of the microDiamond

In this study, the mDD was simulated in two orientations, as the lateral metal contacts (dense parts seen aside the central diamond disc in the radiograph in figure 1) depart the detector from cylindrical symmetry. As described in section 2.3, the first orientation refers to the metal contacts in the rotational plane of the mDD and the second orientation results from rotating the mDD 90° around the long axis so that the contacts are outside the plane. In figures 4, 5 and 7 these two orientations were used. Except for very large rotations $\gtrapprox 95°$ the impact of the orientation was negligible. Above 95° the orientation of the mDD response caused differences up to 1% in p_{ext} (seen in figure 5) which were visible also in the total angular response (seen in figure 4). At these large angles, the sensitive volume of the detector was covered by one of the lateral metal

[9] CSDA range for graphite using a density of $3.5\,{}^{g}/_{cm^3}$ for diamond (Seltzer 1993).

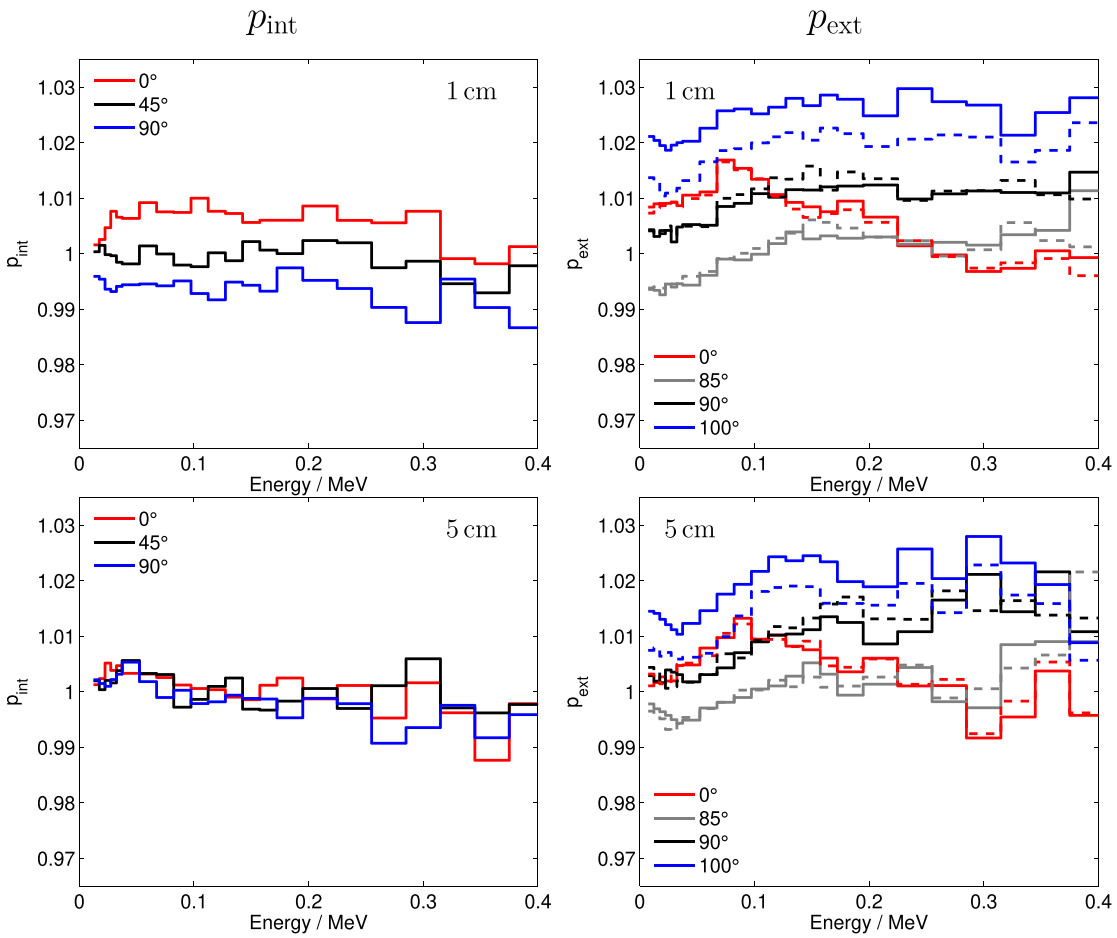

Figure 7. p_{int} (left column) and p_{ext} (right column) of the mDD differential in energy for selected rotation angles at SDDs of 1 cm (top row) and 5 cm (bottom row). Two orientations are shown: with the metal contacts in the rotational plane of the mDD (solid lines) and where the mDD is rotated 90° around the long axis so that the contacts are outside the plane (dashed lines).

contacts shown in the radiograph in figure 1. This was also seen in the works of Kampfer *et al* (2018), Shaw *et al* (2021) and Kawata *et al* (2023) in kilovoltage and megavoltage external beams impinging the mDD from the side.

4.4. Challenges, limitations and outlook

In this work, MC simulations were verified by measurements which were carried out with a rotating robotic arm. To fully cover the detector by the radiation field a minimal distance of 10 cm had to be chosen as SDD. The distance resulted in a very low signal current so that very long measurement times were necessary for noise suppression. In this setup, it was therefore only possible to position the detectors precisely to a very limited extent, e.g. by utilizing the symmetry of the measurement setup. Furthermore, no independent verification of the positioning was available, such as with of a very high-resolution optical camera. For these reasons, a MC based misalignment correction had to be applied in order to obtain meaningful results. This is a potential limitation of the presented work, given that MC and experimental results are not completely independent to each other. However, it is also important to emphasize that the misalignment correction is not an arbitrary adjustment of the data, since the course of the curve is correctly reproduced by the simulations and only small adjustments of the detector position were necessary to achieve a plausible distribution of angular response. Furthermore, correcting alone with the inverse square law is inaccurate, since, as shown in this work, directional dependence is also influenced by detector materials and construction.

The aim of this study is to provide usable data regarding the angular dependence of selected detectors for clinical application. Only a limited number of detectors could be examined for this purpose, but the ionization chambers and the mDD already cover a wide range of usable detectors available on the market.

Only one type of Ir-192 HDR source was examined here; similar behavior can generally be assumed for other Ir-192 sources as the detector response has shown to be nearly independent of parallel or crossed orientation to the source long axis at 1 cm SDD (Failing *et al* 2024).

In the introduction, an approach was cited determining the beam quality correction factor by the mean photon energy at the point of measurement (Chofor *et al* 2016). In a previous study it was found that there is a dependence on the orientation of the ionization chambers towards the source (Failing *et al* 2024). The results presented in this work determine the applicability of the approach for several detectors in water and air.

5. Conclusion

The angular dependent response of four different small detectors (Semiflex, PinPoint, A26 and microDiamond (mDD)) was simulated with MC calculations for irradiation with an Ir-192 brachytherapy source at 1, 3, 5 and 10 cm SSD in water and at 10 cm in air. The simulations in air using identical detector models as in water were experimentally verified with good accordance. The angular dependence of dosimeter response was much more pronounced in the directed radiation in air than in the more isotropic scatter radiation at larger depths in a phantom. In Ir-192 radiation in water, at short distances from the source, angular dependence was predominantly caused by different volume averaging in the sensitive volume at different polar angles in the steep and strongly divergent fluence gradient, described by the internal perturbation factor p_{int}. At larger distances, angular dependence did not completely disappear and was caused by in-scatter of electrons from detector components into the sensitive volume described by the external perturbation factor p_{ext}. For the investigated detectors and Ir-192 radiation in water angular dependence at small angles, as approximation, can possibly be neglected and taken into account as increased uncertainty. For the A26 and the mDD the region where this uncertainty remained below 1% extended up to ≈45°, for the PinPoint and Semiflex detectors with aluminum components up to ≈30°. Above 85°, the mDD showed an abrupt increase in angular dependence which was caused by attenuation of the radiation in the diamond substrate and lateral metal contacts. The complex behavior of photoelectric absorption, Compton scattering and electron scattering cause energy and angular dependence of the perturbation factors together with the steep dose rate gradient as well as distance-dependent changes of the photon spectra of brachytherapy sources in water largely prohibit the use of a constant dose conversion factor f in brachytherapy measurements. For accurate brachytherapy dosimetry this requires that f is determined separately at different positions, detector orientations, rotation angles and should be based on the sensitive volume (as already shown (Failing *et al* 2024)). Although the discussion of the mDD might be somewhat simplified since additional mechanisms may be present in a real detector, the calculation of dose rate correction factors for this detector can possibly be reduced to interactions in carbon and therefore simpler than for most other detectors. The small angular dependence below 85° reduces dose rate correction to mainly the stopping power ratio $s_{\mathrm{w,c}}$ of water to carbon. Therefore, the mDD (as already suggested (Kaveckyte *et al* 2017, Rossi *et al* 2020)) may be particularly suited as detector for brachytherapy dosimetry. If volume averaging is negligible (e.g. at larger distances from the source) or sufficiently taken into account, the A26 is also a good choice for brachytherapy dosimetry in both water and air. Its variation of angular response was smaller than that of the PinPoint although their cavity dimensions are approximately equal. Therefore a definition of the reference point at the center of the sensitive volume causes less angular dependence regarding p_{int}.

Data availability statement

All data that support the findings of this study are included within the article (and any supplementary information files).

Acknowledgments

The authors are very grateful for the technical support of F Grote and A Kasper (PTB, Braunschweig, Germany), who meticulously conducted the experimental work.

Declaration

This work is part of a dissertation project of Technische Hochschule Mittelhessen University of Applied Sciences at the Graduate Center of Engineering Sciences at the Research Campus of Central Hessen.

Appendix. Misalignment correction

As already stated in section 2.2, despite careful positioning there was an unexpected asymmetry in the results in the order of at most 3% for the detectors between positive and negative rotation. During troubleshooting,

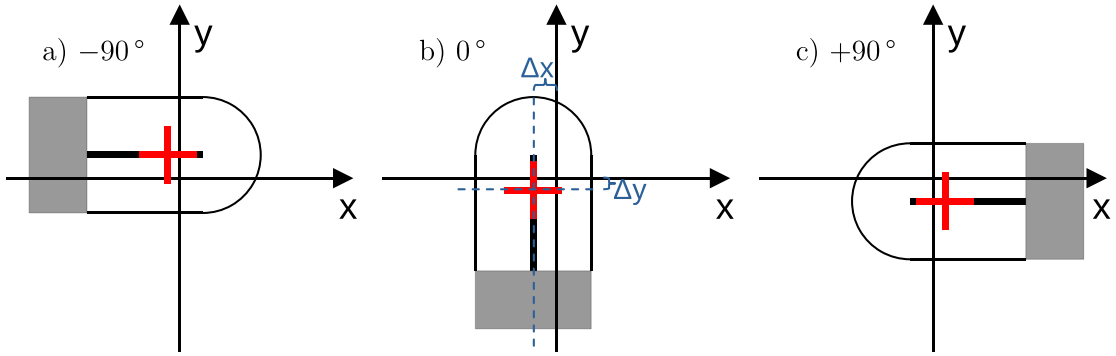

Figure A1. Schematic representation of the misalignments Δx and Δy (defined at 0°) of the detector's reference point (marked by the red cross) to the pivot point and their movement due to rotation during the measurement from (a) −90° to (b) 0° and (c) +90°. In this coordinate system, the source (not shown) is located at ($x = 0\,\text{cm}, y = 10\,\text{cm}$).

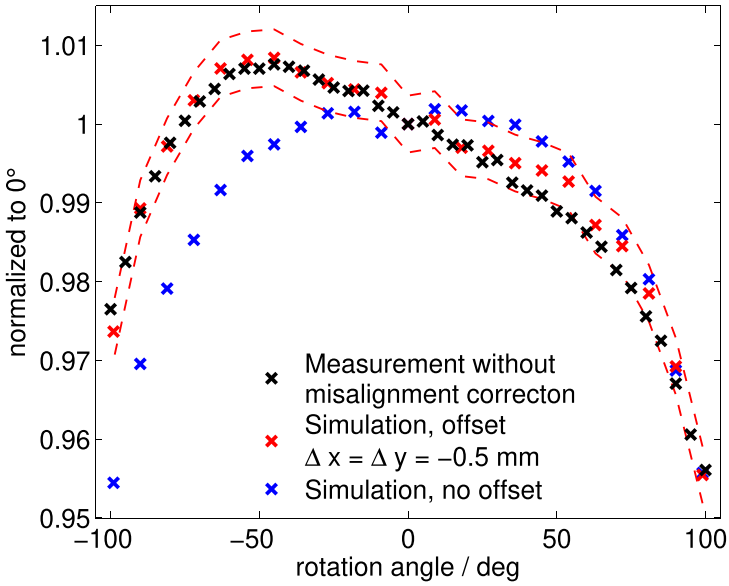

Figure A2. Comparison of the measured and simulated angular dependence of the response for the Semiflex under measuring conditions of 10 cm SDD in air as shown in figure 2 as well as with small misalignments shown in figure A1. The dashed lines show the statistical uncertainties ($k = 1$) of the simulations with offset.

a varying dark current or self-running of the electrometer could be ruled out, as the results were independent of the direction of rotation. Other influences such as air density fluctuations or radioactive decay were corrected. The source could be assumed to be at rest during the measurement as it was mechanically separated from the robot arm and the first measurement point could be reproduced exactly when a measurement run was completed. The repeatability of the robotic arm of 0.1 mm only played a minor role leading to a type B uncertainty of ≈0.2% following the inverse square law.

A possible explanation for the asymmetries and deviations of simulation results was investigated by introducing small shifts (towards and laterally to the source) of the detectors' reference points to the pivot point of the robot arm as shown in figure A1. As an example, figure A2 shows the results regarding the measured and MC simulated angular dependence of the response for the Semiflex under measuring conditions of 10 cm SDD in air as shown in figure 2 as well as with small misalignments shown in figure A1 with $\Delta x = \Delta y = -0.5$ mm. The small shifts were determined by searching for the minimum of the root mean square deviations of data points representing measurement and simulation. Shifts out of the rotational plane had nearly no effect on the angular dependence and were taken into account in the uncertainty budget. Intention of the measurements in air was the verification of the Monte Carlo calculations. Since this objective could be achieved by reproducing the misaligned measurements, an iterative correction of the alignment was abdicated. The corrected data are presented in the text body as illustration of the most probable angular response in air.

ORCID iDs

T Failing https://orcid.org/0000-0002-4554-7769
R Behrens https://orcid.org/0000-0002-4905-7791
F W Hensley https://orcid.org/0000-0003-1720-1821
B Keil https://orcid.org/0000-0003-0805-8330
T Schneider https://orcid.org/0000-0002-8342-6992
K Zink https://orcid.org/0000-0001-5785-4101

References

Akbari F 2023 A comprehensive open-access database of electron backscattering coefficients for energies ranging from 0.1 keV to 15 MeV *Med. Phys.* **50** 5920–9
Almaviva S *et al* 2010 Chemical vapor deposition diamond based multilayered radiation detector: Physical analysis of detection properties *J. Appl. Phys.* **107** 014511
Andreo P *et al* 2020 Determination of consensus k_Q values for megavoltage photon beams for the update of IAEA TRS-398 *Phys. Med. Biol.* **65** 095011
Araki F, Kouno T, Ohno T, Kakei K, Yoshiyama F and Kawamura S 2013 Measurement of absorbed dose-to-water for an HDR ^{192}Ir source with ionization chambers in a sandwich setup *Med. Phys.* **40** 092101
Baglin C M 2012 Nuclear data sheets for A = 192 *Nucl. Data Sheets* **113** 1871–2111
Brookhaven National Laboratory 2018 NUDAT 2.6 Interactive chart of nuclides (available at: www.nndc.bnl.gov/nudat2)
Butler D J, Stevenson A W, Wright T E, Harty P D, Lehmann J, Livingstone J and Crosbie J C 2015 High spatial resolution dosimetric response maps for radiotherapy ionization chambers measured using kilovoltage synchrotron radiation *Phys. Med. Biol.* **60** 8625–41
Campos L T, Magalhaes L A G and de Almeida C E V 2018 Determination of a beam quality conversion factor from ^{60}Co to ^{192}Ir *J. Radiat. Res. Appl. Sci.* **11** 249–54
Cervantes Y, Billas I, Shipley D, Duane S and Bouchard H 2020 Small-cavity chamber dose response in megavoltage photon beams coupled to magnetic fields *Phys. Med. Biol.* **65** 245008
Chofor N, Harder D, Selbach H-J and Poppe B 2016 The mean photon energy $\bar{E}_F$ at the point of measurement determines the detector-specific radiation quality correction factor $k_{Q,M}$ in ^{192}Ir brachytherapy dosimetry *Z. Med. Phys.* **26** 238–50
Ciancaglioni I, Marinelli M, Milani E, Prestopino G, Verona C, Verona-Rinati G, Consorti R, Petrucci A and De Notaristefani F 2012 Dosimetric characterization of a synthetic single crystal diamond detector in clinical radiation therapy small photon beams *Med. Phys.* **39** 4493–501
Delfs B *et al* 2021 The role of the construction and sensitive volume of compact ionization chambers on the magnetic field-dependent dose response *Med. Phys.* **48** 4572–85
Failing T, Hartmann G H, Hensley F W, Keil B and Zink K 2022 Enhancement of the EGSnrc code egs_chamber for fast fluence calculations of charged particles *Z. Med. Phys.* **32** 417–27
Failing T, Hensley F W, Keil B and Zink K 2024 Investigations on the beam quality correction factor for ionization chambers in high-energy brachytherapy dosimetry *Phys. Med. Biol.* **69** 165002
Fernández-Varea J M, Górka B and Nilsson B 2021 Electronic stopping power of diamond for electrons and positrons *Phys. Med. Biol.* **66** 165003
Garcia Yip F, Schneider T, Reginatto M, Behrens R, Buermann L and Grote F 2022 Characterization of small active detectors for electronic brachytherapy dosimetry *J. Instrum.* **17** 03001
Hartmann G H, Andreo P, Kapsch R-P and Zink K 2021 Cema-based formalism for the determination of absorbed dose for high-energy photon beams *Med. Phys.* **48** 7461–75
Hartmann G H, Hensley F W, Kapsch R-P, Poppe B, Sauer O, Würfel J and Zink K 2020 Ermittlung der Wasser-Energiedosis nach der Sondenmethode gemäß DIN 6800 Teil 1: Vorschlag für eine Erweiterung der Grundgleichung *Z. Med. Phys.* **30** 24–39
Hartmann G H and Zink K 2019 A Monte Carlo study on the PTW 60019 microDiamond detector *Med. Phys.* **46** 5159–72
Kampfer S, Cho N, Combs S E and Wilkens J J 2018 Dosimetric characterization of a single crystal diamond detector in x-ray beams for preclinical research *Z. Med. Phys.* **28** 303–9
Kaveckyte V, Malusek A, Benmakhlouf H, Carlsson G A and Tedgren Å C 2017 Suitability of microDiamond detectors for the determination of absorbed dose to water around high-dose-rate ^{192}Ir brachytherapy sources *Med. Phys.* **45** 429–37
Kaveckyte V, Tedgren Å C and Fernández-Varea J M 2021 Impact of the I-value of diamond on the energy deposition in different beam qualities *Phys. Med. Biol.* **66** 125004
Kawata K, Ono T, Hirashima H, Tsuruta Y, Fujimoto T, Nakamura M and Nakata M 2023 Effect of angular dependence for small-field dosimetry using seven different detectors *Med. Phys.* **50** 1274–89
Kawrakow I 2000 Accurate condensed history Monte Carlo simulation of electron transport. I. EGSnrc, the new EGS4 version *Med. Phys.* **27** 485–98
Kawrakow I *et al* 2019 EGSnrc C++ class library *Report* PIRS-898 (National Research Council of Canada) (available at: https://nrc-cnrc.github.io/EGSnrc/doc/pirs898/index.html)
Kawrakow I, Mainegra-Hing E, Rogers D W O, Tessier F and Walters B R B 2001–2015 The EGSnrc code system: Monte Carlo simulation of electron and photon transport *Report* PIRS-701 (National Research Council Canada) (available at: https://nrc-cnrc.github.io/EGSnrc/doc/pirs701-egsnrc.pdf)
Klein O and Nishina Y 1929 Über die Streuung von Strahlung durch freie Elektronen nach der neuen relativistischen Quantendynamik von Dirac *Z. Phys.* **52** 853–68
Lárraga-Gutiérrez J M, Ballesteros-Zebadúa P, Rodríguez-Ponce M, García-Garduño O A and de la Cruz O O G 2015 Properties of a commercial PTW-60019 synthetic diamond detector for the dosimetry of small radiotherapy beams *Phys. Med. Biol.* **60** 905–24
Li Z, Das R K, DeWerd L A, Ibbott G S, Meigooni A S, Pérez-Calatayud J, Rivard M J, Sloboda R S and Williamson J F 2007 Dosimetric prerequisites for routine clinical use of photon emitting brachytherapy sources with average energy higher than 50 keV *Med. Phys.* **34** 37–40

Margaroni V, Pappas E P, Episkopakis A, Pantelis E, Papagiannis P, Marinos N and Karaiskos P 2022 Dosimetry in 1.5 T MR-Linacs: Monte Carlo determination of magnetic field correction factors and investigation of the air gap effect *Med. Phys.* **50** 1132–48
Marinelli M, Prestopino G, Verona C and Verona-Rinati G 2016 Experimental determination of the PTW 60019 microDiamond dosimeter active area and volume *Med. Phys.* **43** 5205–12
McEwen M, DeWerd L, Ibbott G, Followill D, Rogers D W O, Seltzer S and Seuntjens J 2014 Addendum to the AAPM's TG-51 protocol for clinical reference dosimetry of high-energy photon beams *Med. Phys.* **41** 041501
Miller J R, Hooten B D, Micka J A and DeWerd L A 2016 Polarity effects and apparent ion recombination in microionization chambers *Med. Phys.* **43** 2141–52
Nath R, Anderson L L, Luxton G, Weaver K A, Williamson J F and Meigooni A S 1995 Dosimetry of interstitial brachytherapy sources: recommendations of the AAPM radiation therapy committee task group No. 43 *Med. Phys.* **22** 209–34
Pérez-Calatayud J *et al* 2012 Dose calculation for photon-emitting brachytherapy sources with average energy higher than 50 keV: report of the AAPM and ESTRO *Med. Phys.* **39** 2904–29
Pojtinger S, Kapsch R-P, Dohm O S and Thorwarth D 2019 A finite element method for the determination of the relative response of ionization chambers in MR-linacs: simulation and experimental validation up to 1.5 T *Phys. Med. Biol.* **64** 135011
Rivard M J, Coursey B M, DeWerd L A, Hanson W F, Huq S M, Ibbott G S, Mitch M G, Nath R and Williamson J F 2004 Update of AAPM task group No. 43 Report: a revised AAPM protocol for brachytherapy dose calculations *Med. Phys.* **31** 633–74
Rogers D W O 2020 On pathlength and energy straggling of megavoltage electrons slowing down *Phys. Medi.* **75** 40–43
Ross C K 2009 Comments on 'Ionization chamber volume determination and quality assurance using micro-CT imaging' *Phys. Med. Biol.* **54** 23–27
Rossi G, Failing T, Gainey M, Kollefrath M, Hensley F W, Zink K and Baltas D 2023 Determination of the dose rate around a HDR ^{192}Ir brachytherapy source with the microDiamond and the microSilicon detector *Z. Med. Phys.* **33** 463–78
Rossi G, Gainey M, Kollefrath M, Hofmann E and Baltas D 2020 Suitability of the microdiamond detector for experimental determination of the anisotropy function of high dose rate ^{192}Ir brachytherapy sources *Med. Phys.* **47** 5838–51
Safigholi H, Chamberland M J P, Taylor R E P, Martinov M P, Rogers D W O and Thomson R M 2023 Update of the CLRP Monte Carlo TG-43 parameter database for high-energy brachytherapy sources *Med. Phys.* **50** 1928–41
Schoenfeld A A, Harder D, Poppe B and Chofor N 2015 Water equivalent phantom materials for ^{192}Ir brachytherapy *Phys. Med. Biol.* **60** 9403–20
Sechopoulos I, Rogers D W O, Bazalova-Carter M, Bolch W E, Heath E C, McNitt-Gray M F, Sempau J and Williamson J F 2017 RECORDS: improved reporting of Monte Carlo radiation transport studies: report of the AAPM research committee task group 268 *Med. Phys.* **45** e1–e5
Seltzer S M 1987 XCOM-Photon Cross Sections Database, NIST Standard Reference Database 8 (https://doi.org/10.18434/T48G6X)
Seltzer S M 1993 Stopping-Powers and Range Tables for Electrons, Protons, and Helium Ions, NIST Standard Reference Database 124 (National Institute of Standards and Technology) (https://doi.org/10.18434/T4NC7P)
Seltzer S M, Fernández-Varea J M, Andreo P, Bergstorm P M, Burns D T, Krajcar Bronic I, Ross C K and Salvat F 2014 Report 90: key data for ionizing-radiation dosimetry: measurement standards and applications *J. Int. Comm. Radiat. Units Meas.* **14** 10–11
Shaw M *et al* 2021 Characterisation of a synthetic diamond detector for end-to-end dosimetry in stereotactic body radiotherapy and radiosurgery *Phys. Imaging Radiat. Oncol.* **20** 40–45
Taylor R E P and Rogers D W O 2008 An EGSnrc Monte Carlo-calculated database of TG-43 parameters *Med. Phys.* **35** 4228–41
Thrapsanioti Z, Peppa V, Hourdakis C J, Karaiskos P, Lekatou A and Pantelis E 2024 Beam quality correction factors for dose measurements around ^{192}Ir brachytherapy sources *J. Appl. Clin. Med. Phys.* **26** e14575
Walters B R B, Kawrakow I and Rogers D W O 2002 History by history statistical estimators in the BEAM code system *Med. Phys.* **29** 2745–52
Walters B, Kawrakow I and Rogers D W O 2021 DOSXYZnrc users manual *Report* PIRS-794 (National Research Council of Canada) (available at: https://nrc-cnrc.github.io/EGSnrc/doc/pirs794-dosxyznrc.pdf)
Wulff J, Heverhagen J T and Zink K 2008 Monte-Carlo-based perturbation and beam quality correction factors for thimble ionization chambers in high-energy photon beams *Phys. Med. Biol.* **53** 2823
Wulff J, Heverhagen J T, Zink K and Kawrakow I 2010 Investigation of systematic uncertainties in Monte Carlo-calculated beam quality correction factors *Phys. Med. Biol.* **55** 4481–93
Wulff J, Zink K and Kawrakow I 2008 Efficiency improvements for ion chamber calculations in high energy photon beams *Med. Phys.* **35** 1328–36
Zourari K, Pantelis E, Moutsatsos A, Sakelliou L, Georgiou E, Karaiskos P and Papagiannis P 2012 Dosimetric accuracy of a deterministic radiation transport based ^{192}Ir brachytherapy treatment planning system. Part III. Comparison to Monte Carlo simulation in voxelized anatomical computational models *Med. Phys.* **40** 011712

5 Diskussion

5.1 Dosimetrieformalismus basierend auf der beschränkten Cema

Für diese Arbeit wurde in Kapitel 3 ein Dosimetrieformalismus vorgestellt, bei dem die Korrektion aufgrund abweichender Strahlungsqualität, k_Q aus Gleichung 2.12, auf den Verhältnissen der beschränkten Cema unter Kalibrier- und Messbedingungen beruht. Dafür wird Gleichung 3.2 sowohl unter Mess- als auch Kalibrierbedingungen angewandt, um die absorbierte Dosis zu ersetzen. Neben der Anwendbarkeit ermöglicht die beschränkte Cema mit Gleichung 2.8 eine energiedifferentielle Betrachtung der absorbierten Beiträge von Ladungsträgern im betrachteten Volumen. Aufgrund des starken Anstiegs des LET zu niedrigen Energien der Ladungsträger stammt der Großteil der Signalbeiträge aus den niedrigsten Energiebereichen; dies gilt unabhängig von der Strahlungsqualität der Photonen [82]. Die energiedifferentielle beschränkte Cema bietet eine anschauliche Möglichkeit zur Optimierung des Detektordesigns, um Störungen gegenüber der beschränkten Cema in Wasser zu minimieren. Aufgrund der Vielfachstreuung in Brachytherapiefeldern verringert sich die mittlere Energie der Strahlung im Vergleich zur perkutanen Strahlentherapie [90] signifikant mit dem Abstand [16], so dass die Energieabhängigkeit des Detektoransprechvermögens hier noch bedeutsamer ist. Nach Gleichung 3.2 kann der Konversionsfaktor f in den rein materialabhängigen Faktor $s_{w,\mathrm{med}}$, den internen Störungfaktor p_{int} basierend auf Volumenmittelungseffekten sowie den externen Störungsfaktor p_{ext}, welcher alle Störungen durch Detektorbauteile beinhaltet, aufgeteilt werden. In den Untersuchungen dieser Arbeit konnte fast keine Energieabhängigkeit bei p_{int} beobachtet werden, außer bei frontaler Ausrichtung der Ionisationskammern [61, 91], welche in Abb. 3.1 dargestellt ist. Die Energieabhängigkeit des Störungsfaktors p_{ext} setzt sich aus mehreren Faktoren zusammen. Wie in Abschnitt 2.2.7 gezeigt, führen die Bauteile eines Detektors im Vergleich zum bloßen Detektorvolumen zu abweichenden Wirkungsquerschnitten. Insbesondere der Photoeffekt weist eine starke Abhängigkeit von der Energie der absorbierten Photonen und der Ordnungszahl des Absorbers auf (siehe Abb. 2.1). Auch wenn die Reichweite der freigesetzten Elektronen im hier untersuchten Energiebereich klein ist [28], können diese eine zusätzliche Störung durch Hereinstreuen in das sensitive Volumen darstellen [92]. Dieser Effekt ist ebenfalls material- und energieabhängig. Zusammenfassend bilden hoch-Z Materialien sowie hohe Massendichten von Detektorbauteilen die Grundlage zur Energieabhängigkeit von p_{ext}. Eine frontale Ausrichtung der Ionisationskammern begünstigt diesen Effekt, so dass Aluminium Schutzringe maximal zur Störung beitragen können [61, 91].

5.2 Vergleich der Strahlungsqualitäts-Korrektionsfaktoren

In Tabelle 5.1 ist ein Literaturvergleich zur Validierung der in dieser Arbeit ermittelten Werte von k_Q bei Abständen von 1 und 3 cm gezeigt. Für einen möglichst aussagekräftigen Vergleich sollte die Ausrichtung der Detektoren, deren Positionierung sowie die Definition des sensitiven Volumens der Ionisationskammern berücksichtigt werden. Eine parallele oder gekreuzte Ausrichtung der Detektorachse zur Quellenachse erwies sich dabei innerhalb der ermittelten Fehler als äquivalent [61], so dass im Folgenden zur besseren Übersichtlichkeit nur zwischen einer frontalen und seitlichen Ausrichtung der Detektoren unterschieden wird. Alle Detektoren sind bezüglich ihres von der Herstellungsfirma festgelegten Referenzpunkts positioniert. Bei allen Literaturwerten wird die gesamte Luftkavität der Ionisationskammern als sensitives Volumen definiert, woraufhin auch hier nur die entsprechenden Werte dieser Arbeit gezeigt sind. Für alle Simulationen wird der MC Code EGSnrc genutzt (bis auf eine Ausnahme: PENELOPE/penEasy [10]). Die Fehlerangabe in Klammern setzt sich aus der kombinierten statistischen Unsicherheit ($k = 1$) der zugehörigen MC Simulationen zusammen und wirkt sich auf die letzte angegebene Ziffer aus.
Es zeigt sich eine gute Übereinstimmung der ermittelten Werte von k_Q und vergleichbaren Literaturwerten für die Detektoren PTW 31021, PTW 31023 und microDiamond durch die Überlappung der jeweiligen Fehlerbereiche. Die Werte der Detektoren PTW 31010 und microDiamond beruhen auf jeweils vier unabhängigen Quellen. Deren maximale Abweichung vom Mittelwert beträgt 1,2 % für PTW 31010 bei 1 cm Abstand sowie 0,8 % für den microDiamond bei 3 cm Abstand. Die Ursache für Abweichungen der Daten können sehr vielfältig sein. Neben unterschiedlichen Wirkungsquerschnitten, Transportparametern und Materialdefinitionen in den verschiedenen MC Simulationen spielt die Modellierung der Detektorgeometrien innerhalb des steilen Dosisgradienten der Brachytherapie eine viele größere Rolle als in der perkutanen Strahlentherapie. Analog zur Bestimmung der Konsens-Daten von k_Q in der perkutanen Strahlentherapie könnte die Homogenität der MC Simulationen mithilfe eines standardisierten Detektors verifiziert werden [60]. Für die Bestimmung der Konsens-Werte des Dosimetrieprotokolls TRS-398 wurden dort pro Ionisationskammer zwischen zehn und bis zu 126 Datenpunkte aus MC Simulationen sowie in den meisten Fällen auch experimentelle Werte berücksichtigt. Dies deutet darauf hin, dass die Datenlage für aussagekräftige Werte bezüglich k_Q in der Brachytherapie weiter ausgebaut werden muss. Zudem sollte bei der Publikation von entsprechenden Daten die Bestrahlungsgeometrie, das Strahlungsspektrum sowie die verwendeten MC Parameter [93] gut dokumentiert sein.

5.3 Vergleich der Unsicherheiten bei der Bestimmung von $\dot{D}_w$

Die Unsicherheit bei der Bestimmung der Luftkermastärke S_k von hochenergetischen HDR Quellen mithilfe von auf Primärnormale rückführbar kalibrierte Schachtionisationskammern beträgt nach dem gemeinsamen Report der AAPM Task Group No. 138

Tabelle 5.1: Literaturvergleich zur Validierung der in dieser Arbeit ermittelten k_Q-Werte bei Abständen von 1 und 3 cm. Die Fehlerangabe in Klammern setzt sich aus der kombinierten statistischen Unsicherheit ($k = 1$) der zugehörigen MC Simulationen zusammen und wirkt sich auf die letzte angegebene Ziffer aus. Die Werte für Ionisationskammern beinhalten als sensitives Volumen die gesamte Luftkavität.

		k_Q				
		1 cm		3 cm		
Detektor	Ausrichtung	Diese Arbeit	Literaturwert	Diese Arbeit	Literaturwert	Quelle
PTW 31010	seitlich	1.010(2)	0.998(2)	1.001(2)	1.002(2)	[13]
	?		0.996(6)		0.995(6)	[16]
	?		0.988(2)		0.995(2)	[14]
PTW 31021	seitlich	0.965(2)	0.967(2)	0.975(2)	0.978(2)	[18]
PTW 31022	seitlich	0.982(3)	0.993(3)[a]	0.980(3)	1.000(3)[a]	[13]
PTW 31023	seitlich	1.015(3)	1.013(3)[a]	0.988(3)	0.994(3)[a]	[13]
mDD	frontal	1.001(6)	0.997(2)	0.997(7)	0.998(3)	[13]
	frontal		—		1.006(7)[b]	[10]
	?		0.996(6)[a]		0.994(6)[a]	[16]

[a] Vorgängermodell mit fast identischer Simulationsgeometrie
[b] interpoliert, Originalwert 1,005(7) bei 2,5 cm Abstand

und GEC-ESTRO 1,5 % [48] und nach einer aktuelleren Analyse des BIPM und der PTB 1,01 % [94] (beide $k = 2$). Für die Dosisleistungskonstante Λ wurde von der AAPM und ESTRO eine Unsicherheit von 1 % ($k = 1$) bei der Bestimmung von Konsensdaten festgelegt [47]. Daraus ergibt sich nach Gleichung 2.10 des TG-43 Formalismus eine Gesamtunsicherheit der absorbierten Wasser-Energiedosisleistung am TG-43 Referenzpunkt ($r_0 = 1\,\mathrm{cm}, \theta_0 = 90\,^\circ$) von 1,12 % ($k = 1$), welche sich aus den Quadraten der Einzelwerte berechnet. Dieser Wert soll im Folgenden als Benchmark dienen.
Aktuelle Studien beziffern die Gesamtunsicherheit bei experimenteller Bestimmung der absorbierten Wasser-Energiedosisleistung mithilfe von auf die absorbierte Wasser-Energiedosis kalibrierten microDiamond Detektoren mit 1,9 bis 4,3 % bei Abständen zwischen 1,5 und 5,5 cm und $\theta = 90\,^\circ$ [10] sowie 3,0 bis 6,0 % bei Abständen zwischen 1 und 5 cm und Winkeln von 0 bis zu 168 ° [12, 95] (beide $k = 2$).
Die in dieser Arbeit ermittelten Gesamtunsicherheiten bei Messungen von $\dot{D}_w(r_0, \theta_0)$ betrugen mit Ionisationskammern zwischen 1,8 und 2,4 % ($k = 1$) je nach Unsicherheitsbeitrag der Positionierung, Kalibrierung, Reproduzierbarkeit, materiellen Zusammensetzung, Detektorgeometrie sowie Ausrichtung zur Quelle [61], was in guter Übereinstimmung zu den vorher genannten Arbeiten steht. Dabei erwies sich eine parallele Ausrichtung von Detektor und Quellenachse am günstigsten, da so der Einfluss der Exemplarstreuung[1] und die Varianz der Messwerte für alle Ionisationskammern am geringsten waren. Für letztere war es messtechnisch möglich, über mehrere Messpunkte mit gleicher angenommener Dosisleistung zu mitteln. Bei den Messungen am TG-43 Referenzpunkt trugen die Unsicherheiten bezüglich der Positionierungen von Detektor und Quelle am meisten zur Gesamtunsicherheit bei. Die Positionsunsicherheiten können durch Messungen in größeren Abständen reduziert werden, wodurch eine Positionsunsicherheit von 0,1 mm nach dem Abstandsquadratgesetz nur noch zu einer Unsicherheit von 0,39 % bei 3 cm beiträgt. Dadurch würde sich die Gesamtunsicherheit auf $\approx 1{,}0\,\%$ reduzieren, wenn alle sonstigen Unsicherheiten näherungsweise konstant angenommen werden. Damit ist es möglich, die Unsicherheit bei der Messung von $\dot{D}_w$ mit klinischem Equipment gegenüber dem TG-43 Formalismus zu reduzieren. Zum Vergleich beträgt die Standardunsicherheit bei der direkten Messung der absorbierten Wasser-Energiedosis mithilfe der Wasserkalorimetrie 0,9 % an einem Versuchsaufbau der PTB [96].
Bei der Bestimmung von $\dot{D}_w$ mit klinischem Equipment führt ein kleines sensitives Volumen unter Referenz-ähnlichen Bedingungen nicht zwingend zu kleineren Unsicherheiten, da die erwähnte Exemplarstreuung stärker ins Gewicht fällt und beispielsweise für den microDiamond Detektor sogar 2 % ($k = 2$) angenommen wird [12]. Des Weiteren wurden kleinere Varianzen der Messwerte für größere Ionisationskammern beobachtet, was sich anhand eines größeren Signal-Rausch-Verhältnisses erklären lässt. Volumenmittelungseffekte werden zwar in k_Q berücksichtigt, jedoch unter der Annahme, dass die Effizienz der Ladungsträgersammlung über das sensitive Volumen konstant ist. Ein zugehöriger Effekt wie die Ionenrekombination wird in aktuellen Dosimetrieprotokollen zur Referenzdosimetrie von externen Bestrahlungsfeldern berücksichtigt, allerdings ist der Einfluss

[1] Diese wurde in dieser Arbeit aus MC simulierten geometrischen Variationen einzelner Detektorbauteile bestimmt.

dieser Störung dort vergleichsweise klein [2]. Im steilen Dosisgradienten eines Brachytherapiefeldes könnten diese Störungen indes größer sein, da zum Beispiel eine Abhängigkeit von der Kammergeometrie beobachtet wird [97]. Daraus lässt sich ein weiteres Argument für die parallele Ausrichtung von Quellen- und Ionisationskammerachse ableiten, da die Ionisationskammern auch so kalibriert sind.

5.4 Praktische Relevanz

Die Einführung des neuartigen dosimetrischen Formalismus in der Dosimetrie für Anwendungen in der Brachytherapie hat den Vorteil der direkten Messung der absorbierten Wasser-Energiedosisleistung unter definierten Referenzbedingungen ohne den Umweg über die Messung der Luftkermastärke und nachfolgender Überführung zur absorbierten Wasser-Energiedosisleistung. Aktuell geschieht die klinische Messung der Dosisleistung eines Afterloadingstrahlers üblicherweise anhand der Luftkermastärke mithilfe einer kalibrierten Schachtionisationskammer [5]. Dieses Verfahren hat sich aufgrund seiner Robustheit gegenüber der Positionierung der Afterloadingquelle in der Schachtionisationskammer etabliert. Die in dieser Arbeit durchgeführten Messungen nach Gleichung 3.1 in einem Wasserphantom können zu einer kleineren Gesamtunsicherheit von $\dot{D}_w$ gegenüber der Bestimmung anhand des TG-43 Formalismus führen (siehe Abschnitt 5.3), jedoch erweist sich diese Messung als vergleichsweise aufwendig und damit unpraktisch für den klinischen Alltag, um lediglich die absorbierte Wasser-Energiedosisleistung unter Referenzbedingungen zur Qualitätssicherung zu bestimmen. Alternativ könnte dies mithilfe einer geeigneten Detektor-Phantom-Anordnung aus beispielsweise drei auf die absorbierte Wasser-Energiedosis kalibrierten Detektoren in einem wasseräquivalenten Festkörperphantom realisiert werden. Aus dem Verhältnis der Ansprechvermögen ließe sich die dreidimensionale Position des Strahlers ermitteln, um damit auch kleine Positionierungsunsicherheiten im Applikator zu korrigieren. Diese Methodik wurde bereits in ähnlicher Form mit zwei Ionisationskammern durchgeführt [14, 15]. Die Verwendung des Wasserphantoms, insbesondere nach Positionierung des Detektors über Profilmessungen entlang der Raumrichtungen um die Quelle, eignet sich aufgrund der vergleichsweise kleinen Unsicherheit zur Messung der Dosisleistungsverteilung eines Strahlertyps [12, 61, 95]. Innerhalb definierter Bestrahlungsgeometrien und adäquater Korrektion des Ansprechvermögens kann ein größeres Detektorvolumen sinnvoll sein, um Unsicherheiten durch Signalrauschen und Exemplarstreuung zu minimieren. Bei der Verwendung einer Ionisationskammer sollte zudem auf eine seitliche Ausrichtung zur Quelle geachtet werden, so dass geometrische Unsicherheiten des Totvolumens im steilen Dosisgradienten weniger ins Gewicht fallen.

Für Messungen mit vielen Strahlerpositionen, wie etwa bei der Verifikation einer klinischen Dosisleistungsverteilung, kann die Korrektion des Detektoransprechvermögens jeder einzelnen Quellen-Detektor-Anordnung sehr aufwendig sein, so dass neben der Korrektion aufgrund geänderter Strahlungsqualität zusätzlich die Winkelabhängigkeit

in einem definierten Szenario bestimmt werden muss, um dann das Ansprechvermögen für eine bestimmte Messung abschätzen zu können. Für eine solche Korrektion erweist sich eine frontale Ausrichtung der untersuchten Detektoren zur Quelle am günstigsten, da die Änderung des winkelabhängigen Ansprechvermögens mit größeren Auslenkungen zunimmt [91]. Insbesondere beim microDiamond Detektor ist eine große Richtungsabhängigkeit bei Winkeln um $\pm 90\,^\circ$ gegenüber frontaler Ausrichtung zu beobachten, da das Diamantsubstrat, welches in Abb. 2.3 und Röntgenaufnahmen zu erkennen ist [83], bei diesen Winkeln in den Strahlengang der Primärstrahlung eintritt. Unterschiedliche Messumgebungen wie etwa Luft oder Wasser tragen unterschiedlich stark zur Richtungsabhängigkeit der Detektoren bei. In Wasser können zusätzlich gestreute Photonen, welche damit von ihrer primären Richtung abweichen, das sensitive Volumen erreichen, wodurch die Winkelabhängigkeit abnimmt. Dieser Effekt hängt auch vom Abstand ab, da der Anteil gestreuter Photonen mit der Entfernung zunimmt [98]. Für alle untersuchten Szenarien dieser Arbeit betrugen die Winkelabhängigkeiten $< 0,5\,\%$ für Auslenkungen $< 20\,\%$, so dass diese für kleine Winkel zwischen Detektorachse und Quelle in erster Näherung unter Berücksichtigung im Unsicherheitsbudget vernachlässigbar sind [91].
Zusätzlich zeigt sich, dass ein kleines sensitives Volumen sowie die Verwendung möglichst wasseräquivalenter Bauteile zu einer geringeren Variation der Störungsfaktoren p_{int} und p_{ext} aufgrund eines geänderten Abstands oder Winkels zur Quelle führt. Die Lage des durch die Herstellungsfirma definierten Referenzpunkts einer Ionisationskammer kann die Variation von p_{int} im steilen Dosisgradienten künstlich beeinflussen, was bei den fast identisch dimensionierten Kavitäten der Ionisationskammern PTW 31022 und Exradin A26 zu beobachten ist [61, 91]. Die optimale Lage des Detektor-Referenzpunkts bei Messungen in der Brachytherapie sollte deshalb weiter untersucht werden. Des Weiteren konnte mit dieser Arbeit gezeigt werden, dass für eine möglichst exakte Dosimetrie das sensitive Volumen, d.h. bei Ionisationskammern die luftgefüllte Kavität ohne Totvolumen, zu berücksichtigen ist [61, 91].

6 Fazit

Mit dieser Arbeit wurde ein bestehender dosimetrischer Formalismus auf Grundlage der beschränkten Cema für die hochenergetische Brachytherapie angewandt. Dafür wurden auf die absorbierte Wasser-Energiedosis im perkutanen Co-60 Strahl kalibrierte Detektoren untersucht. Ziel könnte ein Paradigmenwechsel der auf Luftkermaleistung basierenden Dosimetrie hin zur absorbierten Wasser-Energiedosisleistung sein. Für Simulationen des Strahlungstransports wurde die sogenannte Cema Approximation validiert und angewandt. Diese erlaubt es unter anderem, das Ansprechvermögen auch energiedifferentiell zu untersuchen, um damit ein tieferes Verständnis über die Signalerzeugung zu erlangen. Die eigentliche Bezugsgröße bestehender Monte-Carlo Applikationen der Strahlentherapie ist die absorbierte Energiedosis, so dass diese für die Ausgabe der beschränkten Cema erweitert und verifiziert wurden. Bisher wurde die Messung der Wasser-Energiedosisleistung mithilfe von aktiven Festkörperdetektoren über eine Kreuzkalibrierung im Feld des Afterloadingstrahlers realisiert. Hier konnte gezeigt werden, dass sich der vorgestellte Formalismus auch für diese Detektoren innerhalb der ermittelten Fehlerbereiche eignet. Es wurden Referenzbedingungen in Wasser für eine möglichst exakte Dosimetrie in der Brachytherapie untersucht; dabei zeigte sich eine deutliche Abhängigkeit des Ansprechvermögens der Detektoren vom Abstand und der Ausrichtung zur Quelle. Es konnte experimentell gezeigt werden, dass die Vernachlässigung des Totvolumens das Ansprechvermögen über die erweiterte Unsicherheit des Messwerts hinaus verfälschen kann. Um den Einfluss geometrischer Unsicherheiten des Totvolumens zu minimieren, sollten Ionisationskammern in einem größeren Abstand als 1 cm, was bisher aufgrund des TG-43 Formalismus als Referenz gilt, und in einer parallelen oder vergleichbaren Ausrichtung der Zentralachse zur Quellenachse positioniert werden. Der steile Dosisgradient und Vielfachstreuung der Photonen in der Brachytherapie bestimmen die Obergrenze dieses geeigneteren Abstands, da dies das Signal-Rausch-Verhältnis verschlechtert und Abweichungen von den Kalibrierbedingungen zunehmen. Die Richtungsabhängigkeit des Ansprechvermögens wurde in Wasser und Luft mithilfe von MC Simulationen sowie experimentell untersucht. Asymmetrien im Aufbau der Detektoren und die Lage des Detektor-Referenzpunkts bestimmten dabei die Variation des Ansprechvermögens. Bei Messungen mehrerer Strahlerpositionen eignet sich eine frontale Ausrichtung zur Korrektion der Winkelabhängigkeit, da die Änderung mit der Rotation aus frontaler Ausrichtung zunahm. Für kleine Auslenkungen kann die Winkelabhängigkeit unter Berücksichtigung im Unsicherheitsbudget vernachlässigt werden.
Die Ergebnisse dieser Arbeit dienen der genaueren und vergleichbaren Dosimetrie in der Brachytherapie, um für aktuelle und zukünftige Entwicklungen, wie etwa der patient*innenspezifischen Dosisberechnung, messtechnisch gerüstet zu sein.

Literatur

[1]F. Guedea, J. Venselaar, P. Hoskin, T. P. Hellebust, D. Peiffert, B. Londres, M. Ventura, J.-J. Mazeron, E. V. Limbergen, R. Pötter und G. Kovacs, "Patterns of care for brachytherapy in Europe: Updated results", Radiotherapy and Oncology **97**, 514–520 (2010).

[2]IAEA, *Technical Report Series No. 398 Rev. 1 Absorbed Dose Determination in External Beam Radiotherapy*, Techn. Ber. (International Atomic Energy Agency, Vienna, 2024).

[3]R. Nath, L. L. Anderson, G. Luxton, K. A. Weaver, J. F. Williamson und A. S. Meigooni, "Dosimetry of interstitial brachytherapy sources: Recommendations of the AAPM Radiation Therapy Committee Task Group No. 43", Medical Physics **22**, 209–234 (1995).

[4]M. J. Rivard, B. M. Coursey, L. A. DeWerd, W. F. Hanson, S. M. Huq, G. S. Ibbott, M. G. Mitch, R. Nath und J. F. Williamson, "Update of AAPM Task Group No. 43 Report: A revised AAPM protocol for brachytherapy dose calculations", Medical Physics **31**, 633–674 (2004).

[5]IAEA, *Technical Report Series No. 492 Dosimetry in brachytherapy – An International Code of Practice for Secondary Standards Dosimetry Laboratories and Hospitals*, Techn. Ber. (International Atomic Energy Agency, Vienna, 2023).

[6]DIN 6814-3:2016-08, *Begriffe in der radiologischen Technik – Teil 3: Dosimetrie*, DIN-Norm (Beuth Verlag GmbH, 2016).

[7]DIN 6803-2:2020-12, *Dosimetrie für die Photonen-Brachytherapie – Teil 2: Strahler, Strahlerkalibrierung, Strahlerprüfung und Dosisberechnung*, DIN-Norm (Beuth Verlag GmbH, 2020).

[8]T. Sander, "Air kerma and absorbed dose standards for reference dosimetry in brachytherapy", The British Journal of Radiology **87**, 20140176 (2014).

[9]G. H. Hartmann, P. Andreo, R.-P. Kapsch und K. Zink, "Cema-based formalism for the determination of absorbed dose for high-energy photon beams", Medical Physics **48**, 7461–7475 (2021).

[10]V. Kaveckyte, A. Malusek, H. Benmakhlouf, G. A. Carlsson und Å. C. Tedgren, "Suitability of microDiamond detectors for the determination of absorbed dose to water around high-dose-rate ^{192}Ir brachytherapy sources", Medical Physics **45**, 429–437 (2017).

[11]A. A. Schoenfeld, K. Büsing, B. Delfs, N. Chofor, P. Jiang, D. Harder, B. Poppe und K. C. Willborn, "Reference conditions for ion-chamber based HDR brachytherapy dosimetry and for the calibration of high-resolution solid detectors", Zeitschrift für Medizinische Physik **28**, 293–302 (2018).

[12]G. Rossi, M. Gainey, M. Kollefrath, E. Hofmann und D. Baltas, "Suitability of the microDiamond detector for experimental determination of the anisotropy function of High Dose Rate ^{192}Ir brachytherapy sources", Medical Physics **47**, 5838–5851 (2020).

[13]Z. Thrapsanioti, V. Peppa, C. J. Hourdakis, P. Karaiskos, A. Lekatou und E. Pantelis, "Beam quality correction factors for dose measurements around ^{192}Ir brachytherapy sources", Journal of Applied Clinical Medical Physics **26**, e14575 (2024).

[14]F. Araki, T. Kouno, T. Ohno, K. Kakei, F. Yoshiyama und S. Kawamura, "Measurement of absorbed dose-to-water for an HDR ^{192}Ir source with ionization chambers in a sandwich setup", Medical Physics **40**, 092101 (2013).

[15]F. Araki, T. Ohno, K. Kakei und S. Kawamura, "Absorbed dose-to-water measurement of an HDR ^{192}Ir source with Farmer ionization chambers in a sandwich setup", Biomedical Physics & Engineering Express **1**, 037002 (2015).

[16]N. Chofor, D. Harder, H.-J. Selbach und B. Poppe, "The mean photon energy $\bar{E}_{\mathrm{F}}$ at the point of measurement determines the detector-specific radiation quality correction factor $k_{\mathrm{Q,M}}$ in ^{192}Ir brachytherapy dosimetry", Zeitschrift für Medizinische Physik **26**, 238–250 (2016).

[17]L. T. Campos, L. A. G. Magalhaes und C. E. V. de Almeida, "Determination of a beam quality conversion factor from ^{60}Co to ^{192}Ir", Journal of Radiation Research and Applied Sciences **11**, 249–254 (2018).

[18]G. Rossi, "Utilizing Monte Carlo Simulation for advanced dosimetry and verification in high energy photon brachytherapy with ^{192}Ir", Diss. (Medizinische Fakultät der Albert-Ludwigs-Universität Freiburg, 2025).

[19]K. Zourari, E. Pantelis, A. Moutsatsos, L. Sakelliou, E. Georgiou, P. Karaiskos und P. Papagiannis, "Dosimetric accuracy of a deterministic radiation transport based ^{192}Ir brachytherapy treatment planning system. Part III. Comparison to Monte Carlo simulation in voxelized anatomical computational models", Medical Physics **40**, 011712 (2012).

[20]Z. Li, R. K. Das, L. A. DeWerd, G. S. Ibbott, A. S. Meigooni, J. Pérez-Calatayud, M. J. Rivard, R. S. Sloboda und J. F. Williamson, "Dosimetric prerequisites for routine clinical use of photon emitting brachytherapy sources with average energy higher than 50 keV", Medical Physics **34**, 37–40 (2007).

[21]E. S. Moura, J. A. Micka, C. G. Hammer, W. S. Culberson, L. A. DeWerd, M. E. C. M. Rostelato und C. A. Zeituni, "Development of a phantom to validate high-dose-rate brachytherapy treatment planning systems with heterogeneous algorithms", Medical Physics **42**, 1566–1574 (2015).

[22]E. P. Pappas, E. Zoros, A. Moutsatsos, V. Peppa, K. Zourari, P. Karaiskos und P. Papagiannis, "On the experimental validation of model-based dose calculation algorithms for ^{192}Ir HDR brachytherapy treatment planning", Physics in Medicine & Biology **62**, 4160–4182 (2017).

[23]S. M. Seltzer, D. T. Bartlett, D. T. Burns, G. Dietze, H.-G. Menzel, H. G. Paretzke und A. Wambersie, "Report 85a (Revised): Fundamental quantities and units for ionizing radiation", Journal of the ICRU **11**, 7–16 (2011).

[24]W. Schlegel, C. P. Karger und O. Jäkel, Hrsg., *Medizinische Physik: Grundlagen – Bildgebung – Therapie – Technik* (Springer Berlin Heidelberg, 2018).

[25]A. M. Kellerer, "Considerations on the Random Traversal of Convex Bodies and Solutions for General Cylinders", Radiation Research **47**, 359 (1971).

[26]A. Allisy, W. A. Jennings, A. M. Kellerer, J. W. Müller, H. H. Rossi und S. M. Seltzer, "Report 60: Fundamental Quantities and Units for Ionizing Radiation", Reports of the International Commission on Radiation Units and Measurements **os-31**, 4–9 (1998).

[27]S. M. Seltzer, J. M. Fernández-Varea, P. Andreo, P. M. Bergstorm Jr., D. T. Burns, I. Krajcar Bronic, C. K. Ross und F. Salvat, "Report 90: Key Data for Ionizing-Radiation Dosimetry: Measurement Standards and Applications", Journal of the ICRU **14**, 9–13 (2014).

[28]S. M. Seltzer, *Stopping-Powers and Range Tables for Electrons, Protons, and Helium Ions, NIST Standard Reference Database 124*, Techn. Ber. (National Institute of Standards und Technology, 1993).

[29]R. M. Sternheimer, M. J. Berger und S. M. Seltzer, "Density effect for the ionization loss of charged particles in various substances", Atomic Data and Nuclear Data Tables **30**, 261–271 (1984).

[30]P. Andreo, D. T. Burns, A. E. Nahum, J. Seuntjens und F. H. Attix, *Fundamentals of Ionizing Radiation Dosimetry* (John Wiley & Sons, 2017).

[31]M. J. Berger, M. Inokuti, H. H. Anderson, H. Bichsel, J. A. Dennis, D. Powers, S. M. Seltzer und J. E. Turner, "Report 37: Stopping powers for electrons and positrons", International Commission on Radiation Units and Measurements (1984).

[32]F. H. Attix, "Energy imparted, energy transferred and net energy transferred", Physics in Medicine & Biology **28**, 1385–1390 (1983).

[33]H. Bouchard, "A theoretical re-examination of Spencer–Attix cavity theory", Physics in Medicine & Biology **57**, 3333–3358 (2012).

[34]G. H. Hartmann, F. Hensley, R.-P. Kapsch, B. Poppe, O. Sauer, J. Würfel und K. Zink, "Ermittlung der Wasser-Energiedosis nach der Sondenmethode gemäß DIN 6800 Teil 1: Vorschlag für eine Erweiterung der Grundgleichung", Zeitschrift für Medizinische Physik **30**, 24–39 (2020).

[35]S. M. Seltzer, *XCOM-Photon Cross Sections Database, NIST Standard Reference Database 8*, (1987) https://dx.doi.org/10.18434/T48G6X.

[36] A. Bielajew, *Fundamentals of the Monte Carlo method for neutral and charged particle transport* (The University of Michigan, 2001).

[37] I. Kawrakow, E. Mainegra-Hing, D. W. O. Rogers, F. Tessier und B. R. B. Walters, *The EGSnrc code system: Monte Carlo simulation of electron and photon transport*, Report PIRS-701 (National Research Council Canada, 2001-2015 [version 2021]).

[38] G. H. Hartmann und P. Andreo, "Fluence calculation methods in Monte Carlo dosimetry simulations", Zeitschrift für Medizinische Physik **29**, 239–248 (2019).

[39] A. M. Kellerer, K. Hahn und H. H. Rossi, "Intermediate Dosimetric Quantities", Radiation Research **130**, 15 (1992).

[40] F. Salvat, "The PENELOPE code system. Specific features and recent improvements", in SNA + MC 2013 - Joint International Conference on Supercomputing in Nuclear Applications + Monte Carlo, hrsg. von D. Caruge, C. Calvin, C. Diop, F. Malvagi und J.-C. Trama, SNA + MC 2013 (2014), S. 06017.

[41] H. Krieger, *Strahlungsmessung und Dosimetrie* (Springer Fachmedien Wiesbaden, 2013).

[42] J. R. Miller, B. D. Hooten, J. A. Micka und L. A. DeWerd, "Polarity effects and apparent ion recombination in microionization chambers: Polarity effects in microionization chambers", Medical Physics **43**, 2141–2152 (2016).

[43] S. Almaviva, M. Marinelli, E. Milani, G. Prestopino, A. Tucciarone, C. Verona, G. Verona-Rinati, M. Angelone, M. Pillon, I. Dolbnya, K. Sawhney und N. Tartoni, "Chemical vapor deposition diamond based multilayered radiation detector: Physical analysis of detection properties", Journal of Applied Physics **107**, 014511 (2010).

[44] I. Ciancaglioni, C. Di Venanzio, M. Marinelli, E. Milani, G. Prestopino, C. Verona, G. Verona-Rinati, M. Angelone, M. Pillon und N. Tartoni, "Influence of the metallic contact in extreme-ultraviolet and soft x-ray diamond based Schottky photodiodes", Journal of Applied Physics **110**, 054513 (2011).

[45] M. J. Rivard, W. M. Butler, L. A. DeWerd, M. S. Huq, G. S. Ibbott, A. S. Meigooni, C. S. Melhus, M. G. Mitch, R. Nath und J. F. Williamson, "Supplement to the 2004 update of the AAPM Task Group No. 43 Report", Medical Physics **34**, 2187–2205 (2007).

[46] J. L. M. Venselaar, D. Baltas, A. S. Meigooni und P. J. Hoskin, Hrsg., *Comprehensive brachytherapy, Physical and clinical aspects*, Imaging in medical diagnosis and therapy, Formerly CIP Uk (CRC Press, Boca Raton, 2013), 495 S.

[47] J. Pérez-Calatayud, F. Ballester, R. K. Das, L. A. DeWerd, G. S. Ibbott, A. S. Meigooni, Z. Ouhib, M. J. Rivard, R. S. Sloboda und J. F. Williamson, "Dose calculation for photon-emitting brachytherapy sources with average energy higher than 50 keV: Report of the AAPM and ESTRO", Medical Physics **39**, 2904–2929 (2012).

[48] L. A. DeWerd, G. S. Ibbott, A. S. Meigooni, M. G. Mitch, M. J. Rivard, K. E. Stump, B. R. Thomadsen und J. L. M. Venselaar, "A dosimetric uncertainty analysis for photon-emitting brachytherapy sources: Report of AAPM Task Group No. 138 and GEC-ESTRO", Medical Physics **38**, 782–801 (2011).

[49]R. Nath, L. L. Anderson, J. A. Meli, A. J. Olch, J. A. Stitt und J. F. Williamson, "Code of practice for brachytherapy physics: Report of the AAPM Radiation Therapy Committee Task Group No. 56", Medical Physics **24**, 1557–1598 (1997).

[50]L. Beaulieu, Å. C. Tedgren, J.-F. Carrier, S. D. Davis, F. Mourtada, M. J. Rivard, R. M. Thomson, F. Verhaegen, T. A. Wareing und J. F. Williamson, "Report of the Task Group 186 on model-based dose calculation methods in brachytherapy beyond the TG-43 formalism: Current status and recommendations for clinical implementation", Medical Physics **39**, 6208–6236 (2012).

[51]M. J. Rivard, J. L. M. Venselaar und L. Beaulieu, "The evolution of brachytherapy treatment planning", Medical Physics **36**, 2136–2153 (2009).

[52]Å. K. Carlsson und A. Ahnesjö, "The collapsed cone superposition algorithm applied to scatter dose calculations in brachytherapy", Medical Physics **27**, 2320–2332 (2000).

[53]Å. Carlsson Tedgren und A. Ahnesjö, "Optimization of the computational efficiency of a 3D, collapsed cone dose calculation algorithm for brachytherapy", Medical Physics **35**, 1611–1618 (2008).

[54]K. Zourari, E. Pantelis, A. Moutsatsos, L. Petrokokkinos, P. Karaiskos, L. Sakelliou, E. Georgiou und P. Papagiannis, "Dosimetric accuracy of a deterministic radiation transport based brachytherapy treatment planning system. Part I: Single sources and bounded homogeneous geometries", Medical Physics **37**, 649–661 (2010).

[55]O. Chibani und J. F. Williamson, "MCPI: A sub-minute Monte Carlo dose calculation engine for prostate implants", Medical Physics **32**, 3688–3698 (2005).

[56]P. Andreo, D. T. Burns, K. Hohlfeld, M. S. Huq, T. Kanai, F. Laitano, V. G. Smith und S. Vynckier, "Technical Report Series No. 398 Absorbed Dose Determination in External Beam Radiotherapy: An International Code of Practice for Dosimetry Based on Standards of Absorbed Dose to Water", International Atomic Energy Agency, Vienna (2000).

[57]J. Sempau, P. Andreo, J. Aldana, J. Mazurier und F. Salvat, "Electron beam quality correction factors for plane-parallel ionization chambers: Monte Carlo calculations using the PENELOPE system", Physics in Medicine & Biology **49**, 4427–4444 (2004).

[58]DIN 6800-2:2020-08, *Dosismessverfahren nach der Sondenmethode für Photonen- und Elektronenstrahlung – Teil 2: Dosimetrie hochenergetischer Photonen- und Elektronenstrahlung mit Ionisationskammern*, DIN-Norm (Beuth Verlag GmbH, 2020).

[59]DIN 6800-1:2016-08, *Dosismessverfahren nach der Sondenmethode für Photonen- und Elektronenstrahlung – Teil 1: Allgemeines*, DIN-Norm (Beuth Verlag GmbH, 2020).

[60]P. Andreo, D. T. Burns, R. P. Kapsch, M. McEwen, S. Vatnitsky, C. E. Andersen, F. Ballester, J. Borbinha, F. Delaunay, P. Francescon, M. D. Hanlon, L. Mirzakhanian, B. Muir, J. Ojala, C. P. Oliver, M. Pimpinella, M. Pinto, L. A. de Prez, J. Seuntjens, L. Sommier, P. Teles, J. Tikkanen, J. Vijande und K. Zink, "Determination of consensus k_Q values for megavoltage photon beams for the update of IAEA TRS-398", Physics in Medicine & Biology **65**, 095011 (2020).

[61]T. Failing, F. W. Hensley, B. Keil und K. Zink, "Investigations on the beam quality correction factor for ionization chambers in high-energy brachytherapy dosimetry", Physics in Medicine & Biology **69**, 165002 (2024).

[62]G. H. Hartmann und K. Zink, "A Monte Carlo study on the PTW 60019 microDiamond detector", Medical Physics **46**, 5159–5172 (2019).

[63]L. V. Spencer und F. H. Attix, "A Theory of Cavity Ionization", Radiation Research **3**, 239 (1955).

[64]D. W. O. Rogers, I. Kawrakow, J. P. Seuntjens, B. R. B. Walters und E. Mainegra-Hing, *NRC user codes for EGSnrc*, Report PIRS-702 (National Research Council Canada, 2011 [version 2021]).

[65]I. Kawrakow u. a., *EGSnrc C++ class library*, Report PIRS-898 (National Research Council of Canada, 2019).

[66]J. Wulff, K. Zink und I. Kawrakow, "Efficiency improvements for ion chamber calculations in high energy photon beams", Medical Physics **35**, 1328–1336 (2008).

[67]B. Walters, I. Kawrakow und D. W. O. Rogers, *DOSXYZnrc Users Manual*, Report PIRS-794 (National Research Council of Canada, 2021).

[68]G. H. Hartmann und K. Zink, "Decomposition of the dose conversion factor based on fluence spectra of secondary charged particles: Application to lateral dose profiles in photon fields", Medical Physics **45**, 4246–4256 (2018).

[69]G. M. Mora, A. Maio und D. W. O. Rogers, "Monte Carlo simulation of a typical ^{60}Co therapy source", Medical Physics **26**, 2494–2502 (1999).

[70]R. Mohan, C. Chui und L. Lidofsky, "Energy and angular distributions of photons from medical linear accelerators", Medical Physics **12**, 592–597 (1985).

[71]J. Borg und D. W. O. Rogers, "Spectra and air-kerma strength for encapsulated ^{192}Ir sources", Medical Physics **26**, 2441–2444 (1999).

[72]A. F. Bielajew und D. W. O. Rogers, "Presta: The parameter reduced electron-step transport algorithm for electron monte carlo transport", Nuclear Instruments and Methods in Physics Research Section B: Beam Interactions with Materials and Atoms **18**, 165–181 (1986).

[73]I. Kawrakow und M. Fippel, "Investigation of variance reduction techniques for Monte Carlo photon dose calculation using XVMC", Physics in Medicine & Biology **45**, 2163–2183 (2000).

[74]S. Chandrasekaran und S. Shanmugasundaram, "Optimization of variance reduction techniques used in EGSnrc Monte Carlo Codes", Journal of Medical Physics **43**, 185 (2018).

[75]J. Pérez-Calatayud, D. Granero und F. Ballester, "Phantom size in brachytherapy source dosimetric studies", Medical Physics **31**, 2075–2081 (2004).

[76]G. Rossi, M. Gainey, B. Thomann, M. Kollefrath, J. Würfel, B. Allgaier und D. Baltas, "Monte Carlo and experimental high dose rate ^{192}Ir brachytherapy dosimetry with microDiamond detectors", Zeitschrift für Medizinische Physik **29**, 272–281 (2019).

[77]S. N. Rustgi, "Application of a diamond detector to brachytherapy dosimetry", Physics in Medicine & Biology **43**, 2085–2094 (1998).

[78]W. U. Laub, "Comparison of TG-43 dose calculations to pinpoint ion chamber and diamond detector measurements", Physics in Medicine & Biology **47**, N315–N318 (2002).

[79]S. Pojtinger, R.-P. Kapsch, O. S. Dohm und D. Thorwarth, "A finite element method for the determination of the relative response of ionization chambers in MR-linacs: simulation and experimental validation up to 1.5 T", Physics in Medicine & Biology **64**, 135011 (2019).

[80]B. Delfs, I. Blum, T. Tekin, A.-B. Schönfeld, R. Kranzer, D. Poppinga, U. Giesen, F. Langner, R.-P. Kapsch, B. Poppe und H. K. Looe, "The role of the construction and sensitive volume of compact ionization chambers on the magnetic field-dependent dose response", Medical Physics **48**, 4572–4585 (2021).

[81]H. K. Looe, I. Büsing, T. Tekin, A. Brant, B. Delfs, D. Poppinga und B. Poppe, "The polarity effect of compact ionization chambers used for small field dosimetry", Medical Physics **45**, 5608–5621 (2018).

[82]T. Failing, G. H. Hartmann, F. W. Hensley, B. Keil und K. Zink, "Enhancement of the EGSnrc code egs_chamber for fast fluence calculations of charged particles", Zeitschrift für Medizinische Physik **32**, 417–427 (2022).

[83]S. Kampfer, N. Cho, S. E. Combs und J. J. Wilkens, "Dosimetric characterization of a single crystal diamond detector in X-ray beams for preclinical research", Zeitschrift für Medizinische Physik **28**, 303–309 (2018).

[84]F. Garcia Yip, T. Schneider, M. Reginatto, R. Behrens, L. Buermann und F. Grote, "Characterization of small active detectors for electronic brachytherapy dosimetry", Journal of Instrumentation **17**, P03001 (2022).

[85]R. E. P. Taylor und D. W. O. Rogers, "An EGSnrc Monte Carlo-calculated database of TG-43 parameters", Medical Physics **35**, 4228–4241 (2008).

[86]M. Marinelli, G. Prestopino, C. Verona und G. Verona-Rinati, "Experimental determination of the PTW 60019 microDiamond dosimeter active area and volume", Medical Physics **43**, 5205–5212 (2016).

[87]M. J. Berger, J. S. Coursey, M. A. Zucker und J. Chang, *Computer programs for calculating stopping-power and range tables for electrons, protons, and helium ions*, (2005) https://dx.doi.org/10.18434/T4NC7P.

[88]M. Shaw, J. Lye, A. Alves, S. Keehan, J. Lehmann, M. Hanlon, J. Kenny, J. Baines, C. Porumb, M. Geso und R. Brown, "Characterisation of a synthetic diamond detector for end-to-end dosimetry in stereotactic body radiotherapy and radiosurgery", Physics and Imaging in Radiation Oncology **20**, 40–45 (2021).

[89]K. Kawata, T. Ono, H. Hirashima, Y. Tsuruta, T. Fujimoto, M. Nakamura und M. Nakata, "Effect of angular dependence for small-field dosimetry using seven different detectors", Medical Physics **50**, 1274–1289 (2023).

[90]N. Chofor, D. Harder und B. Poppe, "Non-reference condition correction factor k_{NR} of typical radiation detectors applied for the dosimetry of high-energy photon fields in radiotherapy", Zeitschrift für Medizinische Physik **22**, 181–196 (2012).

[91]T. Failing, R. Behrens, F. W. Hensley, B. Keil, T. Schneider und K. Zink, "Angular dependence of detector responses in high-energy brachytherapy", Physics in Medicine & Biology **70**, 115020 (2025).

[92]F. Akbari, "A comprehensive open-access database of electron backscattering coefficients for energies ranging from 0.1 keV to 15 MeV", Medical Physics **50**, 5920–5929 (2023).

[93]I. Sechopoulos, D. W. O. Rogers, M. Bazalova-Carter, W. E. Bolch, E. C. Heath, M. F. McNitt-Gray, J. Sempau und J. F. Williamson, "RECORDS: improved Reporting of montE CarlO RaDiation transport Studies: Report of the AAPM Research Committee Task Group 268", Medical Physics **45**, e1–e5 (2017).

[94]C. Kessler, R. Behrens, A. Kasper und F. Grote, "Key comparison BIPM.RI(I)-K8 of high dose-rate ^{192}Ir brachytherapy standards for reference air kerma rate of the PTB and the BIPM", Metrologia **61**, 06002 (2024).

[95]G. Rossi, T. Failing, M. Gainey, M. Kollefrath, F. Hensley, K. Zink und D. Baltas, "Determination of the dose rate around a HDR ^{192}Ir brachytherapy source with the microDiamond and the microSilicon detector", Zeitschrift für Medizinische Physik **33**, 463–478 (2023).

[96]M. Bambynek, A. Krauss und H. J. Selbach, "Calorimetric Determination of Absorbed Dose to Water for an ^{192}Ir HDR Brachytherapy Source in Near-Field Geometry", in *World Congress on Medical Physics and Biomedical Engineering, 2009, Munich, Germany* (Springer Berlin Heidelberg, 2009), S. 89–92.

[97]L. I. R. García, J. F. Pérez-Azorín, M. Anguiano und A. M. Lallena, "Monte Carlo calculation of charge collection efficiencies in ionization chambers", Physics in Medicine & Biology **66**, 045011 (2021).

[98]H. Safigholi, M. J. P. Chamberland, R. E. P. Taylor, M. P. Martinov, D. W. O. Rogers und R. M. Thomson, "Update of the CLRP Monte Carlo TG-43 parameter database for high-energy brachytherapy sources", Medical Physics **50**, 1928–1941 (2023).

Danksagung

Es gibt viele Menschen, denen ich meinen aufrichtigen Dank für die Hilfe bei der Fertigstellung dieser Doktorarbeit aussprechen möchte. An erster Stelle steht mein Doktorvater Prof. Klemens Zink, der mich mit großer Offenheit angenommen und auf diesem Weg mit Geduld und vielen hilfreichen Ratschlägen begleitet hat. Darüber hinaus gilt mein Dank meinem Co-Betreuer Prof. Boris Keil, der mir in seiner zugewandten Art unkomplizierte Unterstützung geboten hat.

Großen Dank an Dr. Frank W. Hensley für die vielen hilfreichen und anregenden Diskussionen sowie sein langjähriges aufbauendes Mentoring. Und an Prof. Günther H. Hartmann für seine Unterstützung in der herausfordernden Anfangsphase. Bei meinem Mitstreiter Dr. Giulio Rossi möchte ich mich für den motivierenden Austausch, die große Hilfe sowie die schöne gemeinsame Zeit bei Messungen und Veranstaltungen bedanken. Herzlichen Dank richtet sich an die vielen Kolleginnen und Kollegen der PTB in Abteilung 6 und insbesondere Arbeitsgruppe 6.34 für die erfolgreiche Kooperation. Dem Evangelischen Studienwerk e. V. Villigst danke ich für die großzügige ganzheitliche Förderung und das mir entgegengebrachte Vertrauen. Vielen Dank an Prof. Stefan Rieken, Prof. Clemens F. Hess und Bernd Thüne aus der Klinik für Strahlentherapie und Radioonkologie der Universitätsmedizin Göttingen für die gebotenen Freiräume zum wissenschaftlichen Arbeiten sowie zum Ermöglichen der klinischen Messungen. Mein Dank gilt auch den vielen hilfsbereiten und zugewandten Menschen bei Elekta, Standard Imaging und PTW, die mir Messmittel und Bauzeichnungen zur Verfügung gestellt haben.

Meiner Familie möchte ich für den liebevollen Rückhalt und die Unterstützung von Herzen Danke sagen. Meinen Kindern Clara und Friedrich sowie meiner Frau Tomke gilt dabei mein besonderer Dank, die mir mit großer Liebe zur Seite standen und mich oft genug missen mussten.

Ich widme diese Arbeit meinem Vater Dr. Klaus Failing.